Computational Studies of Soot Paths to Cylinder Wall Layers of a Direct Injection Diesel Engine

Wan Mohd Faizal Wan Mahmood

B.Sc, M.Sc

Thesis submitted to The University of Nottingham for the degree of Doctor of Philosophy

June 2011

ABSTRACT

COMPUTATIONAL STUDIES OF SOOT PATHS TO CYLINDER WALL LAYERS OF A DIRECT INJECTION DIESEL ENGINE

Wan Mohd Faizal Wan Mahmood, 2011

The investigation reported in this thesis is concerned with the topic of soot formation and soot particle motion in the cylinder of a light duty automotive diesel engine. CFD has been employed to simulate in-cylinder conditions and to investigate the source of particles which are transferred to the oil. The accumulation of soot in the lubricating oil of diesel engines is one of the factors limiting the interval between oil changes and hence service interval. Soot particles can be transferred to oil film on the cylinder wall layers through the complex motion of the fluid flow in the cylinder. The paths of soot particles from specific in-cylinder locations and crank angle instants have been explored using the results for cylinder charge motion predicted by the Kiva-3v CFD code. Using the velocity fields from the simulation data, massless tracking of the in-cylinder soot particles in space and time is carried out employing a particle tracking with trilinear interpolation technique. From this investigation, new computational codes for the prediction of soot particle paths and soot particle size change along a specific path in a diesel engine have been developed. This investigation is the first numerical study into soot particle trajectories within an engine and thus opens up a novel branch of research of soot formation within internal combustion engines.

Computed soot paths from the investigation show that soot particles formed just below the fuel spray axis inside the middle bowl area during early injection period are more likely sources of soot particles on the cylinder wall layers than those formed later.

Soot particles that are formed above the fuel axis have less tendency to be transported to the cylinder wall layers thus are not likely to be the main source of soot at the cylinder walls. Soot particles that are from the bowl rim area are found to be another source of soot transfer to the boundary layer, as they are directly exposed to reverse squish motion during the expansion stroke. Soot particles that are formed near the cylinder jet axis during fuel injection tend to move into the bowl. These soot particles are found to be from the relatively less concentrated area. In contrast, particles from the most concentrated areas tend to be moving into the bowl and pose least risk of contaminating oil films on the liner.

Sensitivity studies of soot particle paths to swirl show that engine operating with low swirl ratios are more vulnerable to soot in oil problem as low swirls cause the bulk fluid flow to be moving closer to the cylinder walls due to fuel jet velocity and reverse squish motions. Decreasing the spray angle lessens the possibilities of soot particles from being transported close the cylinder wall layers while increasing the spray angle increases the possibilities of soot from the bowl region to be transported close to the cylinder wall layers.

The temporal and spatial evolution of soot particle size can be predicted by using the history of temperature, pressure and gas species along the paths. An explorative investigation has been carried out to determine the most suitable method to tackle this soot particle evolution. With proper multipliers, all approaches perform quite satisfactorily in terms of predicting the trend of size change. Soot particles that are likely to be transferred to the cylinder wall layers are predicted to change in size parallel to the average mass profile in the whole cylinder where they quickly peak to maximum at around 18° CA ATDC, and gradually decrease in size through EVO.

ACKNOWLEDGEMENTS

Words are not enough to express my gratitude towards Professor Paul Shayler whose continuous guidance, support and encouragement throughout the course of the studies made this thesis possible.

Thanks to Dr. Bonatesta and Dr. La Rocca for giving input and ideas how to move forward with this study. Thanks to all my research colleagues for their support, encouragement and humour both during difficult and relaxed times.

I am grateful to my family and friends for their love, support and understanding throughout my studies. My parents, Wan Mahmood and Wan Sepiah deserve a special thank from me as without their unwavering love and understanding, I might not be so strong as to finish this study. Finally, I would like to thank my wife, Noralifah for her love and support even during the most trying time for her. Thanks to my daughters Wan Mariah and Wan Qareehah; and my sons Wan Abdul Qayyum and Wan Abdul Matin for cheering me up all the time.

I am indebted to Islamic Development Bank and Universiti Kebangsaan Malaysia for their financial support during this study.

CONTENTS

NOMENCLATURE

A_f	Calibration parameter for soot formation reaction
A_{O_2}	Calibration parameter for oxygen soot oxidation reaction
A_{OH}	Calibration parameter for OH soot oxidation reaction
A_p	Particle surface area
a	Acceleration
C_c	Cunningham slip correction factor
C_D	Drag coefficient
CFL	Courant-Friedrichs-Lewy criterion
D_f	Fractal dimension
D_i	Initial diameter of soot particle
D_{i+1}	Diameter of soot particle at the next time step
D_{soot}	Nominal diameter of soot particle
d_p	Particle diameter
dt	Time step interval
Δt	Time step interval
Δx	Nodal spacing
E_f	Activation energy for soot formation
E_o	Activation energy for soot oxidation
F_D	Drag force

F_i	Net soot formation rate at each time step
k_A, k_B, k_T, k_A	Empiral rate constants for Nagle and Strickland-Constable soot oxidation mechanism
k_1, k_2, k_3, k_4	Slopes for the use of Runge-Kutta method
Kn	Knudsen Number
L	Engine stroke
λ	Gas mean-free path
M_c	Molecular weight of carbon atom
M_{fv}	Concentration of fuel vapour
M_p	Mass of soot particle
M_{sf}	Concentration of soot formed
Ms_i	Initial net mass of soot in cell
Ms_{i+1}	Net mass of soot in cell at the next time step
Msp_i	Initial mass of soot particle
Msp_{i+1}	Mass of soot particle at the next time step
Msp_{i-1}	Mass of soot particle at the previous time step
MW_{OH}	OH molecular weight
m	mass
m_{fuel}	Mass of fuel vapour
m_{soot}	Mass of soot
μ_f	Kinematic viscosity of carrier fluid
N	Speed of engine in revolution per second
N_A	Avogadro Number

N_i	Initial soot number density
P	Pressure
p	Oxygen partial pressure
R	Universal gas constant
Re	Reynolds Number
$\dot{R}_{NSC}$	Soot surface mass oxidation rate based on Nagle and Strickland-Constable soot oxidation mechanism
$\dot{R}_{NSC}$	Net soot oxidation rate by OH
ρ_{soot}	Soot density
ρ_g	Gas density
ρ_p	Particle density
ρ_{sp}	Soot particle density
s	Distance
s_n	Soot particle position
s_{n+1}	Soot particle position at the next time step
T	Temperature
t_n	Current time step
t_{n+1}	Next time step
τ_p	Particle relaxation time
u	Velocity vector
V_p	Particle volume
ν	Average piston velocity
ν_f	Final velocity of a particle

ν_i	Initial velocity of a particle
ν_p	Particle velocity
ω_s	Angular velocity of solid-body rotating flow
X_{O_2}	Oxygen molar fraction
x	fraction of carbon surface covered by a more reactive type

ABBREVIATIONS

ALE	Arbitrary Lagrangian Eulerian
ASI	After Start of Injection
ATDC	After Top Dead Centre
BDC	Bottom Dead Centre
BTDC	Before Top Dead Centre
CA	Crank Angle
CFD	Computational Fluid Dynamics
DI	Direct Injection
EGR	Exhaust Gas Recirculation
EU	European Union
EVO	Exhaust Valve Opening
FV	Fractional Volume
GB	Gigabytes
GHG	Greenhouse Gases
HC	Hydrocarbon
HCCI	Homogeneous Charge Compression Ignition
IDI	Indirect Injection
IVC	Inlet Valve Closing
L/D	Length to Diameter

LANL	Los Alamos National Laboratory
NSC	Nagle and Strickland-Constable
PAH	Poly-aromatic hydrocarbons
PM	Particulate Matters
RK	Runge-Kutta
RK1	First-order Runge-Kutta
RK2	Second-order Runge-Kutta
RK4	Fourth-order Runge-Kutta
SMR	Sauter Mean Radius
SOI	Start of Injection
SR	Swirl Ratio
TAB	Taylor Analogy Breakup
TDC	Top Dead Centre

CHAPTER 1

INTRODUCTION

1.1 Background

Diesel engines are widely used in heavy-duty road and off-road vehicles, sea vessels and power generation units due to their fuel efficiency and long service life. In recent decades, diesel engines have been used in light-duty automotive applications. In some European countries, more than 50% of new passenger cars and light duty commercial vehicles have diesel engines. The negative aspects about diesel engines are their high nitrogen oxides (NO_x), particulate matter (PM) and noise emissions.

PM from diesel exhaust contains solid soot particulates that are harmful to the environment [1-3] and human health [4-6]. It has also been well-known, see [7-9] for example, that in-cylinder soot produced during combustion in a diesel engine can accumulate in the lubricating oil, causing changes in oil quality which can limit the interval between oil changes and hence service interval. To extend service interval of a diesel engine, oil contamination by soot must be reduced. One of the ways to reduce this oil contamination is to minimise the transfer of soot particles to the cylinder wall layers which is a major contributor to the soot in oil as the soot is carried into the oil by the scraping action of the piston rings [10]. To achieve this, further understanding of in-cylinder soot particle movement is necessary.

This thesis will partly deal with the problem of soot contaminating the lubricating oil. This is done through investigation of the movement and evolution of in-cylinder soot particles during a part of engine cycle. The investigation particularly focuses on the soot particles that are likely to be transferred to the cylinder wall layers. The investigation

was carried out computationally employing computational fluid dynamics (CFD) code and a range of Matlab programming routines which will be explained in greater details in this thesis.

These new computational codes and routines are used to investigate the sources of soot particles near the cylinder wall by predicting the trajectories of soot particles from the point they are formed or any point within the engine cylinder. These new codes also predict size change of soot particle on a specific path. As to the author's knowledge this investigation is the first numerical study of soot particle movement in a diesel engine, it is envisaged that the findings of this investigation should be useful to improve the understanding of soot dynamics and soot formation process within internal combustion engines. This numerical study can be a new platform for further research on soot formation process in the internal combustion engine field.

The following sections outline the nature and current status of research in the area of diesel combustion. This chapter also highlights the objective of the thesis and ends with the thesis layout.

1.2 Energy and Environment

As the world population grows and people's lifestyles change, the global demand for energy increases. The ever-increasing demand for energy from fossil fuels has resulted in worsened environmental pollution and global warming problems [11]. The current level of oil production also increases our anxieties over the impending fossil fuel depletion [12]. With these concerns, ongoing research on reducing pollutions, developing energy-efficient systems and developing renewable fuel technologies are considered equally important.

By Rio Convention's definition [13], sustainable development is "the development that meets the needs of the present without compromising the ability of future generations to meet their own needs". This definition can be interpreted that our

efforts to improve the existing technologies and to develop renewable fuel technologies will help future generation in two ways. Firstly, the energy resources we conserve and the ecological habitat that we protect now can be spared to be used by them in the future. Secondly, the renewable fuel technologies that are being developed will be the basis for the new fuel infrastructures for the future. In the spirit of this definition, the present investigation of soot in oil problem was carried out.

1.3 Combustion Research

As the combustion of fossil fuel is still likely to continue as one of the main sources of energy well into the 21st century [11], combustion research will remain vital. Studies and investigations of the correlations of operating conditions with combustion and emission characteristics must constantly be pursued to improve our understanding of various combustion systems.

Recent years have seen many improvements in the way combustion investigations are carried out. Advances in instrumentation and modern computer allow researchers to gather combustion data which are more comprehensive and detailed [14]. To obtain further details of fuel and gas dynamics inside a combustion chamber, researchers have non-intrusive optical and laser diagnostic tools at their disposal. The implementation of these various advanced methods have actually increased our understanding of the characteristics of combustion, flow field and emission characteristics, both quantitatively and qualitatively, in many combustion systems. Yet, the experimental measurements are sometimes invasive, complicated to set up and fairly costly.

Notwithstanding the advances of experimental techniques, understanding of combustion and emission processes is far from complete. Even with probing or imaging capabilities, intrusive or non-intrusive, the experiments on internal combustion engines can only provide information of properties at restricted volumes in the combustion chamber. These are among the issues that are encountered by experimentalists. To a certain extent, these issues can be addressed by computational studies.

CFD is capable of overcoming some of the limitations in experimental techniques and can provide reasonable prediction of the actual combustion process and the interactions of species inside the combustion chamber. The accuracy of the prediction, however, depends on the complexity of the sub-models used in the code and the capacity of the computer in use.

Although some organisations have developed their own CFD codes, commercially available CFD codes such as FLUENT, STAR-CD, CFX, PHOENICS, CHEMKIN-PRO and FLOW-3D are widely used. The usage of these in universities is relatively restricted due to high cost of licensing and limited availability of code adaptation and development prospect to the researchers. Unlike the commercial codes, Kiva CFD code, which was first developed by a fluid dynamics group at Los Alamos National Laboratory (LANL) in the early 1980s [15], has open architecture that allows researchers to understand, investigate and amend the codes with minimal initial cost. This thesis reports the findings obtained from the use of a relatively recent Kiva code, Kiva-3v Release 2.

1.4 Pollutions from Combustion Process

Combustion systems burning fossil fuels in general emit pollutants which include particulate matters (PM) such as soot, fly ash, metal fumes, various aerosols; sulfur oxides, unburned and partially burned hydrocarbons (HC), oxides of nitrogen (NO_x), carbon monoxide, and greenhouse gases (GHG) such as CO_2 and N_2O [16].

In the transport sector, the combustion products emitted from exhaust tailpipes of diesel and gasoline engines become a major source of urban air pollution. The problem with simultaneous reduction of soot and nitrogen oxides for which diesel engines are infamous is a hot topic pursued by engine researchers. High PM emission is one of the problems that deter the widespread use of diesel engines in transportation sector. Soot which forms a major part of PM emitted from diesel engines pollutes the environment and may have caused the exacerbation of diseases related to the respiratory system. In a

more immediate effect, soot particles formed in the engines can easily find their way into engine oil, change the properties of the oil, and thus, increase the engine wear and shorten engine's service interval.

1.5 The Future of Diesel Engines

In transport applications, diesel engines account for a sizeable share of the engine market. In the European Union (EU) for example, diesel powered passenger cars have surpassed the market performance of gasoline powered cars and now account for more than half (53%) of the EU new car market share in 2007 [17]. This rapid growth is due to advantages of modern high-speed diesel engine in terms of fuel economy, remarkable low-end torque and overall performance [18]. Other factors that may have contributed to the growths are more well-informed consumers about the advantages of diesel engines, unequal taxation system and increasing fuel prices. With continuing improvement and progress in the designs of overall combustion systems, diesel engines would remain as one of the main prime movers in the medium term and have a potential to be used in hybrid vehicles to achieve lower emission target in the longer term.

1.6 The Importance of Soot Particle Size and Numbers

The knowledge of soot particle size and its number distribution is important in both areas, environmental and diesel engine maintenance. The importance of this is demonstrated in the legislation implementation draft of Euro 5/6, where a particle number emission limit of 5×10^{11} km^{-1} has been proposed [19]. The key reason for going from mass to number limit is the health hazard posed by the smallest particles which contribute little to mass emitted [7]. However, with current measurement technology, smaller particles could pass through measuring equipment undetected thus giving rise to the concern of meaningless soot emission legislations.

Soot particle size and number distribution also influence the behavior of particles in the environment and within the engine itself. Particle size influences the

environmental impacts of engine exhaust particles in several ways: it influences the atmospheric residence time of the particles, the optical properties of the particles, the particle surface area and ability to participate in atmospheric chemistry, and the health effects of the particles [7]. In the engine environment, soot particle size and its distribution influence how the soot particles grow from nucleation, how they coagulate, agglomerate and oxidize, and finally how the soot particles are transferred to the liner before they are scraped into the engine oil. The size and distribution of in-cylinder soot particles, during the engine cycles, influence the size of soot particles at the exhaust tailpipe. It also affects the interactions between the in-cylinder soot particles and the cylinder wall which may in turn influences the amount of soot entry into the engine oil. Due to these, the investigation of in-cylinder soot particle size and distribution is valuable.

1.7 Soot Modelling Studies

Numerous experimental studies reported in [20-26] have been carried out to measure in-cylinder and engine-out primary soot particle size and its distribution in diesel engines. However, due to experimental limitations, the information from these investigations is not temporally and spatially complete. Modelling studies have also been carried out extensively to overcome the shortcomings of experimental studies. However, the results of most modelling studies have been concentrated on the soot mass and concentration inside the combustion chamber [27-30]. More recently, soot modelling studies that estimate soot particle size distribution and soot particle number density have been reported [31-35].

Several soot models that have been used in diesel engine investigations shall be reviewed in more detailed in the next chapter. In the work carried out by the author, a two-step soot formation model has been used. This was previously implemented in the Kiva-3v CFD code used within the Engine Research Group (ERG) of University of Nottingham [36]. Soot formation and oxidation was represented using a two-step model which combined Hiroyasu's soot formation [37] and Nagle and Strickland-Constable

[38] and Neoh's soot oxidation [39] rate expressions. This allowed prediction of only soot mass distribution throughout the cylinder as function of crank angle. In this model soot formation rate varies only with fuel vapour concentration, in-cylinder pressure and temperature. It shows no influence of the type, composition and structure of fuel used. In addition, the soot oxidation depends only on oxygen partial pressure and soot mass. Nor are the intermediate chemical and physical processes of soot particle formation such as pyrolysis, nucleation, surface growth, coagulation and agglomeration considered. As a consequence, it lacks the capability of providing information on size and numbers of in-cylinder soot particles and other intermediate chemical species. Moreover, the graphical results obtained from the simulation only show the soot cloud at different instants and locations without clear indication of the soot particles movement in the cylinder.

The overall objective of the present study is to add to the previous mass-based in-cylinder soot distribution study, the additional capability of predicting the paths travelled by soot particles and their changes in size along the paths without modifying its mass-based simulation prediction. This approach is believed to be less complex than detailed chemical models or stochastic numerical methods studied by others. Furthermore, this approach provides the continuity in the ongoing soot formation research in this group without altering the previous modelling results.

1.8 Nature of Investigation and Thesis Objectives

The objective of this PhD is to gain a deeper understanding of the in-cylinder soot behaviour that comprises of soot movements, and soot evolution in terms of size, by a computational investigation. Specific objectives are listed as:

a) To analyse the global characteristics of in-cylinder conditions and examine how these conditions contribute to the overall process of soot formation and its in-cylinder distribution with the aid of Kiva-3v Release II CFD code and EnSight post-processing techniques.

b) To further analyse the mass-based in-cylinder soot distribution obtained from CFD simulations with regard to the influence of local properties to the local soot formation process. This was achieved by fragmenting the cylinder into smaller fractional volumes and averaging the local in-cylinder quantities in the volumes.

c) To investigate the spatial and temporal movement of in-cylinder soot particles. In particular, the movement of soot particles from specific locations in the cylinder at specific instants is investigated, assessing the likelihood of those particles being transported to the cylinder wall layers. This objective represents a first step into a complex analysis that aims to track soot particles as well as their evolution along the paths during the combustion process. For this reason an in-house MATLAB code was developed and exercised.

d) To predict the soot particle size and its distribution in the engine cylinder, particularly near the cylinder boundary layer. This is carried out by estimating soot formation and oxidation rates using the quantities obtained from the soot particle paths history.

e) To study the influence of changing initial swirl ratios and spray angles on the soot particle paths and to investigate the possibility of soot transfer to the cylinder wall layers with the changed parameters.

1.9 Layout of Thesis

Following this chapter, a literature review on soot formation and oxidation processes, soot models, soot particle tracking, in-cylinder fluid motion, soot in oil and soot movement is presented in Chapter 2. Chapter 3 is written to describe the computing facilities and modelling setups of the present study. Assumptions used in this study are assessed and discussed in this chapter. Comparison of global and fractional volume in-cylinder characteristics are carried out and discussed in Chapter 4. The investigation of

convergence of soot particle paths is reported in Chapter 5. Further results of the analysis of soot particle paths behaviour can be found in Chapter 6. Soot particle evolution is described next in Chapter 7 where several approaches are discussed on the prediction of the size of soot particles along specific paths. Selected parametric studies have also been carried out and reported in Chapter 8. Chapter 9 will end this thesis with discussion, suggestion for further works and conclusions.

CHAPTER 2

LITERATURE REVIEW

2.1 Introduction

Air pollution greatly affects human health, vegetation, eco-systems and building materials. One of the major sources of air pollution is on-road vehicles which include light and heavy duty vehicles. The air pollutants that carry the most serious environmental and health problems are nitrogen oxides (NO_x) and particulate matters (PM). Carbon monoxide (CO), hydrocarbon (HC) and sulfur dioxide (SO_2) are also of concern despite being so to a lesser extent. Some statistics stated in the following paragraph are of use to appreciate the gravity of the problems.

In Europe, it was reported that NO_x emission from mobile sources (road, air and water) was as high as 57% of the total NO_x emission [40], PM_{10} (particulate matters with size less that 10 μm) from road transport was 25%[41], and SO_2 emission from road transport was 3% [42]. In the USA's 1999 National Emissions report, on-road vehicles produced 34% of total NO_x, 10% of total $PM_{2.5}$ (particulate matters with size less than 2.5 μm) , 51% of total CO and 29% of total HC [43]. From these statistics, it is apparent that the transportation sector is one of the major contributors of air pollution.

2.2 Emission Legislations

Various agencies and bodies have been trusted to manage air pollution in each of the above regions. They are responsible in formulating the emission regulations and legislations. The most stringent emission regulations are practiced in Europe, USA and Japan, and followed accordingly by other countries. In Europe, the European Union (EU)

has been using Euro Emission Standards since 1992. Details of Euro emission standards are shown in Table 2.1. With imminent Euro 5 standards coming into force, car manufacturers are required to reduce NO_x and PM limit for diesel engines, by 28% and 80% respectively. Consequently, research to reduce both NO_x and PM simultaneously is being carried out rigorously by car manufacturers and research institutions alike.

2.3 Strategies to Reduce NO_x and PM Emissions in Diesel Engines

The problem of reducing both NO_x and PM is complicated in diesel engines due to the general NO_x-soot trade-off relation. Simultaneous NO_x and PM reduction can be achieved to some extent by the improvement in engine technologies, such as homogeneous charge compression ignition (HCCI), but to pass the future emission legislations, the requirement of aftertreatment devices is to be expected [44]. A diesel particulate trap may be used to limit PM emission, and a lean NO_x trap may be used to limit NO_x emissions. Both require intermittent regeneration processes which incur a fuel consumption penalty on top of the cost of the components themselves and any service requirements. Thus, the efforts to reduce emissions through improvement of engine design and combustion technologies are essential.

Exhaust gas recirculation (EGR) is another common technology that can reduce the emissions of NO_x effectively. However, the use of EGR results in an increase in PM, hence soot emissions [44]. The investigations by modelling and experiments on EGR influence on soot emissions have been done by many researchers [27-30]. Another method to reduce NO_x, which has been given much attention, is delaying start of injection (SOI). However, this method, like EGR, causes an increase in soot emissions [27, 28, 30, 35, 45].

Other techniques to reduce soot emissions pursued by researchers are increasing injection pressure [29, 30, 45], increasing boost pressure [30], increasing air to fuel ratio [35], and controlling mixing and swirl ratio [30]. In addition, Hsu [45] outlines several other factors that influence the emission of soot, which are bowl shape, location of

injection spray, injection flow rate which is normally caused by manufacturing variation, secondary injection, injector sac volume and injector hole length to diameter (L/D) ratio. Hsu [45] also mentions that lowering inlet air temperature in turbocharging diesel engines and using higher engine compression ratio can reduce NO_x emission and minimize loss in fuel efficiency.

Shayler et al. [46] investigated a split main with a pilot injection fuel injection strategy to optimize emissions and fuel consumption. The variables investigated are ratio of first to second part of the main injection, the separation between injections, the timing of the start of main injection and rate of EGR while pilot injection quantity and timing were fixed. This multiple injections strategy is capable of reducing both soot and NO_x but with higher fuel consumption, hence further optimization is required.

Kawatani et al. [47], as illustrated in Figure 2.1, specifically stated that the strategy to reduce soot is by improving the diffusion combustion by way of optimizing air motion in cylinder as well as injection timing and rate. Kitamura et al. [48] also specified that three main combustion concepts to reduce soot were controlling combustion temperature, improving fuel charge mixture, and reformulating of fuel composition. These combustion strategies and concepts, which encapsulate all the techniques mentioned in the previous section, becomes the basis for further research in spray combustion with regard to soot formation in diesel engines.

2.4 Diesel Particulate Matters

Diesel particulate matter is a complex mixture of organic and inorganic compounds and gas, liquid and solid phase materials [49]. Organic or hydrocarbon compounds include aldehydes, alkanes and alkenes and aromatic compounds. Inorganic compounds include sulfur, oxygen, carbon monoxide, elemental carbon, and oxides of nitrogen (NO_x). The gas phase emissions include NO_x, CO, and SO_2. The solid phase emissions are made up of small spherical carbon particles (soot) while the liquid phase emissions are composed of the organic or hydrocarbon component and sulphate. Some of

the hydrocarbons may be found adsorbed onto the spherical carbon particle and some may be in the gas phase [49]. Figure 2.2 shows the diesel exhaust mixture more clearly.

In measurements of heavy-duty diesel vehicle emissions reported by Lowenthal et al. [50], particulate matter was found to be comprise of nitrate (0.9%), sulphate (9.2%), ammonium (0.31%), organic carbon (29.6%) and elemental carbon (53.4%). This is comparable to the data obtained by Kawatani et al. [47] which showed that soot component (or elemental carbon) made up 43% and 64% of total PM in two cases that they investigated as displayed in Figure 2.3. In Tree and Svensson review paper [51], the density of soot is reported to be in the range of 1.8 – 2.0 g/cm^3 and primary soot particle sizes range from 20 to 70 nm.

2.5 Soot Formation and Oxidation

Soot is formed in the fuel-rich region [16] as a result of high-temperature liquid fuel pyrolysis and by accumulation of oxygen depleted fuel vapour due to improper mixing [52]. To model the soot process in a diesel engine, understanding of how the process actually takes place during the combustion is essential. In simple steps, the soot process can be divided into soot formation and soot oxidation. Review of a few literatures on soot basics [51, 53-55], its formation process can be further divided into i) pyrolysis, ii) formation of precursors iii) particle nucleation, iv) particle condensation, v) particle surface growth, vi) particle coagulation, and vii) particle agglomeration.

2.5.1 Pyrolysis

Pyrolysis is the process of fuels changing their molecular structure in the presence of high temperature without significant oxidation even though oxygen species may be present [51]. This process produces unsaturated hydrocarbons, polyacetylenes and other aromatic compounds such as benzene and phenyl. These molecules then grow into two-dimensional poly-aromatic hydrocarbons (PAH) [55].

2.5.2 Formation of Precursors

At this stage PAH with molecular weight of 500-1000 amu are formed. These larger PAH molecules are formed through reactions of PAH-PAH and the addition of acetylenes onto PAH molecules [54]. Combination of larger PAH molecules then form two-dimensional PAH which will be the precursors for soot nucleation.

2.5.3 Soot Particle Nucleation/ Inception of Particles

The topic on soot particle inception is still debatable. Widely accepted by people in the field, particle inception is a process where the first particle arises from the smaller fuel molecules after the fuel is oxidized and/or pyrolysed [53]. It is when the two-dimensional PAH merge into three-dimensional particle [55] where mass is converted from molecular to particulate system [54]. Details of chemical reactions at this stage are still poorly understood.

According to Amann et al. [56], there were at least eight theories that have been advanced about soot nucleation. Theories such as thermal cracking, condensation reactions and polymerization, and dehydrogenization can be found in other review papers. Amann et al. [56] also stated that the production of soot depends on formation temperature. It is reported that the soot nucleation begins around 1400 K while soot burnout stops below 1300 K [51]. At the lowest temperatures, only aromatics or highly unsaturated aliphatics of high molecular weight are very effective in forming solid carbon through pyrolysis. At intermediate temperatures between 1400 K and 1750 K, different chemical paths are followed for producing soot. At extremely high temperatures, soot nucleation process involves carbon vapour. A reaction mechanism proposed by Graham et al. [57] supports the production of soot in the low and intermediate formation temperature region which is more relevant in the study of soot formation in diesel engines. Figure 2.4 shows the proposed reaction mechanism for the production of soot.

Similarly, at least in the lower temperature region, Kennedy [58] illustrates the soot nucleation process very clearly in the following way; as hydrocarbons pyrolyse, they

produce primarily smaller hydrocarbons (aliphatic hydrocarbons), in particular acetylene. Then, the first aromatic species is formed from these aliphatic hydrocarbons, which marks the initial step of the production of soot. Then, the aromatic species grow by the addition of other aromatic and smaller alkyl species to form larger polycyclic aromatic hydrocarbons (PAH). Continued growth of PAH leads eventually to the smallest identifiable soot particle with diameter of the order of 1 nm with the mass of around 1000 amu.

Haynes and Wagner [53] described the soot particle nucleation as the first condensed phase material that arises from the fuel-molecules via their oxidation and/or pyrolysis products. Such products typically include various unsaturated hydrocarbons, particularly acetylene and its higher analogues (C_nH_{2n-2}); and polycyclic aromatic hydrocarbons (PAH). These two types of molecules are often considered the most likely precursors of soot in flames. The condensation reactions of gas phase species such as these lead to appearance of the first recognizable soot particles (soot nuclei) with size of $d < 2$ nm.

2.5.4 Condensation

This stage is similar to the surface growth stage where smaller molecules of two-dimensional PAH condense on newly-formed three-dimensional soot particles to form bigger soot particles [55]. This condensation process is a process where a chemical species from the gas phase sticks to the surface of soot particles not through chemical reaction but through the weaker van der Waals force [59].

2.5.5 Soot Particle Surface Growth

The majority of soot mass is generated by this process. It involves the attachment of gas phase species to the surface of the particles and their incorporation into the particulate phase. Surface growth occurs when gas phase material is added through chemical reactions with active sites on the soot particles and it is generally agreed that the major growth species in hydrocarbon flames is acetylene (C_2H_2) [58].

2.5.6 Soot Particle Coagulation

During soot particle growth process, surface growth occurs in conjunction with coagulation. When particles are small and surface growth is active, collisions between particles generally lead to the formation of a larger spheroid via the physical process of coagulation [58]. Soot particle coagulation is a physical process that reduces the numbers of soot particles but maintains the total of soot mass.

2.5.7 Soot Particle Agglomeration

Soot particle agglomeration is the extension of soot particle coagulation process. In the early stage when the soot particles are still soft, collision of two soot particles may result in their combination into a single bigger spherical particle. This process can be regarded as soot particle coagulation. At a later stage, when soot particles start to solidify before collision, the collision may cause these particles to form a cluster of soot which may not be spherical. At a final stage, the soot particles may form a chain of discrete spherules which is likely to be due to electrostatic activity [56].

2.5.8 Soot Particle Oxidation

Soot oxidation can occur at anytime during soot formation process, from fuel pyrolysis to agglomeration process. Soot particle oxidation takes place when the temperature is above 1300 K [51]. Oxidation is a two stage process where chemical attachment of the oxygen to the surface (absorption) occurs, and second, desorption of the oxygen with the attached fuel component from the surface as a product [51]. Under lean conditions, oxidation of soot occurs as a result of attack by molecular oxygen, O_2, and OH radical, and under fuel-rich and stoichiometric conditions, OH is likely to dominate the soot oxidation process [51]. However, Haynes and Wagner [53] state that only about 10-20% of all OH collisions with soot are effective at gasifying a carbon atom. Under some conditions, other oxygenated species such as O atom, H_2O and CO_2 may play roles in the soot oxidation [58].

2.5.9 Summary of Soot Process

All of these processes involve a complex series of chemical and physical processes which may occur concurrently in a given elemental mixture packet within the diesel combustion space [56]. To make it even more complex, due to both the heterogeneous nature of the mixture and the duration of fuel injection, different processes are in progress in different packets at any given instant [56].

Figure 2.5 displays a qualitative indication of the changes that occur as a function of time in a premixed flame especially during nucleation and surface growth. Taking all processes into consideration, the elementary soot particles from various combustion processes such as furnace flames, piston engines, turbine combustors and premixed flames under normal operating conditions do not show much variation and they exhibit a log-normal distribution with the size range of 20-40 nm [53]. Table 2.2 shows size of primary and agglomerated soot particles from different combustion systems with different measuring methods.

2.6 Soot in Diesel Engines and Factors Influencing Its Formation

Haynes and Wagner [53] explained that the soot emissions from these engines are influenced by many factors: spray atomization and configuration, air motion, state of turbulence, pressure etc., similar with continuous spray flames. Time-resolved measurements of the soot concentration made using UV-light absorption showed that soot formation commences in the region of the spray cone immediately after ignition. The soot concentration increased rapidly to its maximum ($>10^{-7}$ gm/cm^3) just 5°CA later, or 14°CA after SOI. Turbulent mixing due mostly to swirling air supply, ensures an even soot distribution at 21°CA after SOI. Later in the cycle, the soot comes into contact with oxygen-containing regions, and it burns out. An individual spherical unit of soot is typically 30 nm in diameter. The agglomeration of the primary particles begins within the combustion chamber within 50°ATDC, and further agglomeration is likely to occur in the exhaust and sampling system. This explanation was based on experimental results by

Greeves and Meehan [60], but it was not clearly shown how the soot particles form and grow during the combustion in the engine.

The conceptual model of soot formation in direct injection diesel engines proposed by Dec [61], which is based on laser-sheet imaging, has been widely cited as improving understanding of soot formation mechanism in diesel engines. This model is based on experimental results on a Cummins DI diesel engine at an engine speed of 1200 rpm. Start of injection was 11.5° before top-dead centre (BTDC) and injection duration was around 20° crank angles.

In the illustration of the conceptual model as shown in Figure 2.6, ignition starts at around 4.0° after start of injection (ASI) and soot formation occurs at 6.0° ASI with the existence of small particles throughout the large portions of the downstream region of the fuel jet. These soot particles are formed from the fuel-rich premixed burn. By 6.5° ASI, soot is found throughout the cross section of the downstream region of the jet. At this point, larger soot particles are also observed at the periphery of the fuel jet. This suggests that the effect of the diffusion flame is at play here in the soot formation process at this region.

Between 7.0°-9.0° ASI, that is, during the last part of premixed burn spike, the soot concentration continues to increase throughout the cross section of the sooting region with the greatest increase being toward the leading edge where the head vortex is forming. Whereas, presumably due to turbulent mixing, the bigger soot particles at the jet periphery become distributed inward without spreading into the central region where smaller soot particles exist. The soot particles in the region of head vortex are found to be even larger than the ones at the periphery. Towards the end of the premixed burn as the last of the premixed air is consumed, the small soot particles present throughout the cross section extending to the jet upstream.

From 9.0° ASI to the end of injection at about 18.5° ASI, where the combustion transitions to being purely mixing-controlled, the overall appearance of the jet shows only

moderate changes. The soot concentration is higher and the particles have grown much larger throughout the head vortex. Smaller soot particles are still present at the upstream and the central regions. The soot particles caused by the diffusion flame at the periphery, which are bigger than the ones in the central region but smaller than the ones in the head vortex, are still present. This distribution also suggests a history to the soot formation with the soot initially forming as small particles at some upstream location, and additional formation and particle growth continuing as the soot moves down the jet in the head vortex. This soot distribution pattern continues up through the end of fuel injection until about midway through the mixing-controlled burning region.

At the latter part of the mixing controlled burn, that is the region following the end of injection, images show a higher soot concentration and larger particles in the upstream region of the jet. By 21° ASI, the new soot distribution pattern is well developed with high concentration and larger soot particles in the upstream region as well as in the head vortex. This distribution pattern persists with the soot concentration slowly decreasing until the heat release is nearly completed at about 27° ASI. This suggests that the oxidation process starts to dominate in the whole soot formation-oxidation process.

Soot particles are expected to be oxidized at the jet periphery and at the outside of head vortex at which a diffusion flame occurs and at which OH and oxygen are ample for soot oxidation. The oxidation process occurs in these regions throughout the combustion process.

2.7 Soot Models

The emission of soot from a combustor is determined by the competition between soot formation and oxidation and a comprehensive model of the soot process must include both phenomena [58].

Various models of soot formation and oxidation have been studied by engine researchers. These models can be grouped into three categories; (i) empirical models that

use correlations of experimental data to predict trends in soot loadings, (ii) semi-empirical models that solve rate equations for soot formation with some input from experimental data and (iii) detailed models that seek to predict the concentration of all the species in a flame, from fuel to polyaromatic hydrocarbons to soot by solving the rate equations for elementary reactions that lead to soot [58]. Kennedy [58] and Haynes and Wagner [53] reviewed several soot formation models that have been studied. Apparently, only a few models were applied extensively on practical diesel engines and mostly they fall within the second category. A few soot models that have been recently used to study diesel engine combustion shall be described in the following sections.

2.7.1 Two-Step Empirical Soot Model

The two-step soot formation model that has been used by a number of investigators [31, 36, 62-65] began with Hiroyasu's soot model [37]. In this model, the soot formation process is considered to have only two reaction steps, which are, i) the formation step, in which soot is linked directly to fuel vapour molecules, and ii) the oxidation step, which describes the destruction of soot particles via the attack of molecular oxygen [66].

The net rate of change in soot mass is the difference between the rates of formation and oxidation, as identified by the following equation,

$$\frac{dm_{soot}}{dt} = \left.\frac{dm_{soot}}{dt}\right|_{form} - \left.\frac{dm_{soot}}{dt}\right|_{oxid} \tag{2.1}$$

where the soot formation and oxidation rates are expressed in Arrhenius form as:

$$\left.\frac{dm_{soot}}{dt}\right|_{form} = A_f\, m_{fuel}\, p^{0.5} \exp\left(-\frac{E_f}{RT}\right) \tag{2.2}$$

$$\left.\frac{dm_{soot}}{dt}\right|_{oxid} = A_O\, m_{soot}\, X_{O_2}\, p^{1.8} \exp\left(-\frac{E_O}{RT}\right) \tag{2.3}$$

where, m_{soot}, m_{fuel}, X_{O2} and p are soot mass, fuel vapour mass, oxygen molar fraction and the gas pressure, respectively. The activation energy E_f = 8 x 10^4 (J/mol), E_O=12 x 10^4 (J/mol) were used. The pre-exponential factor, A_f, and A_o are adjustable with measured data [66].

Patterson et al. [67] found out that Hiroyasu et al.'s model or its revision [65] has under-predicted the peak in-cylinder soot concentration. While maintaining the soot formation step, Patterson et al. made use of the semi empirical formula for pyrolytic graphite oxidation proposed by Nagle and Strickland-Constable (NSC) [38] by incorporating it into a new soot oxidation rate formula in the following form [67];

$$\left.\frac{dm_{soot}}{dt}\right|_{oxid} = \frac{6m_{soot}}{\rho_{soot} D_{soot}} M_c \dot{R}_{NSC} \qquad (2.4)$$

where M_c, ρ_{soot}, D_{soot} are the molecular weight of a carbon atom (12.011 g/mole), the soot particle density (2 g/cm^3), and the diameter of a soot particle (30 nm), respectively, and $\dot{R}_{NSC}$ is the overall pyrolytic graphite oxidation rate which is written in the following form:

$$\dot{R}_{NSC} = \frac{k_A p}{1 + k_z p} x + k_B p(1 - x) \qquad (2.5)$$

This formula of NSC is based on the assumption that there are two types of site on the carbon surface, namely A, a more reactive, and B, a less reactive type. By letting x be the fraction of surface covered by A, and 1-x the fraction covered by B, the following processes are assumed possible.

(a) Reaction of oxygen with A sites to give a further A site + 2CO, the rate being between the first and zero order.

$$A + O_2 \rightarrow A + 2CO \qquad (2.5)$$

$$\text{Rate} = \frac{k_A p}{1 + k_z p} x$$

(b) Oxygen reacts with B sites in a first order reaction to give an A site + 2CO.

$$B + O_2 \rightarrow A + 2CO \qquad (2.6)$$

$$\text{Rate} = k_B p(1 - x)$$

(c) A sites undergo a process of thermal rearrangement to give B sites at a rate $K_T x$

$$A \rightarrow B \qquad \text{Rate} = k_T x \qquad (2.7)$$

For a stationary value of x, the rates of (b) and (c) must be equal

$$k_T x = k_B p(1 - x)$$

which gives,

$$x = \frac{1}{1 + (k_T / k_B)\, p}$$

According to this mechanism, the surface will be entirely A at low temperatures, the reaction being of the first order at low pressures but approaching zero order at atmospheric pressure. As the temperature increases, thermal rearrangement produces an increasing proportion of B in the surface: since B sites are less reactive than A, the reaction rate ceases to rise and then begins to fall. At still higher temperatures, the surface is wholly covered with B, the reaction is of the first order at all pressures, and the reaction rate rises with temperature at a rate determined by the activation energy of reaction (b).

To fit the known experimental results, the following values are adopted by Nagle and Strickland-Constable [38] for the constants, and with R=1.987 cal/mole-K:

$$k_A = 20 \times e^{-30,000/RT} \ g/cm^2.s.atm$$
$$k_B = 4.46 \times 10^{-3} \times e^{-15,200/RT} \ g/cm^2.s.atm$$
$$k_T = 1.51 \times 10^5 \times e^{-97,000/RT} \ g/cm^2.s$$
$$k_Z = 21.3 \times e^{4,100/RT} \ atm^{-1}$$

This modified version of the two-step soot model is widely employed by workers in multi-dimensional diesel engine simulations due to its simplicity. Despite its widespread acceptance, it is not without limitations. The NSC formula is based on lower oxygen partial pressures than the ones usually found in diesel engines. More accurate data taken from more appropriate diesel engine conditions are clearly necessary to improve the prediction of the model. Furthermore, the oxidation of soot by OH attack is not properly accounted [58]. Ladommatos et al.[68] measured diesel soot oxidation rates and compared with NSC [38] and Lee's [69] oxidation model. Their measurements showed that diesel soot oxidation rates were lower than NSC but higher than Lee's models. They also argued that by using their modified NSC and Lee's formula, improved predictive capability in soot models could be obtained. The modified formula could readily be applied by adjusting the four rate constants in NSC model as proposed by Ladommatos et al. [68].

As can be noticed, this two-step model does not take into account the detail steps of soot particle formation as described in the preceding section of the review. It neither provides information regarding the size of soot particles. This deficiency has been dealt with by the model proposed by Fusco et al. [32] and it shall be discussed in the next section.

2.7.2 Multi-Step Phenomenological Soot Model

This soot model is a phenomenological model which incorporates via global rate expressions the physical processes of pyrolysis, inception, surface growth, coagulation

and oxidation [32]. These physical processes are shown and labelled in Figure 2.7. By pyrolysis, a portion of fuel is converted into soot precursor radicals (represented by process (1)), and growth species, assumed to be C_2H_2 (2). A portion of soot precursors is oxidized (3), and the rest is converted to soot particles (5). The growth species can increase the mass of soot particles (6) and they can be oxidized into inert products (4). Soot particles in turn, undergo oxidation (7) and coagulation (8).

Reactions (1) through (8) are used to provide a balance on four variables predicted by the model. The variables are particle number density, soot precursor radicals, acetylene (assumed to be the soot growth species), and soot volume fraction [32]. The resulting four governing differential equations solved by the model are given in Table 2.3. When the equations are solved, the particle number density and volume fraction can be used to estimate an average particle diameter under the assumption of monodispersed spherical soot particle [32]. The rate constants for each of the global kinetic expressions are given in Table 2.4. The rate constants of process (1), (2), (3), (4) and (5) are in the form of global Arrhenius expressions. The rate of soot surface growth in process (6) is adopted from Leung et al. [70]. For the kinetic rate of soot surface oxidation in process (7), the Nagle and Strickland-Constable oxidation model is utilized.

Kazakov and Foster [33] modified the Fusco model by including another process into the kinetic model which is direct deposition of precursor species onto the soot particle surface, as shown in Figure 2.8, and introducing a new coagulation rate constant that is valid from the free-molecular regime to the near-continuum regimes. Kazakov and Foster's model was successfully applied by Sung et al. [31] and Lee et al. [35] to study soot distribution in a diesel engine by changing start of injection timing and air/fuel ratio.

Tao et al.[71] revised the Foster's model by neglecting the process of direct deposition of soot precursors species in the model, but adding another oxidation process of soot particles which is oxidation by OH. Neoh [39] oxidation model was used to provide the OH-attack oxidation rate constants. The study by Tao et al. [71] shows that the prediction by the model is similar to Dec's [61] diesel conceptual model in many

aspects. The study also exhibits the agreement between the model prediction and engine-out soot emission.

A comparison of Foster model, Belardini's and a combination of Hiroyasu and NSC model were carried out by Kim and Sung [62], and they discovered that the soot mass at EVO predicted by the combination of Hiroyasu and NSC models was empirically matched.

2.7.3 Complex-Chemistry Coupled Phenomenological Soot Model

A chemical mechanism that couples a phenomenological soot model with complex chemistry mechanism was proposed by Tao et al. [34]. The mechanism consists of 65 species and 273 elementary reactions. The mechanism is a combustion mechanism that consists of four parts: the n-heptane auto-ignition chemistry (reactions 1-41); the low hydrocarbon oxidation chemistry (reactions 42 – 149); the formation reactions of PAHs (up to two aromatic rings) (reactions 150-264); and the NOx formation chemistry (reactions 265-273), with all the reactions listed in the appendix of Tao et al.'s paper [34].

The soot formation model in this mechanism includes all important steps: particle inception, in which naphthalene ($C_{10}H_8$) and diacetylene (C_4H_2) grow irreversibly to form soot; surface growth via the addition of acetylene (C_2H_2); and surface oxidation via OH and O_2 attack. The n-heptane ignition chemistry and small hydrocarbon oxidation chemistry are added to form the overall combustion mechanism. The soot model in this whole mechanism is in parallel with Fusco et al. [32] and Kazakov et al. [33] models but with some modification. The modification is done by replacing the precursor formation steps by the detailed gas-phase kinetics of PAH (naphthalene, $C_{10}H_8$) and polyyne (diacetylene, C_4H_2).

Further work has been done by Tao and coworkers [72] recently. The nucleation of soot particles is based on the idea of Lindstedt et al. [70, 73] but it is assumed that nucleation takes place at sites where diacetylene and naphthalene exists. The soot surface growth is described using Frenklach and Wang's active site model with some

modification, and the oxidation mechanism includes both Nagle and Strickland-Constable's (NSC) molecular oxygen oxidation and Neoh's hydroxyl oxidation models [72]. For particle coagulation process, a monodisperse size distribution is assumed and the process is described by the Smoluchowski equation with the revised rate from Graham [72]. This model has been applied to n-heptane spray combustion, and the prediction of the spatial and temporal soot distributions is in good agreement with experimental results. The studies also support that, in addition to its important role in soot surface oxidation, OH radical also plays a role as a growth agent crucial for the soot surface growth. However, sensitivity studies have shown that the spatial and temporal predictions of soot concentrations were significantly affected by inception rates, the surface reaction schemes, grid size and turbulence models [72].

2.7.4 Other soot models

Other models have also been studied to simulate the chemical and physical process of soot formation in flames. The following examples are models that usually include a detailed chemistry mechanism for soot formation.

Kraft [59] reviewed population balance models which include homogeneous gas phase reaction mechanism, particle inception, particle agglomeration, surface reactions, condensation and sintering, of organic and inorganic nanoparticles. The numerical methods such as method of moments, sectional, finite element and Monte Carlo methods that are associated with the population balance models were also reviewed. The method of moments has been identified as a suitable method to efficiently simulate laminar flame.

Balthasar and Frenklach [74] used the method of moments with interpolative closure (MOMIC) which was coupled with a detailed chemical kinetics mechanism of soot formation aggregation in laminar premixed flames. The analysis of the modeling results showed a complex interaction of particle nucleation, surface growth and coagulation. In this model, soot volume fraction, soot particle size and soot particle number density were plotted against the distance from burner.

Morgan et al. [75] used a population balance model, which is governed by particle nucleation, coagulation and surface growth; and stochastic numerical methods to simulate the particle size distributions of soot particles in laminar premixed flames. The model is able to capture the evolution of mass and surface area, and full structural details of the particles. In this model, soot particle size and soot particle number density were plotted against time.

As opposed to the studies mentioned above which have been applied to open flames, Hong et al.[76] developed a model for diesel engines that included the broad scope of the physical and chemical mechanisms. The moment method was used in this study to describe the soot formation process. The model was compared with experimental results but the model did not yield similar results due to the difficulties in optimizing three main parameters, which were, the correction factor used in nucleation submodel, the rate coefficient of the surface reaction, and the size of primary soot particles. As an example, increasing the nucleation rate correction factor increases the number density of soot particles but decreases the average particle size similar to the effect of decreasing the size of primary soot particles.

2.8 Soot particle tracking

Computational studies on in-cylinder soot particle size distribution has been carried out by a number researchers [31-34, 77], but previous studies on lagrangian soot particle tracking in a diesel engine are difficult to locate. The most similar study has been carried out by Hessel et al. [78] which analyses paths of packets of intake charge in time and space in a HCCI engine by employing EnSight 8.2 post processing software [79]. Another computational study in combustion engineering application was carried out by Apte et al.[80] in which movements of large number of glass-particles in coaxial-jet combustor were predicted with large-eddy simulation (LES) on unstructured grids.

Several other studies on soot particle tracking in open diffusion flames have also been carried out by Katta et al.[81], Barve et al.[82] and Fuentes et al.[83]. Katta et al. found that soot particles closely follow the gas flow, while Barve et al. tracked fluid particle flow to understand soot particle evolution which also implies soot particles following the fluid flow. Fuentes et al. tracked the history of soot particles from nucleation to oxidation along their simulated trajectories. Particle tracking studies in different fields using interpolated velocity vector have recently been carried out by others [84-91].

2.9 In-cylinder Fluid Motion

Fluid motion within a combustion chamber is important to speed up evaporation of the fuel, to enhance air-fuel mixing, and to increase combustion speed and efficiency. Besides the desired turbulent flows in the cylinder, other additional motions generated are swirl, squish and tumble motions. Swirl is generated during air intake where the intake system gives a tangential component to the intake flow as it enters the cylinder. Squish is the radial inward motion of the gas mixture from the outer radius of the cylinder as the piston approaches TDC and compresses the gases. When combustion starts and the piston moves away from TDC, reverse squish occurs where the burning gases are propelled radially outward to fill the now-increasing outer volume along the cylinder walls. This reverse squish helps to spread the flame front during the latter part of the combustion. Tumble is a secondary rotational flow generated by the squish motion that occurs about a circumferential axis near the outer edge of the piston bowl. Tumble motions are becoming important in achieving air-fuel mixture stratification. Contouring of the piston face and variable timing and lift of the intake valves are subjects of on-going research to achieve stratified combustion [14].

As engine speed increases, in-cylinder motion increases, with a corresponding increase in swirl, squish and turbulence. This increases the rate of fuel evaporation due to air-fuel mixing and combustion. When the flow is turbulent, particles experience random fluctuations in all directions. This makes it impossible to predict the exact flow

conditions at any given time and position. Turbulence in a cylinder is high during intake, and then decreases as the flow rates slow near BDC. It increases again during compression as swirl, squish and tumble increase near TDC.

However, there are fluid motions that are detrimental to the engine condition. These motions are crevice flow and blowby. Crevice flow is the flow where gases enter and get trapped in tiny crevices in the clearance between the piston and cylinder walls, imperfect fit in the threads of the fuel injector, gaps in the gasket between head and block, and unrounded corners at the edge of the combustion chamber and around the edges of valve faces. It accounts only 1-3% of the total clearance volume, but it can reach as much as 20% of the total mass at peak pressure [14]. This is due to high density of trapped gases in the crevice as pressure is high but temperature is as low as the wall temperature. These trapped gases contribute to hydrocarbon (HC) emissions, and lowering combustion and engine thermal efficiencies. Blowby is a flow of gases past the compression rings through the ring grooves as the piston moves towards and reverse from TDC. It is also contributed by the leak through the gaps where the ends meet in piston rings.

The complexity of the fluid motion in a cylinder illustrates the difficulties involved in investigating the movement and behaviour of soot particles inside a cylinder of an engine. With additional soot chemical kinetics and physical processes to be accounted for, the study of in-cylinder soot particles is quite a daunting task.

2.10 Soot in Oil

The accumulation of soot in the lubricating oil of a diesel engine is one of the factors limiting the interval between oil changes and hence service interval. The soot is formed in the cylinder and transferred to the oil film on the liner [8, 9]. It causes wear to the engine component when it gets into the lubricating oil system. It has not been known clearly at which region of the cylinder and at what instant the soot came from, and how the soot distribution and particle size influence soot transfer to the liner.

2.10.1 The Effects of Soot on Engine Oil

The effects of soot in oil have been investigated by many researchers. Wear to the engine component caused by soot in oil has been studied by Rounds [92] about thirty years ago. Through their studies, Gautam et al. [93] also showed that wear increased with higher soot concentration, and the wear mechanism involved could be inferred as an abrasive wear mechanism. Kim et al. [94] also observed that wear increased as the concentration of soot in the used oil increased.

In his study, Mainwaring [95] found that soot has a direct influence on wear, and the overall rate of wear depends on the balance between rates of film formation and film attrition, which in turn, depends on the oil film thickness, the soot particle size and soot concentration. In terms of the effect of soot to thermal performance of engine oils, Lockwood & Zhang [96] observed that soot caused a slight positive effect on the oil where the heat transfer coefficient of oil improved.

2.10.2 Soot Pathways into Oil System

Recent developments in emission regulations that required low NO_x emissions exacerbate the oil contamination problem due to increase in emission of soot caused by EGR, injection timing retardation, high piston rings and high cylinder pressure. As soot generated in the combustion chamber increases, and no modification in engine designs such piston bowl shape, is made, it is fair to say that a higher amount of soot will enter the engine oil through the narrow clearance between piston and the liner [10]. The amount of soot entry into the oil is not known exactly, but present day diesel engines could possibly experience more than 5% of it [10].

Dahlen [97] says that soot in oil is believed to be caused by deposition of soot in the oil film on the liner and the subsequent scraping of contaminated oil to the crank case by the piston ring. He further postulates that the rate of the deposition depends on i) the soot concentration in the outer regions of the combustion chamber; ii) thermophoresis, which is the dominating transport mechanism within the viscous sub-layer; and iii) the

topland height which influences the fraction of oil hence the mass of soot that will be scraped down to the crank case. The theory of thermophoresis as the main transport mechanism in transporting particles to the cylinder walls is also espoused by Eastwood [10].

2.10.3 Mechanisms of Soot Deposition onto In-cylinder Walls

Several mechanisms have been assumed to be the mechanisms of soot deposition on combustion chamber walls in diesel engines. The possible deposition mechanisms are thermophoresis, Brownian diffusion, turbulent diffusion, inertial impingement, electrophoresis and gravitational sedimentation. The explanations of these mechanism can be found in reference [8] and are summarized here**.**

2.10.3.1 Thermophoresis

Thermophoresis is the mechanism that causes particles, suspended in a gas, to travel down a temperature gradient. In a diesel engine, the temperature of chamber walls is typically 400K to 500K, while that of bulk gas temperature can be greater than 2500K. Therefore, there exist a thermal boundary layer between the walls and the bulk gases. During combustion, soot is produced and distributed throughout the bulk gas by the turbulent motion, but as the soot comes in contact with the thermal boundary layer, it may be transported to the wall by thermophoresis mechanism.

2.10.3.2 Brownian Diffusion

Brownian diffusion is a mechanism whereby a suspended particle moves down a concentration gradient, as opposed to temperature gradient in thermophoresis mechanism. It follows Fick's law which states that the mass flux of a constituent per unit area is proportional to the concentration gradient. Brownian diffusion could take place within the laminar sublayer where the concentration gradient exists.

2.10.3.3 Turbulent Diffusion

Turbulent diffusion is convection in a turbulent field which also follow Fick's law and usually presented as an enhancement to Brownian diffusion. In diesel combustion, turbulent diffusion would take place during the early stages when soot is being produced at the turbulent flame front. Concentration gradients exist between the flame regions and the rest of the chamber. Turbulent diffusion may be the predominant soot transport mechanism up to the laminar sublayer, at which point some other mechanism would take over to deliver the soot to the wall.

2.10.3.4 Inertial Impingement

If the soot particle has large enough mass to aerodynamic drag ratio to be thrown out of the turbulent eddy and travel to the wall, it could be transferred to the wall by inertial deposition mechanism. However, if mass to drag ratio is small, the particles will follow the flow very closely and will not be able to break away from an eddy.

2.10.3.5 Electrophoresis

Electrophoresis is the process by which a particle carrying an unbalanced charge is transported in an electric field. This process would require that the particles acquire an uneven charge when they are formed and that the combustion chamber walls carry a static charge distribution. The soot particles might conceivably be charged through a thermal ionization process.

2.10.3.6 Gravitational Sedimentation

This mechanism is almost unlikely to occur in a combustion chamber due to small particle size and high turbulence. The sedimentation of a particle this size and density take minutes or even hours, whereas time scales involved in diesel engines are very short.

Thus, this mechanism is not taken into account in the study of soot deposition mechanisms.

Models were constructed for four of these mechanisms, i.e. thermophoresis, Brownian diffusion, electrophoresis and inertial impingement and they were compared. Thermophoresis was found to be the significant contributor to soot deposition on combustion chamber walls [8]. However, how the mechanisms were compared and studied is not clearly stated in the article.

Suhre and Foster [8] then carried out an experiment to prove that thermophoresis mechanism was the significant deposition mechanism in diesel engines. They used an engine with optical window with temperature-controlled feature, on top of the cylinder. What they found out was when the window is cool, more soot is deposited while when the window is hot, less soot is transferred to the optical window. The results were consistent with the finding of model comparison.

Kittelson and Ambs [9] also compared the thermophoresis model and experimental results. The results agreed well. The soot deposited onto the wall is between 20 to 45% of the exhaust mass, and possible reentrainment during exhaust blowdown could be detrimental to soot control strategy that is based on in-cylinder oxidation. Kittelson and Ambs [9] also noticed that oil contamination is another problem that was caused by soot deposition on walls by thermophoresis. A significant amount of soot (10-20% of the mass deposited in chamber) is deposited on cylinder walls. These soot particles would be incorporated in the oil film and some of them would end up in the sump. A combustion model with a submodel of thermophoresis was studied by Abraham[98]. He did a comparison between model without and the model with the thermophoresis model. He found out that when thermophoresis submodel was used, higher mass of soot is observed at the walls.

2.11 Conclusions

Review of soot phenomenon, regulations, investigations and problems associated with it has been briefly carried out in this chapter. In view of the importance of soot particle size and how it evolves in time, soot formation process and its development in a conceptual diesel flame was discussed in a great detail. A few recent soot models that have been used to study diesel engine combustion were reviewed. The chapter finishes with a review of soot in oil problem and the possible mechanism of soot transfer to the liner.

Studies that deal with in-cylinder soot movement and its evolution, particularly with regard to soot in oil problem, can hardly be found in the literature. The present investigation was carried out to shed some light into this subject, especially the connection between location and instant the soot is formed, and its possibility to be transferred to the cylinder wall layers.

As mentioned in the previous chapter, a two-step semi-empirical soot model has been used in this study. While other soot models (multi-step and complex-chemistry) are closer to the soot physical process and able to provide soot particle size information directly from CFD simulation, their uses entail relatively high computational costs and are so much dependent on the physical and chemical rates used in the models formulations. Using a simple and a relatively low-computational-cost two-step mass-based soot model, the present study accomplishes further analysis of the soot particle through post-processing of CFD simulation data, thus decoupling the problem of soot mass and soot particle diameter and its movement. Computed flow fields were used to track the paths of soot particle movement in the cylinder. This approach is a Lagrangian approach by which the history of soot and other species along the paths can be recorded and analysed. This approach also allows more flexibility and more prospects for future improvement while preserving the CFD simulation results.

CHAPTER 3

MODEL SETUP AND DATA MANAGEMENT

3.1 Introduction

The investigation of in-cylinder soot formation and movement using CFD and particle tracking requires an understanding of the code and the various simplifications and assumptions to characterise the actual physical and chemical phenomena. These simplifications and assumptions have to be evaluated for their appropriateness so that the results of the study are reliable.

This chapter describes the computer setup, data creation, data management, computer programmes created and modified, and cylinder volume model setup. Sub-models that are used in Kiva-3v CFD code are also explained in brief with references given to assist the readers. Approaches taken to perform desired calculations are explained in full. At the end of the chapter, simplifications made and assumptions considered are assessed and discussed.

3.2 PC Setup for Kiva-3v Simulation

A newly built desktop PC was used for Kiva-3v CFD simulation, post-processing and data analysis. A dual-booting configuration was set up on this PC to allow Kiva-3v to be run on a Linux platform, and related softwares, namely EnSight post-processer, Matlab and other word-processers and spreadsheets to be run on Windows platform. While it was possible to work on only one platform (i.e. Linux), it was a matter of preference of the author to carry out data processing and data analysis works on Windows

platform. The specifications of the computer hardware and software are shown in Table 3.1 and Table 3.2, respectively. Redhat Linux distribution was used due to its performance as the most competent operating system to support Kiva-3v application onto personal computer [36]. In this investigation, Redhat Linux 9 was used due to its compatibility with recent computer hardware, in place of Redhat Linux 6.1 and Redhat Linux 8 that were used in previous investigations [27, 30, 36].

3.3 Kiva-3v CFD Code and Sub-models

The CFD code used is Kiva-3v Release II. This is made up of three main parts; preprocessor or grid generator (K3PREP), main solver (KIVA3V) and postprocessor (K3POST). Each contains a set of one main program driver, subroutines, user-defined functions, common block, block data and external subprograms that are referenced by the main driver. K3PREP was used to generate computational grid which contained in a file called by a generic file name itape17. This file contains all the grid coordinates, x, y, z, flags F and FV, six connectivity arrays, three cell-face boundary condition arrays, and a region identifier array [99]. KIVA3V, which reads file itape17, was then used to run the simulation from which data on combustion and pollutant emissions in various formats were produced. In place of K3POST, a translation programme, called K2E is currently used to convert KIVA3V data in binary form into EnSight-readable format.

Kiva-3v main solver generates data in a few types of formats where some can readily be used in a spreadsheet, namely dat.* files, while others are in forms that require another process of conversion. The most important file is itape9 in which all simulation results are contained. This file is in binary form which requires K2E programme to translate it into a postscript file that will be readable by EnSight post-processing software. EnSight is used to illustrate the simulation results in graphical forms and can also be exploited to display the results in many perspectives.

To extend the usage of these simulation data beyond graphical representation by EnSight software, namely soot particle tracking and soot growth modelling, these data

need to be formatted in an appropriate structure. To accomplish this, K2E programme is modified to translate itape9 data into a format that are easily accessible and readable by soot particle tracking and soot growth modelling programmes. The running sequence and the associated input/output files are shown in Figure 3.1 and Table 3.3.

The original version of Kiva-3v Release II was ported onto a PC platform in previous investigation [36] and employed Surovikin's soot model [77] in its soot calculation. In subsequent investigations [27, 30, 100], modification was made to the code where Surovikin's soot model was replaced with a two-step soot model that made use of Hiroyasu's soot formation, and NSC and Neoh's soot oxidation expressions.

The two-step soot formation model gained widespread use in combustion community due to its simplicity and its robustness to uncertainties in user-defined parameters [51, 62, 66]. In this model, the soot formation process is considered to have only two reaction steps, which are, i) the formation step, in which soot is linked directly to fuel vapour molecules, and ii) the oxidation step, which describes the destruction of soot particles via the attack of molecular oxygen [66] and hydroxyl radicals, OH [39].

The net rate of change in soot mass is the difference between the rates of formation and oxidation, as identified by the following equation,

$$\frac{dm_{soot}}{dt} = \left.\frac{dm_{soot}}{dt}\right|_{form} - \left.\frac{dm_{soot}}{dt}\right|_{O_2\_oxid} - \left.\frac{dm_{soot}}{dt}\right|_{OH\_oxid} \quad (3.1)$$

where the soot formation and oxidation rates are expressed in Arrhenius forms as:

$$\left.\frac{dm_{soot}}{dt}\right|_{form} = A_f m_{fuel} p^{0.5} \exp\left(-\frac{E_f}{RT}\right) \quad (3.2)$$

$$\left.\frac{dm_{soot}}{dt}\right|_{O_2\_oxid} = A_{O_2} \frac{m_{soot}}{\rho_{soot} D_{soot}} M_c \dot{R}_{NSC} \quad (3.3)$$

$$\left.\frac{dm_{soot}}{dt}\right|_{OH\_oxid} = A_{OH}\frac{m_{soot}}{\rho_{soot}D_{soot}}M_c\dot{R}_{Neoh} \tag{3.4}$$

where

$$\dot{R}_{NSC} = \frac{k_A p}{1+k_z p}x + k_B p(1-x) \tag{3.5}$$

as previously explained in Section 2.7.1.

The net rate of OH oxidation, $\dot{R}_{Neoh}$ is defined as follows [30];

$$\dot{R}_{Neoh} = W_c\rho_{OH}\frac{N_A}{MW_{OH}}\sqrt{\frac{RT}{MW_{OH}\cdot 2\pi}} \tag{3.6}$$

Here, M_c, is the molecular weight of a carbon atom (12.0 g/mole), ρ_{soot}, the soot particle density (2.0 g/cm^3) [67, 101],and D_{soot}, the diameter of a soot particle (30 nm) [53, 67]. The diameter of soot of 30 nm is selected as this is the average diameter of in-cylinder soot particle as referred in the cited articles above, and it is in the right range of measured in-cylinder soot particle size shown in Table 2.2. This value is used in this Kiva-3v simulation to calculate the rate of soot formation and oxidation to obtain the net rate of in-cylinder soot mass formation at each time step.

A_f, A_{O_2} and A_{OH} are calibration parameters that can be adjusted for a particular application to obtain accurate prediction. These calibration parameters partly compensate for uncertainties in values of the average soot particle diameter, D_{soot} [30]. The values of A_f, A_{O_2} and A_{OH} that have been used in the study are 65, 20 and 2.5×10^{-3}, respectively. The soot mass calculated at EVO using these values was calibrated against measured soot mass at the engine exhaust in the previous study [30].

As these soot formation and oxidation rates are represented by Arrhenius type of expressions, the rates are highly dependent on temperature. The formation rate is

proportional to the fuel vapour concentration while oxidation rate is proportional to the soot mass, oxygen partial pressure and number of OH molecules. Hence, soot concentration is found to be the highest in the fuel rich region and high oxidation rates at high concentration of oxygen and OH. Changing operating condition will affect the in-cylinder gas motion hence fuel distribution, mixing and heat release patterns. Consequently, local concentrations of fuel, oxygen and OH species and temperature distribution are affected thus influence local soot formation rates. A total amount of soot at each crank angle can be predicted as the summation of all of local soot formation processes.

Sub-models that represent spray dynamics also play very crucial roles in influencing the fuel distribution as well as gas flow patterns in the cylinder due to mass, momentum and energy exchange between fuel spray droplets and the surrounding in-cylinder gas. Fuel droplet oscillation and breakup, droplet trajectories, droplet collision and coalescence, droplet evaporation, droplet turbulent dispersion and wall film dynamics are represented with various sub-models and subroutines in this code. Droplet breakup is represented by Taylor Analogy Breakup (TAB) model [102], droplet collision, coalescence, dispersion and evaporation by Monte Carlo-based discrete particle technique [102] and wall film dynamics by particle-based liquid wall film model [103, 104]. Droplet radius at injection in terms of Sauter mean radius (SMR) was set at 74.5×10^{-6} m with monodisperse distribution. This SMR value of the droplet radius follows the radius of the injector hole. The governing equations in these models and other models are discretised both in time and space and are solved with finite-difference approximations which is based on arbitrary Lagrangian-Eulerian (ALE) finite volume method [102]. These sub-models were used without modification in this study.

Since soot formation depends heavily on the local fuel concentration which in turn depends on fuel droplet distribution and in-cylinder gas flow, familiarity with the operation as well as the limitations of these spray dynamics sub-models are necessary. The treatment of fuel droplet-gas and droplet-droplet interactions in this Kiva-3v code was found to be prone to errors as it is strongly mesh dependent [105-107]. The inherent

problems lie in prediction of the droplet-gas relative velocity through inaccurate two-way momentum coupling and fuel droplet size through droplet-droplet collision and coalescence processes. It was shown by Abani et al. [106] that even with adequate resolution, drop sizes are predicted poorly and spray penetration is over-predicted. However, modification of these spray sub-models has not been the focus in the present study thus these sub-models have been used without modification. Keeping this inherent weakness of these spray models in mind, the results of the simulation have been used for further treatment of soot particle movement.

The above sub-models and other important sub-models used in this Kiva version are listed in Table 3.4. Detailed discussions on these sub-models could be found in [99].

3.4 Setup of Computational Model

Simulations were carried out for a combustion system and injector arrangement of a diesel engine. The combustion system has a bowl-in-piston and flat cylinder head face configuration, with a seven-hole injector installed vertically and centrally. The compression ratio was 18.2:1 and the swept volume was 500 cc. The schematic diagram of the engine and piston crown configuration is shown in Figure 3.2. The initial and boundary conditions of the simulation were based on a specific case of an experimental engine with specific test conditions. The simulation only covered the closed part of the engine cycle, that is, from inlet valve closing (IVC) to exhaust valve opening (EVO). Initial and boundary conditions for the simulation as well as model validation were based on real data from experimental tests [100]. In-cylinder pressure, heat release rate, and soot and NO_x concentration at engine exhaust were used for calibration purposes. Table 3.5, Table 3.6 and Table 3.7 show the specifications of the experimental engine, specifications of the fuel injector and the test conditions, respectively. These test conditions have been selected to represent a high speed high load operating condition which is one of the cases to test engine emissions by Ford motor company and experimental results of the emissions are provided in an internal report [108].

Computational domain of full combustion chamber volume was generated with K3PREP to represent the cylinder volume of the experimental engine. Baseline mesh configuration of 150 divisions in azimuthal direction, three (at TDC) to 22 (at BDC) divisions in vertical direction, and 37 divisions in radial direction, was used to produce a maximum number of mesh of 200,000 cells. This number of cells has been found to give sufficient grid independent in-cylinder pressure, temperature and cumulative heat release as obtained for this combustion system in previous studies [30, 36]. Grid size is approximately 1.16 mm in the radial direction, 0.6 to 3.1 mm (above the bowl) and 1.1 mm (within the piston bowl) in the axial direction with the azimuthal grid spacing of 2.4°. The mesh configuration is shown in Figure 3.3. Other input variables in the input file itape5 were set to closely follow the setting in the previous study [30]. The squish volume was adjusted to account for the absence of a crevice submodel and match the compression ratio of the experimental engine [30].

A need for the use of full combustion chamber volume for the computational model was identified to accomplish correct calculations of soot particle tracking. This was realised during the course of the initial investigation when one-seventh of the volume was used. With the setup of one-seventh of the volume, deactivated or dummy cells were created at the two faces in the angular direction by K3PREP programme. With modified K2E programme, these dummy cells could be detected and deleted but it produced gaps when the sector was replicated. When they were not deleted, it produced overlapping of sectors. Both were found to cause irregular soot particle paths and discontinuities in the species and condition history along the paths. To overcome this problem and generate smooth paths without discontinuities, a full cylinder volume setup was found to be the solution but at the expense of computational resources.

3.6 Data Storage and Runtime Requirements

In this investigation, the amount of output data (otape9) generated by each Kiva-3v simulation depends on mesh configuration (spatial resolution) and the frequency of data recording (temporal resolution). The higher the spatial resolution and recording frequency the larger the computer storage required.

For instance, increasing the spatial resolution from 150,000 cells per computational volume to 200,000 and 250,000 cells at temporal resolution of 0.25° CA will increase computer storage from 25 GB to 40 GB and 50 GB respectively. Accordingly, actual runtime time also increases from 22 hours to 38 and 70 hours, respectively. Figure 3.4 summarises the storage and runtime requirements for these mesh configurations.

With the mesh configuration of 200,000 cells, 14 gigabytes (GB) is required when recording with 1°CA resolution. Increasing temporal resolution to 0.25° CA and 0.1° CA increases the storage requirement to 40 GB and 110 GB, respectively. Due to the heavy use of computer storage and the limitation of interactive data recording capability of the PC in use, the recording of the data is carried out in batches, and Kiva-3v simulation needs to stop and restarted when file size reaches its maximum storage capacity in each batch.

While the actual runtime of a particular mesh size with three temporal resolutions does not differ, file management tasks carried out in-between intermediate stops and restarts of Kiva-3v also increase the overall time. In average, increasing temporal resolution from 1°CA to 0.25° CA and 0.1° CA increases these file management time from 1 hour to 2 and 4 hours, respectively. Time required to post-process the simulation data into final structure for particle tracking calculation also increases immensely. It increases from 3 hours to 9 and 20 hours, respectively. Even though it is not quantified,

idling time that associates with restarts of Kiva-3v simulations and batch post-processing will also increase as temporal and spatial resolutions are increased. Figure 3.5 and 3.6 show the cost of increasing temporal resolution to the data storage and total time requirements.

3.7 Soot Particle Tracking with Trilinear Interpolation Technique

Soot particle paths have been obtained by tracking an individual or a parcel of soot particles from a specific location and instant through pre-computed flow field calculated by Kiva-3v in time and space. These pre-computed Kiva-3v data are arranged into proper structures/formats and used by a particle tracking programme written in Matlab routine. In this section, the basics of particle tracking and interpolation techniques are laid down and explained.

A soot particle at the start of tracking location and instant is assumed to take on the velocity vector of the flow field at the same point, as its velocity. The velocity vector of a soot particle at a given position S_n within an element can then be written as

$$u(s_n, t_n) = \frac{ds}{dt} \tag{3.7}$$

where s_n is the current particle position and t_n the current time step. The position of the soot particle at the next time step is obtained by approximating the time derivative by one-step forward difference as described by the equation below:

$$s_{n+1} = s_n + u(s_n, t_n)\Delta t \tag{3.8}$$

where $\Delta t = t_{n+1} - t_n$, which is the time interval between the current to the next time steps. The nanoscale soot particle is assumed massless which means that the forces such as gravitational and drag, that normally act on a moving particle in a moving body of fluid

are considered to have negligible effect on the soot particles. Therefore, the particle is expected to follow the bulk gas flow in the cylinder. Consequently, the soot particle position at the next time step is only the outcome of Equation 3.5. This assumption will be further justified in Section 3.9.

The simplest form to calculate the new position of the soot particle is through Euler's method which is also called first order Runge-Kutta method. In this investigation, Euler's method directly takes the velocity at a given point as its velocity estimate to calculate the distance travelled by the soot particle. This method does not give sufficiently accurate results if the underlying function, in this case soot path, is non-linear in the time step. The accuracy of the path can be increased by using higher order one-step forward difference methods. All one-steps methods can be represented by the general form of Equation 3.5, with higher order methods differs only in the manner the velocity is estimated. Further discussion and comparison of the first-order Runge-Kutta method with higher order methods will be presented in Chapter 5.

Locations of the soot particles at each time step depend on the velocity vectors in the previous time steps. These locations can be anywhere in the computational domain and most of the time they do not fall on the cell nodes. However, the velocity vector and other species scalars are discrete and known only at cell nodes. The nearest-node method has been used in the early stage of the study only to show that soot particle paths are plagued with discontinuities. To use the nearest-node method to obtain continuous particle paths, spatial resolution of the computational domain needs to be increased greatly. Without having to increase spatial resolution, an accurate velocity vectors at the actual particle locations can be interpolated by considering the velocity vectors from surrounding cell nodes. For this purpose, a trilinear interpolation technique is considered.

Trilinear interpolation is a technique of spatial interpolation on a 3-dimensional regular grid. It approximates the value of an intermediate point (x,y,z) within the local hexahedral cell linearly, using data on the surrounding cell nodes. With this technique, velocity vector at any location in the domain can be estimated. A typical cell used in the

simulation is shown in Figure 3.7. However, cells in the computational domain have non-uniformed cell shapes and sizes at different locations and change quantity and sizes with time in the region above the bowl. Therefore, identification of eight corners of the cells surrounding the interpolated point is accomplished by a Matlab subroutine which is able to perform in any region in the computational domain. After finding the eight points, the subroutine finds four interpolated values along z-direction (light red-circles). These four values are then interpolated along radial distance, (ρ) to obtain two interpolated values (blue circles). Finally, these two values are interpolated along angular direction, (θ) to obtain the final interpolated value (red-circle) at the point of interest. This subroutine is included in the particle tracking programme. In addition to velocity vectors, soot, fuel, temperature, pressure, oxygen and OH are also interpolated to be used later in soot growth model.

This particle tracking programme with trilinear interpolation can basically be used to track soot particles from any location and instant in the cylinder. From Kiva-3v simulation, soot is identified to start forming at around 1°CA ATDC. Therefore, soot particle tracking in this thesis is started out at or above this crank angle. The soot particle can normally be tracked until EVO, but in some cases, the tracking stop earlier. The early stopping of the tracking occurs when soot particle goes beyond the computational domain due to very high velocity it experience in the previous time step. This normally happens when the soot is tracked inside the fuel jet during fuel injection period where the velocity of the fuel is very high (up to 15 m/s). Currently, the soot particle is assumed to impinge on the bowl walls without further treatment of what will happen next to the particle. Besides depositing to the walls, other possible physical phenomena that would happen to the particle could be rebounding from the wall, or just rolling along the wall. Treatment of the soot particle during these possible physical processes requires other sub models which at this point are not dealt with in this thesis.

3.8 Soot Growth Model

History of flow fields and species along soot particle paths is collected by soot particle tracking programme. This history indicates the local condition of the cylinder and species concentrations as the soot particle traverses through the path. Another Matlab routine is written to predict the size evolution of soot particles along the paths using these local condition and species concentrations. From now on, this Matlab routine shall be called soot growth model.

This soot growth model specifically makes use of temperature, pressure, fuel, soot, O_2 and OH concentrations history to predict the size evolution of soot particles along the paths. Soot particle size at a particular location and instant depends on the amount of soot formed and soot oxidized. In this soot growth model calculation, the soot particle is assumed spherical in shape and the entire amount of soot formed is assumed to contribute to the growth of soot particle sizes and be distributed equally onto the surface of available soot particles. This assumption seems to neglect the contribution of nucleation process to the amount of soot formed. Yet, it is a practical assumption since many published works agreed that soot growth process contributes to the majority of the soot formed in flames [10, 53]. Nonetheless, this assumption does not discount the importance of nucleation process to provide nucleus for further soot growth, and its significance in controlling the soot particle number density that directly influence physical processes of coagulation and agglomeration. In this model however, coagulation and agglomeration processes are not taken into account to predict soot particle sizes.

The amount of formed and oxidized soot experienced by a soot particle along a path are calculated using the same Hiroyasu soot formation and Nagle-Constable Strickland and Neoh's soot oxidation rate expressions as the ones used in Kiva-3v simulation as described earlier in Section 3.3. To obtain the rate of size change of a soot particle, an appropriate multiplication factor needs to be introduced in the equations. Several possibilities have been explored and assessed as to what is the best way to model soot particle growth along the paths. This exploration shall be discussed and explained in greater details in Chapter 7.

3.9 Evaluations of Assumptions

In the present investigation, soot particles have been treated as massless when tracking and mono-disperse unaffected by the processes of growth and coagulation. According to Dec's report [61], soot particles continue to nucleate until the end of injection in the upstream region of the fuel jet and grow in size as they move to the downstream region. Haynes and Wagner [53], reported that agglomeration starts late at around 50º CA ATDC but current studies [109] suggest that agglomeration process may start earlier during soot formation process as soot size distribution during soot formation does not differ much with that of later crank angles and of the exhaust. The average measured engine-out primary soot particles range between 10 to 70 nm and agglomerated soot can be in the range of 100 to 300 nm as shown in Table 2.2. Soot agglomerate, which has a fractal dimension, D_f, of about 1.8 [110, 111], behave dynamically different from and has smaller drag coefficient than the identical size of a spherical soot particle by a factor of 0.8 [111]. This fact however does not significantly influence the soot movement in the engine studied in this thesis as shall be shown later.

In addition to assuming soot particles are massless when tracking individual particles, in the Kiva simulations used to define gas state and velocity fields which dictate the particle path, soot is assumed to be a continuous-phase species. These fields are computed taking into account interactions of continuous phase of gas and discrete phase of fuel droplets. When tracking particle paths through these fields, the effect of the particle on the field is assumed to be negligible. In other words, in the tracking the soot particle with the post-processed data, it is also assumed that the particle movement has no effect on the fluid flow field and the fluid flow has no influence on the particle movement. Another assumption is that soot particles have a sufficiently low number density for particle-particle interactions to be neglected and each particle to be considered as an independent body. This assumption is important as particle-particle interactions would produce other forces which may affect the particle movement. The soot particle is assumed spherical for the reason stated in section 3.8 and this spherical assumption is

used to justify the overall assumption that the soot particles follow the in-cylinder bulk gas flow.

To justify that soot particles follow the in-cylinder bulk gas flow field, soot particle motion in the cylinder can be described with Newton's second law of motion taking only drag force into consideration. A soot particle with radius r travels through a continuous gas phase with density ρ_g from a static position or after changing direction at a right angle during a motion to reach velocity ν_p is considered. The soot particle experiences drag force due to its shape and the difference in velocity with the continuous phase. An equation to determine the time taken by a particle to reach the velocity ν_p which is also the average piston velocity is obtained in Equation 3.8 from the force balance equation.

$$F_D = ma \tag{3.9}$$

$$\frac{1}{2}\rho_g v_p^2 C_D A_p = \rho_p V_p \left(\frac{v_f - v_i}{\Delta t}\right) \tag{3.10}$$

where $\nu_f = \nu_p$ and $\nu_i = 0$, thus,

$$\Delta t = \frac{8}{3}\left(\frac{\rho_p}{\rho_g}\right)\frac{r}{v_p C_D} \tag{3.11}$$

where

soot density, ρ_p = 2000 kg.m^{-3}; gas density, $\rho_g \approx 20.0$ kg.m^{-3} [112]

ν = average piston velocity = 7.1 ms^{-1}, (ν = 2LN) where

N is the speed of engine in revolutions per seconds (2500 rpm=41.67 rps)

L is the of engine stroke in meter (0.086 m)

C_D = 0.5 for spherical object (smaller by a factor of 0.8 for soot agglomerates)

A_p = cross-sectional area of the soot particle

The maximum size of soot particle that can be considered massless can then be obtained by equalising Equation 3.9 to the crank angle step used in this study, which is

0.25 CA. At the engine speed of 2500 rpm, this crank angle step is equivalent to 1.67×10^{-5} seconds. The maximum diameter of soot particle can be calculated to be about 400 nm. This means that soot particle with the diameter below 400 nm will reach piston velocity and follow the fluid flow within the specified time step. As the in-cylinder soot particles or agglomerates are mostly around 100 nm, the soot particles tracked in the present study are shown to behave as massless particle and follow the in-cylinder bulk fluid flow. This is also supported by the work of Abraham [98] which shows that distribution in-cylinder soot outside of the boundary layer is mainly influenced by turbulent eddy and bulk fluid convection. Due to minimal effect of agglomerated soot on the soot particle drag [111], the shape of soot considered in the particle tracking model can also be simplified as spherical. In their studies of diffusion flame, Katta et al.[81] and Roquemore et al.[113] also found that nanoscale soot particles follow the surrounding gas flow.

Another approach that can be used to demonstrate that the in-cylinder soot particles behave as massless particles and follow the bulk fluid flow is by applying particle relaxation time equation. Particle relaxation time, τ_p, is the characteristic time for a particle velocity to respond to changes in the surrounding gas and can be defined as follows [114],

$$\tau_p = \frac{C_C \rho_p d_p^{\,2}}{18\mu_f} \tag{3.12}$$

where C_C is the Cunningham slip correction factor and μ_f is the dynamic viscosity of the carrier fluid. The Cunningham slip correction factor can be estimated by the expression

$$C_c = 1 + Kn\left[1.257 + 0.4\exp\left(-\frac{1.1}{Kn}\right)\right] \tag{3.13}$$

where the Knudsen number, Kn, is

$$Kn = \frac{2\lambda}{d_p} \tag{3.14}$$

From the relaxation time, τ_p, equation, it can be illustrated that tiny particles possess a very short relaxation time so that they follow the continuous flow without delay, whereas, owing to inertia, large particles need a certain time to adjust themselves to changes in the flow field [115]. With Knudsen numbers, Kn, in a range of around one [24, 116] and viscosity of carrier fluid, μ_f, at 1500ºC around 5×10^{-5} $kgm^{-1}s^{-1}$ [117] in a typical diesel engine conditions, τ_p can be calculated. Yet the use of τ_p is restricted to particle motion in the Stokes region where the Reynolds particle number is less than unity [118]. Reynolds particle number is given by the equation below.

$$Re = \frac{\rho_g v d_p}{\mu_f} \tag{3.15}$$

where the variables and their values are the same as explained above.

To satisfy the condition of $Re < 1$, d_p is calculated to be less than 387 nm. Since in-cylinder soot particles are around 100 nm, the use of relaxation time is justified. With this value of diameter, maximum τ_p is calculated to be around 7.5×10^{-7} s, which illustrates that a soot particle with the size less than 387 nm will require less than 7.5×10^{-7} s to follow the continuous flow around it, and this length of time is much less than the time step used, hence the assumption of in-cylinder soot particles mainly follow the bulk fluid flow is justified.

The usage of these two approaches to justify the assumption the massless characteristics of soot particles that allows the particles to follow the in-cylinder bulk fluid flow is still not acceptable if the time step used in this study is too large to produce numerical stability in resolving the flow field in continuous carrier gas phase [119]. To show numerical stability is achieved in this study, Courant–Friedrichs–Lewy (CFL) criterion is used. The CFL number requires that the distance travelled by a discrete

particle during one time step is not larger than one spatial increment (an element). Mathematically, for one dimensional case, the CFL criterion is given by

$$\frac{\nu\Delta t}{\Delta x} \leq \mathrm{CFL} \qquad (3.16)$$

where CFL must be between 0 and 1 for numerical stability, ν average linear velocity, Δt incremental time step and Δx nodal spacing. In this study, ν is 7.1 m/s, Δt 1.67×10^{-5} s and Δx 6×10^{-3} m (the smallest nodal spacing in the computational domain) which gives CFL a value of 0.198 that satisfies the CFL criterion, hence reinforces the above assumptions.

As mentioned in Section 3.7, soot particles that are tracked from inside the fuel jet are most likely to impinge on the bowl walls due to the high velocity of the jet. In the present study, the processes that take place after the particle impingement are not considered. At this point, it is assumed that these soot particles are deposited onto the bowl walls by inertial impingement and could be involved in the soot reentrainment during exhaust blowdown or soot oxidation by subsequent flame fronts. These assumption was made based on experimental findings by Kittelson et al.[9], Dec & Tree [120] and Tree & Dec [121] about the deposition of soot onto the bowl walls.

The consideration then continues to deal with the soot particles that travel close to cylinder walls. The discussions about possibility of soot particles making contact with the cylinder wall layers that will follow in the next few chapters, depends on how close they are to the cylinder walls. To suppose that these soot particles that travel close to the walls will end up on the cylinder wall layers requires further discussions on the thickness of boundary layer of the in-cylinder walls. The boundary layer is the layer of fluid in the immediate vicinity of a solid surface as a body of fluid passes through it. It is assumed to consist of a thin film layer immediately adjacent to the cylinder wall and a “buffer zone” between this and the turbulent bulk flow [122]. Experimental findings by Heywood [123] and Hultqvist et al. [124] show that the thickness of the boundary layer in an engine

is between 1-3 mm, depending on the combustion chamber design. In their computational studies of inhomogeneities effects in HCCI engine, Maigaard et al. [122] used 3 mm as the thickness of the boundary layer. In this thesis, the discussions of possible soot transfers to the cylinder wall layers will be based on a boundary layer thickness of 3 mm parallel to the above findings and study.

3.10 Conclusions

Computer setup, computational model, Kiva-3v CFD codes and data post-processing methods described above form the basic structure for this study. From this structure, fundamental understanding of in-cylinder soot formation and distribution process through Eulerian and mass-based analysis is accomplished. An extension of this basic structure to offer further insight of the soot formation phenomena through Lagrangian and particle-based analysis is achieved by means of soot particle tracking and soot growth programmes that exploit the post-processed data. The flow of work outlined above is a unique way to undertake to gain further insight into the study of in-cylinder soot particle movement and distribution.

Several challenges have been met during the setting up of the whole structure, thus various options and possibilities have been explored and evaluated to overcome them. The two main challenges are related to particle tracking model whose correct functioning depends heavily on the simulation data. One of them lies in the basic structure itself, namely, in computational model setup, in which full cylinder volume must be used as opposed to one-seventh sector despite higher computational effort. Another is found in the extension work, namely, in the interpolation technique that is used in the particle tracking model. The interpolation technique is found to be the more correct approach to generate soot particle paths without discontinuities in them. The overcoming of these two main challenges commences a new branch of research in soot formation, soot oxidation, soot travel and soot evolution along a soot path in a diesel engine.

Evaluations of the assumptions made in this study which are explained at length in this chapter are carried out to rationalise the approach taken in this computational study. These assumptions will serve as foundations for the analysis and discussions of the results in the next few chapters.

CHAPTER 4

KIVA-3V MASS-BASED IN-CYLINDER SOOT MOVEMENT AND DISTRIBUTION

4.1 Introduction

Outputs from Kiva-3v simulation are in two main formats with the first data files give averaged temporal in-cylinder combustion and pollutants information and second, detailed spatial and temporal data with information on each cell nodes. With the aid of EnSight post-processing software, temporal and spatial in-cylinder conditions and soot and other species concentrations are visualised. Local conditions and emissions are analysed by fragmenting the cylinder volume into smaller fractional volumes to gather more information on the influence of local in-cylinder conditions to soot formation and distribution.

In this chapter, soot formation and its distribution in the cylinder is the main focus. Where required, the influence of temperature, pressure, oxygen and fuel vapour concentration on soot formation process are discussed. Coloured cut planes from EnSight that display species concentrations and cylinder conditions are used to explain the soot formation, movement and distribution. These coloured planes however do not clearly show the local variations of in-cylinder conditions and species concentrations in time. Local in-cylinder conditions and species concentrations are extracted from fractional volumes to further explain the in-cylinder soot formation process. The overall characteristics of average in-cylinder temperature, pressure and soot concentration are then compared with the local ones to obtain further understanding of the in-cylinder soot formation process.

4.2 Global Characteristics

This section shows and discusses the global characteristics of in-cylinder combustion and soot emission and distribution.

4.2.1 In-cylinder Global Conditions

Crank-angle resolved profiles of in-cylinder pressure, temperature; and fuel vapour, oxygen and soot concentrations are shown in Figure 4.1 with operating conditions listed in Table 3.7. These profiles show that soot formation process dominates during the fuel injection period where average in-cylinder temperature (>1200K) and fuel vapour concentration are high. This continues until around 40° ATDC where soot oxidation process begins to take over thus reduce the amount of net soot in the cylinder as shown in Figure 4.1. The total soot concentration in Figure 4.1(d) is also seen to reduce in time, due to oxidation process. In these figures, only the average of soot concentration in the cylinder is shown and it does not tell us about its distribution throughout the cylinder. The use of EnSight post-processing software enables the in-cylinder distribution to be studied and analysed in more detailed.

4.2.2 In-cylinder Soot Distribution

The development of in-cylinder soot distribution from as early as 1°CA ATDC until 120°CA ATDC at EVO is shown in Figure 4.2. These soot distribution maps were captured on a plane passing through the axis of the fuel jet as the representation of in-cylinder soot distribution. Two-dimensional slice can be visually misleading as it does not show the movement of soot into and out of the slice as the soot can virtually move anywhere in the cylinder volume. For the purpose of explaining the movement of soot in a simpler manner, these coloured planes are sufficient. Around 5°CA ATDC, soot is observed to reach the impingement point on the bowl walls and starts to split into two main directions, upwards into the squish region, and downwards into the bowl region. As early as 30°CA ATDC, soot can already be seen to progress towards the liner at the upper

part of the squish region. From 40°CA ATDC to EVO, soot continues to move into the upper part of the squish region, and an increasing amount of soot is seen to move into the lower squish region. The soot that moves and maintains its existence in the upper squish region early in expansion stroke is observed to move within 3 mm cylinder boundary layer and thus have higher likelihood to be transferred to the liner.

Figures 4.3-4.5 show in-cylinder distributions of fuel, oxygen and temperature, respectively. These distributions can be used to further explain the development of soot distribution, as follows. In-cylinder fuel in Figure 4.3 shows similar distribution to that of soot up to 30°CA ATDC, thus demonstrating the significant influence of high concentration of fuel to the formation of soot. Beyond 30°CA ATDC, soot starts to move away from high fuel concentration region suggesting that soot distribution is now not only influenced by the regional soot formation process, but also by the soot transport. In-cylinder oxygen distribution in Figure 4.4 shows a reverse pattern to the fuel distribution where it is low at high fuel concentration such as inside the fuel jet, inside the bowl piston and the middle of squish region, and high near the cylinder axis and the cylinder wall layers. This distribution demonstrates that the fuel spray has displaced the oxygen during its injection. It also suggests that the combustion process has consumed the oxygen in the high concentration fuel region. Temperature distribution in Figure 4.5 shows similar spatial distribution to that of soot demonstrating the significant influence of temperature on soot formation. Maximum temperature decreases from around 2400 K in the earlier crank angles to about 1500 K at EVO. High temperature and high fuel concentration region provides more opportunity for soot to form, while high oxygen concentration region influence the soot oxidation process. This relationship between oxygen, temperature and soot oxidation shall be discussed in the following sections.

By looking at all these graphical results, it is still unclear how soot moves during combustion and expansion strokes, and how part of it ends up near the liner in the squish region and another in the bowl. It is useful to know from which location and at what instants the soot near the liner is coming from, so that, not only can the soot be prevented from coming close to the liner at the later stage, but also can be avoided from forming

and progress to the liner in the early stage of soot formation process. It is also beneficial to know how this soot gets transferred to the squish region in the early part of expansion stroke. These graphical representations of soot, fuel, temperature, oxygen distributions alone could not provide the desired information, so further investigation was carried out. The next sub-section covers another set of graphical results that could answer some of the questions posed above.

4.2.3 In-cylinder Soot Transport/Diffusion

To further investigate where the soot that travels to the upper squish region comes from, another Kiva-3v simulation was carried out. In this particular simulation, soot formation and oxidation processes were stopped at 2°CA ATDC by terminating the simulation at the crank angle. The simulation was then resumed with the soot formation and oxidation process in the input file (itape5) is kept deactivated leaving the transport of soot and other combustion and emission formation processes turned on. This allowed us to follow the movement of soot that had been formed up to 2°CA ATDC. This particular soot distribution is shown in Figure 4.6. In this figure, the velocity vector map is also included to further relate the soot movement to the fluid motion in the cylinder.

As shown in Figure 4.6, soot is observed to impinge on the bowl walls around 5°CA ATDC. This batch of soot is then observed to be split by the high velocity of the fuel jet into two regions, squish and bowl, and follow the bulk fluid flow as can clearly be seen at 10°CA ATDC. As in this version of Kiva-3v, soot is modelled as a dispersed, continuous species like oxygen and OH, and no soot deposition model is included, soot that seems to impinge on the bowl walls is actually only following the fluid flow. Movement of soot at this point not only depends on flow dynamics due to swirl and piston movement, but also on the flow perturbation caused by high velocity fuel jet. As piston moves down in the expansion stroke, more soot is seen to be moving into the squish region. This movement of soot is most likely to be attributed to the reverse-squish flow as the piston moves down where the velocity vectors demonstrating the squish flow activity in the bowl can still be seen at 20°CA ATDC.

As the piston moves further down, it is evident in the figure that starting from 40°CA ATDC, the majority of the soot that was formed early (before 2°CA ATDC) is in the squish region and travels close to the liner. From this observation, it appears that fluid motion during the early part of injection causes the soot particles that are formed during this period to move into the squish region. These are then more likely to be transferred to the liner than soot that are formed later in the combustion process. In other words, the soot particles that travel close to the liner and have high possibility to be transferred to the liner are most likely to be originated from the soot particles that are formed during early injection period.

4.3 Local Characteristics

Further investigation of local in-cylinder soot distribution and local characteristics of combustion and emissions is necessary to add to the understanding of in-cylinder soot formation phenomenon. To that end, the cylinder volume is divided into smaller volumes that expand as the whole cylinder volume expands. These volumes are here called fractional volumes. There are three sets of cylinder fractional volumes starting with bigger to smaller volumes.

The purpose of this exercise is to investigate the local distribution of soot and the characteristics of fractional volumes of the cylinder. Then, it is important to evaluate whether the profiles of fuel, soot, oxygen, pressure and temperature of the whole cylinder volume are preserved in smaller fractional volumes. By looking at smaller fractional volumes, the investigation of the influence of temperature, pressure, oxygen and fuel concentrations on soot formation and oxidation processes at local cylinder areas are made possible. The final aim is to observe the consistency of soot, temperature and oxygen profiles along the soot paths (obtained with tracking method) as they pass through the fractional volumes with the profiles obtained as they pass through much smaller Kiva-3v computational cells. This final aim will be discussed further in Chapter 6.

The first set is the cylinder volume with four angular, three axial and three radial divisions in the volume above the piston bowl. The piston bowl is divided into four angular, two axial and two radial divisions. In total there are 52 fractional volumes. The second set have eight angular, three axial and six radial divisions above the bowl, and eight angular, two axial and two radial divisions in the piston bowl. The second set comprises of 176 fractional volumes. Further divisions with 16 angular, three axial and 12 radial above the bowl region, and 16 angular, two axial and two radial divisions in the piston bowl give the third set of 640 fractional volumes.

This number of fractional volumes is relatively small when compared with the number of cells used in Kiva-3v simulation, which amounts to 200,000 cells. The biggest volume of cells used in the simulation is about 0.006 cm^3 which is 0.0012% of the total cylinder volume. Whereas, the biggest fractional volume in the first, second and third sets represent only 5%, 1.2% and 0.3% of the total cylinder volume, respectively. These three sets of fractional volumes and Kiva cells are shown schematically in Figure 4.7.

4.3.1 Conditions in Fractional Volumes

The profiles of fuel, soot and temperature of fractional volumes in time are significantly different from the global profiles obtained from the in-cylinder average profile previously shown in Figure 4.1. Characteristics of fractional volumes differ according to the location of the volume in the cylinder. The soot is found in high concentration in the middle of the squish region and at the wall side of the piston bowl. These are also the areas where the fuel concentration is high, allowing more combustion to occur, hence high temperatures of above 1200 K can be observed. In other areas such as inside and outside squish area, and upper bowl near the pip area, the fuel concentration is low, less combustion occurs, thus low temperature and low soot concentration is observed in these areas. Oxygen concentration is observed to be almost consistent in all regions except where the fuel concentration is very high, i.e. inside the piston bowl and the middle of the squish regions, where fuel displaces the oxygen and combustion process consumes the oxygen. These trends can be observed in the diagram of fractional volumes

shown in Figure 4.8. In this particular figure, temporal distributions of soot, temperature and oxygen of only the first set of fractional volumes are displayed. This first set is to be an example of the other sets with which similar yet more refined profiles could be seen.

While oxygen plays important roles in soot oxidation process, its concentration profiles do not significantly influence the net soot profile. Rather, the concentration of fuel and temperature strongly determines the shape of the net soot profile in fractional volumes. This observation corresponds to the relationship of soot particle burnout with temperature and pressure put forward by Haynes and Wagner [53] in their review paper. They stated that below 1800 K, soot burnout lifetime is largely insensitive to the oxygen concentration, and totally depends on temperature. Figure 4.9 shows the relationship between soot burnout lifetime with temperature and pressure. What it means in this particular case is that soot oxidation rates in these fractional volumes, where temperature ranges from 1200 K to 2000 K during most of the time except during early combustion where temperature reaches 2400 K, are significantly influenced by temperature variations, and only slightly by oxygen partial pressure.

4.3.2 Soot Transport in Fractional Volumes

As mentioned in the earlier section (4.2.2), soot is not transported homogeneously to the whole cylinder volume, but rather concentrates inside the piston bowl and the upper and lower region in the middle of squish area. Soot in the piston bowl is observed to be constituted in greater part from the soot that is formed there. This fact is demonstrated by the occurrence of high concentration of fuel and high temperature in the bowl which cause high soot production.

Combining Figure 4.2-4.5 and Figure 4.8, it can be observed that soot that exists in the lower part of the middle of the squish region in earlier crank angle (i.e. before 20°CA ATDC) is the soot that is formed there due to the high concentration of fuel and high temperature similar to the soot inside the bowl. However, it can be observed that, after 20°CA ATDC, a significant fraction of the soot mass from a highly concentrated

piston bowl area in the earlier crank angle is convected to the squish region through reverse squish flow motion.

In the upper region of the squish area, it is also implied that majority of soot is convected to this region from high concentrated soot region in the earlier crank angles as soot formation process is low in this area since the fuel concentration is lower than the other parts of the cylinder. Soot that remains in this area until EVO can be said to be transported from the soot that is formed during the earlier part of injection period as demonstrated by graphical soot representation in Figure 4.3.

4.4 Conclusions

For the conditions defined in Table 3.7, with swirl ratio 1.9, temporally, global in-cylinder soot concentration is observed to reach its peak at around 18° CA ATDC and gradually decrease towards EVO. However, this global trend does not represent the soot profile of each local zone in the cylinder. By looking at soot profiles in smaller fractional volumes, it can be observed that soot peaks at different time depending on the local zones. These fractional volumes not only demonstrate the local process of soot formations as the source of soot, but also transport process that carry soot around from neighbouring zones. Spatially, soot is observed to be split into two regions of high concentration, that is, in the piston bowl and in the lower region of the middle squish region starting from 10° CA ATDC to EVO. By isolating soot that is formed before 2° CA ATDC, it is demonstrated that the soot that presents at the upper squish region is the soot that is transported from soot formation region in the fuel jet at 2° CA ATDC.

Kiva-3v global data can only show the average temporal profiles of in-cylinder conditions and species concentrations. The use of EnSight post-processor however, can provide both temporal and spatial information of the conditions and species concentrations. With a little manipulation, EnSight graphics can also be used to follow the progress of soot from the time it is formed. However, it is still not possible to follow a soot particle from a specific location in the cylinder by using these graphics, thus the

location from which the soot near the liner comes cannot be identified. The soot particle can be followed by a Lagrangian particle tracking method that was described in Section 3.7, and shall be explained and discussed further in next few chapters.

CHAPTER 5

INFLUENCE OF MESH CONFIGURATIONS, TIME STEPS AND NUMERICAL METHODS ON PREDICTED SOOT PATHS

5.1 Introduction

Accuracy of any simulation results depends on several factors. These include mesh configuration, time step used in the simulation work, and the method of numerical analysis to solve the desired equation.

In the present study of particle motion, Eulerian velocity fields and other combustion and emission quantities were pre-computed and recorded using Kiva-3v CFD code. Spatial resolution for this CFD data depends on mesh configuration defined by the user, and the temporal resolution set internally by the Kiva-3v programme itself. Increasing the mesh density, recording simulation data at higher frequency and employing higher order numerical methods increases the computational cost and storage.

In this chapter, the effects of different mesh configurations, time step intervals and numerical methods on the predicted soot particle paths are discussed. It is also the aim to demonstrate that the grid configuration, time step and numerical method which has been used throughout this thesis is an optimum combination to generate accurate results of the in-cylinder soot particle paths.

5.2 Influence of Mesh Configuration to Soot Particle Paths

In previous studies [30, 36], a mesh resolution of 200,000 cells was shown to be adequate to give grid-independent results. The results are based on the studies which considered in-cylinder pressure in the grid independence study. However, the sensitivity of mesh configuration to the velocity fields hence soot particle paths has not been investigated in the previous studies. Therefore, three mesh configurations which contain 150,000, 200, 000 and 250,000 cells have been selected to demonstrate the influence of different spatial resolutions to the flow fields and hence soot particle paths. Figure 5.1 shows the comparison of the average in-cylinder pressure of the three mesh configurations and that of the experimental. It is evident that the average in-cylinder pressure among the three different meshes and the experimental result only varies as much as 10%. Yet, it is still not clear how much influence the differences in mesh configurations have on the predicted soot particle paths. This influence shall be analysed and discussed in this section.

Sufficiently small time steps must also be used to minimise any temporal discretisation errors, thus any error in the resulting soot paths can be attributed to inadequate spatial discretisation [125]. Four temporal resolutions of 0.1°, 0.25°, 0.5° and 1° CA steps at engine speed of 2500 rpm have been used to study the influence of time steps to the in-cylinder soot particle paths. The influence of time steps on the predicted soot particle paths shall be discussed in Section 5.3. As 0.25° crank-angle step has been found to be the acceptable resolution to give accurate prediction of soot particle paths, this mesh configuration study was carried out with this crank-angle step.

Velocity fields created by these three mesh configurations can be first compared using Eulerian representation. A few fixed points inside the cylinder were selected and the changes of fluid velocity at these fixed points in time were recorded. The points were selected to represent the velocities of different regions in the cylinder, namely, piston bowl, bowl rim, inside of spray and squish regions. Figure 5.2 to Figure 5.7 show the location of these points relative to the spray and bowl position, the time history of

velocity components at these selected points, and the relative velocity errors at selected instants. Soot distribution is represented by four scales of grey which refer to different concentration ranges. Light grey indicates cells with soot concentration greater than zero. Grey represent those cells that have a soot concentration greater than $1x10^{-7}g/cm^3$ while the dark grey clouds show those cells having a soot concentration greater than $1x10^{-6}$ g/cm^3. Black clouds indicate regions where the soot concentration is greater than $1x10^{-5}$ g/cm^3. Higher concentrations, or darker clouds, would overlay the less concentrated one. The same scales are used throughout the thesis.

Velocities at earlier crank angles between 8-18° CA ATDC especially inside the piston bowl, are observed to vary rapidly in time across three mesh configurations and the variations are not consistent with the different mesh configuration. These rapid and inconsistent variations contribute to high percentage of relative velocity errors for these different mesh configurations. At later crank angles, temporal variations of velocities dissipate and almost reach a steady state at EVO. Macroscopically, the profiles of these Eulerian velocities demonstrate that the flow fields of the three mesh configurations are fairly consistent.

A quantitative comparison of velocity profiles from different mesh configurations under investigation are carried out to obtain the relative error of the velocities at different instants. Plots of relative velocity errors, which are shown in Figure 5.3(b) to Figure 5.7(b), demonstrate that the relative errors mostly fall within 20% margin. When considering Lagrangian representation of velocity profiles, these errors may become local errors that can accumulate and be amplified as the fluid is tracked along its path. These errors could be reduced by increasing spatial resolution but not without a cost. To increase spatial resolution, say, to 350,000 cells, will significantly increase computer storage and computational time, as has been shown in Chapter 3. However, increasing the spatial resolution improves the non-convergence of velocity fields to only an extent as spray formulation in Kiva-3v code is known to be strongly mesh dependent and it does not yield grid independent results for the spray structure, penetration length and drop sizes [106, 107, 126] due to spray dynamics models used in the code. Spray structure,

penetration length and drop sizes directly influence the surrounding gas phase hence the liquid-gas relative velocity.

Consequently, on the ground of the results of previous studies, relative consistency of Eulerian velocities and consideration on computational cost and inherent Kiva-3v spray modelling weakness, the second mesh configuration of 200,000 cells shall be used in the next sensitivity studies. The Lagrangian representation of soot particle paths for different mesh configurations are shown in Appendix A.

5.3 Selection of Time steps

In Kiva-3v code, time step is selected automatically even though the user can set the maximum time step in the input file. The time step normally used in Kiva-3v is in the order of one microsecond. The gas-phase solution procedure is based on ALE finite volume method which divides each cycle in two phases, a Lagrangian phase and a rezone phase [102]. In the Lagrangian phase, the vertices move with the fluid velocity and there is no convection across cell boundaries [102]. In the rezone phase, the flow field is frozen, the vertices are moved to new user-specified positions, and the flow field is remapped onto the new computational mesh. In this phase, calculations of material convection are done explicitly and can be subscycled an arbitrary number of times and submultiplied of the main computational time steps [102]. Therefore, Kiva-3v code can carry out calculations of gas-phase convection and movements in smaller time steps than the fluid velocity calculation. To correctly follow the paths of in-cylinder fluid flow, hence soot particles, temporally using Lagrangian approach, the Kiva-3v simulation data must be recorded at the same time step used for its calculation in a Lagrangian phase. However, recording data at such small time step is considered impractical as Kiva-3v calculations are done at every microsecond which is around every 0.025° CA at the engine speed of 2500 rpm used in this study, and this would take a huge amount of computer storage.

Thus, the right selection of time step to record the Kiva-3v data which are used in the particle tracking exercise is crucial in obtaining adequate prediction of in-cylinder soot particle paths. Data recording with large time steps require less computational effort but more prone to error when the flow fields are complex. Data recording with small time step close to Kiva-3v time step is ideally required to give accurate soot particle paths, yet it requires more computational effort. For this reason, recording of a few sets of simulation data at much larger time steps than Kiva-3v time steps have been carried out. The different sets of recorded data with different time steps are used and investigated to demonstrate the convergence of the soot particle paths.

In the present study, three sets of data have been collected at every 1°, 0.25°CA and 0.1° with the second mesh configuration of 200,000 cells. With smaller time steps than these, not only computer storage constraint needs to be coped with, but further post-processing and data management would be highly resource-intensive. With these limitations in mind, time step effects on the predicted soot particle paths and their convergence have been investigated.

Qualitative analysis of soot particle paths is carried out based on Figure 5.8 to Figure 5.10. Figure 5.8 shows eight cases of predicted soot particle paths with different time steps and calculated with first-order Runge-Kutta numerical method. In half of the cases (Case 1-3, and Case 7), the use of 1°CA time step and first-order Runge-Kutta is shown to be sufficient to accurately predict the paths. In Case 6 and Case 8, the convergence of the paths can be obtained by decreasing the time steps. However, as demonstrated by Case 4 and Case 5, a mere time step reduction is not sufficient to give particle paths convergence. In these last cases, the turbulent flow fields that exist inside piston bowl (as shown in Figure 4.6) which possess rapid variation of velocity in space and time cannot be adequately solved by first-order numerical method at the smallest time step under study. Further reduction of time step can finally solve these divergences but at much higher computational cost. Another way to solve this turbulent flow fields is by using higher-order numerical methods which can improve the estimate of velocity at

each point thus increase the accuracy of the path predictions. The sensitivity of different numerical methods on soot particle paths is discussed in the next section.

5.4 Numerical Methods

Different numerical methods produce results with different accuracies and precisions. A low-accuracy method may use less computational effort than a high-accuracy one but may pose more difficulties in reaching convergence even with very small time step. In this present study, three different one-step methods have been used to solve an ordinary differential equation in the form of Equation 3.7:

$$\frac{ds}{dt} = u(s_n, t_n) \qquad (5.1)$$

as described in Chapter 3.

The three methods are different only in terms of how the velocity is identified. The first method is first-order Runge-Kutta method or more commonly known as Euler's method. In this method, the velocity at the beginning of the interval is taken as an approximation of the average velocity over the whole interval [127] to give the estimated distance. The equation is as simple as follows,

$$s_{n+1} = s_n + u(s_n, t_n)\Delta t \qquad (5.2)$$

The second method used is Heun's method, which is a variation of second-order Runge-Kutta method. With this method, the velocity is determined by taking the average of two velocities, one at the beginning and another at the end of the interval. The Heun method is a predictor-corrector approach and can provide improved estimate of the slope. The equation is shown below.

$$s_{n+1} = s_n + \frac{u(s_n, t_n) + u(s_{n+1}, t_{n+1})}{2}\Delta t \qquad (5.3)$$

The third method used in the present study is classical fourth-order Runge-Kutta method. This method uses multiple estimates to determine the average velocity and entails the use of mid-point data to obtain the intermediate slope. The equation in use is as the following:

$$s_{n+1} = s_n + \frac{1}{6}(k_1 + 2k_2 + 2k_3 + k_4)\Delta t \qquad (5.4)$$

where

$$k_1 = u(s_n, t_n)$$

$$k_2 = u\left(s_n + \frac{1}{2}\Delta t, t_n + \frac{1}{2}k_1\Delta t\right)$$

$$k_3 = u(s_n + \Delta t, t_n - k_1\Delta t + 2k_2\Delta t)$$

$$k_4 = u(s_n + \Delta t, t_n + k_3\Delta t)$$

Figure 5.9 shows the same eight cases with second-order Runge-Kutta method. It can be observed that with this method, accuracy of the soot paths improves substantially where predicted soot paths with different time steps are move closer to each other. It also improves the divergence problem in Case 4. However, Case 5 proves that this method is not sufficient to produce path convergence in every case even when the time step is made very small, i.e. 0.1°CA. As previously shown in Figure 5.8, the paths with different time steps diverge during the expansion stroke where fuel is still injected and when soot particles are still inside the piston bowl. During this time, the variation of velocity in this area is too rapid to be resolved by this method. A higher accuracy method is clearly necessary.

Figure 5.10 compares the predicted soot paths calculated with the classical fourth-order Runge-Kutta method. This figure demonstrates that this particular method is sufficient to give soot path convergence in every case under study. The benchmark display of path convergence in this figure is Case 5, in which lower order methods are not

sufficient to produce even with smaller time steps. The two soot paths with time steps 0.25° and 0.1° CA are very close to convergence. In the next section, quantitative analysis of soot paths and the convergence criteria shall be discussed.

5.5 Quantitative Analysis and Convergence Criteria

While the comparison of predicted soot paths with different time steps and numerical methods has been done qualitatively in the previous section, it is also important to show it quantitatively in which the convergence criteria are demonstrated. As the classical fourth-order method is previously shown to be the most favourable method, only the analysis for this method is shown and discussed. A few cases of different difficulty levels in reaching the convergence were selected to be analysed.

Figure 5.11 – 5.14 show the predicted paths for the selected cases, the velocity components along the paths, and relative errors of point-to-point velocities and of point-to-origin distances. From these figures it can be demonstrated that the relative error of distance from selected points to the origin between two paths generated with 0.25° and 0.1°CA time steps is well within 5%. While it was realised that this type of relative error alone was not adequate to prove convergence, point-to-point comparison of velocity profiles along the paths were also carried out. The highest relative velocity errors obtained were 9% and 12% at 80° and 120° CA ATDC, respectively, which can be observed in Case 5. This difference in velocity however does not significantly change the location of the final destination of the soot particle hence, is considered acceptable. Other cases have shown that the velocity relative errors were within 5%. With previously discussed qualitative figures, and these quantitative results, the classical fourth-order Runge-Kutta method with 0.25°CA time step is regarded as a sufficient and optimum combination, as smaller time step of 0.1°CA does not yield significant difference in the predicted soot paths.

5.6 Conclusions

The main aim in this sensitivity study was to demonstrate the convergence of soot paths calculated with different mesh configurations, time steps and numerical methods. Results of in-cylinder velocity profiles with different mesh configurations under investigation show that the velocities at different points are consistent. However, rapid variations of velocity at early crank angles may have impact on the soot particle paths when the soot particle passes through this period. Relatively high variation of velocity in all cases presented may also contribute to overall errors in soot particle paths.

First-order Runge-Kutta method is highly vulnerable to local errors especially when the time step is large. Reducing the time step reduces the errors in estimating the velocity and predicting the position of the particle. With higher order numerical methods, the error is decreased at a faster rate with decreasing time step. The faster rate of error decrease means the faster rate of convergence of soot particle paths thus reducing the high computer storage requirement. In their particle tracking exercise, Cheng et al. [128] also demonstrated that average-velocity approaches should be used to trace fictitious particles both accurately and efficiently.

Based on the sensitivity study in this chapter, the second mesh configuration of 200,000 cells, 0.25°CA time step and the fourth-order Runge-Kutta numerical method are used in all the analysis throughout the remaining chapters of the thesis.

CHAPTER 6

PREDICTION OF SOOT PARTICLE PATHS

6.1 Introduction

To investigate where a soot particle located at a specific location at a given time travels to, tracking of the in-cylinder soot particles in space and time is required. Results of a Kiva-3v simulation that contain in-cylinder combustion and emission data, (including pressure, temperature, soot mass and in-cylinder velocity field) were post-processed. The technique developed in the present study uses the pre-computed velocity field and the assumption of massless soot particles to obtain paths of soot particles movement in a modern design of a DI diesel cylinder. Trilinear interpolation technique was used to interpolate the velocity at each particle position in the cylinder volume as the function of velocities at the surrounding cell vertices. The positions of the injector and fuel spray inside the cylinder from top and side views are shown in Figure 6.1. The spray angle for the baseline case is 74° from the cylinder axis and spray cone angle is 14° with solid cone type. Lines indicating the angular position of 0° and 50° are also drawn to indicate the position of the fuel spray and soot plume; and the angular range in which the soot particle tracking were carried out. The actual value of one-seventh sector of cylinder is 51.43°, namely 360° divided by seven injector holes. The thickness of the boundary layer at the cylinder wall, assumed to be 3 mm, is also marked. The position of the piston and the soot distribution shown in this figure is at 2° CA ATDC instant. Side views of half of the cylinder and top views of the whole domain which show different soot concentrations at a range of crank angle instants of 2° to 30° CA ATDC, in relation to spray and piston positions, are shown in Figure 6.2.

6.2 In-Cylinder Flow Patterns

As seen from top views in Figure 6.2, soot distribution is influenced by the swirl motion in the cylinder. At 6º- 10º CA ATDC, it can clearly be seen that the swirl motion moves the soot mass in the bowl and in the squish region in the clockwise direction. These swirl motion affects not only the soot distribution but also fuel spray positions hence fuel distribution. Fuel sprays which are initially injected at 30º (as shown in Figure 6.1) are affected by the swirl motion so that the axes of the sprays after a few crank angle degrees are no more at 30º. This fact is recognised so that the starting point of soot particle tracking can be properly selected, as the velocities in the fuel sprays reduce with the distance from the spray axes. Selecting a starting point of tracking at these modified fuel spray axes will produce a short soot particle path where it hits the bowl wall immediately after tracking as the velocity at the point is very high. In this instance, the soot particle is assumed deposited on the bowl wall as discussed in Section 3.9. Therefore, the starting points of the tracking in this study are selected more towards the periphery of the fuel sprays.

Figure 4.6 shows the velocity vectors of the in-cylinder fluid motion on a plane of near the axis of a fuel spray. From 1º- 10º CA ATDC, fuel is seen being injected, as it produces very high velocity vectors near the spray axis. This high velocity fuel injection affects the surrounding gas by creating vortices above and below the spray. With the swirl motion and reversed squish in action, it also generates chaotic velocity distribution inside the cylinder especially at the bowl rim and near the axis of the cylinder as can be seen in the figure at 5º CA ATDC. As the piston moves away from TDC, amplified by the reversed squish motion as the volume increases in the squish region, the high velocity of the fuel injection pushes and splits the surrounding gas, hence the soot cloud into two main regions, inside the piston bowl and the squish region as can be seen in the figure at 10º CA ATDC. As the fuel injection stops, vortices and reversed squish motion persist to transport part of the soot into the squish region, while the other part of soot is maintained inside the bowl as seen at 20º CA ATDC. After 30º CA ATDC, the velocity profile is

relatively uniform and soot clouds are already distributed almost evenly in the squish and the bowl region as can also be seen in Figure 6.2.

As the exercise of soot particle tracking in this study depends a great deal on the in-cylinder velocity vectors during the fuel injection, proper selection of the starting points of the tracking during fuel injection duration is crucial to obtain meaningful results. More importantly is the understanding of the physical phenomena in the cylinder so that assumptions made during the study are justified. Bearing this in mind, soot particle tracking exercise was carried out.

The following few sections discuss the results of the particle tracking exercise that was carried out at different starting instants in different regions of the cylinder volume. This exercise was carried out in an effort to identify the sources of the soot particles that transported near the cylinder boundary layer. This exercise is to give more insight and understanding of in-cylinder soot particle movement.

6.3 Soot Particle Paths from Different Starting Instants

The movements of soot particles from above, below and sides of the spray are followed with the particle tracking programme. These different locations are selected as preliminary studies have shown that soot particles from these regions are likely to move towards the cylinder walls. Soot concentrations in these locations are relatively high and exposed to the surrounding fluid motions thus merit further investigation. Velocities at these regions are not extremely high (as opposed to the ones at the spray axis), so tracking of soot particle can be continued until EVO although some paths stopped earlier as soot particles impinge on the bowl walls. Soot concentration inside the spray head is the highest and soot particles from this area have low possibilities to move to the cylinder wall boundary layer as shall be shown later, thus pose less risk to the oil on the cylinder wall layers.

The movement of soot particles from these selected regions is investigated with different starting instants (in crank angle degrees), and to a certain extent, with the changing of angular positions of the starting locations. Different paths are generated with the range of starting instants from 2° to 30° CA ATDC, and the range of angular positions from 5° to 45°, at a few fixed positions in the cylinder. Summary of starting points are shown in Table 6.1. In each particle tracking exercise, care has been taken to ensure that soot is present at the starting locations by making the Matlab soot particle tracking routines to detect soot presence at these locations. Therefore, the paths obtained can be considered soot particle paths, not fluid paths.

Figure 6.3 to Figure 6.8 show different paths from different regions in the cylinder. The cylinder schematics on the left hand side in each figure show the locations of starting points of particle tracking relative to the fuel spray. The schematics only show the position of piston top and soot distribution at 2° CA ATDC. Similarly, soot particle paths plotted in the schematics on the right hand side only show the positions of piston top at crank angle instant of 2° CA ATDC (at 10.0 cm axial distance) and at EVO, which is at 120° CA ATDC (at 3.0 cm axial distance).

Figure 6.3 shows the soot paths from the region above and at the downstream of the fuel spray. Relatively near the spray in angular positions (20° and 25°), soot particles from all crank angle instants have no tendency to be transported to the cylinder boundary layer. Most of the soot particles are observed to be moving around in the top region of the cylinder and may have some possibilities to also hit the cylinder roof, while some of them which come from 6-14° CA ATDC move into the middle of squish region and move downwards following the piston motion. However, soot particles which are relatively farther away from the spray axis in angular positions (10° and 40°) are more likely to travel close to the cylinder boundary layer. These soot particles are specifically the ones from the starting crank angle instants of 6° to 10° ATDC.

In Figure 6.4, the soot paths from the region below and at the downstream of the fuel spray are plotted. Soot particles below the spray from 6° to 12° CA ATDC are observed to show consistent behaviour of moving close the boundary layer of the cylinder wall. Combination of swirl motion, vortices in the bowl and reverse squish motion is responsible to carry the soot particles close to the boundary layer. Angular positions have very small influence on the movement of soot particles from these regions, as most soot from this region are likely to end up near the cylinder wall layers. Interestingly, soot particles from later instants (i.e. 24° to 28° CA ATDC) are also seen to move relatively close to the cylinder wall boundary layer. The remaining motions of swirl, vortex and reverse squish together with lower position of bowl rims at these instants allow more soot to move close to the boundary layer at later crank angle instants.

Tracking soot particles from the upstream of fuel spray is carried out to study the effect of changing starting radial positions on the soot particle paths. At the upstream of fuel spray, there is no soot present at angular position of 40° until 16° CA ATDC, as soot is not convected towards that direction in the early crank angle instants. Consequently, soot particle paths can only be started at 16° CA ATDC in that angular position for both cases. Figure 6.5 and Figure 6.6 show soot particle paths from above and below of the spray axis at the upstream of fuel spray respectively. Soot particles from these regions have very low likelihood to be transported near the cylinder wall boundary layer and most of soot particles travel downwards in helical fashion following the piston motion.

Figure 6.7 shows soot particle paths calculated from the sides of the spray. Farther away from the spray axis (i.e. at 5° and 45°) soot is not present at the early starting instants. As swirl motion is clockwise, soot starts to be present at 4° CA ATDC at 5° angular position. At 45° angular position, it takes some time for soot to diffuse, thus soot is found to start to be present at 8° CA ATDC. It is observed that soot particles from 14° to 18° CA ATDC have the highest possibilities to be transported to the cylinder boundary layer. Soot particles at later crank angle instants (22° to 26° CA ATDC) also have relatively high possibilities to move close to the boundary layer, especially at angular positions of 35° and 45° from the spray axis. Soot particles from other crank

angle instants tend to stay inside the bowl and the middle of squish region thus have less likelihood to be transported to the boundary layer.

As early as at 6° CA ATDC as shown in Figure 6.2, soot is observed to move over the bowl rim. It is also worthwhile to track the movement of soot particles from this region. Figure 6.8 shows soot particle paths tracked from different angular positions with varying crank angle instants as done with other cases. Results show that soot particles from the ranges of crank angle instants of 6° to 10° ATDC and 20° to 26° ATDC are most likely to reach the 3 mm cylinder boundary layer.

These observations especially the cases in which soot particles are likely to reach the cylinder wall boundary layer is tabulated in the last column in Table 6.1. From the above observations and the tabulated summary, it can be concluded that there are three main ranges of crank angle instants that soot particles at the liner boundary layer are likely to come from. The first range is from 6° to 10° CA ATDC during which the high velocity of the fuel spray is mainly responsible to create high vortices in the bowl area that force the soot particles towards the cylinder wall which is observed in all cases discussed above. The second range is from 14° to 18° CA ATDC during which only soot particles from the sides of the spray are observed to travel close to the cylinder wall. This may be due to later effects of spray-to-spray interaction that changes the fluid flow in these regions. The third range is between 24° and 26° CA ATDC. At these instants, the remaining vortices inside the bowl and the lower position of the piston top relative to the starting positions permit the movement of soot particles towards the cylinder walls. Spatially, sources of soot at the liner are most likely from the soot that present inside the bowl (below the spray), at both sides of the spray, above yet relatively far from spray axis, and above the bowl rims.

6.4 Soot Particle Paths with Different Radial and Axial Distances

The above analysis alone is insufficient to conclude on the regions of sources of soot particles transfer to the cylinder wall layers. Further analysis of soot particle paths from different radial and axial distances in the crank angle instants of interest is necessary. Three crank angle instants of 8° CA, 16° CA and 24° CA ATDC have been selected to represent the ranges of crank angles that soot at the cylinder wall are most likely to come from. At 8° CA ATDC, soot particle paths from inside the bowl and above the spray are obtained with different radial and axial distances. The radial and axial soot path analysis at the bowl rim at the crank angle instant of 8 °CA ATDC cannot be carried out because at this crank angle instant, soot is not distributed farther into the squish region and the squish region is still constricted.

Figure 6.9(a) and 6.9(b) respectively show different radial and axial initial tracking locations, and soot particle paths of soot above the spray axis. The angular position is set at 10°. From this figure, it is demonstrated that soot particles that are between radial distance of 1.6 to 2.0 cm, and axial distance of 9.5 to 9.8 cm are more likely to travel into the squish region with a few cases of the paths extend close to the 3 mm boundary layer. More cases of different axial distances are also carried out at angular position of 25° and 40° which is shown in Figure 6.9 (c). This figure shows that the closer the soot particles to the spray axis angularly, and the more distant axially, the higher the possibility of soot to be transferred to the cylinder wall layers. Figure 6.10 shows soot particle paths from inside the bowl with different radial and axial distances. It is clear in this figure that, soot between the radial distance of 1.6 and 1.8 cm, and the axial distance of 8.6 and 9.2 cm, are most likely to reach the boundary layer.

Figure 6.11 shows soot particle paths from the crank angle instant of 16° CA ATDC at one side of the spray, namely at angular position of 5°. It is demonstrated in this figure that soot particles between the radial distance of 1.6 and 2.0 cm at this instant are most likely to reach the boundary layer, while others below radial distance of 1.6 cm stay inside the bowl.

Soot particle paths from the crank angle instant of 24° CA ATDC with different axial and radial starting positions are shown in Figure 6.12 and Figure 6.13. Figure 6.12 demonstrates that soot particles from inside the bowl between the radial distance of 1.6 and 1.8 cm, and axial distance of 9.0 and 9.4 cm are most likely to travel close to the to the boundary layer. In Figure 6.13, it can be seen that radial and axial positions of the soot in the bowl rim region do not have significant effect on the soot paths, and most of the soot particles from this region at this instant are likely to be transported to the wall layers.

From all of these observations of the sensitivity of soot particle paths to crank angle instants and angular, axial and radial positions, maps of regions of soot that are most likely to be the source of soot at the cylinder wall layers can be drawn. These maps are illustrated in Figure 6.14 to 6.16. Figure 6.14 shows the regions of possible sources of soot transfer to the cylinder wall from the crank angle of 8°CA ATDC. This map represents the map for possible sources of soot at the cylinder wall during the middle duration of fuel injection period, namely, 6°CA ATDC to 10°CA ATDC. Similarly, Figure 6.15 shows the regions of possible sources of soot transfer to the cylinder wall from the crank angle of 16°CA ATDC which represents the map for possible sources of soot from instants of a few degrees after the end of injection, namely 14°CA ATDC to 18°CA ATDC. Figure 6.16 shows a representation map of possible sources of soot from 22°CA ATDC to 28°CA ATDC. The regions are marked with different colours only to distinguish the regions when viewed from top and side views. The colours do not necessarily represent the degree of possibilities of soot to be transferred to the cylinder wall. An illustrative figure will be shown in Figure 9.1 in the discussion and conclusions chapter.

6.5 Paths of Soot Particles from the Highest Concentration Region

In this section, points with the highest soot concentrated are tracked for different swirl ratios of 1.3, 1.6, 1.9, 2.1 and 2.4 at the three time instants (8°, 18° and 35° CA

ATDC). The aim of this exercise is to investigate whether soot particles from the highest concentration regions, if any at all, get close the liner. The effects of different swirl ratios are also investigated.

Figure 6.17 shows soot paths from 20 highest concentration soot locations at different swirl ratios. At 8° CA ATDC, the highest soot concentration occurs inside the piston bowl. Points in this area were selected and soot particle tracking were carried out with five different swirl ratios. It can be seen that the particles have no tendency to get close to the cylinder wall layers to contaminate the oil. It can also be seen that the paths are very varied in spite of the starting points being very close together.

Similarly, soot particle tracking with the highest soot concentration was carried out at starting instants of 18° CA ATDC and 35° CA ATDC. Figure 6.18 and 6.19 show the soot paths tracked from 20 highest concentration soot locations from crank angle instants of 18° CA ATDC and 35° CA ATDC, respectively. At 18° CA ATDC, the highest soot concentration occurs in the piston bowl while at CA 35° ATDC, at the bowl rim. Again, with both starting instants, not a single path is seen to move close to the wall layers. The soot particles from these regions tend to move helically downwards into the piston bowl area.

From this exercise, it is evident that soot particles starting from points with the highest soot concentration do not get close to the cylinder wall layers. This suggests that the probability of particles getting close to the wall layers does not depend on the soot concentration but on its position relative to the fuel spray jet, which significantly influences the velocity of the fluid. The paths of the soot particles are extremely sensitive to in-cylinder location at earlier crank angles.

6.6 Soot Particle Paths through Fractional Volumes

It was mentioned in Chapter 4 that one of the aims of fractional volume exercise was to study the consistency of soot, temperature and oxygen profiles along the soot

paths as they pass through the fractional volumes with the profiles extracted as they pass through Kiva-3v computational cells.

In this section, the soot particle paths that were obtained using velocity vectors from Kiva-3v simulation with second mesh configuration of 200,000 cells, were used to record the average profiles of soot as they pass through different sizes of fractional volumes. It is expected that the soot profiles through fractional volumes are consistent with the ones obtained through Kiva-3v computational cells. The idea is to gain consistency as the fractional volumes are made smaller and smaller.

From Figure 6.20 (a)-(d), it is demonstrated that the consistency is not reached with the current configuration of fractional volume. However, the soot profiles with the current size of fractional volumes have shown good trends to reach consistency. It is apparent that current configuration of fractional volume is not adequate to show the consistency of soot concentration along the paths. Much smaller volumes need to be created to approach consistency but the high computational time at this point does not allow the analysis of smaller volumes. For example, the smallest of fractional volumes with 640 small volumes takes more than 60 hours to be discretised and to calculate the average concentration of each species. With Matlab, this process needs to be done in batches to avoid maximum usage of computer memory.

One point that could be drawn from this exercise is the gradient of soot concentration is very steep even in a fractional volume of 0.3% of the total cylinder volume. Consequently, assuming that soot concentration in the piston bowl, for example, is homogeneous, can be misleading. This information is very important to be acknowledged while pursuing the study of in-cylinder soot particle size evolutions for different paths from the same region as small variations in soot paths may lead to different profiles of species concentrations.

6.7 Conclusions

In the simulation study reported in this chapter, soot particles are assumed massless and other forces are considered negligible due to the dominant turbulent fluid force. Paths that were obtained at various instants and geometrical locations of the cylinder show shat the sources of soot transfer to the cylinder wall layers are most likely to be from three ranges of crank angle instants, which are 6° to 10° CA ATDC, 14° to 18° CA ATDC and 22° to 28° CA ATDC. The paths from the first range of crank angle instants, however, display the highest possibilities of soot transfer to the liner.

The occurrence of multiple ranges of time instants as the sources of soot particles travel to the cylinder wall layers makes the controlling of oil contamination by soot at the liner more complicated. Advanced injection timing may reduce the possibilities of soot transfer to the liner as when fuel injection is stopped earlier, soot particles are less likely to be influenced by the high shear velocity of the fuel jet to be pushed closer to the cylinder wall as the piston moves down in the expansion stroke. As the first range of crank angle instants is observed to be the most consistent source of soot transfer to the cylinder walls, split or multiple injections strategies with early injection supplied with oxygenated fuel may also reduce the possibility of early soot transfer to the liner. These suggestions need to be investigated further to come to a definite conclusion.

Several regions in the cylinder have been identified as the sources of soot transfer to the liner with the soot from below the spray axis in the middle of bowl are the most likely source. The paths from this indicated region display consistent trends of soot particle paths reaching the 3 mm cylinder boundary layer. Other regions which have relatively high possibilities to be the source of soot at the cylinder walls, based on soot paths that go beyond the middle of the squish region are the region above the fuel spray, above the bowl rim and each sides of the spray. These are the regions where soot concentration is relatively lower and outside of fuel spray plume. Soot particles that are present at the locations below 1.6 cm radial distance from the cylinder axis are observed to mostly stay inside the bowl.

Bowl shape and swirl-generating apparatus are designed to provide proper mixing hence improved combustion and less pollutant formation. The type of bowl shape and swirl ratio used under current investigation are observed to do just that by creating high turbulent motion especially inside the bowl. Optimising the bowl shape and swirl ratio to reduce the problem of soot transfer to the liner may do the trick but may cause reduced engine performance and increased pollutant formation. Priorities need to be carefully considered when dealing with this issue. It is also suggested that the upper part of the liner should not be lubricated, for example by increasing the topland height. Non-lubrication would reduce oil contamination by soot but would most likely increase scuffing and friction between the piston crown and the liner. However, advanced materials such as nickel and silicon carbide matrix coating, and improved surface engineering could help dealing with that.

Investigation of soot paths through fractional volumes proves that the gradient of soot concentration is so steep that consistency of soot concentration along a path can only be obtained with very small fractional volumes. Thus, average profiles of soot and other species along the paths that pass through the fractional volumes may not be sufficient to show the trends along the paths. This demonstrates that, the best way to accurately track the soot and other species concentration along a tracked path is by tracking it using the volume of cell size used in the simulation which also shows that the smaller the cell size the better the accuracy should be. It is also important to acknowledge that small variations in the predicted soot paths of the same region may lead to different profiles of species concentration history along the paths, so the soot particle size prediction maybe significantly different.

CHAPTER 7

SIZE CHANGE OF SOOT PARTICLE ON A SPECIFIC PATH DUE TO SURFACE GROWTH

7.1 Introduction

In Chapter 6, the analysis of soot particle paths was presented. From hundreds of paths generated, a few paths have been selected to be the representative paths for the regions and instants previously discussed.

The next objective is to model soot particle evolution (i.e. size change) by employing Hiroyasu soot formation and Nagle and Strickland-Constable soot oxidation expressions along the paths. Neoh's soot oxidation expression is not considered in this exercise as it contributes to around only 10% of the total oxidation which is consistent with [53]. Soot size evolution investigation at this point considers only surface growth and surface oxidation processes without taking into account the physical process of particle-to-particle coagulation. The initial expectation was soot particle diameter profiles along the tracked paths would follow the trend shown by the overall net soot in the whole cylinder as shown in Figure 4.1. This expectation may or may not be the case since the soot particle paths that have been obtained from selected starting regions follow different paths and pass through different conditions depending on starting tracking positions hence soot diameter profile might evolve differently than the initial expectation. However, consideration on overall high rates of soot formation during early crank angles and domination of oxidation process at later crank angles may have the dominant effect on all soot particle paths. This will be investigated in this chapter.

The evolution of soot particle along the paths is influenced by the state/conditions along the paths. In-cylinder properties along paths are retrieved by using the same trilinear interpolation method. The properties are fuel concentration, pressure, temperature, oxygen and OH concentration. These properties were then used in soot formation and oxidation equations to get the soot particle evolution along the paths. Depending on the method used, history of soot along the paths is used to normalise the rate of soot formation and oxidation.

Several approaches of soot evolution due to surface growth and oxidation have been explored. The main aim is to predict the size changes as the soot particles pass through the conditions in the cylinder volume following the trajectories obtained from particle tracking technique. Different methods produced different results. Each method explored is explained in detail in the following few sections.

7.2 Approach 1: Direct Association with Net Soot and Conserving Initial Soot Particle Number

This is the simplest approach explored in this investigation. The soot particle size evolution is directly associated with the net soot interpolated along the path. The initial soot particle size was set to 4 nm as in other approaches. The initial interpolated net soot value at the starting of the path was used to calculate the initial soot particle number density. In the next time step, this number density was kept constant when new diameter was calculated. This was continued until the end of the path. A simple algorithm is shown below.

i) Initial soot diameter, $D_i = 4 \times 10^{-9}$ m (4 nm)

ii) $$\text{Soot number density}(N_i) = \frac{\text{Initial net soot}(Ms_i)}{\text{Mass of soot particle of } D_i \text{ diameter}\,(Msp_i)} \left(\frac{\#}{cm^3}\right) \quad (7.1)$$

iii) Mass of the soot particle in the next time step;

$$Msp_{i+1} = \frac{Ms_{i+1}}{N_i} \tag{7.2}$$

iv) Diameter of the soot particle in the next time step

$$D_{i+1} = 2 \times \left(\frac{3}{4} \frac{Msp_{i+1}}{\rho_{sp} \pi} \right)^{1/3} \tag{7.3}$$

This approach produces a diameter profile that replicates the profile of net soot along the path. It also depends heavily on the initial net soot mass which determines the number density, hence the diameter of the soot particle. This simple approach is acceptable when accompanied by the assumption that all the net soot mass interpolated along the path until the end point comes from the initial point or region. Yet, physically, the net soot mass along the path are the outcome of soot formation process at the interpolated cell and net soot transport or diffusion into/out of the cell from/to surrounding cells. With current Kiva-3v code setup, it was impractical to differentiate between the two sources of soot in a particular cell.

7.3 Approach 2: Association with In-cylinder Conditions along the Path

To avoid heavy dependence on the initial net soot, this approach was explored. The in-cylinder properties, namely temperature, pressure, fuel and oxygen concentrations were used to calculate the rates of soot formation and soot oxidation. The rates were calculated using the Hiroyasu's soot formation and NSC soot oxidation equations exactly as they were used in Kiva-3v code. The soot formation calculated is the rate of soot conversion from the amount of soot contains in 1 cm^3 of cylinder volume. Similarly, the oxidation rate is the rate obtained from the existence of soot in 1 cm^3 of cylinder volume. Therefore, these rates do not represent rates for one soot particle under consideration. To find the average rate for a soot particle, the rates were normalised with the concentration

of soot along the path. From these rates, fractional mass change, F_i, for a soot particle was calculated. Finally, the diameter of the soot particle in the current time step can be calculated. The steps of the calculation are shown below.

i) Normalised Hiroyasu's soot formation

$$\frac{dM_{sfi}}{M_{sni}.dt} = \frac{A_f M_{fvi} P_i^{0.5} e^{\frac{-E_{sf}}{RT_i}}}{M_{sni}} \qquad (7.4)$$

ii) Normalised NSC's soot oxidation

$$\frac{dM_{soi}}{M_{sni}.dt} = \frac{A_o \frac{MW_c}{\rho_s D_s} M_{sni} \dot{R}_{NSCi}}{M_{sni}} \qquad (7.5)$$

iii) $F_i = [(7.4)-(7.5)] \times dt$ (F_i is the net formation rate at each time step) (7.6)

iv) $M_{sp_i} = M_{sp_{i-1}} + \left(M_{sp_{i-1}} \times F_i\right)$ where M_{sp} is mass of a soot particle (7.7)

v) $$D_i = 2 \times \left(\frac{3}{4} \frac{M_{sp_i}}{\rho_{sp} \pi} \right)^{1/3} \qquad (7.8)$$

The results of soot diameter in Figure 7.2 to Figure 7.6 show that in majority of the cases, oxidation process dominates, thus causing soot particles to be disappearing as they travel along the paths. With this approach, the influence of soot concentration included in the calculation especially in the soot oxidation process, is significant. High soot concentration which may be caused by soot transport into the volume of interest has been seen to cause over-prediction of soot oxidation, and under-prediction of soot formation rates in that volume.

7.4 Approach 3: Association with In-cylinder Conditions along the Path with Modified Hiroyasu's Equation

This approach was formulated to overcome the weakness in Approach 2 particularly on the normalising effect of soot formation rates to the soot concentration. Hiroyasu's equation was modified to consider the contribution of fuel vapour to growth process of a soot particle. In this approach, soot oxidation was calculated the same way as the previous approach where NSC's equation was normalised with net soot in the volume.

In this approach, the assumption was that for a particular soot particle, there was a cloud of fuel vapour that was responsible for the growth of the soot particle. The amount of fuel vapour can be specified in two ways, by volume or diameter. In this section, fuel vapour by volume is explained. Hiroyasu's soot formation equation needs to be rewritten in terms of soot particle and fuel vapour mass. The relation between a soot particle and a cloud of fuel vapour is shown in Figure 7.1.

Again, Hiroyasu's soot formation equation is shown below.

$$\frac{dM_{sf}}{dt} = A_f M_{fv} P^{0.5} e^{\frac{-E_{sf}}{RT}} \qquad (7.9)$$

From this figure, the following expressions were obtained.

Mass of fuel vapour, $M_v = M_{fv} V$ (M_{fv} : concentration of fuel vapour, g/cm^3)

Mass of particle, $M_p = M_{sf} V$ (M_{sf} : concentration of soot formed, g/cm^3)

Then, normalisation to get a fractional change for one soot particle is carried out as follows;

$$\frac{dM_{sf}}{dt.M_{sf}} = A_f \frac{M_{fv}}{M_{sf}} P^{0.5} e^{\frac{-E_{sf}}{RT}} \quad (7.10)$$

$$\frac{dM_{sf}}{dt.M_{sf}} = A_f \frac{\frac{M_v}{V}}{\frac{M_p}{V}} P^{0.5} e^{\frac{-E_{sf}}{RT}} \quad (7.11)$$

Then the increment of mass in a cubic centimetre is assumed to be equal to that of one particle.

$$\frac{dM_{sf}}{dt.M_{sf}} = \frac{dM_p}{dt.M_p} \quad (7.12)$$

$$\frac{dM_p}{dt.M_p} = A_f \frac{M_v}{M_p} P^{0.5} e^{\frac{-E_{sf}}{RT}} \quad (7.13)$$

$$\frac{dM_p}{dt.M_p} = A_f \frac{\rho_v (x)(\frac{4}{3}\pi r^3)}{\rho_p (\frac{4}{3}\pi r^3)} P^{0.5} e^{\frac{-E_{sf}}{RT}} \quad (7.14)$$

$$\frac{dM_p}{dt.M_p} = A_f \left(\frac{\rho_v}{\rho_p}\right)(x) P^{0.5} e^{\frac{-E_{sf}}{RT}} \quad (7.15)$$

With the current data,

$\rho_v = M_{fv}$

The final modified Hiroyasu's soot formation equation is as follows, where **x** represents the multiplication factor of fuel vapour volume with respect to soot particle volume.

$$\frac{dM_p}{dt.M_p} = A_f \left(\frac{M_{fv}}{\rho_p}\right)(x) P^{0.5} e^{\frac{-E_{sf}}{RT}} \quad (7.16)$$

The NSC's oxidation equation was used as in the previous approach where it was normalised with the concentration of soot. A multiplication factor, y, was introduced in this equation

$$\frac{dM_{so}}{dt} = A_o \frac{MW_c}{\rho_s D} M_n \dot{R}_{NSCi} \qquad (7.17)$$

$$\frac{dM_{so}}{dt.M_n} = yA_o \frac{MW_c}{\rho_s D_i} \dot{R}_{NSCi} \qquad (7.18)$$

Then, the calculation of soot particle diameter was done as in the previous approach.

In this approach, fractional mass increment by growth is not tied with the net soot in the volume and the soot formation and oxidation rates are solely dependent on the conditions along the paths. However, multiplication factors of x and y need to be introduced order to get comparable soot formation and oxidation rates. In this exercise x was set to be 1.0×10^{2} and y, 1.0×10^{-2}. These multiplication factors were chosen based on trial and error approach in which many attempts were carried out to obtain profiles of soot formation and soot oxidation rates that closely resemble the overall soot formation rates in Kiva-3v simulation data.

The results from this approach are different from that of previous methods in a sense that none of the soot particles of interest disappear as they follow the paths. This is partly attributed to the independence of the equations on the soot concentration along the paths, and partly by the introduction of multiplication factor x and y.

7.5 Approach 4: Association with In-cylinder Conditions along the Path with the Use of NSC's Pyrographite Surface Mass Oxidation Rate, w

This approach is similar to Approach 3 in which cylinder conditions along the paths were used. One of the differences was that, the Hiroyasu's soot formation equation was used in its original form with the introduction of multiplication factor of 2×10^{-10} as shown below. The method of selection of the multiplication factor is the same as in the previous approach.

$$\frac{dM_{sfi}}{dt} = \left(2\times10^{-10}\right)A_f M_{fvi} P_i^{0.5} e^{\frac{-E_{sf}}{RT_i}} \qquad (7.19)$$

Another difference was, instead of using a derived NSC's soot oxidation equation for diesel engine, the original NSC equation for pyrographite surface mass oxidation equation was used. The equation which was shown in Chapter 2 previously is again shown below.

$$\dot{R}_{NSC} = \frac{k_A p}{1+k_z p} x + k_B p(1-x) \qquad (7.20)$$

The formulation gives a surface mass oxidation rate with the unit of $g/cm^2.s$. This equation was used to find the mass loss due to oxidation based on surface area available from a soot particle.

The advantage of this approach is the mass loss per particle can be calculated easily using the above equation and the conditions along the soot paths. Unlike approach 3, the only multiplication factor of 2×10^{-10} in the Hiroyasu's soot formation equation can easily be changed without the need to change any other factor. The factor can be implied to be the inverse value of soot particle number density ($particle/cm^3$) despite on the lower side. Heywood [123] reported that cylinder average particle number density in an IDI

diesel engine was between 1×10^{9}-3×10^{9} particle/cm^{3} while Tree and Foster [129] in their article mentioned that the value was 1×10^{12}-1×10^{14} particle/cm^{3} for a DI diesel engine.

All of these approaches are summarised in Table 7.1 in which some more remarks are detailed out to explain about the assumptions of each approach. These approaches are different in terms of their association with the species concentration along the paths. These approaches are attempted in different ways in order to lessen the numbers of variables the equations be influenced by. The first approach has direct association with the soot concentration along the path such that soot particle size profile duplicates the profile of the soot concentration. The second and third approaches have indirect link to the soot concentration as the formation and oxidation rates are normalised with it, thus variations in the soot concentration tend to have an influence on the particle size profiles. The fourth approach is not linked with the soot concentration in anyway as the others, but only with responsible species for soot formation and oxidation processes, and the local cylinder conditions along the paths. However, each approach requires the introduction of multiplication factors in each soot formation and oxidation rates to obtain a comparable soot size profile. These multiplication factors are kept constant for each path under investigation.

7.6 Results and Discussion of Various Approaches

The above approaches are implemented to predict soot particle size profile for several paths that are most likely to reach the cylinder wall layers. Three paths considered are the ones from the instant of 8° CA ATDC and two others from 14° and 24° CA ATDC. History of species concentration and local condition that are used in soot formation and oxidation calculations are extracted from each path and are shown in Figure 7.2 to Figure 7.6.

At the bottom of each figure, comparisons of soot particle size profiles along each path with different approaches are displayed. Looking at the diameter profiles as a whole, all the approaches show similar trends which show that soot particles that move

close to the cylinder wall layers reduce in size as they reach EVO. Soot particles from earlier crank angle (i.e. 8° CA ATDC) are observed to sharply increase in size to the maximum at around 18° CA ATDC and gradually decrease in size as it moves to around 60° CA ATDC, after which the size remains almost constant. These trends meet the initial expectation of the general soot size profile which follows soot concentration profile. Soot particles from later crank angles (i.e. 14° and 24° CA ATDC) are observed to immediately but gradually decrease in size right after the tracking. This happened as the soot particles from later crank angle do not experience much of surface growth process as soot formation process has slowed down at these instants. This result is in agreement with experimental results reported by Haynes and Wagner [53] that show soot concentration is at the maximum at 14° CA after start of injection, and with Dec [61] who, by laser-sheet imaging, showed that soot concentration starts to decrease after 21°CA after start of injection. This emphasises that the overall soot formation process starts to be dominated by soot oxidation process very early in the expansion stroke. There are significant differences in maximum predicted soot size with the different approaches with the fourth approach are observed to provide the high side of the size prediction in most cases.

The size changes in the second to the fourth approaches are heavily influenced by the multiplication factors introduced. Given that the right multiplication factors are employed, any of these approaches may be used to predict the size changes of soot particles along the paths.

7.7 Conclusions

Up to this point, all of the approaches were carried out taking into account only soot surface growth and soot surface oxidation processes without consideration to other important physical processes that contributes to size and shape changes, i.e., coagulation and agglomeration. The overall trend of soot particle size along paths can be observed to preserve the average in-cylinder soot concentration profile as shown in Figure 4.1(d) where the curve peaks at around 20°CA ATDC, after which it gradually decreases before

becoming almost constant after 60°CA ATDC. Along predicted paths, this trend is expected as oxidation process is observed to be dominating after that crank angle as the overall in-cylinder temperature decreases thus reduces the soot formation rates, and the soot particles are also observed to move away from the flame plume and enters the region where more oxygen and hydroxyl molecules are available for higher soot oxidation rates. Thus, it can be seen that the soot particle size along predicted paths decreases more sharply than average in-cylinder soot concentration profile as most of the soot particles tracked in this study are observed to be moving away from the flame plume.

If coagulation and agglomeration processes were to be considered in the model, the particle size would increase rapidly as the processes start to develop as illustrated in Figure 2.5. It is useful to note that to characterise the size of soot agglomerate, radius of gyration, which refers to the square of the distance from the centre of each primary particle to the geometric center of the agglomerate [10], is used. With these two processes, the soot particle size across a path is expected to be about 10 times bigger than the one predicted in this study as in-cylinder measurement with scanning mobility particle analyser (SMPS) by Pungs et al. [109] shows that soot particle sizes range from 30 to 110 nm, whereas in this study soot particle sizes are predicted to be mostly from 4 to 10 nm. However, as far as the trend of size change is concerned, the trend of increasing to a peak size and decreasing towards later crank angle is expected to be preserved. However, when coagulation and agglomeration are included, the slope of the size decrease after the peak would not be as sharp as has been seen in the present study, as when these processes are taken into account, the soot particle surface areas available for oxidation process are reduced as a result of these processes, thus the soot oxidation rates are expected to be reduced.

With further refinement and inclusion of coagulation and agglomeration factors these approaches can be used to predict soot particle size changes along the tracked paths. Nevertheless, with current settings, these approaches are able to show that the trends of soot particle size changes along the predicted paths. The soot particles that move close to the cylinder walls are most likely to reduce in size to about 20% of the size at the peak.

The second to the fourth approaches produce smooth soot particle size profiles. However, the second and the third approaches are still linked to the soot concentration thus might be vulnerable to its variations due to soot transport to/from neighbouring cells. The fourth approach however, has no dependency on soot concentration thus has one less variable of the sources of instability in the prediction. With further optimization of the multiplication factors, this approach would be a more robust approach to predict the soot particle size along any path.

CHAPTER 8

INFLUENCE OF PARAMETER CHANGES TO PARTICLE PATHS

8.1 Introduction

Soot formation and oxidation processes are affected by numerous parameters. From the review of soot processes by Tree and Svensson [51] and Heywood's engine fundamentals [123], it can be concluded that these parameters can be categorized into four groups, engine operating parameters, engine design parameters, fuel structures and fuel composition.

The following explanation can be found in Tree and Svensson article [51]. Due to their relevance to the work, the explanations are included here. Engine operating parameters are engine load and speed. Engine design parameters include combustion chamber shape and geometry, fuel injection related parameters such as injector type, size and number of injector holes, injection timing, multiple injections, air swirl, intake temperature and pressure, auxiliary air injection and water emulsified fuel. Different types of diesel fuels contain different fuel composition and have different fuel molecular structures. The amount of different elements in the fuel determines its composition and the location and type of bond making up the molecules in the fuel determines the fuel structure [51]. The important fuel components in soot processes are carbon, oxygen, hydrogen and sulfur. Higher carbon content would cause higher soot production, whereas higher oxygen content reduce the production of soot. Fuel that contains more ring or aromatic structure has higher sooting tendency, and fuel with more branched chain molecules soots more than the one with more straight chain molecules [51].

Changing the above parameters would affect the fuel air mixing, combustion and thus soot formation. The fundamental physical properties that are influenced by changing the above parameters are local in-cylinder temperature, pressure and stoichiometry which determine the overall soot formation and oxidation processes. Temperature is the most important factor in affecting the soot formation and oxidation process by increasing all the reaction rates in the process [51]. In-cylinder temperature increase would result in a decrease in exhaust gas particulate because at higher temperatures, even though the soot formation rate increases, soot oxidation rates of soot in the flame as well as in the post injection also increases and dominates the overall soot process [51]. Similarly, higher in-cylinder pressure reduces in-cylinder soot and exhaust particulates by increasing the amount of entrained air into the fuel jet and shortening jet penetration and liquid length that minimizes the problem of fuel impingement to wall and jet-jet interactions that were known to cause high soot emissions [51]. Fuel-air mixture stoichiometry affects the overall soot processes through the oxygen amount in the fuel or in the premixing of fuel and air, where in general, increased oxygen amount in the fuel would reduce soot formation, while increased in fuel-air mixture tends to increase soot formation due to increased reaction zone temperature on the fuel side [51].

Details partially presented above demonstrate the complexity of the influences of changing the parameters to the in-cylinder soot processes. There are also numerous parameters that influence the processes either individually or jointly. Thus, it is not possible to address the influence of each parameter in this thesis. Nevertheless, a few engine design parameters, namely air swirl and spray angle, are selected for parametric studies. These parameters are selected not so much for their influences on the amount of soot generated per se, but more for their significant influence on soot transfer to the cylinder wall layers which is more specific to the objective of this thesis.

8.2 Swirl

Swirl is one of the in-cylinder fluid motions that influence the rates of air-fuel mixing, fuel evaporation and combustion. It is generated by constructing the intake

system to give a tangential component to the intake flow as it enters the cylinder through shaping and contouring the intake manifold, valve ports and piston face [14], and through masking off or shrouding part of the peripheral inlet valve open area [123]. As swirl increases, it shortens the overall duration of combustion process and influences the fuel-air equivalence ratio as fuel-air mixing rate changes hence affects emissions level [123]. It shown that as swirl increases, fuel consumption, particulate and CO emissions decrease; and NO_x emission increases [123]. Bonatesta et al. [100] however, through their computational study, found out that at different loads and engine speeds, over-swirling increases soot production in the cylinder. Other studies [130, 131] have also shown that increasing swirl reduces soot emissions up to certain extent beyond which the soot emissions start to increase.

Swirl ratio (SR) is defined as the angular velocity of a solid-body rotating flow ω_s, which has equal angular momentum to the actual flow, divided by the crankshaft angular rotational speed

$$SR = \frac{\omega_s}{2\pi N} \qquad (8.1)$$

In this thesis, a range of initial swirl ratios of 1.3 to 2.4 with an increment of 0.3 were used in the simulations to study their influences on in-cylinder soot particle paths. For each initial swirl ratios, a different Kiva-3v simulation was carried out. Each initial swirl ratio was set in the input file (itape5).

8.2.1 Effects of Changing Swirls on Soot Paths

Figure 8.1 shows the predicted path of the points starting in Zone 1, 2 and 3 at CA 8° ATDC for various swirl ratios. It can be observed that changing the swirl ratio in these three zones has insignificant impact on the final destination of the soot particles. In all cases, soot particles end up very close to the cylinder wall layers. Significant impact of swirl ratio in these zones is on the axial distribution of the soot particles where it can

be observed that as swirl ratio is increased, soot particles tend to move closer to the cylinder roof. This shows that the higher swirl ratio, the stronger is its influence in holding back the downward motion of the fluid induced by the piston movement. With higher swirl ratios, soot particles tend to move faster than the ones with lower swirl ratios. An important observation is that most of the particles that move very close to the liner move up towards the top of the cylinder initially, some particles stay close to the top of the cylinder and the rest move downwards as the stroke progresses.

Figure 8.2 shows the paths of the points starting in Zone 4, 5 and 6. The sensitivity to the swirl ratio on the predicted path is clearly evident in these cases. Soot particle paths with lower swirl ratio, namely 1.3, 1.6 and 1.9, are inclined to move closer to the cylinder wall layers. On the other hand, higher swirl ratios of 2.1 and 2.4 are more likely to send the soot particle to the cylinder central region. It can also be concluded that the soot particles initiating in the bowl region are most affected by the different swirl ratios. It is clear that the particles formed in the bowl region initially move upwards because of the upward facing vortices in the bowl.

At the starting instants of CA 18° ATDC, influence of swirl ratio to the soot particle paths is not significant. Except for the particles starting in Zone 4, the soot particle paths do not change the radial distance with the swirl ratios. In general, similar axial trend of soot paths of CA 8° ATDC is observed here, where the higher the swirl ratios, the closer the paths are to the cylinder roof. In Zone 4, where tumble and reverse squish motions are high, soot particles with lower swirl ratios of 1.3-1.9 have higher tendency to move closer to the liner. These trends are shown in Figure 8.3.

The influence of swirl ratios to the soot particle paths tracked at CA 35° ATDC is not significant to the problem of soot in oil as all soot particle paths are not leading towards the cylinder wall layers as shown by the paths with only 1.9 swirl ratio. The paths are shown in Figure 8.4.

From the point by point comparison it can be concluded that depending on when and where the soot particles are formed during the stroke, the swirl ratio has different effects on the path of the particles. At different locations and instants the particles get close to the liner at different swirl ratios.

8.3 Spray Angle

Spray angle is an important parameter in a sense that its variations can change the fuel jet impingement point, thus changing the distribution of fuel, hence soot, and influence the gases motions in the cylinder. Its variations can also influences the mixing rate of fuel and air in the cylinder. In a computational study by Abraham and Khan [132], it is shown that as the angle of the fuel jet centre line with the cylinder axis decreases, the mixing rate decreases and vice versa. It was also found that there was an optimum spray angle that maximises mixing under the conditions studied.

In the present study, spray angle is varied to investigate its influence on soot processes as a whole, and to study the possibility of soot transfer to the liner. Two different spray angles with the spray axis of 69° and 79° measured from the cylinder axis are used in the simulations. The soot particle paths obtained from the post processing of simulation data are compared with the ones with the baseline case of 74° spray angle. Soot particle paths from two regions of interest, below and above the spray axis, are calculated.

8.3.1 Effects of Changing Spray Angles on Soot Paths

Figure 8.5 and 8.6 show soot particle paths from above and below the spray axis with the setting of spray angle at 69°. Soot particles from different instants and angular locations are tracked to study the effect of starting instants and positions to the soot paths, as previously done in Chapter 6. From these figures, it can be observed that lowering the spray angle from 74° to 69° reduces the likelihood of soot particles from above and below the spray regions to be transferred close to the liner. This fact can be seen across

all starting points and instants, with only a few paths show some likelihood to hit the cylinder wall.

Lowering spray angle would reduce the turbulence level in the bowl area, thus reduces the mixing rate as pointed above. While it seems that lowering the spray angle might reduce soot particle numbers that come close to the cylinder wall layers, the overall effect of it in reducing the mixing rate might increase the soot formation rate thus end up with more soot at the liner.

Figure 8.7 and 8.8 shows the same paths from the same locations with the setting of spray angle at 79°. Soot particles from above the spray (Figure 8.7) are observed to behave in a similar fashion as the soot particles with spray angle 74°. Most of the soot particles travel into the middle of squish region and some are observed to travel close to the liner sporadically. Soot particle paths tracked from below the spray, shown in Figure 8.8 demonstrate that increasing the spray angle from 74° to 79° increases the possibility of soot particles from inside the bowl to travel very close to the boundary layer of the cylinder wall. Starting locations and instants almost do not matter with this spray angle. This is very interesting observation when the normal expectation of increasing the spray angle would be that the soot particles from above the spray are more prone to be transferred to the cylinder wall layers, yet the reverse happens.

It can also be concluded that increasing the spray angle from 74° to 79° increases the turbulence level with stronger vortices inside the bowl region thus produces higher forces to carry more soot particles very close to the boundary layer of the cylinder. The results also give the impression that 74° spray angle is the optimum angle to provide good mixing rate but lower likelihood of oil contamination by soot particles.

8.4 Conclusions

Swirl ratios are found to be less significant in influencing the already high tendency of soot in the early injection duration to travel close the cylinder wall layers.

Neither lowering nor increasing swirl ratios does reduce the likelihood of soot from early instants to reach the cylinder wall layers. However, depending on location and time, lower swirl ratios are more likely to cause soot to be transferred close to the liner. This finding demonstrates that lower angular momentum provided by lower swirl is overcome by the radial momentum produced by the high velocity fuel jet to carry soot particles closer to the liner.

Spray angles have significant influence on the likelihood of soot particle transfer to the cylinder wall layers. Reducing the spray angle decreases its likelihood, but causes mixing rate to be lower. Increasing the spray angle increases the likelihood of soot particles from inside the bowl to be transferred to the cylinder wall layers without affecting much on soot particles above the spray. However, further increase in spray angle may significantly increase soot particle transfer at the liner, as the fuel spray may pass the bowl rim and impinge directly on the cylinder wall which is not beneficial for good combustion.

CHAPTER 9

DISCUSSION AND CONCLUSIONS

9.1 Introduction

The work reported in this thesis is concerned with computational studies of in-cylinder soot, its distribution, temporal and spatial changes in this and the evolution of particle size during the expansion stroke. The main aim is to investigate the possible sources of soot particles at the cylinder wall layers and to gain further insight of the overall in-cylinder soot behaviour. CFD simulation programme, Kiva-3v Release II, EnSight post-processing software and various Matlab routines have been used in the investigation.

Throughout the investigation, new computational codes and routines that can be employed to make predictions of soot particle trajectories and soot particle size change of on a specific path have been developed. The predictions of soot trajectories and size changes along the trajectories would be helpful to engine designers to improve their understanding of soot particle behaviour within an engine. This investigation would also serve as a new juncture for a new branch of research in the field of soot formation within internal combustion engines.

This chapter is divided into three sections beginning with discussion section that reviews the techniques and methods employed in this work. Where appropriate, the aims and the results of the investigation and their implications on the subject are reiterated and discussed. Limitations and weaknesses of the current investigation are also addressed and further improvements to overcome them are covered in further work section. The main conclusions drawn from the work are stated at the end of the chapter.

9.2 Discussion

Kiva-3v CFD code with two-step soot model has been employed to furnish the investigation with simulated in-cylinder combustion and pollutants data which is post-processed to accomplish the objectives of the thesis. While different soot models employed by others are capable to predict in-cylinder soot particle size distribution, the tracking of a particle or a parcel of soot in an engine cylinder during the running of the simulation has not been carried out, thus the sources of soot particles at the wall layers have not been investigated by others. Post-processing of the simulated data is seen as one of the practical methods to investigate the sources of soot at wall layers.

The approach of post-processing of CFD simulation data can be time and cost-saving in the investigation for an optimised engine design but assumptions have to be made and justified when accurate sub-models and detailed chemical and physical processes are not included. As with any code, sub-models used within Kiva have weaknesses and limitations as discussed in Section 3.3, but these were considered to sufficiently minor to use the sub-models without amendment in this study. More challenging problems were faced in the way the setup of the computational combustion chamber model. Despite the fact that using one seventh sector of the cylinder volume can save computational resources and can reach grid independence of, for example, in-cylinder pressure with higher mesh resolution, it was found out that this setup caused discontinuities in the soot paths as well as in the history of species concentrations and conditions along the paths when the sector was replicated seven times to make up a whole cylinder volume.

Another factor found to cause irregularities in the soot particle paths was the way the velocity at each point was estimated. Nearest-node method was used in the beginning, believing that the cell vertices were sufficiently close together thus velocities at those vertices were not significantly different. Apparently, this was not the case, as the in-cylinder motions were random due to complex combination of fluid motions caused by turbulence, swirl, tumble and squish motions. A space function to interpolate and

estimate the velocity was recognised to alleviate this problem, and a simple trilinear interpolation technique was used in this study.

Computational studies always have concerns about mesh and time step independence and the accuracy of numerical method used. To a certain extent, all of these issues are addressed in Chapter 5. Flow fields inside the cylinder were observed to be in turbulent state, highly dynamics and in steep velocity gradient between different fluid phases (i.e. fuel jet and surrounding gas) with the directions highly spread out. The regions inside the cylinder with these flow fields could be identified as the region inside the bowl, the central axis of the fuel jet, the boundary between high-velocity fuel jet and the surrounding gas and the region near the bowl rim. These are the areas that need careful investigation of the soot particle paths. Sensitivity study of paths to small difference in starting locations in these regions has been carried out. Efforts have been made to use the smallest time step and the highest mesh resolution when dealing with these regions. In the present study, the mesh density is basically fixed and it does not accommodate the needs of different mesh density at different regions in time. Other meshing method such as zonal meshing or adaptive meshing is envisaged to be able to solve some of the accuracy problem in soot particle path prediction.

The accuracy of the path prediction can also be increased by a small fraction by using higher order numerical methods and to a large extent with smaller time steps nearing the time step used in Kiva calculations. Both entail high computational resources. To continue improving the accuracy of the path analysis through post-processing analysis and saving computational runtime, automated data recording at the desired time steps coupled with higher computer specifications would be deemed to be one of the solutions. The application of cluster and grid computing may also be useful in this situation. A long term solution can be the inclusion of the tracking procedures inside Kiva code so that the time step used in the tracking is equivalent to the time step used in Kiva calculations, thus avoiding errors due to larger time step in post-processing tracking technique.

Recognising the CFD sub-models and computational setting limitations, the findings from this study are the first steps towards understanding the movement of in-cylinder soot particles and the possible sources of soot at the cylinder wall layers. With this tracking technique, it is possible to pinpoint the regions and instants from which the sources of soot particles at the wall layers are. Soot particles from the periphery of the fuel jet especially the ones inside the bowl during early injection period are found to be the most likely sources of the soot at the cylinder walls as they are predicted to be transported close to the cylinder wall from those locations and instants. Soot from later crank angles are also susceptible to forces carrying it to the wall layers, as the piston top moves down while turbulence and reverse squish motions are still present in the bowl. These findings are difficult to obtain through experiments and not easy to be traced internally during a CFD simulation. For a bowl-in-piston cylinder configuration, these findings can be asserted as a general description of in-cylinder soot particles, as when looking at overall view of the predicted path results, this fact does not depend so much on the mesh configurations or time steps used in the study. Different mesh configurations and different time steps do not demonstrate much difference in the positions of the soot particles relative to the cylinder walls but only demonstrates the differences in the exact coordinates of the final positions of the soot particles.

Load, speed, fuel injection parameters, air swirl and piston top design influence the performance, efficiency and emissions of a compression ignition engine [123]. In this study, load and speed is fixed and a fuel injection parameter, that is, fuel spray angle, and air swirl ratio are the parameters investigated for their influence on the in-cylinder soot movement.

The effect of high velocity of fuel jet injection on the surrounding gas during fuel injection period is one of the main driving forces to transport the soot particles to the nearest region to the cylinder wall layers. The soot particles that are involved are the ones that are formed within diffusion combustion at the fuel jet periphery and these soot particles are able to get away from the flame and travel to towards the cylinder wall layers following the in-cylinder gas flow as they are mainly affected by the high shear region around the fuel jet. Soot particles from the centre of the fuel jet which formed

from premixed combustion tend to impinge and most probably be deposited on the bowl walls, or/and dwell inside the bowl region until EVO.

The shape of the bowl on the piston top is also observed to play important role in directing the soot particles to get affected in the tumble motions in the middle of bowl and then pushed away more strongly into the squish region by the reverse squish motion. Different bowl shape will create different kind of motions thus affect the movement of soot particles in the cylinder. However, the effect of different bowl shapes to soot particle paths are not investigated here.

Swirls are found to affect the amount of in-cylinder soot both in soot formation and soot oxidation processes. Some intermediate level of swirl, which depends on engine operating condition has been found to produce lower engine-out soot [10, 100]. In terms of preventing soot particles from moving close to the cylinder walls, higher swirl is more desirable as the tangential force provided by the swirl prevents the soot particles from being convected to the region near the cylinder walls. This is a conflict of interest. As engine-out soot can be reduced with intermediate level of swirl, it may cause more soot at the cylinder wall layers thus more oil contamination by soot. Therefore, it is important that in the pursuit of low particulate emissions, the soot-in-oil problem is not to be neglected. Of course swirl is not the only method to reduce soot, both engine-out and in oil, other methods such as spray angle, spray cone angle and injection timing should be optimised to obtain benefits in both areas. Swirl ratio and injection timing were predicted to have the strongest influence on the transport of soot in and around the combustion chamber when compare to EGR, rail pressure and boost pressure in one of the studies of in-cylinder soot distribution. EGR, rail pressure and boost pressure only affect the bulk soot content and have a much weaker influence on in-cylinder soot distribution [30].

Spray angle plays an important part on the possibility of soot to be transported near the cylinder wall. It was expected that a more horizontally positioned fuel spray would risk direct impingement of soot particles that are formed above the spray onto the cylinder wall. However, the results from additional study shows that at higher spray angle, soot particles from below the spray have more likelihood to be transferred to the

cylinder wall. Soot particles are carried into squish region by the effect of fuel injection on the bowl surface that creates higher vortex or tumble motion, and then strengthened by the reversed squish motion as the piston travels downwards. The spray that is positioned more vertically is observed to cause less soot particles from inside the bowl to be transported to the squish region. It is to be noted, that the two spray angles used in this parametric study are only 5° different in both directions from the base line spray angle which is 74° from the horizontal line as shown in Figure 6.1.

The injector used in this study has seven holes. Increasing the number of holes with hole diameter and pump capacity left unchanged will reduce injection pressure and duration, and consequently will decrease velocity of nozzle exit and penetration length [133]. As the velocity of fuel jet is decreased, soot transport to the near cylinder wall region can be implied to be reduced. Conversely, decreasing the hole numbers with unchanged hole diameter and pump capacity would induce more soot particles reaching near the cylinder wall as higher fuel jet velocity may create stronger vortex in the bowl that pushes the soot farther into the squish region. However, if injection pressure and duration are to be maintained, hole diameter needs to be reduced. By doing so, fuel-air mixing rate would be increased as atomisation is increased with smaller hole diameter. The overall effect would be less amount of soot generated in the cylinder thus lesser amount of soot particles would likely to be transferred to the cylinder wall.

From this study it was found soot particles from early injection period are more likely to move near the cylinder wall. Spray angle, swirl, injection velocity and bowl design have been observed to play active roles in directing the movement of gas motion, hence soot particles in the cylinder. Lower spray angle and high swirl should be used to prevent soot from reaching the cylinder wall but not at the expense of soot at the exhaust. Thus, spray angle and swirl should be optimised to not only reduce soot particle propensity to move to the cylinder but also reduce wall soot at the exhaust. By lowering the injection pressure, hence injection velocity, less soot moving towards the cylinder wall can be expected, but it causes poor air-fuel mixing hence more soot formation during the injection which probably results in more soot available to be transported towards the cylinder wall. Controlling soot formation process during injection period is also a key to

reduce soot at the cylinder wall. This can be achieved, for example, with the introduction of oxygenated diesel [134] fuel during early injection thus less soot is generated, thus less probability of soot to be transferred to the cylinder wall. Additional air injection during fuel injection to prevent soot from moving towards the cylinder wall, and also to promote turbulence thus promotes air-fuel mixing leading to less soot formation, and soot-air mixing leading to more soot oxidation [10] could also be carried out to reduce soot transfer at the cylinder wall. Split injections with properly optimised cessation length to provide sufficient time to provide leaner and sufficiently high-temperature environment for the next injection [10] is also another strategy that would reduce the overall soot formation and consequently the amount soot transfer to the cylinder wall. All of these injection parameters have complex interactions and without further investigations, a clear-cut strategy to reduce soot at the cylinder wall could not be stated. Another direct measure to prevent soot particles from reaching the cylinder wall is through the introduction of cylinder wall coated with thermal barrier ceramics [135]. Increasing the topland height [97] can also help in preventing soot particles that already transferred to the wall from being scraped into the oil system by the piston rings.

Several other Matlab routines have also been written to provide the means to predict the soot particle size changes along the tracked paths but with limited success. Difficulties arose in obtaining the right multiplication factors that work in each and every case. One approach was found to be more robust than the others to be improved further as a predictive tool for soot particle size changes along the tracked paths. Soot particle size prediction along the paths is important as the prediction can be utilised to model soot transfer mechanism from the main flow to the cylinder wall through the thermal boundary layer. Thus the inclusion of the effects of coagulation and agglomeration processes to the soot particle along a path is crucially required for further investigation. As of now, the predicted soot path and the trends of soot size along the path can be used to understand the possible movement and soot size profile with only surface growth process.

The whole approach is not only useful in the current setting of the engine, but can also be employed to study particle tracking in any other engine configurations and engine with different fuels. This approach can also be applied in any fluid/particle tracking in

other fields as mentioned briefly in Chapter 2. As this approach is developed in-house, further development and investigation will always be possible. Comparison studies can also be carried out when new subroutines are developed.

9.3 Further Works

The work in the present study answers some important questions about in-cylinder soot particle movements, especially the ones that relate to soot in oil problem. Nevertheless, more works are necessary to fully understand soot particle behaviours in an engine cylinder. The possibilities are inexhaustive, but among other works that can be pursued to complement this work in the near future shall be discussed below.

The present work is limited to the tracking of soot particles from its formation instant until exhaust valve opening (EVO). The possibilities of soot transfer to the liner were discussed only based on this duration. Possibility of soot transfer to the liner could also be contributed to the soot particles that move during the exhaust stroke. Thus, soot particle tracking can be extended to include soot paths during the exhaust stroke. To be able to do this, a new cylinder volume and valve computational setup needs to be carried out as current model only simulate the combustion in a closed part of the cycle.

To address the issue of mesh dependence, sensitivity of soot particle paths to mesh configuration should be carried out with either adopting adaptive meshing method or creating denser meshing at the high turbulence region, such as in the piston bowl. Parallel investigation of modified spray sub-models could also be carried out to further study the spray dynamics. Considering that many references have been found in other fields which reported particle tracking as a sub-model in the main CFD code, a logical step forward would be to include soot particle tracking technique into the main Kiva-3v code.

This particle tracking technique can also be extended to include other forces such gravitational, buoyancy, surface and drag forces to be compared with massless tracking

technique. Thermophoresis and other transfer mechanisms can also be included to study the soot transfer to the liner through the boundary layer.

The model of soot evolution can be further fine-tuned to predict the changes in soot particle sizes along the tracked paths. Other physical processes of soot particle coagulation and agglomeration will impose further difficulties in predicting in-cylinder soot particle sizes, yet preliminary studies with simple methods could prove to be useful in solving the soot in oil issue.

Investigation on the size of soot particles on the cylinder wall should also be carried out by taking soot particle samples at the cylinder wall. This experimental data can be used for the validation of the soot growth model.

9.4 Conclusions

The investigations reported in this thesis have been carried out for a range of conditions representative of high-load, high engine speed operation, that is at the engine speed of 2500 rpm and load of 1200 kPa brake mean effective pressure. With respect to the soot particles approaching the cylinder walls and posing a source of soot transferred to oil, the following conclusions are drawn:

Soot particles that are formed early in the fuel injection period and are located just below the fuel spray in the small region in the middle of the bowl are most likely to be the sources of soot particles at the cylinder wall layers. Soot particles that are already at the bowl rim during early injection duration and later in the expansion stroke are also likely to be transferred close to the wall layers.

Soot particles that are formed immediately after injection but are located farther from fuel jet axis, namely in-between fuel jets, are also likely to be transported close to the cylinder wall layers. This is thought to be the later effects of high velocity fuel jet, swirl and jet-to-jet interactions. Soot particles from other regions have lesser likelihood to be transferred to the wall layers as they only transported into the middle of the squish

region during the expansion stroke. Illustrations of the likelihood of soot particle transfers to the cylinder wall layer during fuel injection period are shown in Figure 9.1 to summarise the findings.

In addition, these soot particles are mostly from relatively low soot concentration region as the soot particles from the most concentrated regions at various crank angle instants were shown to have the least likelihood to be transported close cylinder wall layers, and all of them stay inside the piston bowl.

The movements of these soot particles close to the liner in the squish region are caused by high reverse squish and tumble motions when piston moves down during early part of the expansion stroke. These motions are intensified by the high velocity fuel jets that impinge on the bowl walls and split into two forceful motions along the bowl walls and the bowl rims. The intensity of these motions gradually diminishes as piston moves down, and soot particles that are formed later, especially after fuel injection duration, are found to have less likelihood to be transferred close to the liner.

Soot concentration gradient is very steep in the cylinder thus a small difference in soot particle paths translates to substantial difference in soot concentration along the paths. This fact shows that the evolution of soot diameter along similar paths could be difference. Consequently, meticulous particle tracking at various locations of interest should be done to gather more information on the possible soot particle size distribution at EVO.

Sensitivity studies of soot particle paths to swirl show that engine operating with low swirl ratios are more vulnerable to soot in oil problem. Low swirls are seen to be relatively weak in opposing the fluid motions caused by high velocity fuel jet, reverse squish and tumble motion during the early expansion stroke.

Decreasing the spray angle from 74° to 69° lessens the possibilities of soot particles from being transported close the cylinder wall layers. Increasing the spray angle

from 74° to 79° increases the possibilities of soot from the bowl region to be transported close to the cylinder wall layers.

REFERENCES

1. Lammel, G., Novakov, T., Water nucleation properties of carbon black and diesel soot particles. Atmospheric Environment, 1995. **29**(7): p. 813-823.

2. Weingartner, E., Burtscher, H., Baltenspergertx, U., Hygroscopic properties of carbon and diesel soot particles. Atmospheric Environment, 1997. **31**(15): p. 2311-2327.

3. Kirchstetter, T.W., Aguiar, J., Tonse, S., Failey, D., Novakov, T., Black carbon concentrations and diesel vehicle emission factors derived from coefficient of haze measurements in California: 1967-2003. Atmospheric Environment, 2008. **42**: p. 480-491.

4. Bernstein, J.A., Health effects of air pollutions. J Allergy Clin Immunol, 2004. **114**(5): p. 1116-1123.

5. de Kock, T.M.C.M., Driece, H.A.L., Hogervost, J.G.F., Briede, J.J., Toxicological assessment of ambient and traffic-related particulate matter: A review of recent studies. Mutation Research, 2006. **613**: p. 103-122.

6. Maynard R.L., Howard, C.V. , ed. Particulate Matter: Properties and Effects Upon Health 1999, BIOS Scientific Publishers Limited: Oxford.

7. Kittelson, D.B., Engines and Nanoparticles: A Review. Journal of Aerosol Science, 1997. **29**(5/6): p. 575-588.

8. Suhre, B.R. and Foster, D.E., In-cylinder soot deposition rates due to thermophoresis in a direct injection diesel engine. SAE Papers, 1992(921629).

9. Kittelson, D.B. and Ambs, J.L., Particulate emissions from diesel engines: influence of in-cylinder surface. SAE Papers, 1990(900645).

10. Eastwood, P., Particulate Emissions from Vehicles. Wiley-PEPublishing Series. 2008, Chichester: John Wiley and Sons. 512.

11. Bilger, R.W., Future progress in turbulent combustion research. Prog. Energy Combust. Sci., 2000. **26**: p. 367-380.

12. Ramadhas, A.S., Muraleedharan, C., Jayaraj, S., Performance and emission evaluation of a diesel engine fueled with methyl esters of rubber seed oil. Renewable Energy, 2005. **30**: p. 1789-1800.

13. Report of the World Commission on Environment and Development: Our Common Future 1987, World Commision on Environment and Development, United Nations (UN).

14. Pulkrabek, W.W., Engineering Fundamentals of the Internal Combustion Engine. 2 ed. 2004, Upper Saddle River: Pearson Prentice Hall. 478.

15. Amsden, A.A. and Amsden, D.C., The Kiva Story: A Paradigm of Technology Transfer. IEEE Transactions of Professional Communication, 1993. **36**(4): p. 190-195.

16. Turns, S.R., An Introduction to Combustion: Concepts and Applications. 2nd ed. 2000, Singapore: McGraw-Hill. p. 550.

17. Smolinska, J., European Union Economic Report - February 2008. 2008, European Automobile Manufacturers' Association (ACEA): Brussels. p. 186.

18. Walker, A.P., Controlling particulate emissions from diesel vehicles. Topics in Catalysis, 2004. **28**(1-4): p. 165-170.

19. Emission Standards: European Union - Car and Light Trucks. 2007 [cited 2009 16 June]; Available from: http://www.dieselnet.com/standards/eu/ld.php.

20. Mathis, U., Mohr, M., Kaegi, R., Influence of diesel engine combustion parameters on primary soot particle diameter. Environment Science Technology, 2005. **39**: p. 1887-1892.

21. Kolodziej, C., Wirojsakunchai, E., Foster, D.E., Schmidt, N., Kamimoto, T., Kawai, T., Akard, M., Yoshimura, T., Comprehensive characterization of particulate emissions from advanced diesel combustion. SAE Papers, 2007(JSAE 20077142, SAE 2007-01-1945).

22. Furuhata, T., Arai, M., Yaga, M., Lee, J.H., Chun, K.M., Effect of fuel properties on diesel PM components. SAE Papers, 2007(JSAE 20077189, SAE 2007-01-1941).

23. Lapuerta, M., Martos, F.J., Herreros, J.M., Effect of engine operating conditions on the primary particles composing diesel soot agglomerates. Aerosol Science, 2007. **38**: p. 455-466.

24. Kock, B.F., Tribalet, B., Schulz, C., Roth, P., Two-color time-resolved LII applied to soot particle sizing in the cylinder of a Diesel engine. Combustion and Flame, 2006. **147**: p. 79-92.

25. Tree. D.R. and Dec, J.E., Extinction Measurements of In-Cylinder Soot Deposition in a Heavy-Duty DI Diesel Engine. SAE Papers, 2001(2001-01-1296).

26. Bougie, B., Ganippa, L.C., van Vliet, A.P., Meerts, W.L., Dam, N.J., ter Muelen, J.J. , Soot particulate size characterization in a heavy-duty diesel engine for different engine loads by laser-induced incandescence. Proceeding of Combustion Institute, 2007. **31**: p. 685-691.

27. Ng, H.K. and Shayler, P.J. CFD Investigation of the Effects of Split Main Fuel Injection Parameters on Combustion and Emissions in a Light-Duty Diesel Engine. in Regional Conference in Vehicle Engineering and Technology (RIVET). 2005. UTM, Malaysia.

28. Kong, S.C., Patel, A., Yin, Q., Klingbeil, A. and Reitz, R.D, Numerical Modeling of Diesel Engine Combustion and Emissions Under HCCI-Like Conditions With High EGR Levels. SAE Papers, 2003(2003-01-1087).

29. Richards, K.J., Subramaniam, M.N. and Reitz, R.D. , Modeling the Effects of EGR and Injection Pressure on Emissions in a High-Speed Direct-Injection Diesel Engine. SAE Papers, 2001(2001-01-1004).

30. Ng, H.K., Shayler, P.J. and Willcock, M. Investigations of Pollutant Formation and Emissions from HPCR Diesel Engines. in Proceeding of Fisita World Automotive Congress. 2006. Yokohama, Japan.

31. Sung, N., Lee, S., Kim, H. and Kim, B., A Numerical Study on Soot Formation and Oxidation for a direct injection diesel engine. Proc. Instn Mech Engrs: Part D: Journal of Automobile Engineering, 2003. **217**: p. 403-413.

32. Fusco, A., Knox-Kelecy, A. and Foster, D.E. . Application of a Phenomenological Soot Model for Diesel Engine Combustion. in The Third International Symposium on Diagnostics and Modeling of Combustion in ICE. 1994. Yokohama, Japan.

33. Kazakov, A. and Foster, D.E. , Modeling of Soot Formation During DI Diesel Combustion Using a Multi-Step Phenomenological Model. SAE Papers, 1998(982463).

34. Tao, F., Golovitchev, V.I. and Chomiak, J. . Application of Complex Chemistry to Investigate the Combustion Zone Structure of DI Diesel Sprays under Engine-Like Condition. in The Fifth International Symposium on Diagnostics and Modeling of Combustion in Internal Combustion Engines. 2001. Nagoya.

35. Lee, S., Shin, D., Lee, J. and Sung, N. , Soot Emission from a Direct Injection Diesel Engine. SAE Papers, 2004(2004-01-0927).

36. Ng, H.K., The simulation of combustion in diesel engines using Kiva-3v on a PC Platform, in School of Mechanical, Materials and Manufacturing Engineering. 2003, The University of Nottingham: Nottingham.

37. Hiroyasu, H. and Nishida, K., Simplified Three-dimensional Modeling of Mixture Formation and Combustion in a D.I. Diesel Engine. SAE Papers, 1989(890269).

38. Nagle, J., and Strickland-Constable, R.F. Oxidation of Carbon Between 1000-2000 ℃. in Proc of the Fifth Conf. On Carbon. 1962. Pennsylvalnia State University, University Park, Pennsylvania: Pergamon Press.

39. Neoh, K.G., Howard, J.B., and Sarofim, A.F. , Effect of Oxidation on the Physical Structure of Soot. Proc. Combust. Inst., 1974. **20**: p. 951-957.

40. Position Paper on Air Quality: nitrogen dioxides. Working Group on Nitrogen Dioxide 1997 [cited 2006 11 July]; Available from: URL:http://ec.europa.eu/environment/air/ambient.htm.

41. Ambient Air Pollution by Particulate Matters Position Paper. Working Group on Particles 1997 [cited 2006 11 July]; Available from: URL:http://ec.europa.eu/environment/air/ambient.htm.

42. SO2 Position Paper. Working Group on SO2 1997 [cited 2006 11 July]; Available from: URL:http://ec.europa.eu/environment/air/ambient.htm.

43. Mobile Source Emissions - Past, Present, and Future. 2006 [cited 2006 11 July]; Available from: URL: http://www.epa.gov/oms/invntory/overview/pollutants/index.htm.

44. Blakeman, P.G., Chiffey, A.F., Phillips, P.R., Twigg, M.V. and Walker, A.P. , Developments In Diesel Emission Aftertreatment Technology. SAE Papers, 2003(2003-01-3753).

45. Hsu, B.D., Practical Diesel-Engine Combustion Analysis. 2002, Warrendale: Society of Automotive Engineers.

46. Shayler, P.J., Brooks, T.D., Pugh, G.J. and Gambril, R. , The Influence of Pilot and Split-Main Injection Parameters on Diesel Emissions and Fuel Consumption. SAE Papers, 2005(2005-01-0375).

47. Kawatani, T., Mori, K., Fukano, I., Sugawara, K. and Kayama, T., Technology for Meeting the 1994 USA Exhaust Emission Regulations on Heavy-Duty Diesel Engine. SAE Papers, 1993(932654).

48. Kitamura, T., Ito, T. and Fujimoto, H., Mechanism of smokeless diesel combustion with oxygenated fuels based on the dependence of the equivalence ratio and temperature on soot particle formation. Int J Engine Research, 2002. **3**(4): p. 223-248.

49. Johnson, J.H., Bagley, S.T., Gratz, L.D. and Leddy, D.G., A Review of Diesel Particulate Control Technology and Emissions Effects – 1992 Horning Memorial Award Lecture. SAE Papers, 1994(940233).

50. Lowenthal, D.H., Zielinska, B., Chow, J.C., Watson, J.G., Gautam, M. Ferguson, D.H., Neuroth G.R. and Stevens, K.D., Characterization of Heavy-Duty Diesel Vehicle Emissions. Atmospheric Environment, 1994. **28**(4): p. 731-743.

51. Tree, D.R. and Svensson, K.I., Soot processes in compression ignition engines. Progress in Energy and Combustion Science, 2007. **33**: p. 272-309.

52. Crua, C., Kennaird, D.A. and Heikal, M.R., Laser-induced incandescence study of diesel soot formation in a rapid compression machine at elevated pressures. Combustion and Flame, 2003. **135**: p. 475-488.

53. Haynes, B.S. and Wagner, H. Gg. , Soot Formation. Prog. Energy Combust. Sci., 1981. **7**(4): p. 229-273.

54. Richter, H. and J.B. Howard, Formation of polycyclic aromatic hydrocarbons and their growth to soot--a review of chemical reaction pathways. Progress in Energy and Combustion Science, 2000. **26**(4-6): p. 565-608.

55. Dederichs, A.S., Flamelet Modelling of Soot Formation in Diffusion Flames, in Department of Fire Safety Engineering. 2004, Lund Institute of Technology: Lund. p. 147.

56. Amann, C.A. and Siegla, D.C., Diesel Particulates - What They Are and Why. Aerosol Science and Technology, 1982. **1**: p. 73-101.

57. Graham, S.C., Homer, J.B. and Rosenfeld, J.L.J., The formation and coagulation of soot aerosols generated by the pyrolysis of aromatic hydrocarbons. Proceeding of Royal Society of London, 1975. **A344**: p. 259-285.

58. Kennedy, I.M., Models of Soot Formation and Oxidation. Prog. Energy Combust. Sci., 1997. **23**(2): p. 95-132.

59. Kraft, M., Modelling of particulate processes. KONA, 2005(23): p. 18-35.

60. Greeves, G. and Meehan, J.O. Measurements of Instantaneous Soot Concentration in a Diesel Combustion Chamber. in Combustion in Engines. 1975. Cranfield: Institution of Mechanical Engineers.

61. Dec, J.E., A Conceptual Model of DI Diesel Combustion Based on Laser-Sheet Imaging. SAE Papers, 1997(970873).

62. Kim, H. and Sung, N., Combustion and Emission Modeling for a Direct Injection Diesel Engine. SAE Papers, 2004(2004-01-0104).

63. Kim, H. and Reitz, R.D., Modeling combustion and emissions of HSDI diesel engines using injectors with different included spray angles. SAE Papers, 2006(2006-01-1150).

64. Wang, R.C., Fang, T. and Lee, C.F., Comparisons of computed and measured results for a HSDI diesel engine operating under HCCI mode. SAE Papers, 2006(2006-01-1519).

65. Belardini, P., Bertoli, C., Ciaojolo, A., D'Anna, A. and Del Giacomo, N., Three dimensional calculations of DI diesel engine combustion and comparison with in cylinder sampling valve data. SAE Papers, 1992(922225).

66. Tao, F., Srinivas, S., Reitz, R.D. and Foster, D.E. , Comparison of Three Soot Models Applied to Multi-Dimensional Diesel Combustion Simulations. JSME International Journal, 2005. **Series B, 48**(4): p. 671-678.

67. Patterson, M.A., Kong, S.-C., Hampson, G.J. and Reitz, R.D., Modeling the Effects of Fuel Injection Characteristics on Diesel Engine Soot and NOx Emissions. SAE Papers, 1994(940523).

68. Ladommatos, N., Song, H. and Zhao, H., Measurements and predictions of diesel soot oxidation rates. Proc Instn Mech Engrs Part D: J Automobile Engineering, 2002. **216**: p. 677-689.

69. Lee, K.B., Thring, M.W. and Beer, J.M. , On the rate of combustion of soot in a laminar soot flame. Combustion and Flame, 1962(6): p. 137-145.

70. Leung, K.M., Lindstedt, R.P., and Jones, W.P., A Simplified Reaction Mechanism of Soot Formation in Nonpremixed Flames. Combustion and Flame, 1991. **87**: p. 289-305.

71. Tao, F., Foster, D.E. and Reitz, R.D., Characterization of soot particle distribution in conventional, non-premixed DI diesel flame using a multi-step phenomenological soot model. Proceedings of the Combustion Institute, 2007. **31**(2): p. 2991-2998.

72. Tao, F., Golovitchev, V.I. and Chomiak, J., A Phenomenological model for the prediction of soot formation in diesel spray combustion. Combustion and Flame, 2004. **136**: p. 270-282.

73. Lindstedt, P.R., Simplified soot nucleation and surface growth steps for non-premixed flames, in Soot Formation in Combustion: Mechanisms and Models, H. Bockhorn, Editor. 1994, Springer-Verlag: Heidelberg. p. 417-441.

74. Balthasar, M. and Frenklach, M., Detailed kinetic modeling of soot aggregate formation in laminar premixed flames. Combustion and Flame, 2005. **140**: p. 130-145.

75. Morgan, N., Kraft, M., Balthasar, M., Wong, D., Frenklach, M. and Mitchell, P., Numerical simulations of soot aggregation in premixed laminar flame. Proceedings of the Combustion Institute, 2007. **31**: p. 693-700.

76. Hong, S., Wooldridge, M.S., Im, H.G., Assanis, D.N. and Pitsch, H., Development and application of a comprehensive soot model for 3D CFD reacting flow studies in a diesel engine. Combustion and Flame, 2005. **143**: p. 11-26.

77. Surovikin, V.F., Analytical description of the processes of nucleus-formation and growth of particles of carbon black in the thermal decomposition of aromatic hydrocarbons in the gas phase. Solid Fuel Chemistry (Khimiya Tverdogo Topliva), 1976. **10**(1): p. 111-122.

78. Hessel, R.P., Foster, D.E., Steeper, R.R., Aceves, S.M. and FLowers, D.L., Pathline analysis of full-cycle four-stroke HCCI engine combustion using CFD and multi-zone modeling. SAE Papers, 2008(2008-01-0048).

79. EnSight User Manual for Version 8.2. 2006, Computational Engineering International Inc.

80. Apte, S.V., Mahesh, K., Moin, P. and Oefelein, J.C., Large-eddy simulation of swirling particle-laden flows in a coaxial-jet combustor. International Journal of Multiphase Flow, 2003. **29**: p. 1311-1331.

81. Katta. V.R., Blevins, L.G. and Roquemore, W.M., Dynamics of an inverse diffusion flame and its role in polycyclic-aromatic-hydrocarbon and soot formation. Combustion and Flame, 2005. **142**: p. 33-51.

82. Barve, V.V., Clemens, N.T., Ezekoye, O.A. and Katta, V.R., Soot production rates in strongly forced methane-air laminar diffusion flames. American Institute of Aeronautics and Astronautics, 2006(AIAA 2006-3286).

83. Fuentes, A., Rouvreau, S., Joulain, P., Vantelon, J. -P., Legros,G., Torero, J. L., and Fernandez-Pello, A. C. , Sooting behavior dynamics of a non-buoyant laminar diffusion flame. Combustion Science and Technology, 2007. **179**(1-2): p. 3-19.

84. Popov, P.P., McDermott, R. and Pope, S.B., An accurate time advancement algorithm for particle tracking. Journal of Computational Physics, 2008. **227**: p. 8792-8806.

85. Tomiyama, A., Zun, I., Higaki, H., Makino, Y. and Sakaguchi, T., A three-dimensional particle tracking method for bubbly flow simulation. Nuclear Engineering and Design, 1997(175): p. 77-86.

86. Petera, J., Weatherley, L.R., Hume, A.P. and Gawrysiak, T., A finite element algorithm for particle/droplet trajectory tracking, tested in a liquid-liquid system in the presence of an external electric field. Computers and Chemical Engineering, 2007(31): p. 1369-1388.

87. Greenfield, C. and Quarini, G., A Langrangian simulation of particle deposition in a turbulent boundary layer in the presence of thermophoresis. Applied Mathematical Modelling, 1998(22): p. 759-771.

88. Coppola, G., Sherwin, S.J. and Peiro, J., Nonlinear particle tracking for high-order elements. Journal of Computational Physics, 2001. **172**: p. 356-386.

89. Pokrajac, D. and Lazic, R., An efficient algorithm for high accuracy particle tracking in finite element. Advances in Water Resources, 2002. **25**: p. 353-369.

90. Pozorski, J. and Apte, S.V., Filtered particle tracking in isotropic turbulence and stochastic modeling of subgrid-scale dispersion. International Journal of Multiphase Flow, 2009. **35**(118-128).

91. Ma, B., Ruwet, V., Corieri, P., Theunissen, R., Riethmuller, M. and Darquenne, C., CFD simulation and experimental validation of fluid flow and particle transport in a model of alveolared airways. Aerosol Science, 2009. **40**: p. 403-414.

92. Rounds, F.G., Carbon: Cause of Diesel Engine Wear? SAE Papers, 1977(770809).

93. Gautam, M., Chitoor, K., Durbha, M. and Summers, J.C, Effect of diesel soot contaminated oil on engine wear – investigation of novel oil formulations. Tribology International, 1999. **32**: p. 687-699.

94. Kim, C., Passut, C.A. and Zang, D.M., Relationships Among Oil Composition Combustion-Generated Soot, and Diesel Engine Valve Train Wear. SAE Papers, 1992(922199).

95. Mainwaring, R., Soot and Wear in Heavy Duty Diesel Engines. SAE Papers, 1997(971631).

96. Lockwood, F.E. and Zhang, Z.G., Effect of Soot Loading on the Thermal Characteristics of Diesel Engine Oils. SAE Papers, 2001(2001-01-1714).

97. Dahlen, L., On Applied CFD and Model Development in Combustion Systems Development for DI Diesel Engines: Prediction of Soot Mediated Oil Thickening. 2002, Royal Institute of Technology: Stockholm.

98. Abraham, J., Thermophoretic effects on soot distribution in a direct-injection diesel engine. SAE Papers, 1996(960320).

99. Amsden, A.A., KIVA-3: A KIVA Program with Block-Structured Mesh for Complex Geometries. 1993, Los Alamos National Laboratory: Los Alamos.

100. Bonatesta, F., La Rocca, A., Shayler, P.J. and Wahab, E. The influence of swirl ratio on soot quantity and distribution in the cylinder of a diesel engine. in European Combustion Meeting. 2007. Chania, Crete, Greece.

101. Park, C., and Appleton, J.P., Shock-Tube Measurements of Soot Oxidation Rates. Combustion and Flame, 1973. **20**: p. 369-379.

102. Amsden, A.A., O' Rourke, P.J. and Butler, T.D. , KIVA-II - A Computer Programe for Chemically Reactive Flow with Sprays. 1989, Los Alamos National Laboratory.

103. Amsden, A.A., KIVA-3V: A Block-Structured KIVA Program for Engines with Vertical or Canted Valves. 1997, Los Alamos National Laboratory.

104. Amsden, A.A., KIVA-3V, Release 2, Improvements to KIVA-3V. 1999, Los Alamos National Laboratory.

105. Schmidt, D.P. and Senecal, P.K., Improving the Numerical Accuracy of Spray Simulations. SAE Papers, 2002(2002-01-1113).

106. Abani, N., Munnannur, A. and Reitz, R.D., Reduction of numerical parameter dependencies in diesel spray models. Journal of Engineering for Gas Turbine and Power, 2008. **130**.

107. Shuai, S., Abani, N., Yoshikawa, T., Reitz, R.D. and Park, S.W., Simulating low temperature diesel combustion with improved spray models. International Journal of Thermal Science, 2009. **48**: p. 1786-1799.

108. Bonatesta, F., La Rocca, A., Mitchell, S. and Shayler, P.J., Simulation of in-cylinder conditions to examine factors influencing exhaust emissions and soot deposition in oil. 2006, The University of Nottingham.

109. Pungs, A., Pischinger, S. and Backer, H., Analysis of the particle size distribution in the cylinder of a common rail DI diesel engine during combustion and expansion. SAE Papers, 2000(2000-01-1999).

110. Gwaze, P., Schmid, O., Annegarn, H., Andreae, M.O., Huth. J. and Helas, G., Comparison of three methods of fractal analysis applied to soot aggregates from wood combustion. Aerosol Science, 2006. **37**: p. 820-838.

111. Tandon, P. and Rosner, D.E, Translational Brownion Motion diffusion coefficient of large (multiparticle) suspended aggregates. Ind. Eng. Chem. Res., 1995. **34**: p. 3265-3277.

112. Espey, C. and Dec., J.E., The Effect of TDC Temperature and Density on the Liquid-phase Fuel Penetration in a D.I. Diesel Engine. SAE Papers, 1995(952456).

113. Roquemore, W.M., Katta, V., Stouffer, S., Belovich, V., Pawlik, R., Artingstall, M., Justinger, G., Gord, J., Lynch, A., Zelina, J. and Roy, S., Soot studies of laminar diffusion flames with recirculation zones. Proceeding of Combustion Institute, 2009. **32**: p. 729-736.

114. Zhang, J. and Li, A., CFD simulation of particle deposition in a horizontal turbulent duct flow. Chemical Engineering Research and Design 2008 **86**: p. 95-106.

115. Breuer, M., Baytekin, H.T. and Matida, E.A., Prediction of aerosol deposition in 90o bends using LES and an efficient Lagrangian tracking method Aerosol Science 2006 **37** p. 1407-1428.

116. Kock, B.F., Eckhardt, Th. and Roth, P., In-cylinder sizing of diesel particles by time-resolved laser-induced incandescence (TR-LII). Proceedings of the Combustion Institute, 2002. **29**: p. 2775-2781.

117. Zhao, J.X. and Lee, C.F., Modeling of blow-by in a small-bore high-speed direct-injection optically accessible diesel engine. SAE Papers, 2006(2006-01-0649).

118. Hinds, W.C., Aerosol Technology. 1982, Boston: John Wiley & Sons.

119. Mahgerefteh, H., Rykov, Y. and Denton, G., Courant, Friedrichs and Lewy (CFL) impact on numerical convergence of highly transient flows. Chemical Engineering Science, 2009. **64**: p. 4969-4975.

120. Dec, J.E. and Tree, D.R., Diffusion-flame / Wall Interactions in a Heavy-Duty DI Diesel Engine. SAE Papers, 2001(2001-01-1295).

121. Tree, D.R. and Dec, J.E., Extinction Measurements of In-Cylinder Soot Deposition in a Heavy-Duty DI Diesel Engine. SAE Papers, 2001(2001-01-1296).

122. Maigaard, P., Mauss, F. and Kraft, M., Homogeneous charge compression ignition engine: A simulation study on the effects of inhomogeneities. Journal of Engineering for Gas Turbines and Power, 2003. **125**: p. 466-471.

123. Heywood, J.B., Internal Combustion Engine Fundamentals. 1988, New York: McGraw-Hill

124. Hultqvist, A., Christensen, M., Johansson, B., Franke, A., Richter, M. and Alden, M., A study of the homogeneous charge compression ignition combustion process by chemiluminescence imaging. SAE Papers, 1999(1999-01-3680).

125. Tambasco, M. and Steinman, D.A., On Assessing the Quality of Particle Tracking Through Computational Fluid Dynamic Models. Journal of Biomechanical Engineering, ASME, 2002. **124**: p. 166-175.

126. Subramaniam, S. and O'Rourke, P.J., Numerical Convergence of the KIVA-3 Code for Sprays and Its Implications for Modeling. 1998, Los Alamos National Laboratory.

127. Chapra, S.C. and Canale, R.P., Numerical Methods for Engineers: With Software and Programming Applications. 4th ed. 2002, Boston: McGraw-Hill. 926.

128. Cheng, H.-P., Cheng, J.-R. and Yeh, G.-T., A particle tracking technique for the Lagrangian-Eulerian finite element method in multi-dimensions International Journal for Numerical Methods in Engineering, 1996. **39**: p. 1115-1136.

129. Tree. D.R. and Foster, D.E., Optical measurements of soot particle size, number density, and temperature in a direct injection diesel engine as a function of speed and load. SAE Papers, 1994(940270).

130. Benajes, J., Molina, S., Garcia, J.M. and Riesco, J.M., The Effect of Swirl on Combustion and Exhaust Emissions in Heavy-duty Diesel Engines. Proc. Instn. Mech. Engrs: Part D:J. Automobile Engineering, 2004. **218**: p. 1141-1148.

131. McCracken, M.E. and Abraham, J., Swirl-Spray Interactions In a Diesel Engine. SAE Papers, 2001(2001-01-0996).

132. Abraham, J. and Khan, A., Jet-Jet and Jet-Wall Interactions of Transient Jets from Multi-Hole Injectors. SAE Papers, 1999(1999-01-0513).

133. Kim, B.-S., Yoon, W.H., Ryu, S.H. and Ha, J.S., Effect of the Injector Nozzle Hole Diameter and Number on the Spray Characteristics and the Combustion

Performance in Medium-Speed Diesel Marine Engines. SAE Papers, 2005(2005-01-3853).

134. Karas, L.J., Kesling, H.S., Liotta, F.J. and Nandi, M.K., Low emission oxygenated diesel fuel, in Symposium on Oxygenates as Fuel Additives 1994, American Chemical Society, Fuel Division: San Diego.

135. Winkler, M.F. and Parker, D.W., Ceramic thermal barrier coatings provide advanced diesel emissions control and improved management of combustion-exhaust system temperatures. SAE Papers, 1993(931106).

136. Collings, N. and Graskow, B.R., Particles from internal combustion engines - what we need to know. Philosophical Transaction of Royal Society London 2000. **A358**: p. 2611-2623.

137. Naydenova, I., Marquetand, J. and Warnatz, J. Soot formation simulation of shock tube experiments with the use of an empirical model. in Third European Combustion Meeting 2007. 2007. Crete.

138. Crookes, R.J. and Sivalingam, G., Formation and oxidation of soot particulates in a diesel fuel spray flame. Clean Air, 2006. **7**: p. 77-91.

139. di Stasio, S., Konstandopoulos, A.G. and Kostoglou, M., Cluster-CLuster Aggregation Kinetics and Primary Particle Growth of Soot Nanoparticles in Flame by Light Scattering and Numerical Simulations. Journal of Colloid and Interface Science, 2002. **247**: p. 33-46.

140. Zhao, B., Yang, Z., Li, Z., Johnston, M.V. and Wang, H., Particle size distribution function of incipient soot in laminar premixed ethylene flames: effect of flame temperature. Proceedings of the Combustion Institute, 2005. **30**: p. 1441-1448.

141. Xu, F., Sunderland, P.B. and Faeth. G.M., Soot Formation in Laminar Premixed Ethylene/Air Flames at Atmospheric Pressure. Combustion and Flame, 1997. **108**: p. 471-493.

142. Flynn, P.F., Durret, R.P., Hunter, G.L., Loye, O. A. and Akinyemi, O.C., Diesel Combustion: An Integrated View Combining Laser Diagnostics, Chemical Kinetics, and Empirical Validation. SAE Papers, 1999(1999-01-0509).

TABLES

Table 2.1 EU Emission Standards for Diesel Passenger Cars (g/km) [19]

Tier	Date	CO	HC	$HC+NO_x$	NO_x	PM
Euro 1	1992.07	2.72	-	0.97	-	0.14
Euro 2, IDI	1996.01	1.0	-	0.7	-	0.08
Euro 2, DI	1996.01	1.0	-	0.9	-	0.10
Euro 3	2000.01	0.64	-	0.56	0.50	0.05
Euro 4	2005.01	0.50	-	0.30	0.25	0.025
Euro 5	2009.09	0.50	-	0.23	0.18	0.005
Euro 6	2014.09	0.50	-	0.17	0.08	0.005

Table 2.2 Primary and agglomerated soot particle size from various combustion sources with different measuring methods

	Soot Primary Size (nm)	Agglomerated Soot size (nm)	Method of Measurement	Reference
Engine out	17.5 – 32.5 nm		Transmission Electron Microscopy (TEM)	Mathis et al. (2005) [20]
		10-400 nm Peaks around 50-60 nm	Scanning Mobility Particle Analyzer (SMPS)	Mathis et al. (2005) [20]
		7-250 nm Peaks around 50-90 nm	Scanning Mobility Particle Analyzer (SMPS)	Kolodziej, C. et al. (2007)[21]
	35 – 45 nm (SMD)		Scanning Electron microscope (SEM)	Furuhata et al. (2007)[22]
		120 nm	Centrifugal sedimentation analysis	Furuhata et al. (2007)[22]
		10 – 500 nm	Scanning Mobility Particle Analyzer (SMPS)	Furuhata et al. (2007)[22]
	10 – 45 nm (mean 25 nm)		Transmission Electron Microscopy (TEM)	Lapuerta et al. (2007)[23]
		10 -120 nm	Scanning Mobility Particle Analyzer (SMPS)	Collings & Graskow (2000) [136]
	10 – 50 nm		Transmission Electron Microscopy (TEM)	Kock et al. (2006) [24]
In-cylinder	10 – 40 nm		Optical diagnostic (scattering/extinction, & radiation./scattering	Kazakov & Foster (1998)[33]
	10-40 nm		Optical diagnostic (scattering/extinction, & radiation./scattering	Tree & Foster (1994)[129]
	30 – 100 nm		Laser-induced incandescent (LII)	Bougie et al. (2007)[26]
	25 – 80 nm		Time-resolved laser-induced incandescent (TR-LII)	Kock et al (2006)[24]
Burner/ Open Flame/ Shock tube	5 – 28 nm		Time-resolved laser light extinction-scattering technique	Naydenova et al. (2007)[137]
	34.7 – 53.6 nm		Transmission Electron Microscopy (TEM)	Crookes & Sivalingam (2006) [138]
	5 – 45 nm		Scanning Electron microscope (SEM)	di Stasio et al. (2002)[139]
		25 – 350 nm	Light Scattering Technique	di Stasio et al. (2002)[139]
	3 – 50 nm	2 – 70 nm	Scanning Mobility Particle Analyzer (SMPS)	Zhao et al. (2005)[140]
	15 – 40 nm		Transmission Electron Microscopy (TEM)	Xu et al. (1997) [141]

Table 2.3 Soot Model variables and Differential Equations

Variable	Rate Equation
N, Soot Number Density (cm^{-3})	$\frac{dN}{dt} = N_A(r_5 - r_8)$
R, precursor radical density ($mol\ cm^{-3}$)	$\frac{dR}{dt} = r_1 - r_3 - r_5$
C_2H_2, growth species density ($mol\ cm^{-3}$)	$\frac{d[C_2H_2]}{dt} = r_2 - r_4 - r_6$
f_v, soot volume fraction	$\frac{d(f_v)}{dt} = \frac{1}{\rho_s}\left(r_5 M_R + r_6 M_C - r_7 M_C\right)$

** N_A = Avogadros Number
M_c = molecular weight of Carbon
M_R = molecular weight of radical precursor

Table 2.4 Processes, Chemical reactions, Rates of Reactions, Activation Energies and Pre-exponential Factors used in Fusco's Soot Model [32]

Process (i)	Chemical Reaction	Rate of reaction, r_i	Activation Energy, E_i (cal/mol)	Pre-exponential Factor, A_i (mol cm s)
(1) Radical formation	$C_mH_n \rightarrow m/2\ R$	$r_1 = m/2\ A_1 e^{-E_1/RT}[\text{fuel}]$	120,000	0.7×10^{12}
(2) C_2H_2 formation	$C_mH_n \rightarrow m/2\ C_2H_2$	$r_2 = m/2\ A_2 e^{-E_2/RT}[\text{fuel}]$	49,000	2×10^{8}
(3) Radical oxidation	$R + O_2 \rightarrow$ products	$r_3 = A_3 e^{-E_3/RT}[R][O_2]$	40,000	1×10^{12}
(4) C_2H_2 oxidation	$C_2H_2 + O_2 \rightarrow 2CO + H_2$	$r_4 = A_4 e^{-E_4/RT}[C_2H_2][O_2]$	50,000	6×10^{13}
(5) Particle inception	$R \rightarrow P$	$r_5 = A_5 e^{-E_5/RT}[R]$	50,000	1×10^{10}
(6) Particle growth	$P + C_2H_2 \rightarrow P$	$r_6 = A_6 e^{-E_6/RT}[C_2H_2]S^{1/2}$ where $S=pD^3N$, $D \cong 25nm$	12,000	4.2×10^{4}
(7) Particle oxidation	$P + O_2 \rightarrow P$	$r_7 = \left[\frac{k_A p}{1+k_z p} x + k_B p(1-x)\right]$		
		Where $x = \left\{1 + \frac{k_T}{k_B p} x + k_B p(1-x)\right.$		
		$k_A = 20 \times e^{-E_A/RT}$	30,000	
		$k_B = 4.46 \times 10^{-3} e^{-E_B/RT}$	15,200	
		$k_T = 1.51 \times 10^{5} e^{-E_T/RT}$	97,000	
		$k_z = 21.3 \times e^{E_Z/RT}$	4,100	
(8) Particle coagulation	$xP \rightarrow P$	$r_8 = K_{coag} T^{1/2} f_v^{1/6} N^{1/6}$ where $K_{coag}=1.05 \times 10^{-7}$ (cm^1 mix s^{-1} $K^{-1/2}$)		

Table 3.1: Specifications of computer hardware

Processor	Intel Pentium 4, 3.40 GHz Processor CPU with heat sink fan
Motherboard	ASUS P5LD2-VM Motherboard
System memory	2 x 1GB DDR2 memory
Graphics setup	Integrated Intel Graphics Media Accelerator 950
Hard disk	2 x 200 GB Seagate Barracuda ATA Hard disk

Table 3.2: Configurations of computer system software

BIOS	AMIBIOS Version 0508
Operating System	Microsoft Windows XP Professional, Version 2002, Service Pack 3 Red Hat Linux 9.0
System Partitioning	Built-in Automatic Partitioning tools included in the installation programmes in Redhat Linux 9 CD is used to partition the hard disk to allow separate operations of two operating systems and their respective files.
Dual-booting configuration	GRUB (GRand Unifed Bootloader) included in the installation programmes in Redhat Linux 9 CD is used to load a variety of operating systems on a PC. Either Microsoft Windows XP or Redhat Linux 9, can be selected each time the computer is turned on.
Datafile transfers	DiskInternals Linux Reader 1.1 which is installed on Microsoft Windows platform is used to extract the data from Linux partition into Windows partition.

Table 3.3: Kiva-3v running sequence and the associated I/O files

Input Files	Tools	Output Files
iprep	Pre-processor: k3prep	otape11, otape17
itape17 (renamed from otape17), itape5 (engine conditions)	Main code: kiva3v	dat.* files, otape9 (graphics post-processing file) otape12 (general alphanumeric simulation information file)
itape9 (renamed from otape9), enspec	Post processor: k2e (translator from Kiva3v to EnSight)	Postscript files
Postscript files	EnSight 8.2	Graphics

Table 3.4: Sub-models used for the simulation

Sub-models of Kiva-3v Release II	
Combustion	Arrhenius (at auto-ignition point) Mixing-controlled turbulent combustion
Soot model	Two-step Soot model
Intake flow	Assumed initial in-cylinder flow
Heat transfer	Modified law-of-the-wall
Fuel model	$C_{12}H_{26}$
Wall film dynamics	Particle-based with splash models
Dynamics of evapourating spray	Monte Carlo-based discrete particle technique
Turbulence model	Modified RNG κ-ε
NO_x model	Extended Zeldovich
Fuel vapourization	Single component
Drop breakup/distortion/oscillation	Taylor Analogy Breakup model
Drop drag	Distorting spherical drop

Table 3.5: Specifications of the Engine

Parameters	Specifications
Engine Type	4 valve DI diesel (Puma)
Bore x Stroke	86.0 x 86.0 mm
Compression Ratio	18.2:1
Displacement	500 cm^3
Piston Geometry	Bowl-in-piston

Table 3.6: Specifications of the Fuel Injector

Parameters	Specifications
Injector type	
Diameter of nozzle hole	0.15 mm
Number of nozzle hole	7, uniformly spaced
Start of Injection (SOI)	-2.0° CA ATDC
Duration of injection pulse	13° CA
Spray Mean Cone Angle	14°
Angle of fuel jet axis (from cylinder axis)	74°

Table 3.7: Test conditions

Parameters	Conditions
Engine speed	2500 rpm
BMEP	1180 kPa
Boost Pressure	101.7 kPa
Air Mass	248 kg/h
Fuel	10.894 kg/h
Fuel	36.311 mg/stroke
Intake Temperature	60.2°C
EGR %	3.5 %
Swirl Ratio	1.3, 1.9, 2.4

Table 6.1 Starting positions of soot particle paths tracked from crank angle instants of 2° to 30° ATDC

Starting Region	Angular position (°)	Radial distance (cm)	Axial distance (cm)	Observations: Crank angle instants from which soot particles are likely to reach cylinder boundary layer (° CA ATDC)
Above the spray axis (spray downstream)	10	1.7	9.8	6 – 10
	20	1.7	9.8	- (the closest – middle squish)
	25	1.7	9.8	- (the closest – middle squish)
	40	1.7	9.8	6 – 10
Below the spray axis (spray downstream)	10	1.7	9.1	6 – 12 24 – 28
	20	1.7	9.1	6 – 12 24 – 28
	25	1.7	9.1	6 – 12 24 - 28
	40	1.7	9.1	6 – 12 24 – 28
Above the spray axis (spray upstream)	10	1.0	9.85	- (bowl)
	20	1.0	9.85	- (bowl)
	25	1.0	9.85	- (bowl)
	40	1.0	9.85	- (bowl)
Below the spray axis (spray upstream)	10	1.0	9.45	- (bowl)
	20	1.0	9.45	- (bowl)
	25	1.0	9.45	- (bowl)
	40	1.0	9.45	- (bowl)
Sides of the spray	5	1.6	9.5	14 – 18
	20	1.6	9.5	14 – 18
	35	1.6	9.5	14 – 18 22 – 26
	45	1.6	9.5	14 – 18 22 – 26
Above the bowl rim	10	2.3	10.1	6 – 10 20 – 26
	20	2.3	10.1	6 – 10 20 – 26
	30	2.3	10.1	6 – 10 20 – 26
	40	2.3	10.1	6 – 10 20 – 26

Table 7.1 Comparison of Different Approaches of Soot Particle Size Evolution

No	Approach	Formulation	Assumptions	Notes
1	Direct association with net soot and conserving the soot particle numbers from initial point	$Msp_{i+1} = \frac{Ms_{i+1}}{N_i}$ $D_{i+1} = 2 \times \left(\frac{3}{4} \frac{Msp_{i+1}}{\rho_{sp} \pi} \right)^{1/3}$	-Number of soot particles does not change along the path -All soot amount in the volume contributes to particle growth -Soot diffusion is not considered	-Soot diameter profiles exactly follow the net soot profile along the paths
2	Association with the cylinder conditions along the path, and use normalised Hiroyasu's and NSC's with net soot, to find the net soot growth	$\frac{dM_{sfi}}{M_{sni}.dt} = \frac{A_f M_{fvi} P_i^{0.5} e^{\frac{-E_{sf}}{RT_i}}}{M_{sni}}$ (a) $\frac{dM_{soi}}{M_{sni}.dt} = \frac{A_o \frac{MW_c}{\rho_s D_s} M_{sni} \dot{R}_{NSCi}}{M_{sni}}$ (b) Fract. mass change, (F)= [(a)-(b)].dt $Msp_{i+1} = Msp_i + (Msp_i \times F_{i+1})$ $D_{i+1} = 2 \times \left(\frac{3}{4} \frac{Msp_{i+1}}{\rho_{sp} \pi} \right)^{1/3}$	-All amount of soot in the volume involves in the growth process -Soot diffusion is not considered	-In majority of the cases, oxidation process dominates, thus leaving soot particles to be very small -This could be explained by the fact that most of tracked particles are out of fuel plume and pass through high oxygen and temperature regions.
3	Association with the cylinder conditions along the path. Hiroyasu's is modified to consider the contribution of fuel vapour to soot particle growth. NSC's is normalised with net soot in the volume	$\frac{dM_p}{dt.M_p} = xA_f \left(\frac{M_{fv}}{\rho_p} \right) P^{0.5} e^{\frac{-E_{sf}}{RT}}$ (a) $\frac{dM_{so}}{dt.M_n} = yA_o \frac{MW_c}{\rho_s D_i} \dot{R}_{NSCi}$ (b) Fract. mass change, (F)= [(a)-(b)].dt $Msp_{i+1} = Msp_i + (Msp_i \times F_{i+1})$ $D_{i+1} = 2 \times \left(\frac{3}{4} \frac{Msp_{i+1}}{\rho_{sp} \pi} \right)^{1/3}$	- A certain amount of fuel vapour is responsible for soot surface growth on a particle -By doing this way, fractional mass increment by growth is not tied with the net soot in the volume -However, the soot oxidation process is still linked to the net soot in the volume	-The factorials of x and y are selected in order to get comparable soot formation and oxidation rates ($x=1.0\times10^{2}$, $y=1.0\times10^{-2}$) -Soot diameter profiles are different from other methods but they are all depend on the values of x and y which their combinations can be changed infinitely (?)

Table 7.1 Comparison of Different Approaches of Soot Particle Size Evolution (Cont.)

No	Approach	Formulation	Assumptions	Notes
4	Association with the cylinder conditions along the path. A multiplication factor (which implied the average particle number density, particle/cm^3, in the cylinder) is introduced in Hiroyasu's equation to obtain mass formed per particle. NSC's equation in terms of surface mass oxidation rate, w, is used	$\frac{dM_{sfi}}{dt} = (x)A_f M_{fvi} P_i^{0.5} e^{\frac{-E_{sf}}{RT_i}}$ $w = \dot{R}_{NSC} = \frac{k_A p}{1+k_z p} x + k_B p(1-x)$ where the unit is in g/cm^2.s Multiplying by the surface area of a particle, mass oxidation rate per particle can be obtained. $\frac{dM_{net}}{particle} = (dM_{sf} - w \cdot SA_{part}).dt$ $M_{sp(i+1)} = M_{sp(i)} + \Delta M_{net}$ $D_{i+1} = 2 \times \left(\frac{3}{4} \frac{Msp_{(i+1)}}{\rho_{sp} \pi} \right)^{1/3}$	-soot particle surface is smooth thus all computed surface area is involved in the oxidation -as in all cases, soot particles are assumed monodispersed locally, but can be different at different location in the cylinder -All mass formed contributes to the surface growth process	x = 2e-10 The results from this approach show similar trends with Approach 3. However, when the soot particles undergo soot growth, the can reach over 120 nm at the peak. This approach is deemed to be the most robust among all the approaches, because: 1) Surface oxidation rate, w, obtained from the equation and data along the paths, is in the right range when compare to the original NSC's experimental data 2) The multiplication factor used implies the average particle number density reported by Heywood (1×10^9 #/cm^3) and Tree & Foster (1×10^{12} -1×10^{14} #/cm^3)

FIGURES

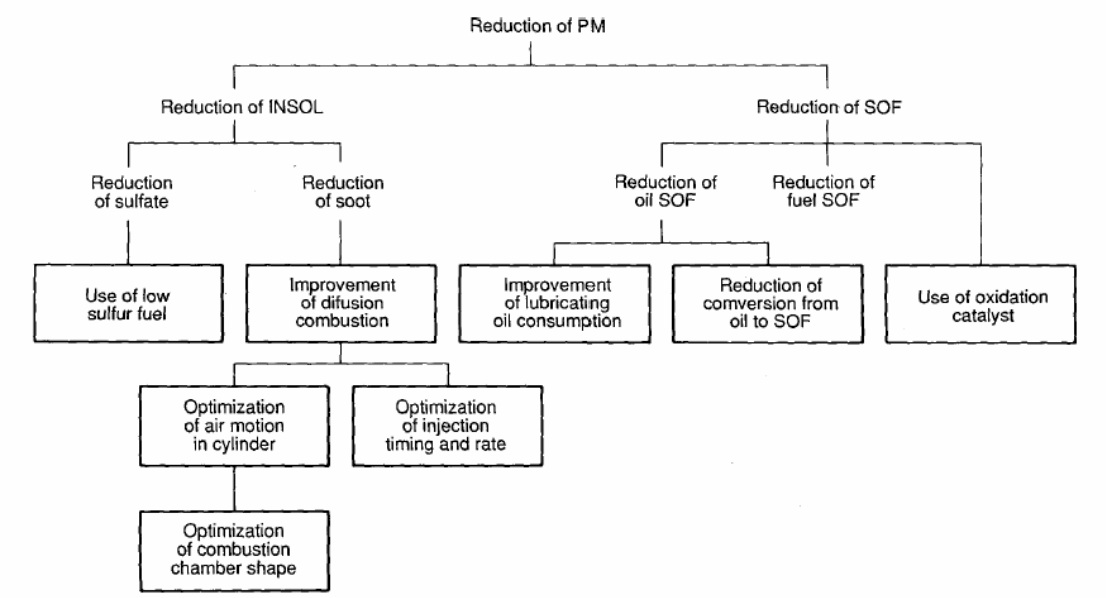

Figure 2.1 Particulate reduction strategy [47]

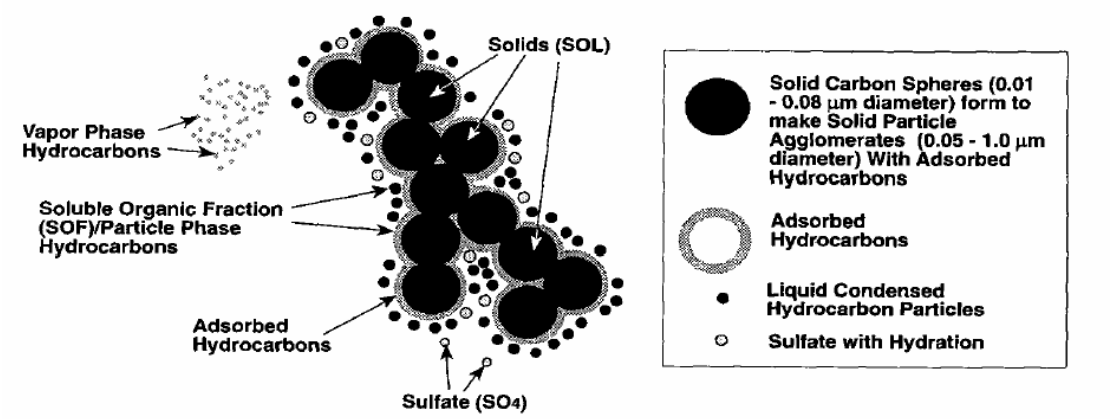

Figure 2.2 Schematic of Diesel Particles and Vapour Phase Compounds [49]

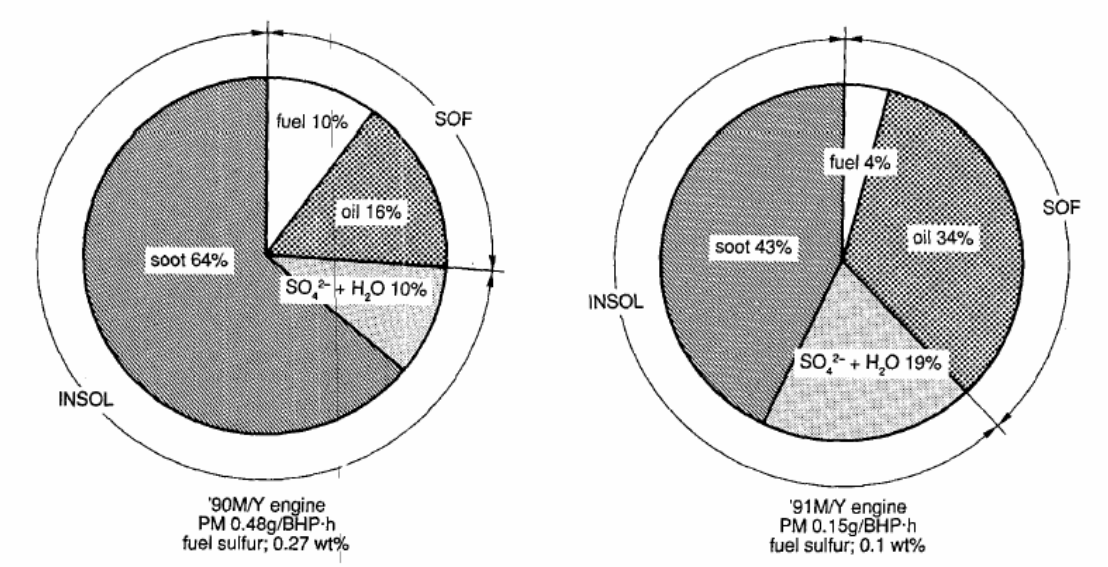

Figure 2.3 HDDE transient particulate composition from base engine [47]

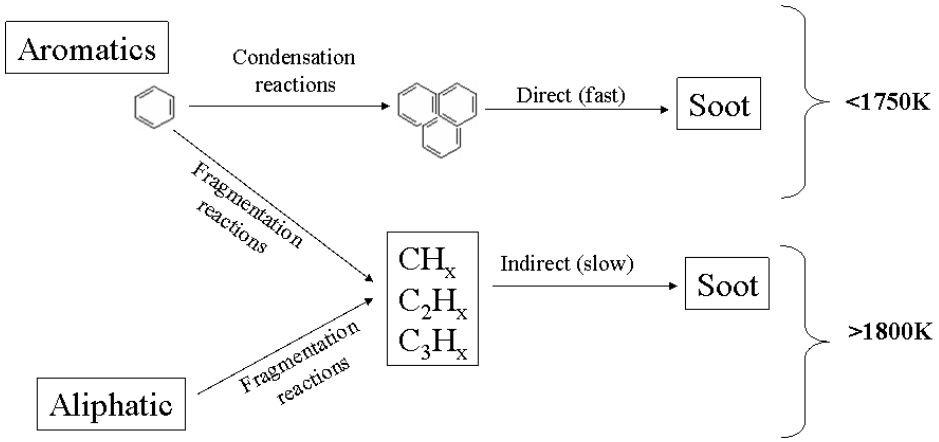

Figure 2.4 Reaction mechanism for soot nucleation [56]

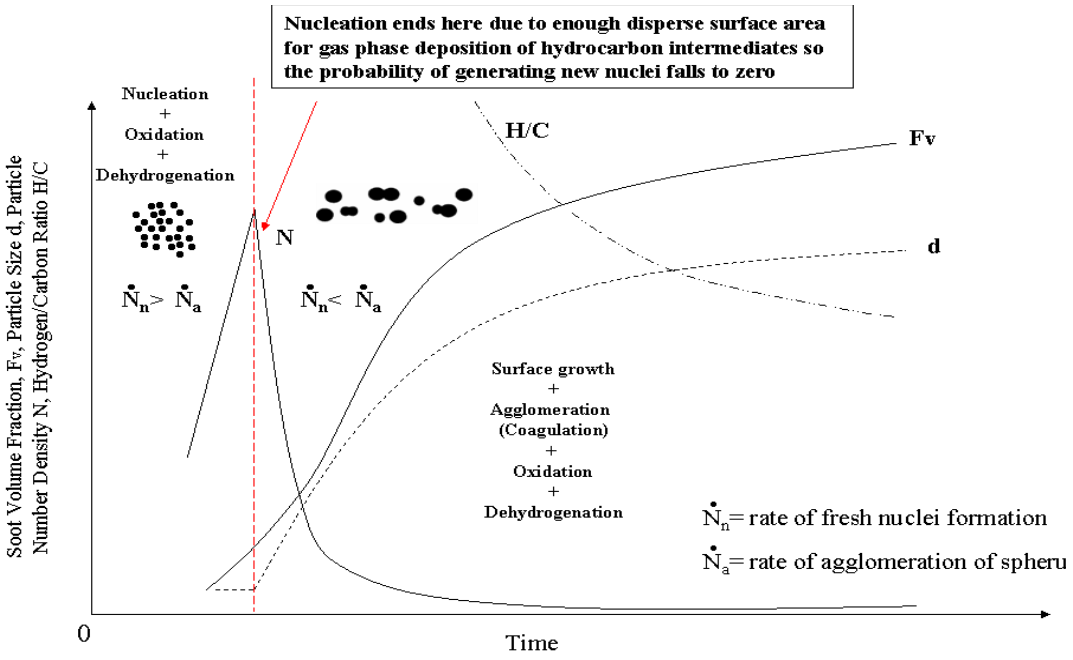

Figure 2.5 Variation in soot volume fraction Fv, Particle Number Density N, Particle Size d, and soot hydrogen/carbon ratio with time in flame (modified from [56]

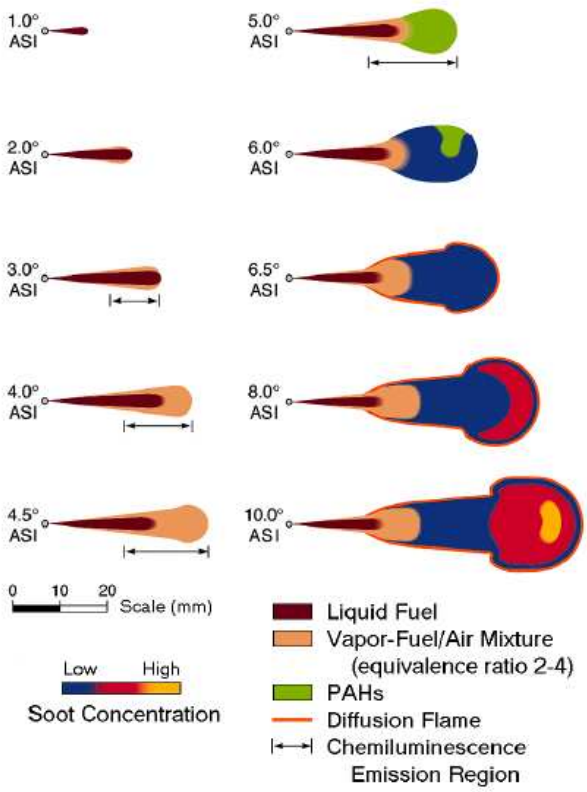

Figure 2.6 Schematics of early flame images from laser measurements [142]

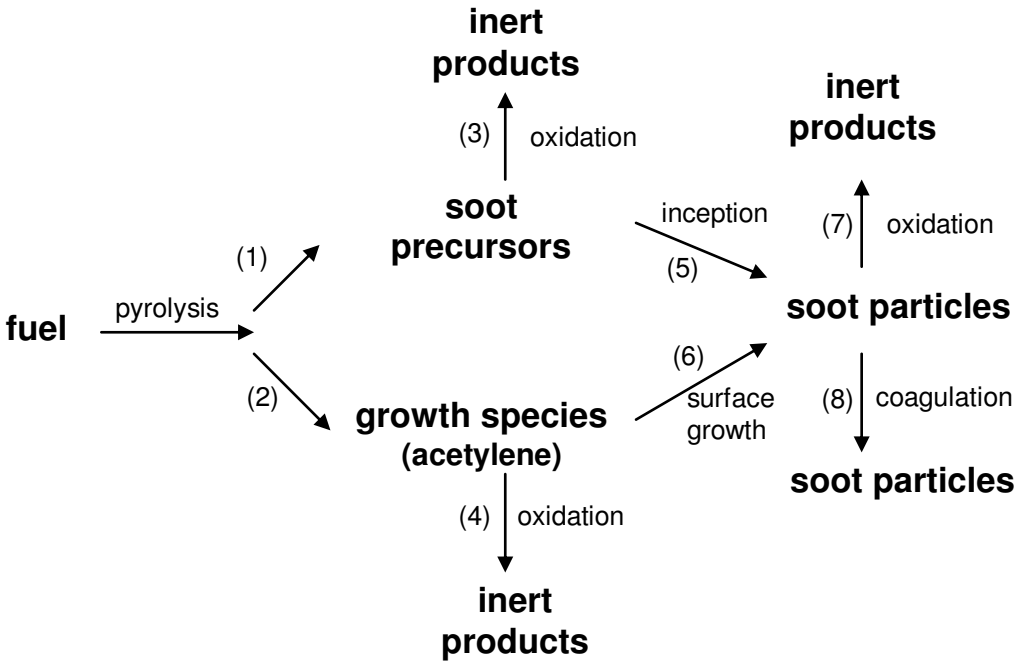

Figure 2.7 Schematic diagram of soot model processes by Fusco et al. [32]

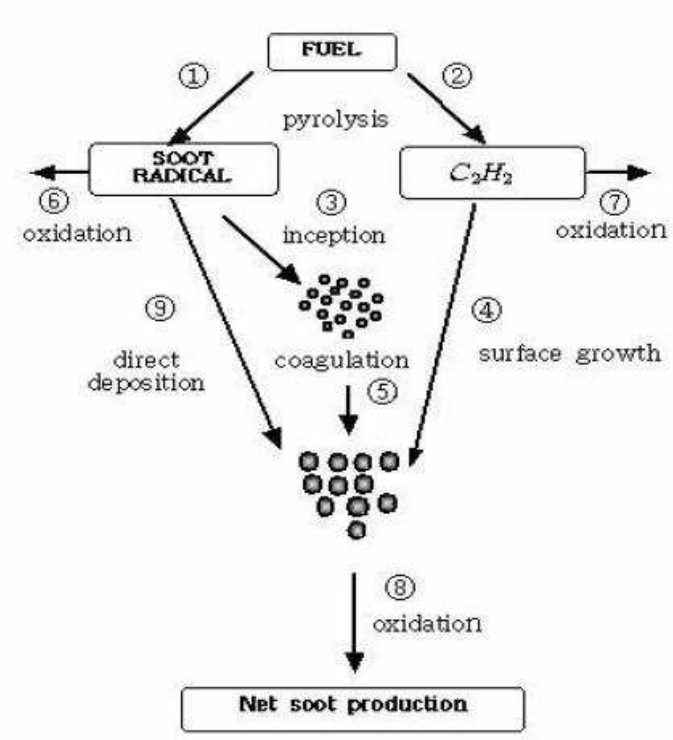

Figure 2.8 Schematic diagram of Foster soot model modified by Kazakov and Foster [35]

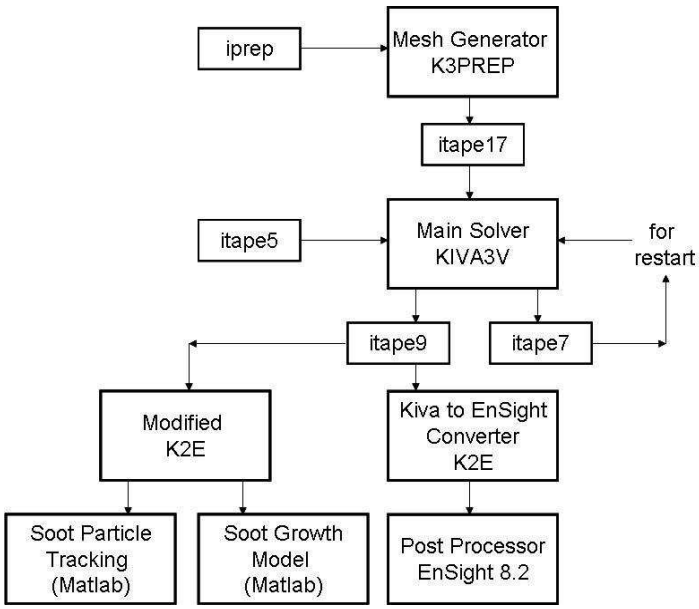

Figure 3.1: Flow Chart of Kiva-3v Input Output

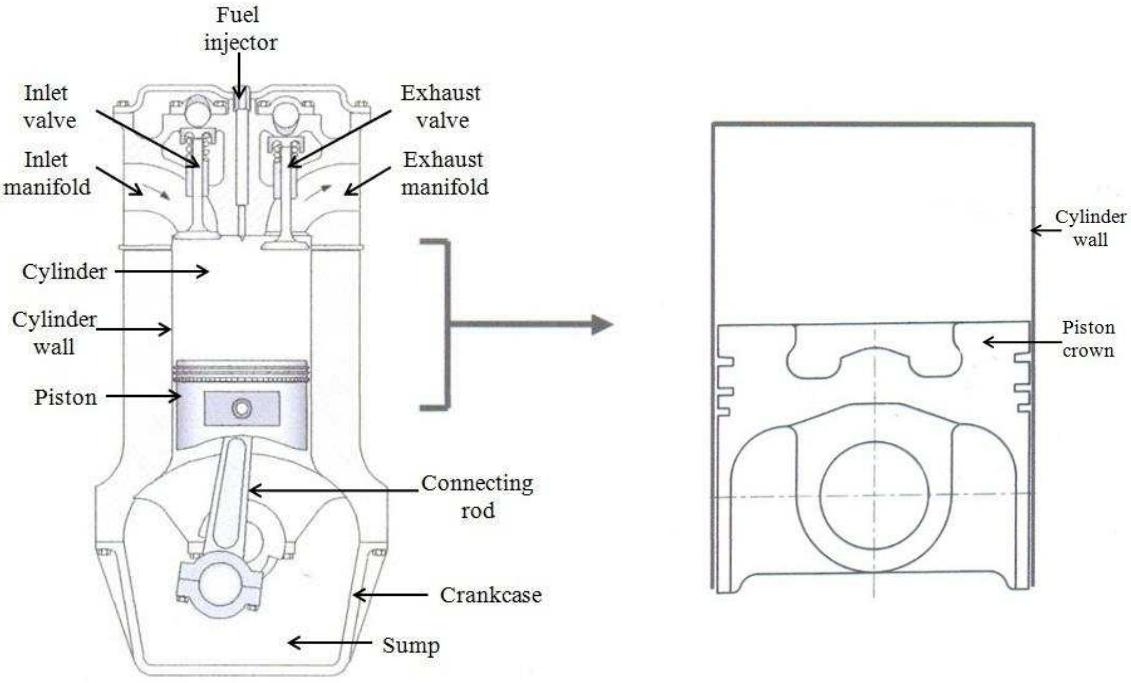

(a) Schematic of the engine (b) Piston crown configuration

Figure 3.2 Actual configuration of the direct injection combustion engine system (modified from [36])

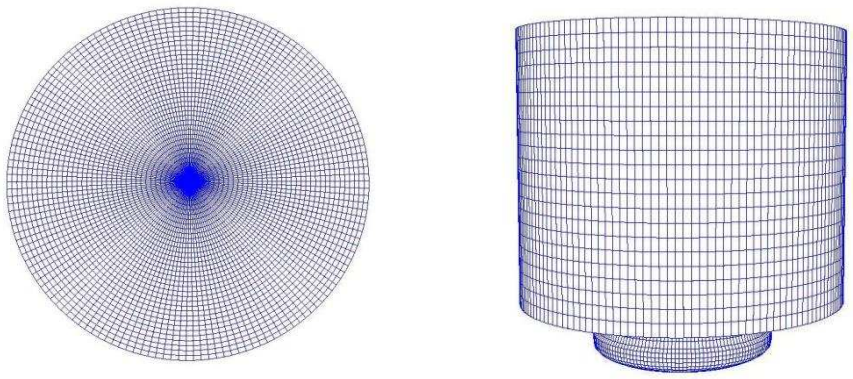

Figure 3.3 Mesh configuration of computational domain of the combustion chamber volume

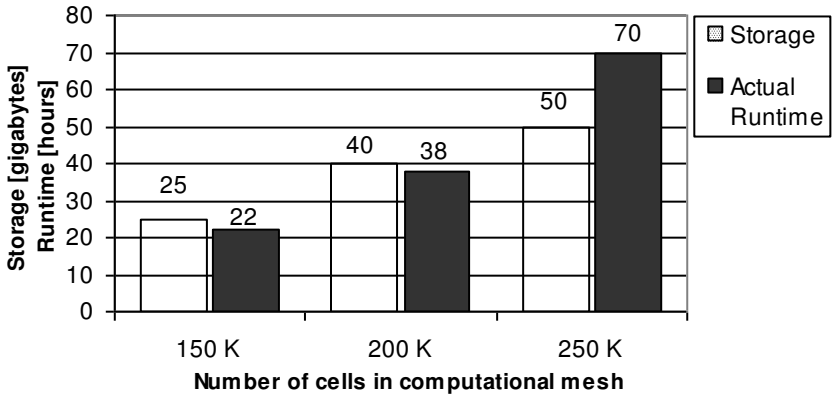

Figure 3.4 Storage and actual runtime of three different mesh at 0.25 CA time step

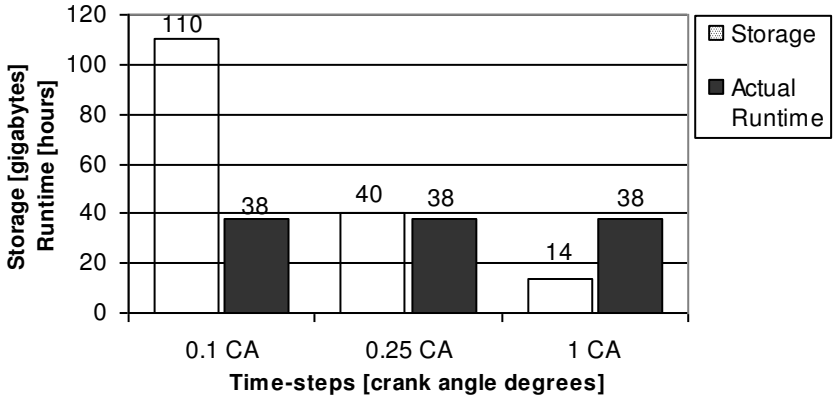

Figure 3.5 Storage and actual runtime of mesh of 200,000 cells with different time steps

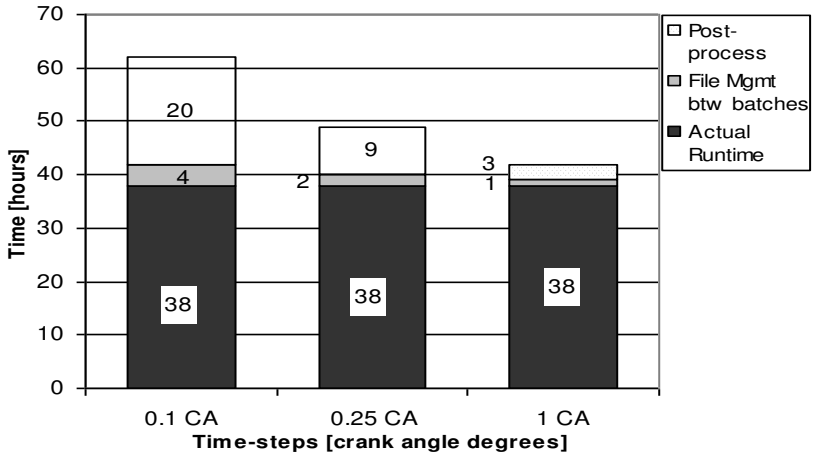

Figure 3.6 Simulation time requirement of mesh of 200,000 cells with different time steps

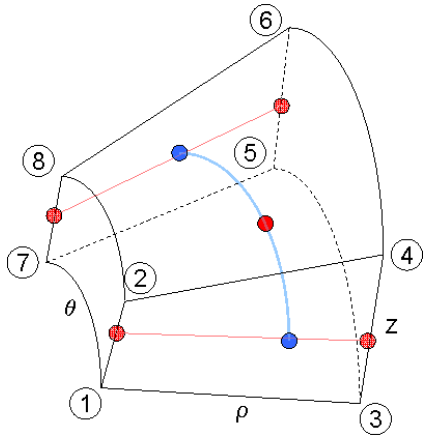

Figure 3.7 A typical cell used in Kiva3v simulation with points for trilinear interpolation

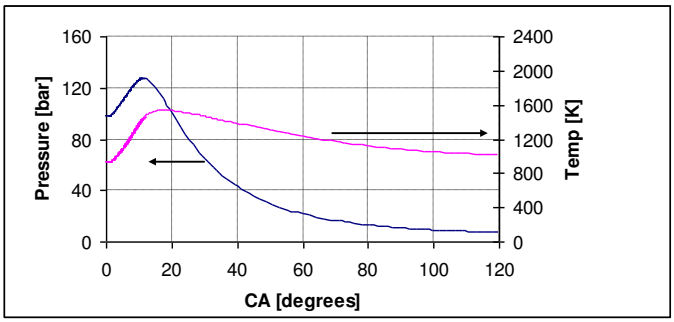

(a)

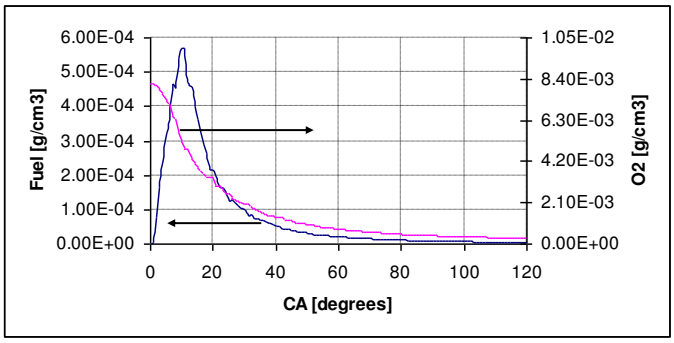

(b)

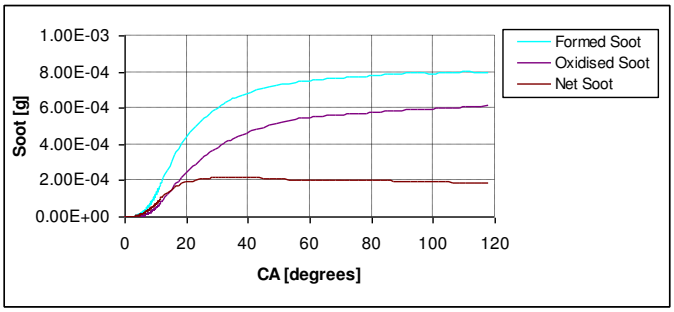

(c)

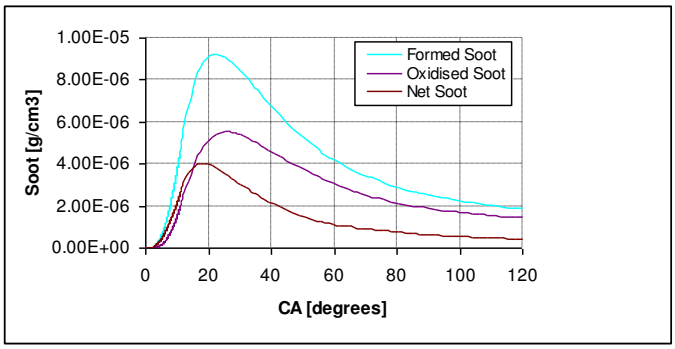

(d)

Figure 4.1 Global In-cylinder conditions : a) Temperature and pressure b) Fuel and oxygen concentration c) Cumulative soot mass d) Soot concentration

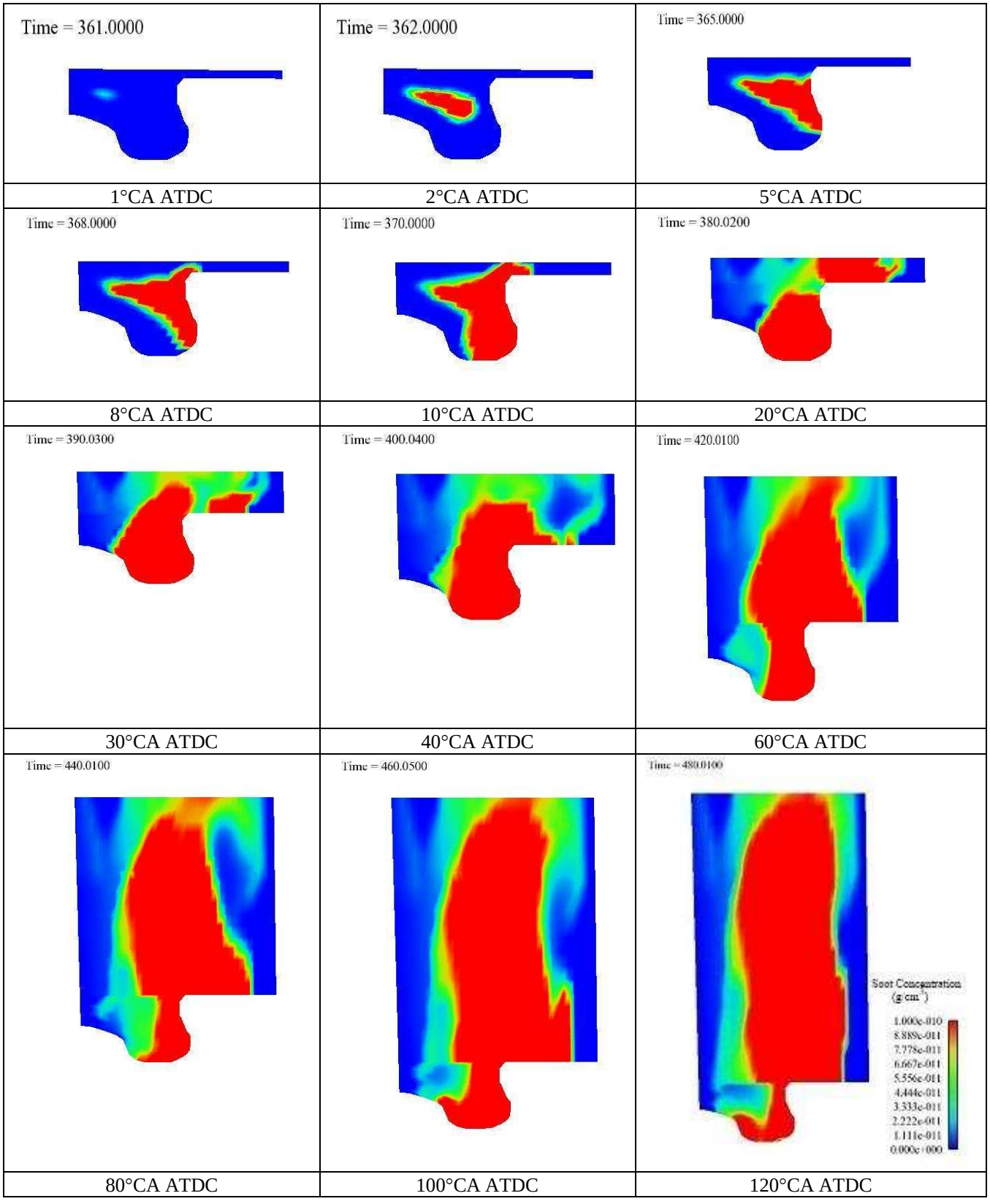

Figure 4.2 Development of in-cylinder soot distribution on a plane of a fuel jet axis as the cylinder volume expands from 1°CAATDC until EVO at 120°CA ATDC

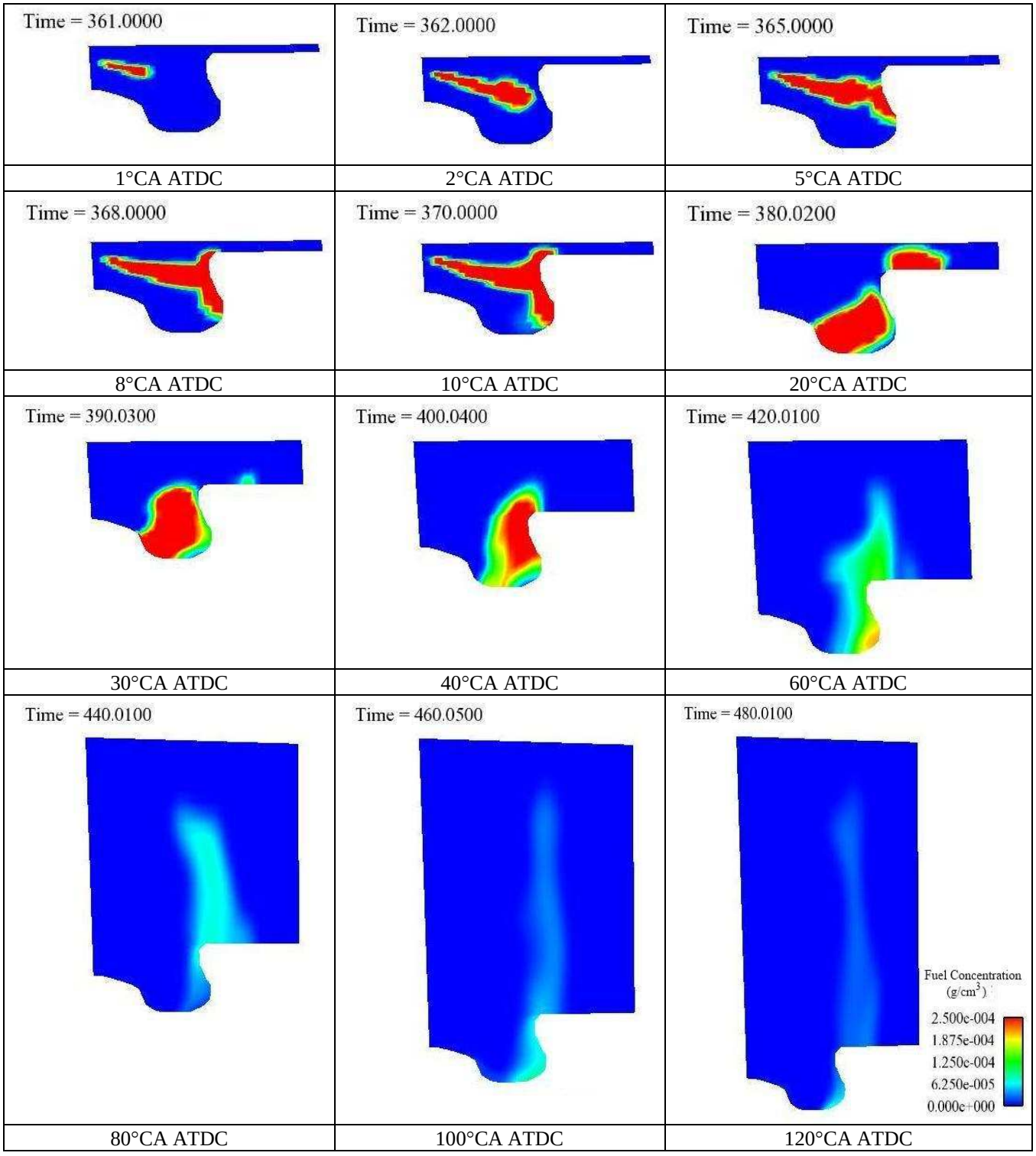

Figure 4.3 In-cylinder fuel distribution on a plane of a fuel jet axis as the cylinder volume expands from 1°CAATDC until EVO at 120°CA ATDC

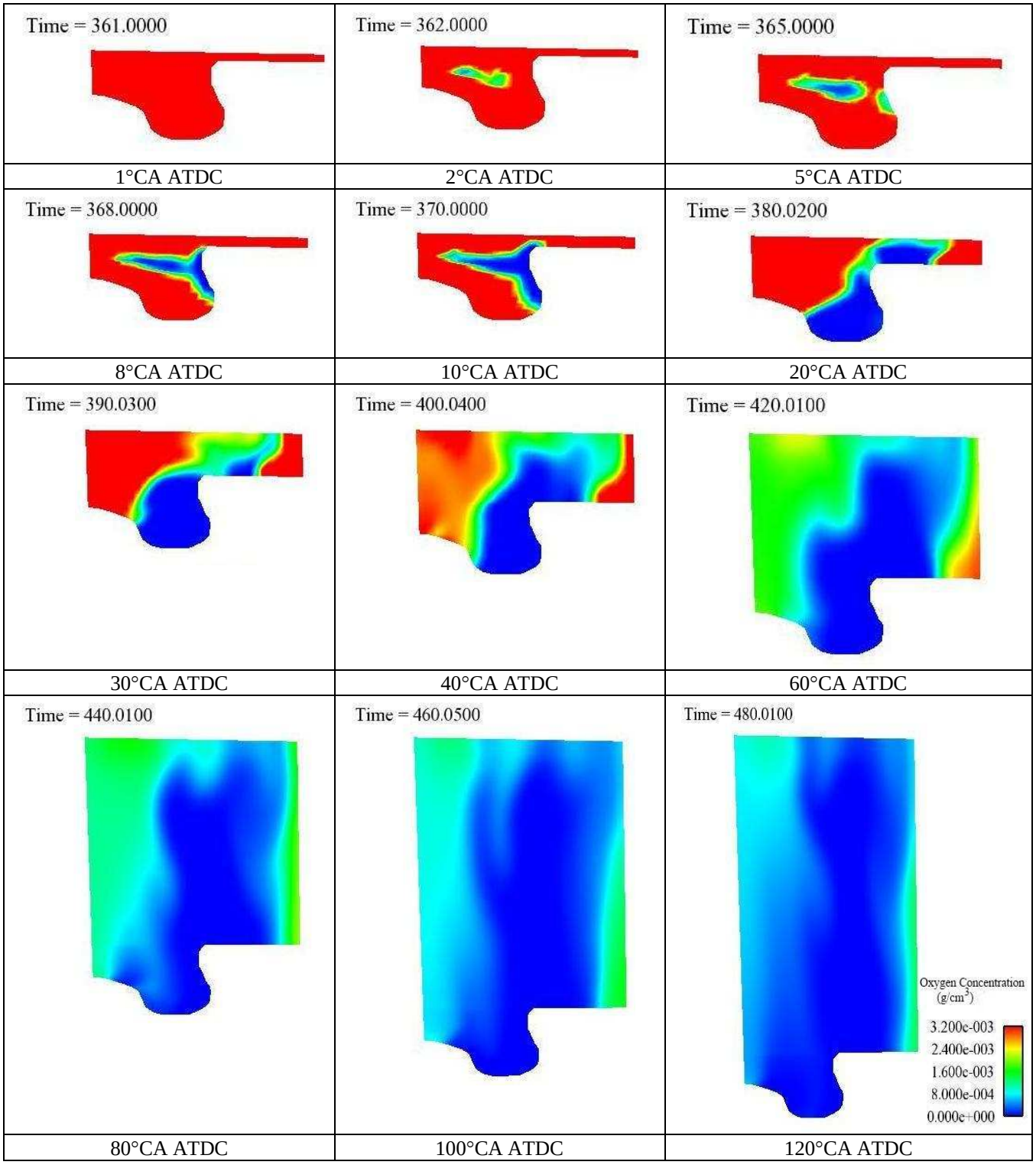

Figure 4.4 In-cylinder oxygen distribution on a plane of a fuel jet axis as the cylinder volume expands from 1°CAATDC until EVO at 120°CA ATDC

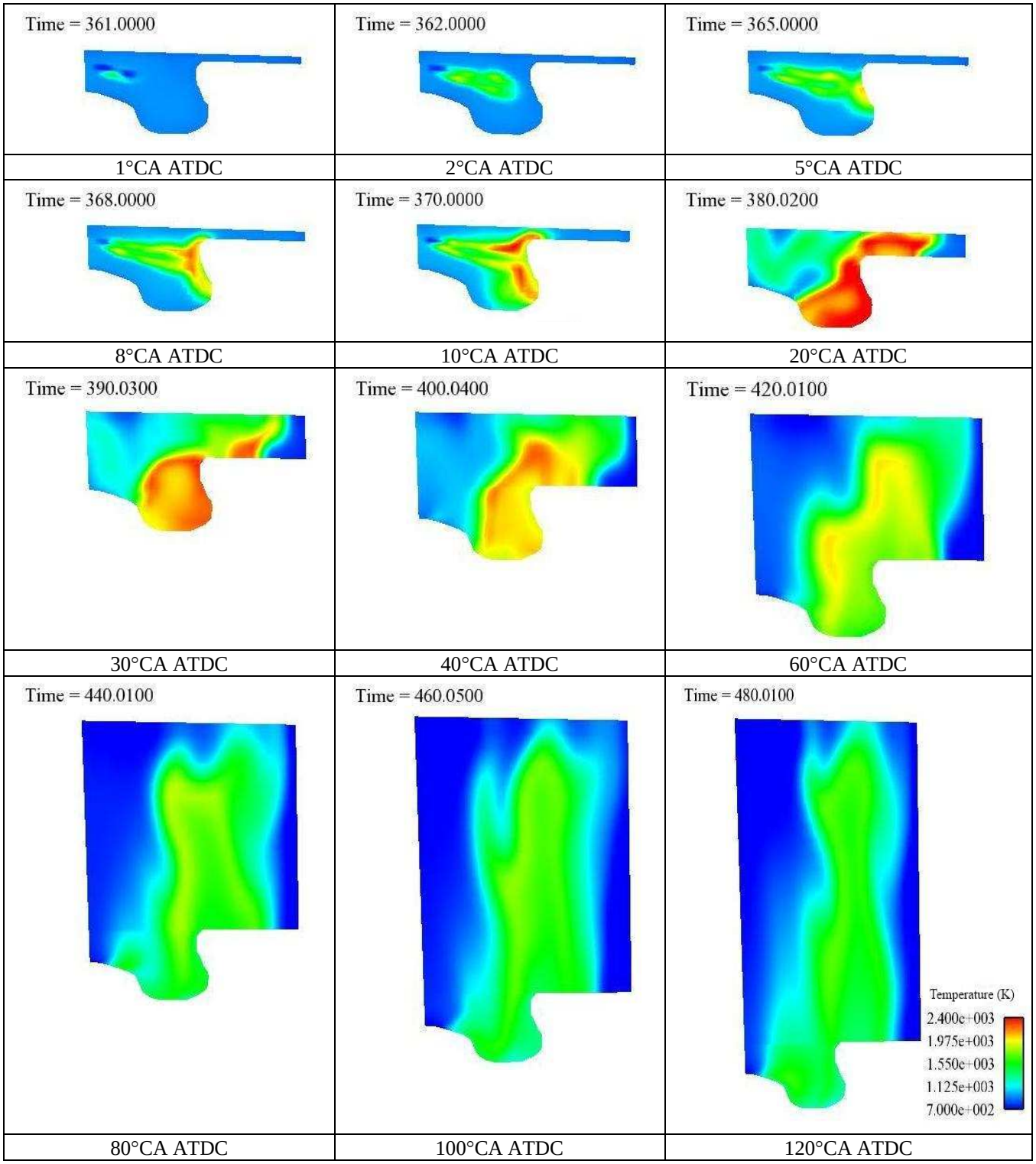

Figure 4.5 In-cylinder temperature distribution on a plane of a fuel jet axis as the cylinder volume expands from 1°CAATDC until EVO at 120°CA ATDC

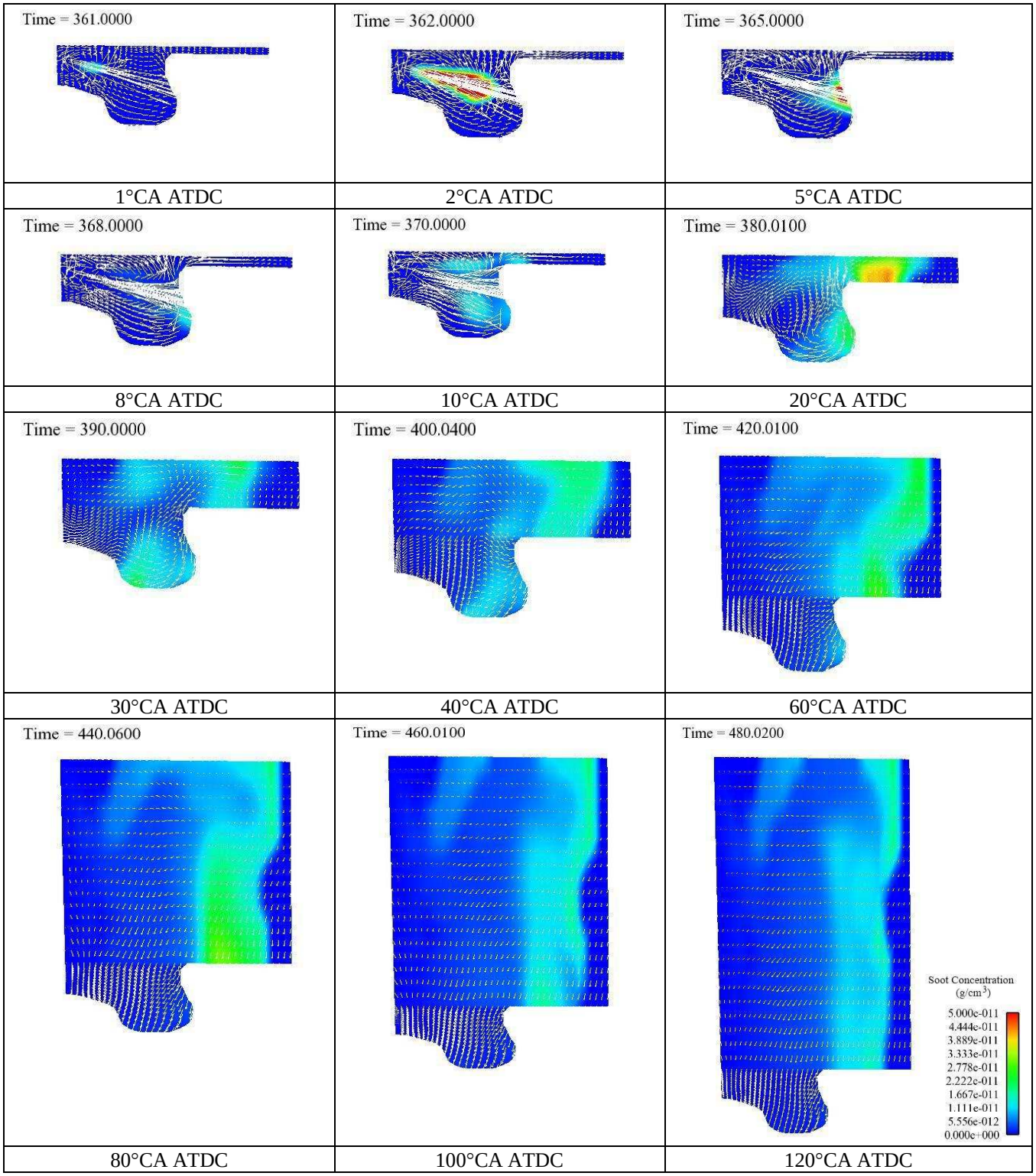

Figure 4.6 Development of in-cylinder soot formed before 2°CA ATDC and velocity vectors of fluid motion on a plane of a fuel jet axis as the cylinder volume expands from 1°CA ATDC until EVO at 120°CA ATDC

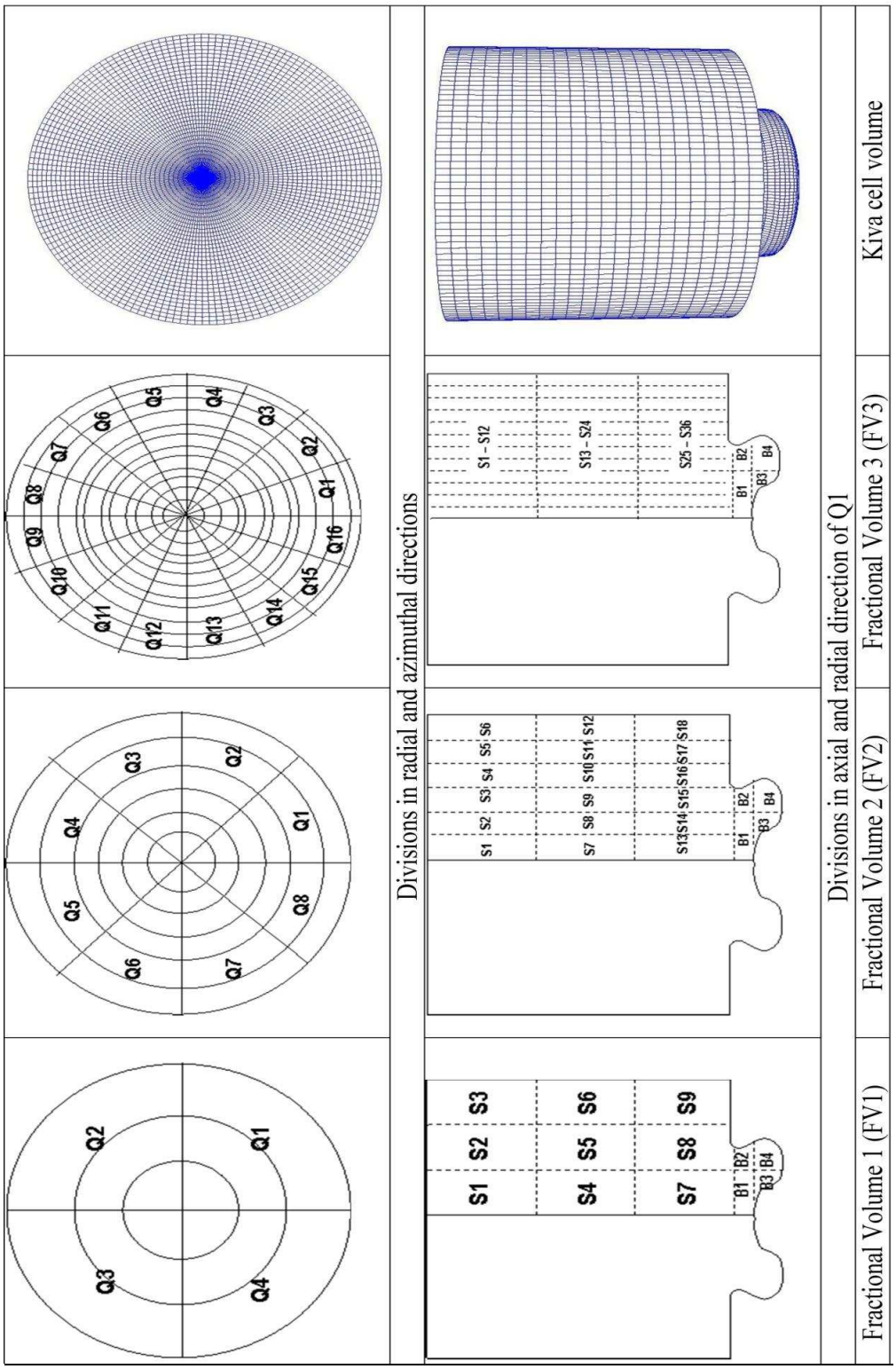

Figure 4.7 Schematic diagrams of three sets of cylinder volume with different size of fractional volumes in comparison with Kiva cells

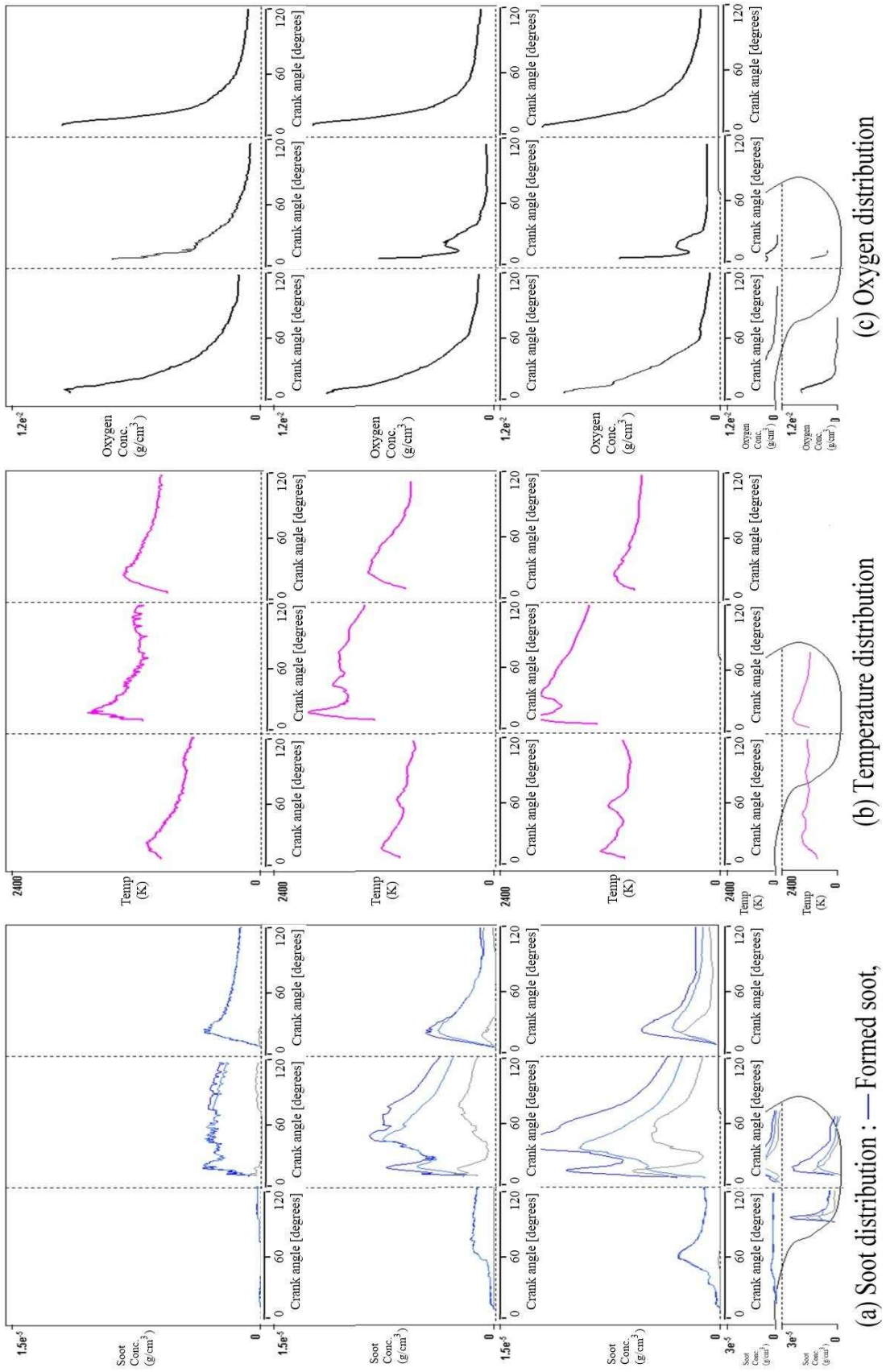

Figure 4.8 Temporal in-cylinder distributions of soot, temperature and oxygen from 8°CA ATDC to EVO at 120°CA ATDC of the first set of fractional volumes

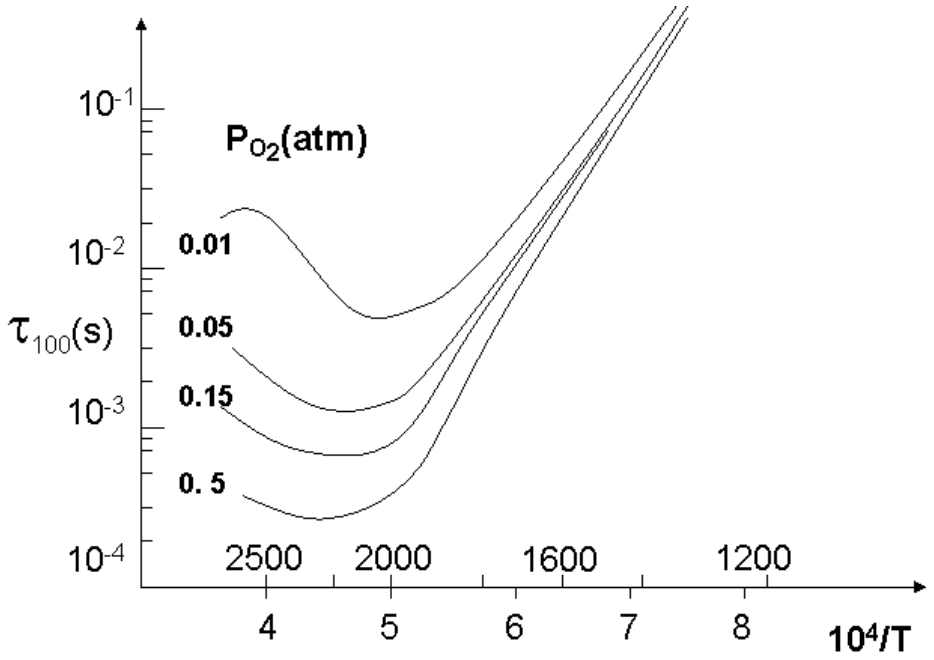

Figure 4.9 Burnout lifetime τ for a 100 Å diameter soot particle as a function of oxygen partial pressure and temperature (reproduced from [53])

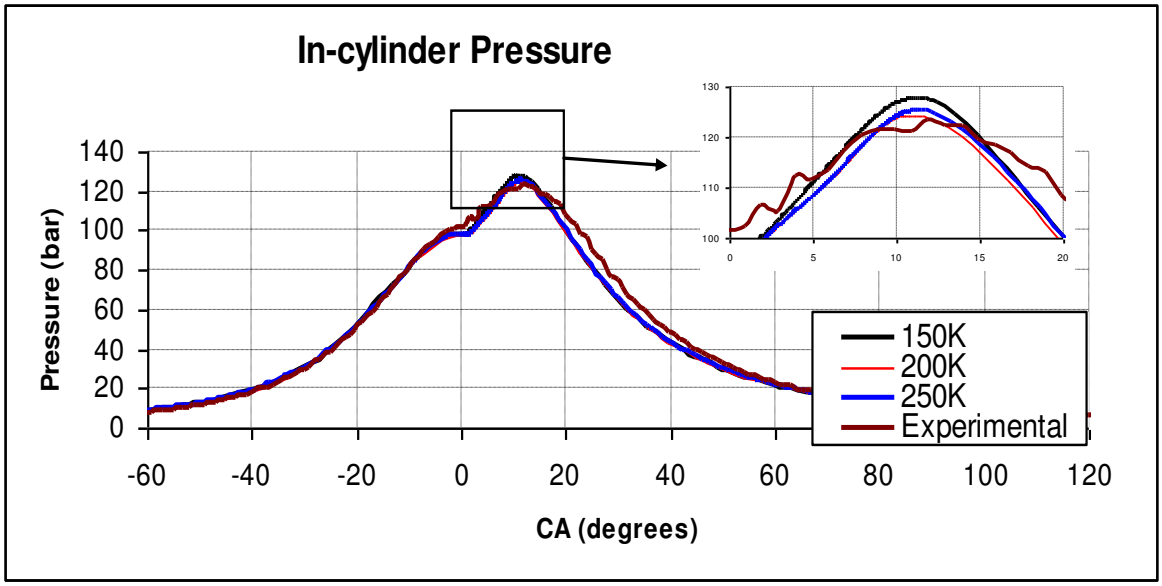

Figure 5.1 Average in-cylinder pressure of experimental and three mesh configurations

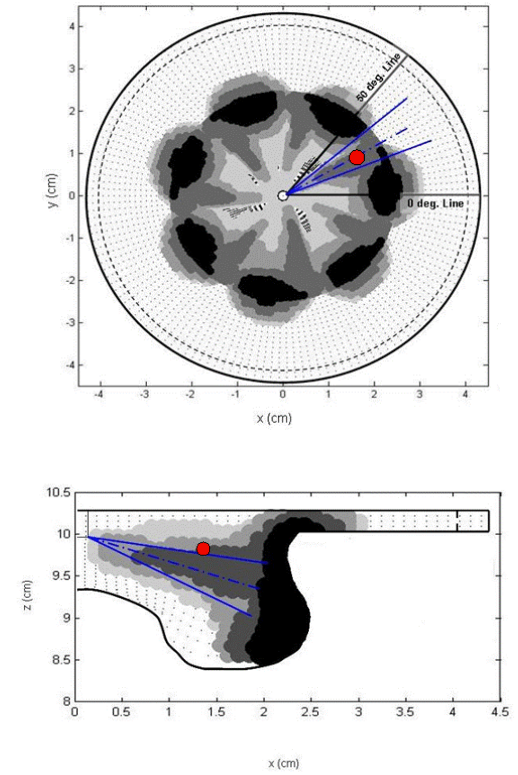

(a) Position of a fixed point relative to spray position and piston bowl at 8° CA ATDC

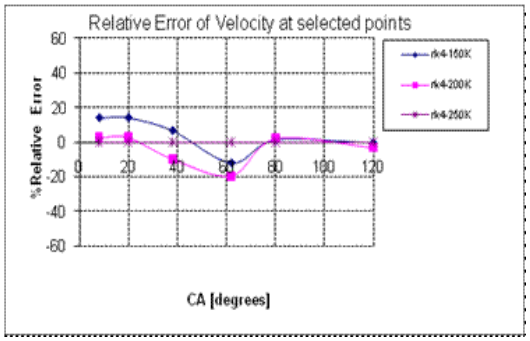

(b) Velocity relative error

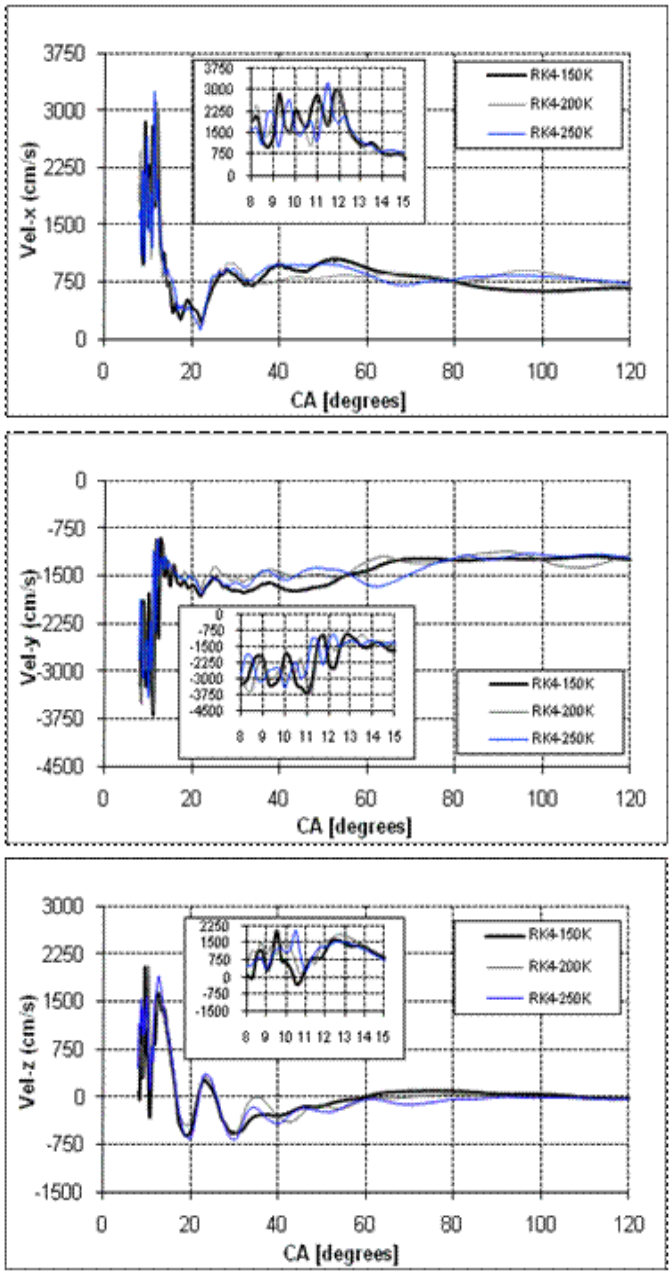

(c) Temporal velocity profiles at the fixed position

Figure 5.2 Comparison of crank-angle resolved velocity profiles and relative velocity error for three different mesh configurations of a fixed point above the spray axis (Radial distance: 1.4 cm, Angular position: 28°, Axial distance: 9.85 cm)

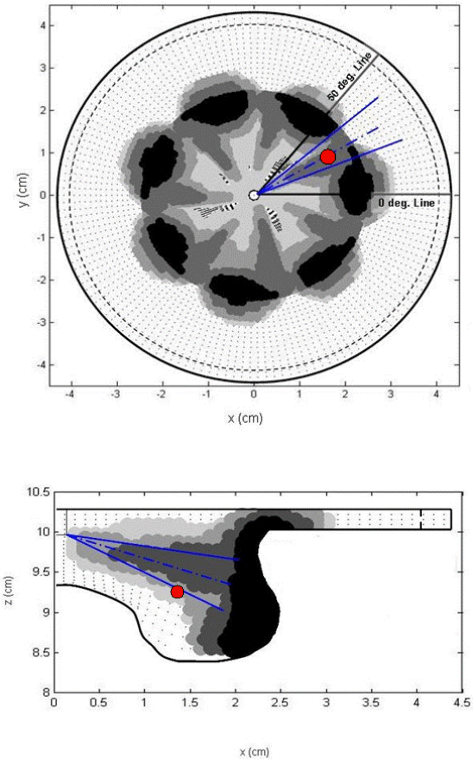

(a) Position of a fixed point relative to spray position and piston bowl at 8° CA ATDC

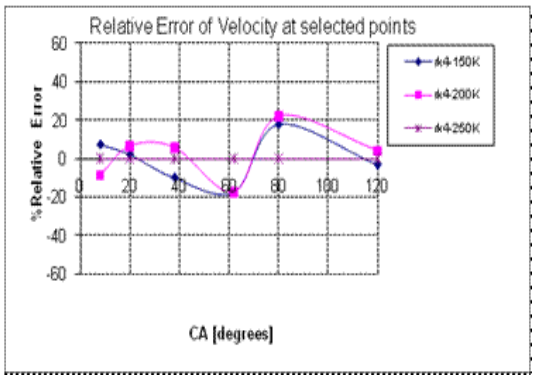

(b) Velocity relative error

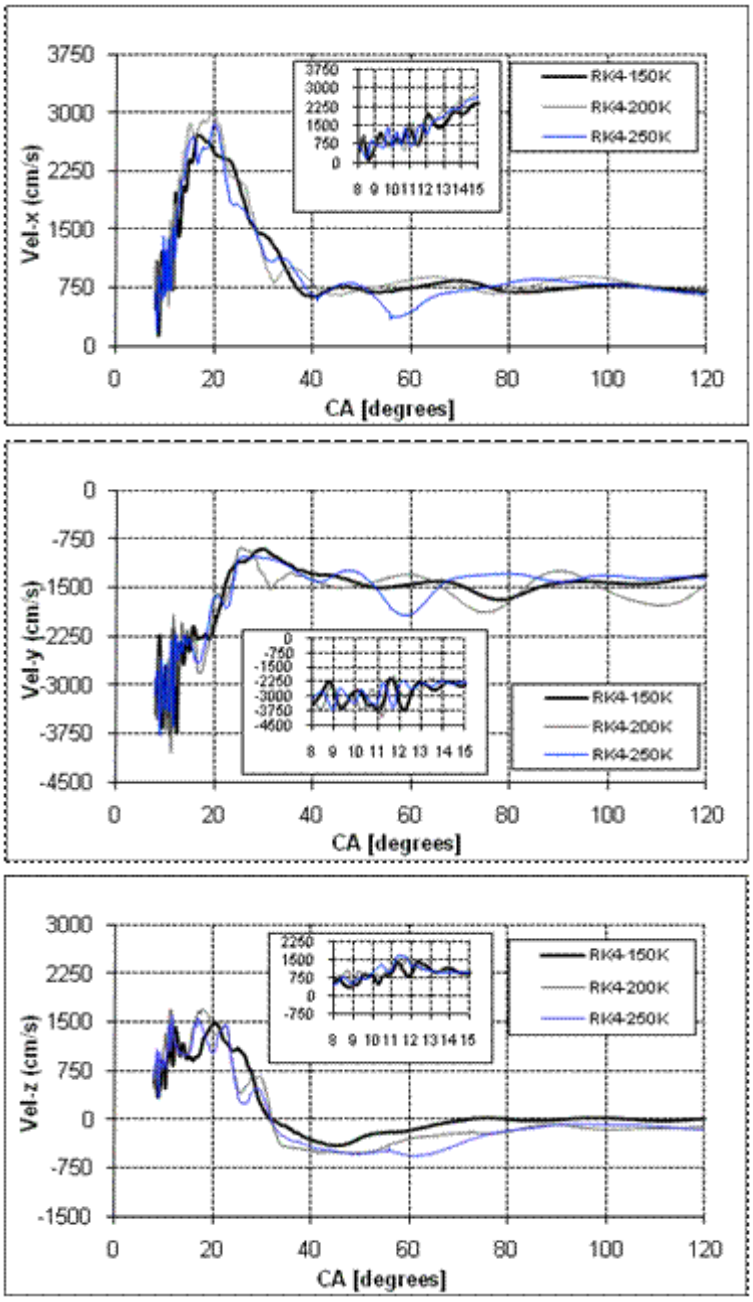

(c) Temporal velocity profiles at the fixed position

Figure 5.3 Comparison of crank-angle resolved velocity profiles and relative velocity error for three different mesh configurations of a fixed point below the spray axis (Radial distance: 1.45 cm, Angular position: 28°, Axial distance: 9.1 cm)

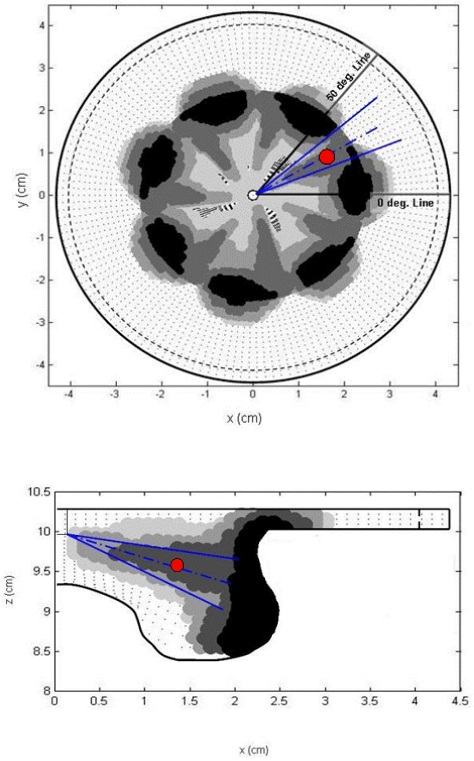

(a) Position of a fixed point relative to spray position and piston bowl at 8° CA ATDC

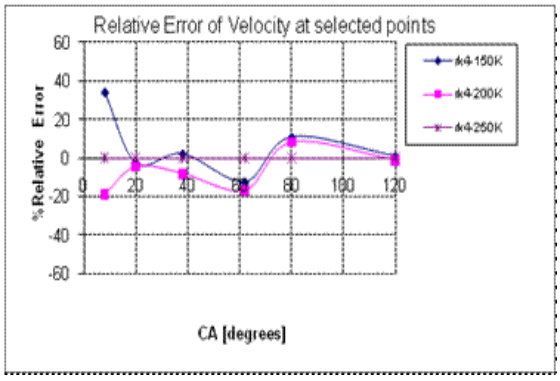

(b) Velocity relative error

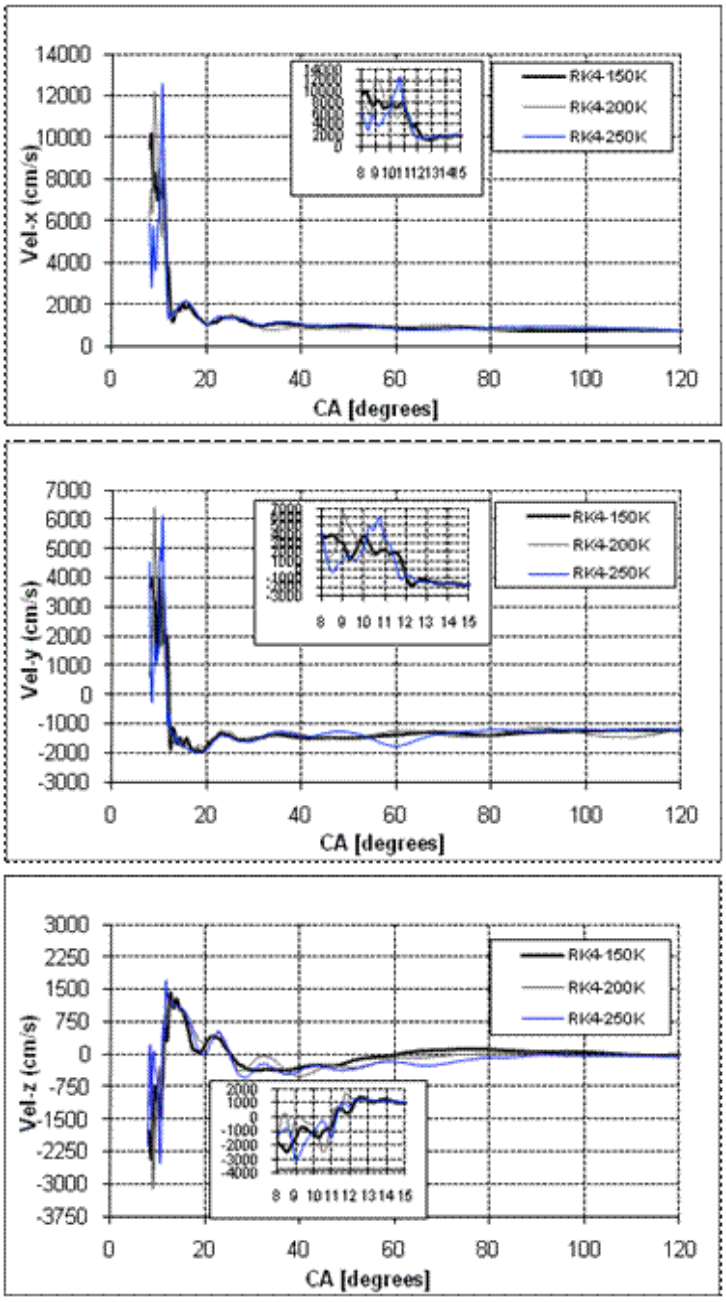

(c) Temporal velocity profiles at the fixed position

Figure 5.4 Comparison of crank-angle resolved velocity profiles and relative velocity error for three different mesh configurations of a fixed point on the spray axis (Radial distance: 1.4 cm, Angular position: 30°, Axial distance: 9.55 cm)

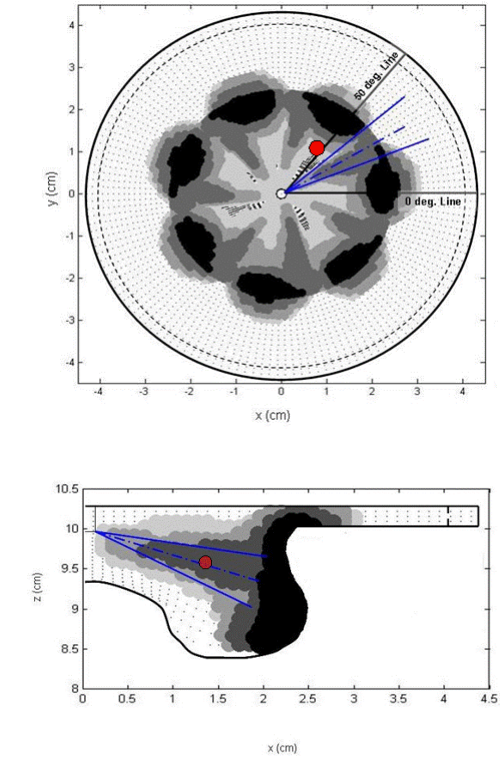

(a) Position of a fixed point relative to spray position and piston bowl at 8° CA ATDC

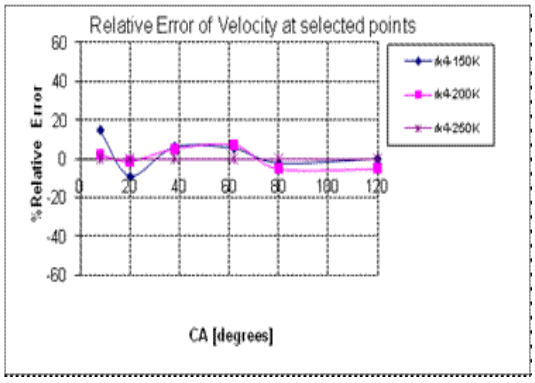

(b) Velocity relative error

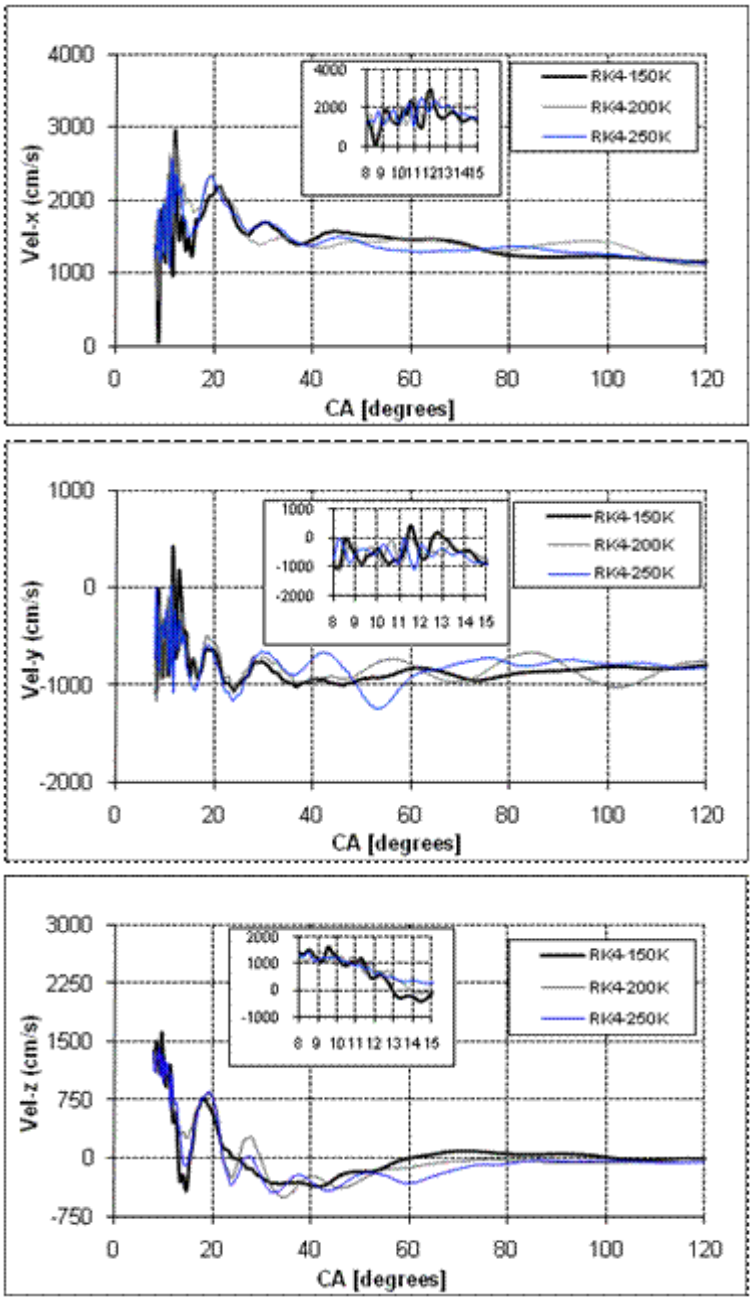

(c) Temporal velocity profiles at the fixed position

Figure 5.5 Comparison of crank-angle resolved velocity profiles and relative velocity error for three different mesh configurations of a fixed point between two sprays (Radial distance: 1.4 cm, Angular position: 55°, Axial distance: 9.55 cm)

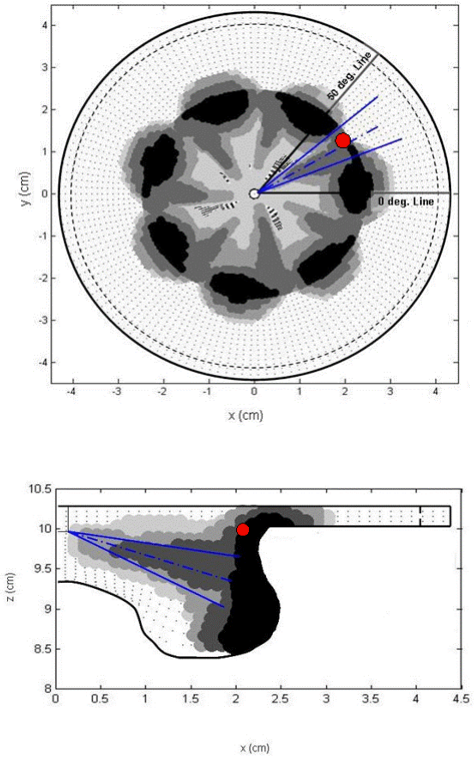

(a) Position of a fixed point relative to spray position and piston bowl at 8° CA ATDC

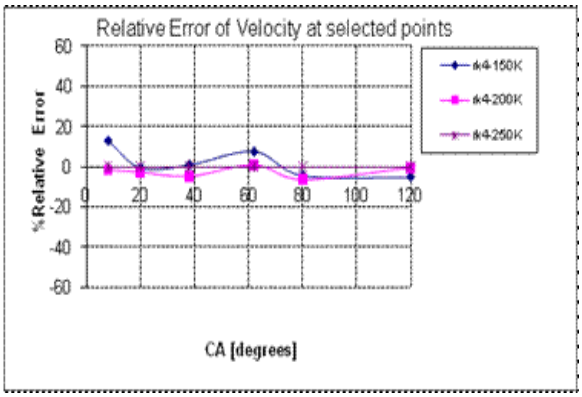

(b) Velocity relative error

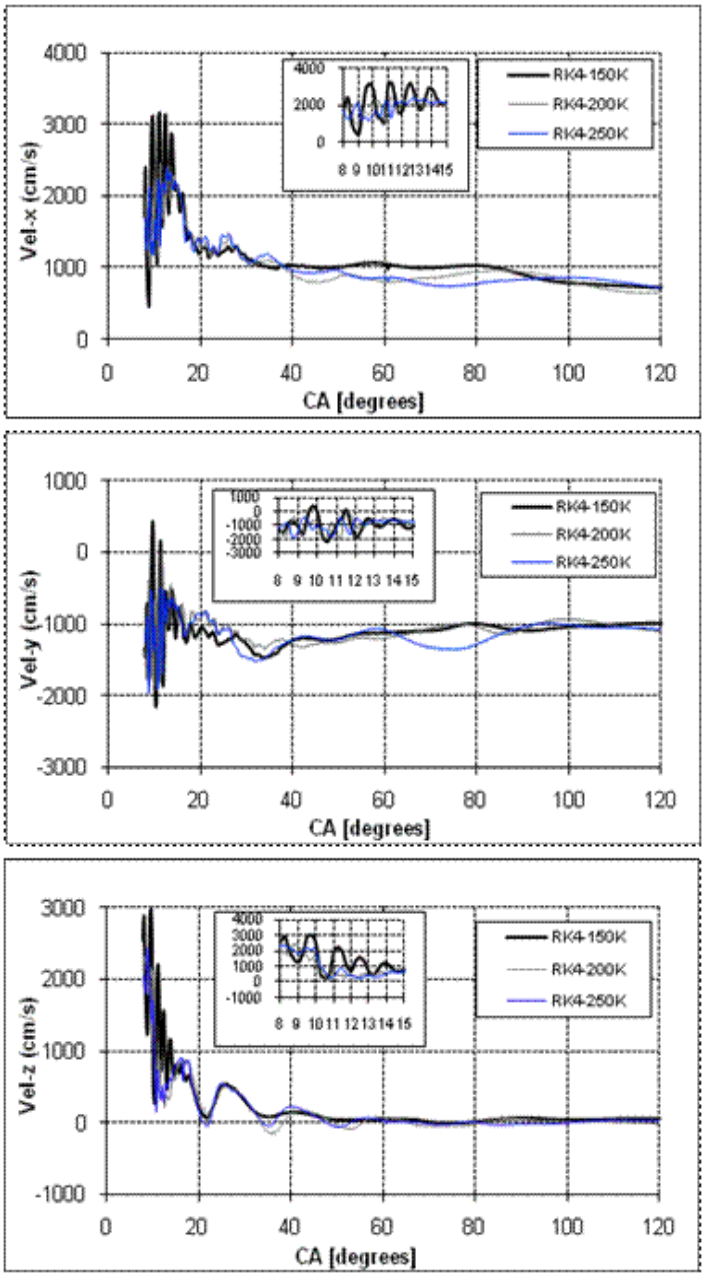

(c) Temporal velocity profiles at the fixed position

Figure 5.6 Comparison of crank-angle resolved velocity profiles and relative velocity error for three different mesh configurations of a fixed point near bowl rim (Radial distance: 2.1 cm, Angular position: 30°, Axial distance: 10.0 cm)

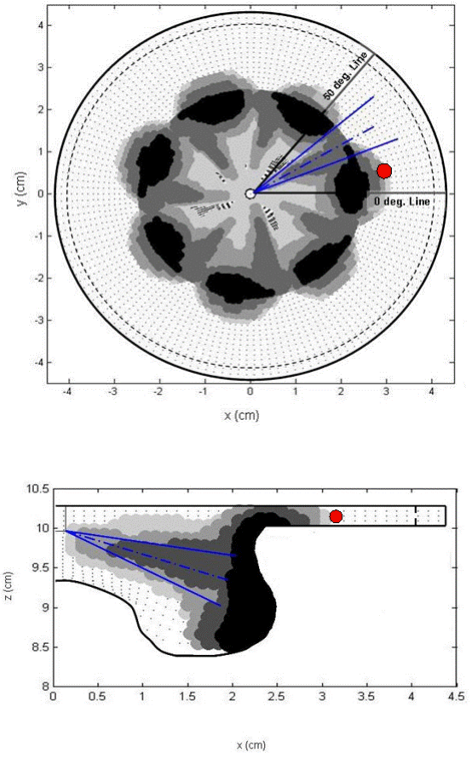

(a) Position of a fixed point relative to spray position and piston bowl at 8° CA ATDC

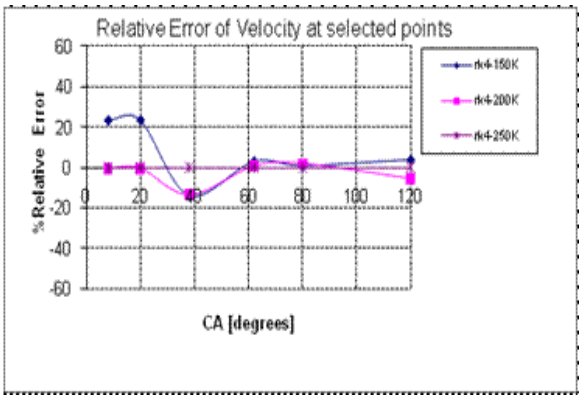

(b) Velocity relative error

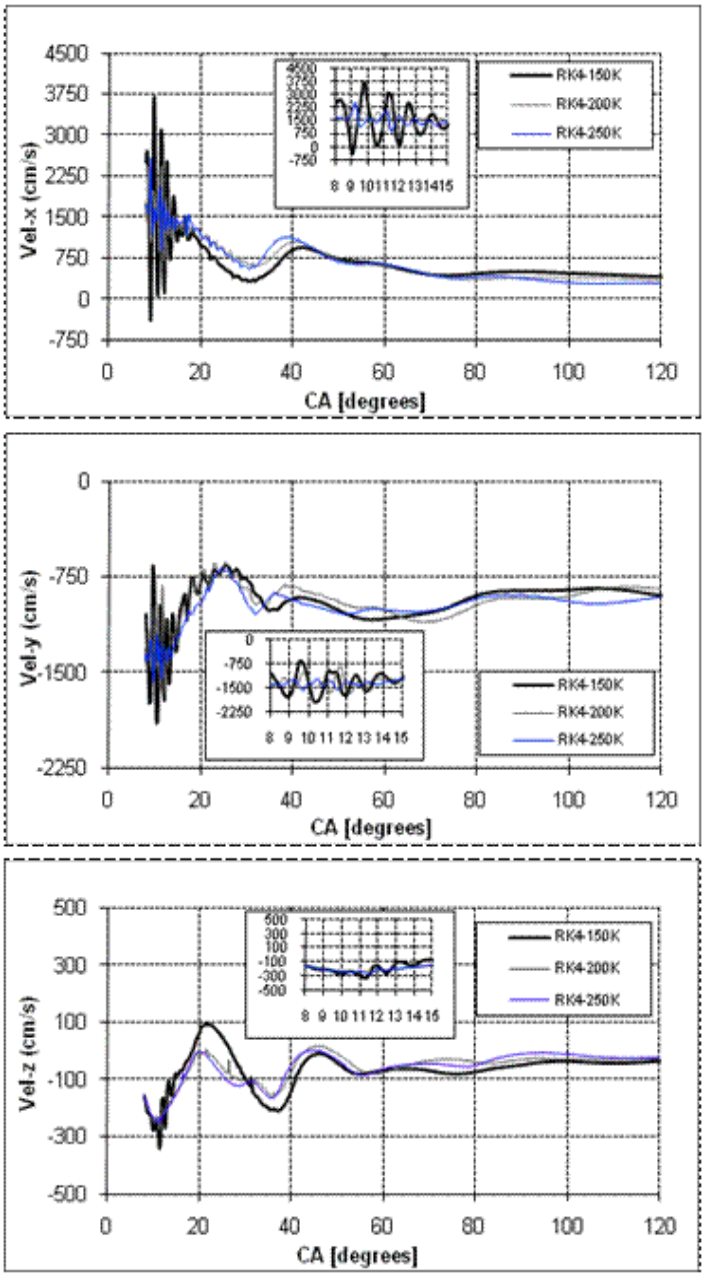

(c) Temporal velocity profiles at the fixed position

Figure 5.7 Comparison of crank-angle resolved velocity profiles and relative velocity error for three different mesh configurations of a fixed point in the middle of squish region (Radial distance: 3.4 cm, Angular position: 10°, Axial distance: 10.1 cm)

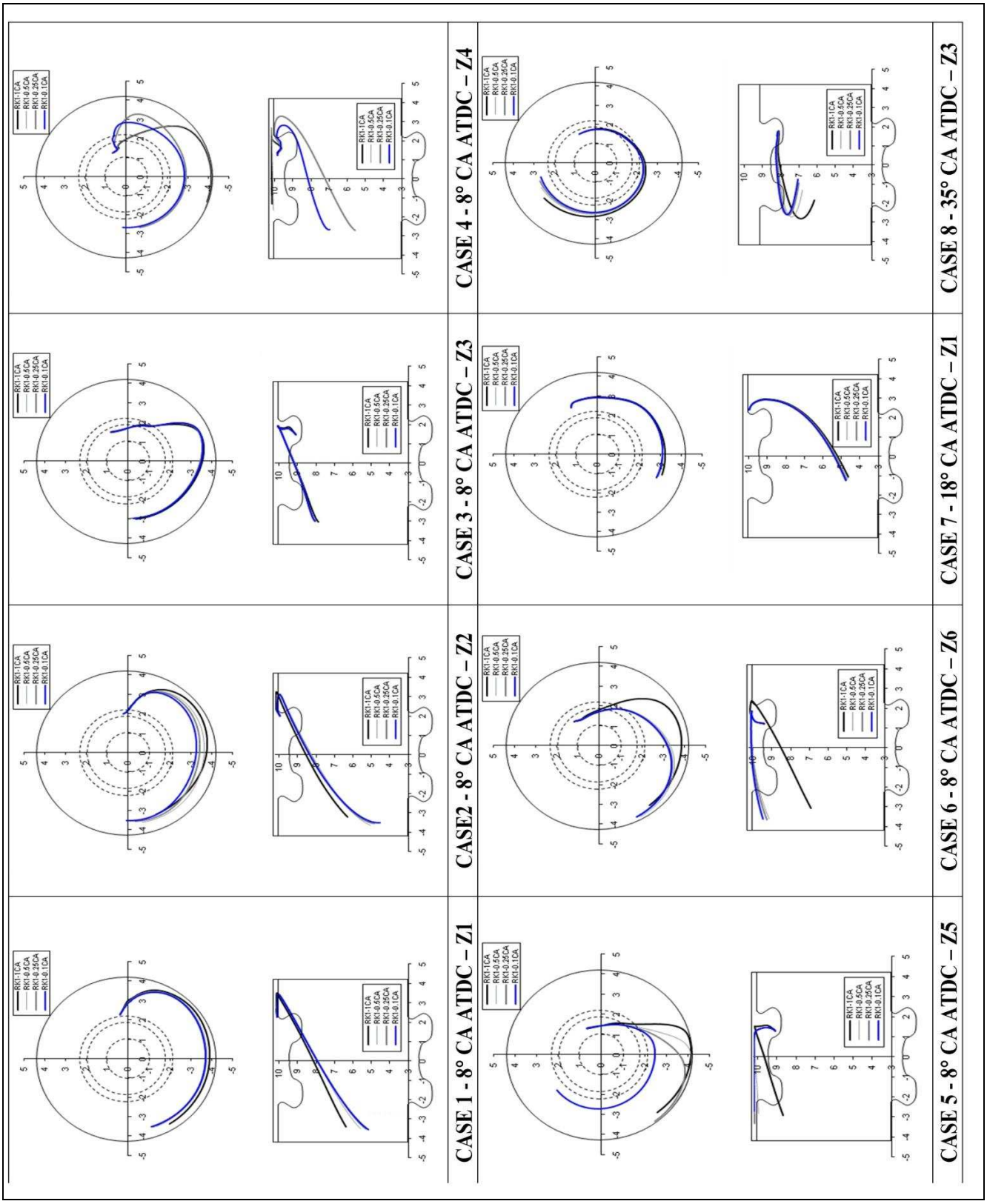

Figure 5.8 Predicted soot paths with different time steps using first-order RK method (Euler's method)

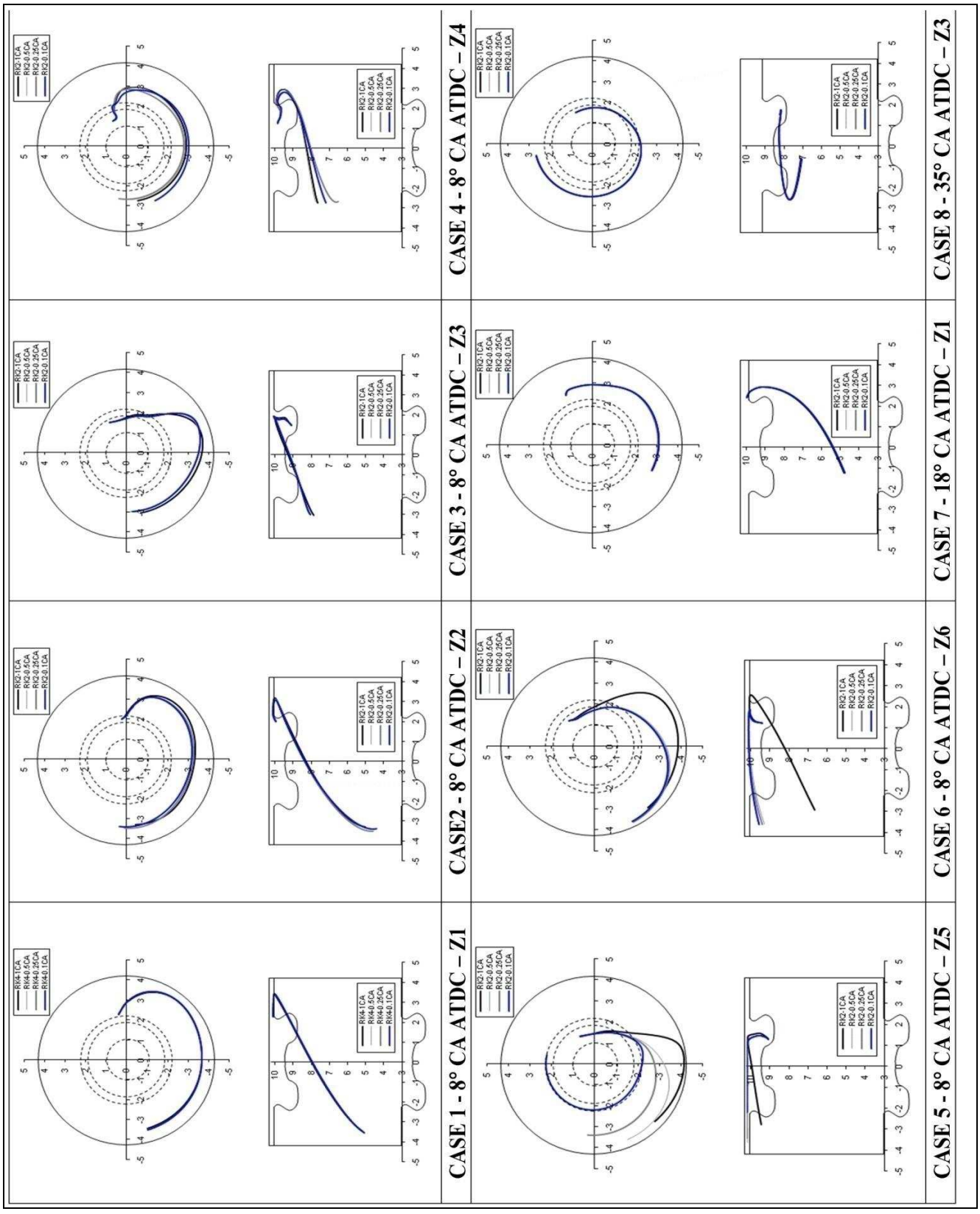

Figure 5.9 Predicted soot paths with different time steps using second-order RK method (Heun's method)

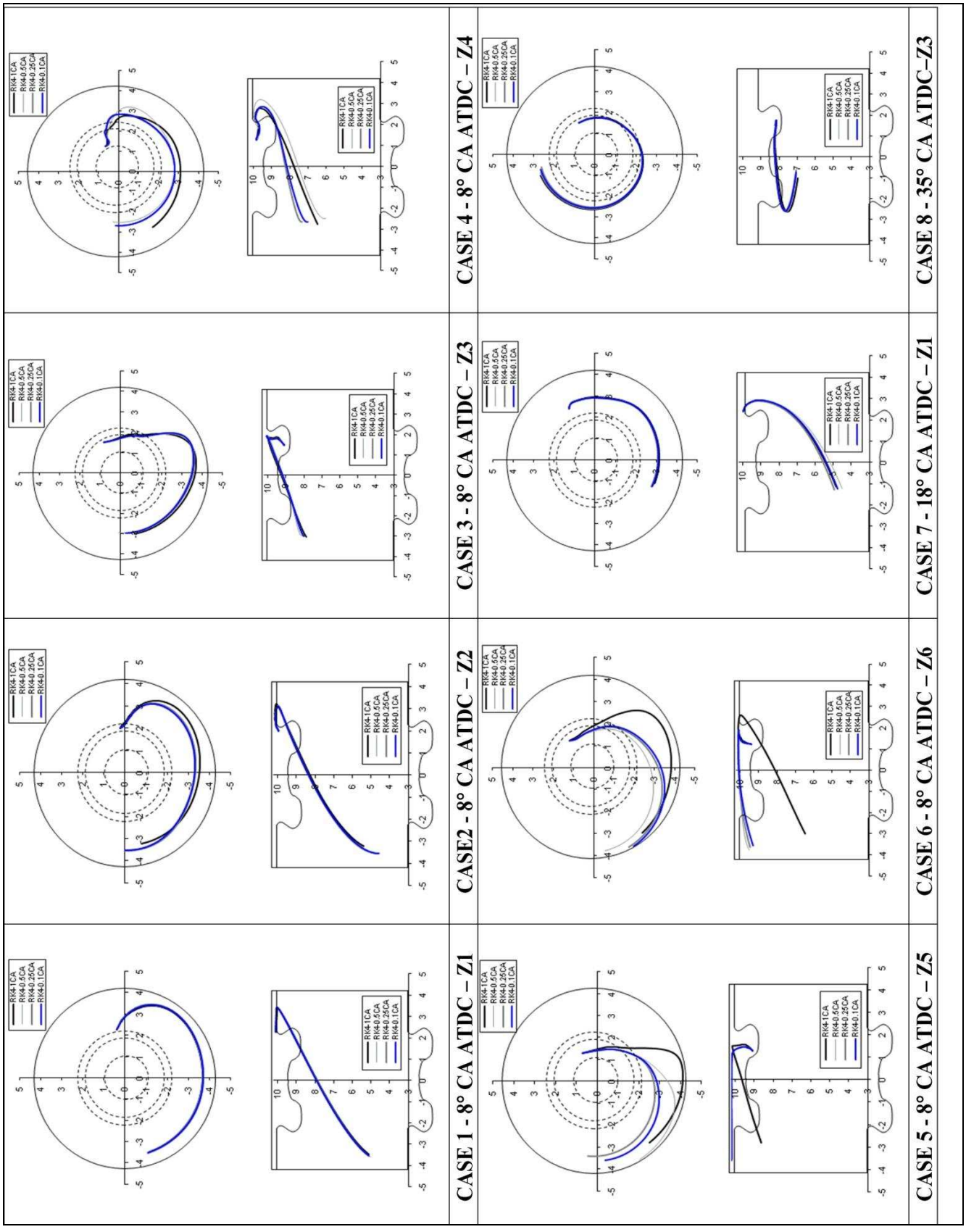

Figure 5.10 Predicted soot paths with different time steps using classical fourth-order RK method (RK4)

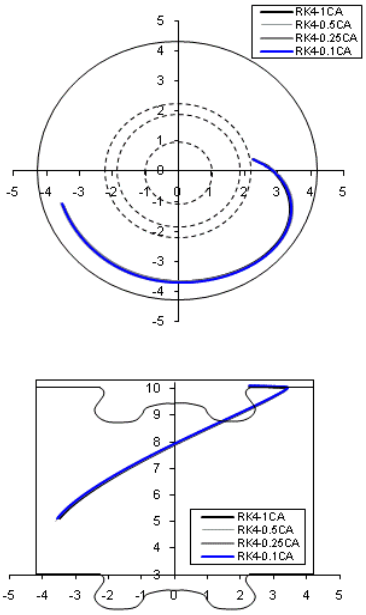

(a) Particle paths

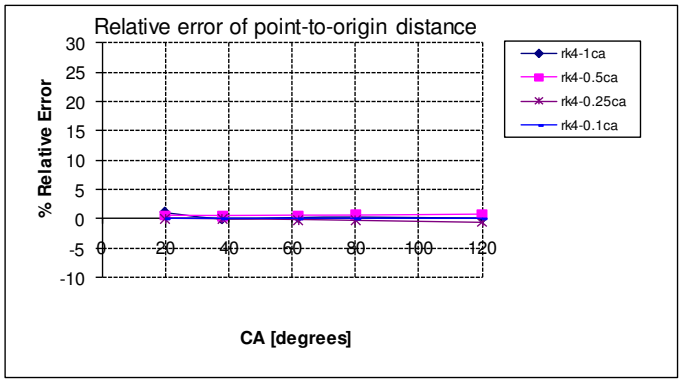

(b) Relative error of distance of selected points in the paths to origin

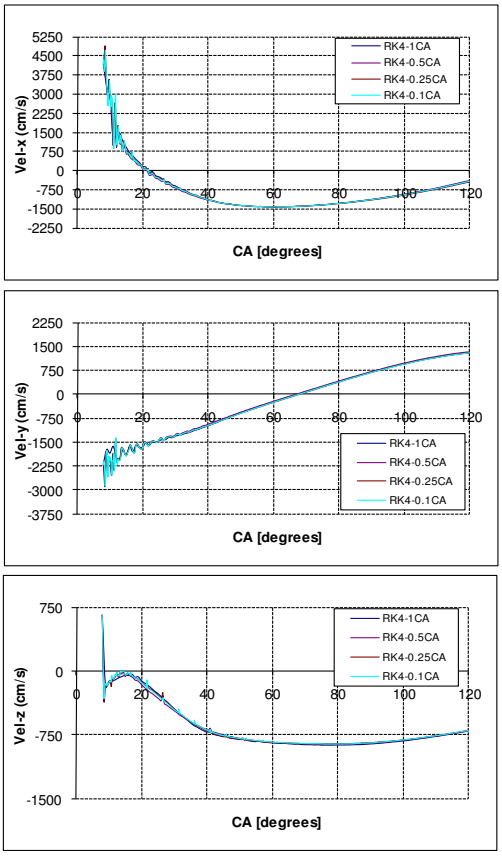

(c) Velocity profile along paths

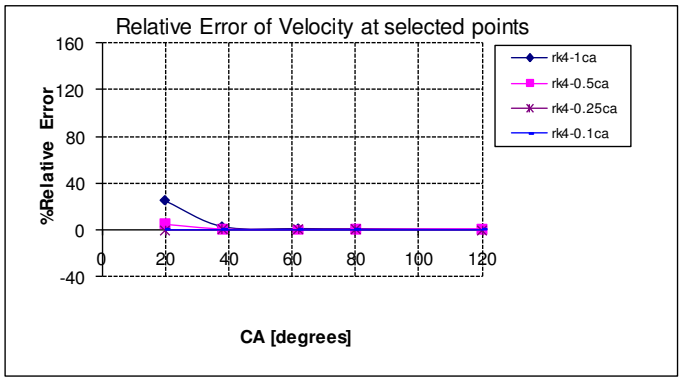

(d) Relative error of point-to-point velocities

Figure 5.11 Convergence criteria for Case 1

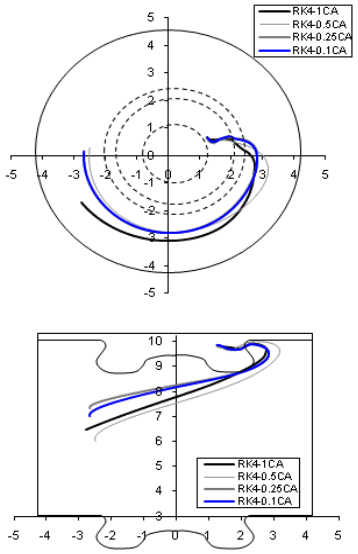

(a) Particle paths

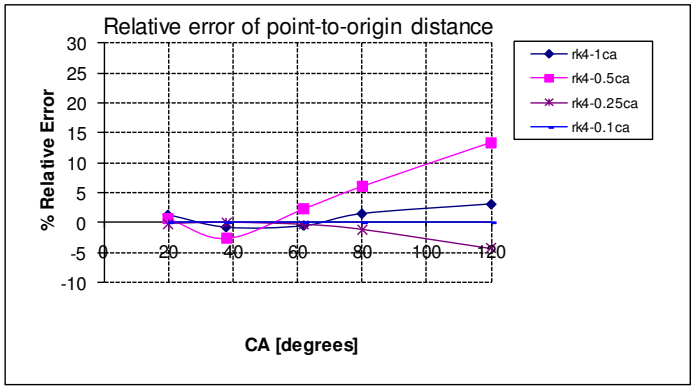

(b) Relative error of distance of selected points in the paths to origin

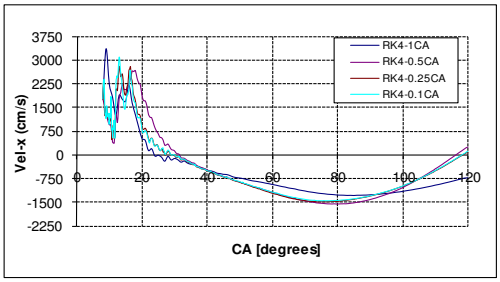

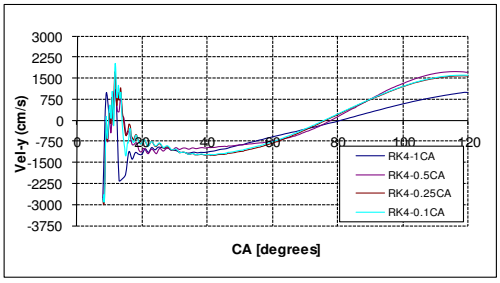

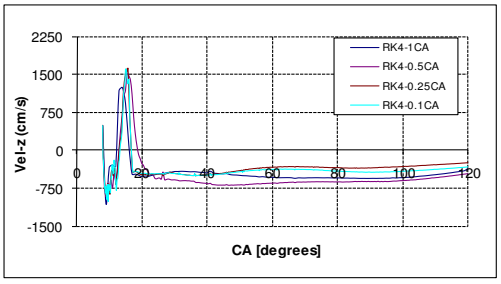

(c) Velocity profile along paths

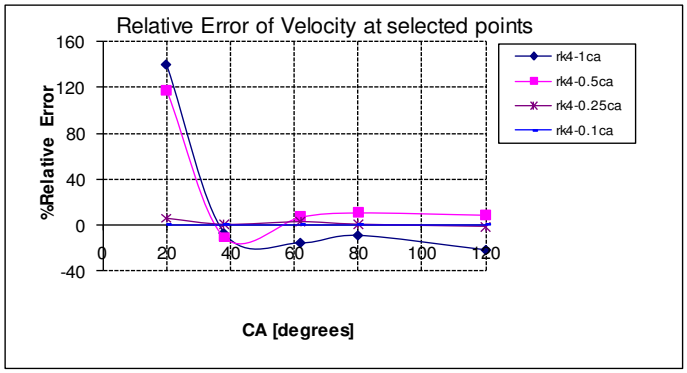

(d) Relative error of point-to-point velocities

Figure 5.12 Convergence criteria for Case 4

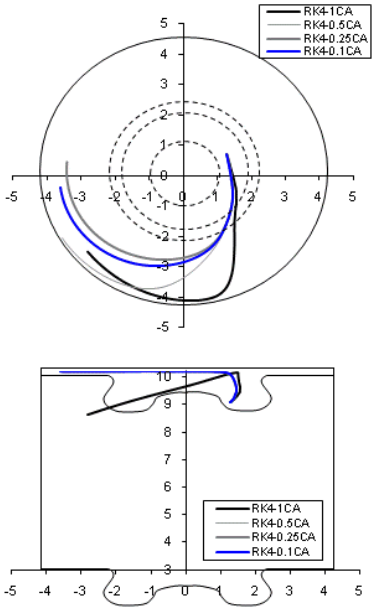

(a) Particle paths

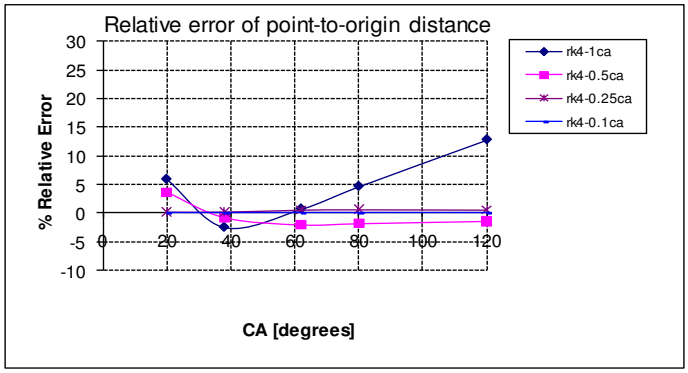

(b) Relative error of distance of selected points in the paths to origin

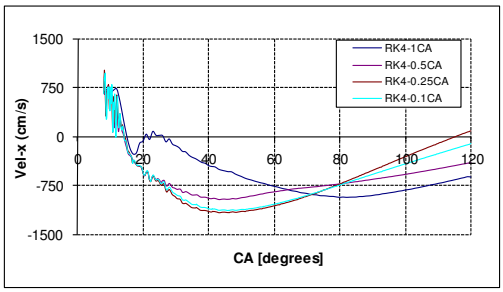

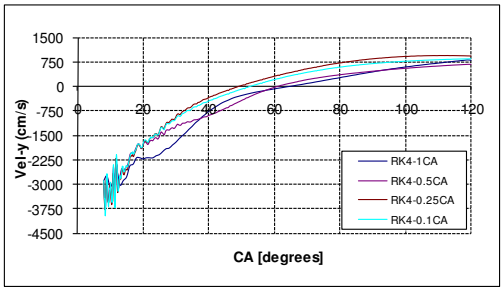

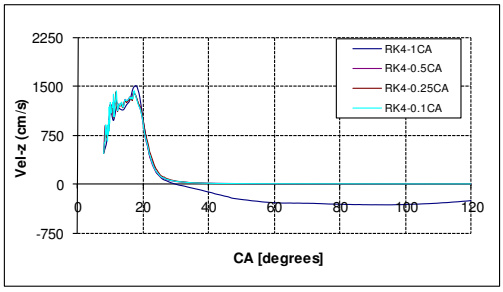

(c) Velocity profile along paths

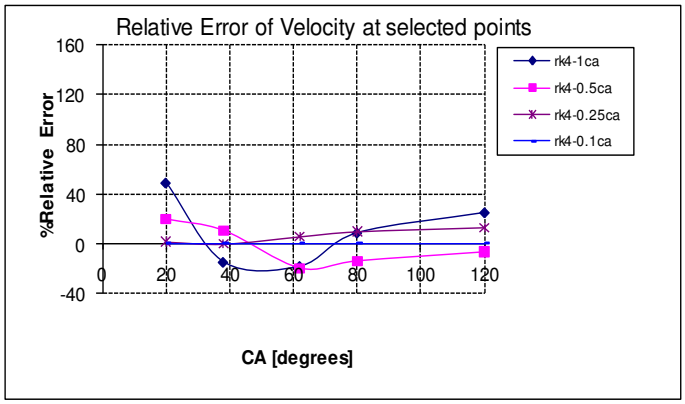

(d) Relative error of point-to-point velocities

Figure 5.13 Convergence criteria for Case 5

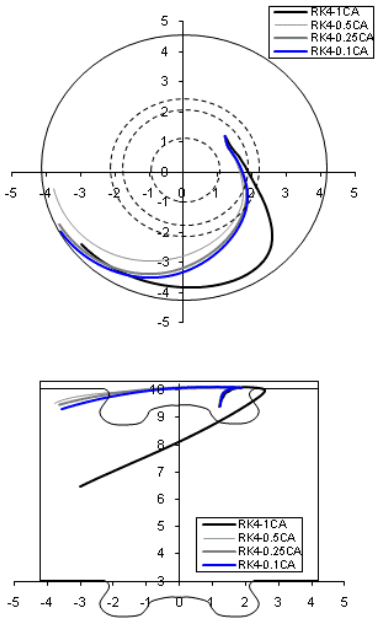

(a) Particle paths

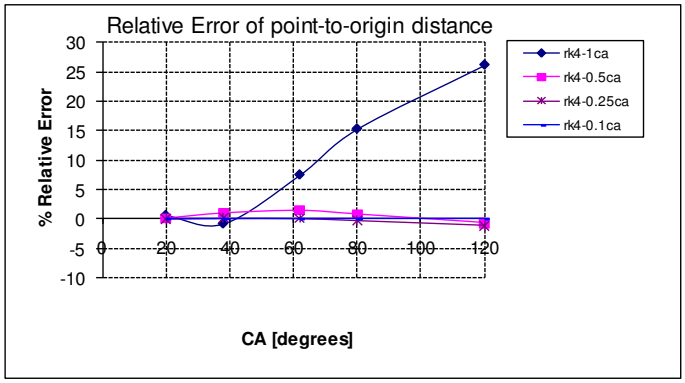

(b) Relative error of distance of selected points in the paths to origin

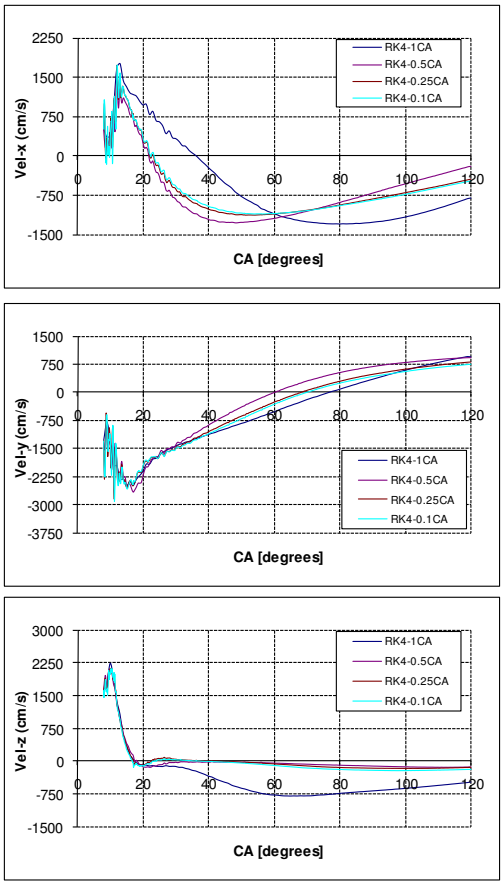

(c) Velocity profile along paths

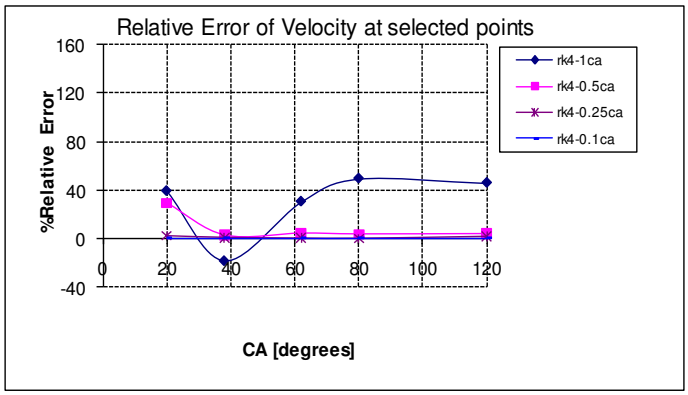

(d) Relative error of point-to-point velocities

Figure 5.14 Convergence criteria for Case 6

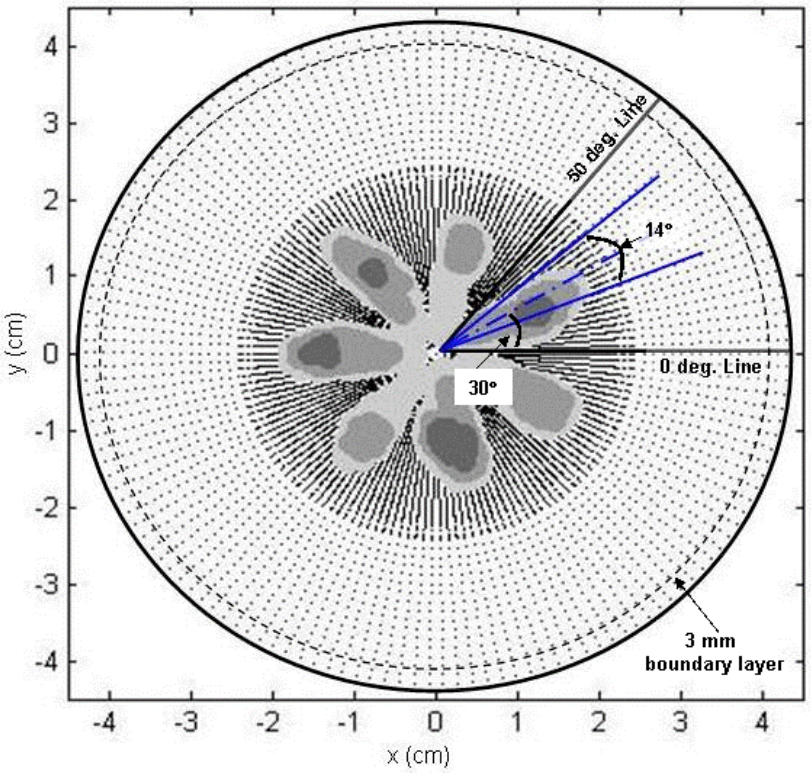

(a) Top view of the cylinder

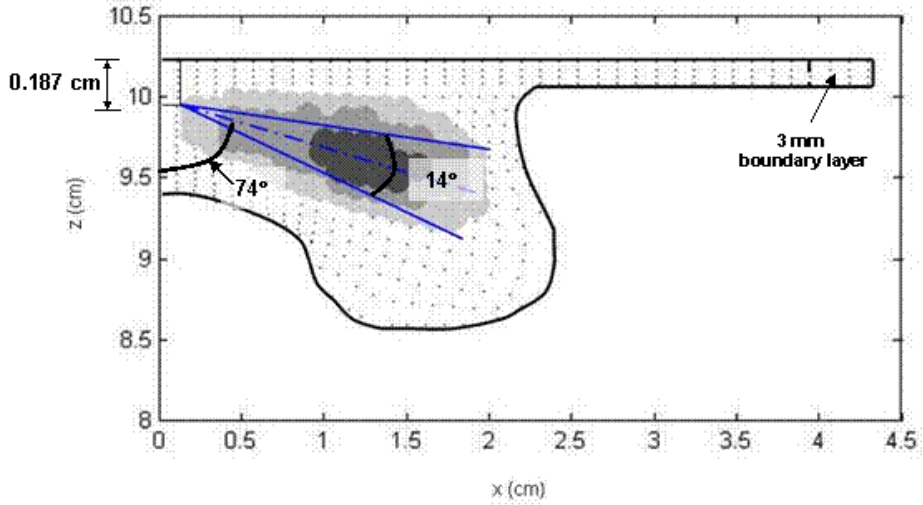

(b) Side view of half of the cylinder

Figure 6.1 See-through view of the cylinder showing the spray angle and spray cone angle of the spray under investigation; and the thickness of boundary layer assumed. In (a), angular position of 0° and 50° lines are also shown between which soot particle paths are tracked. In (b), the piston position shown is at crank angle 2° ATDC

(● > 0 g/cm^3, ● > 1×10^{-7} g/cm^3, ● > 1×10^{-6} g/cm^3, ● > 1×10^{-5} g/cm^3)

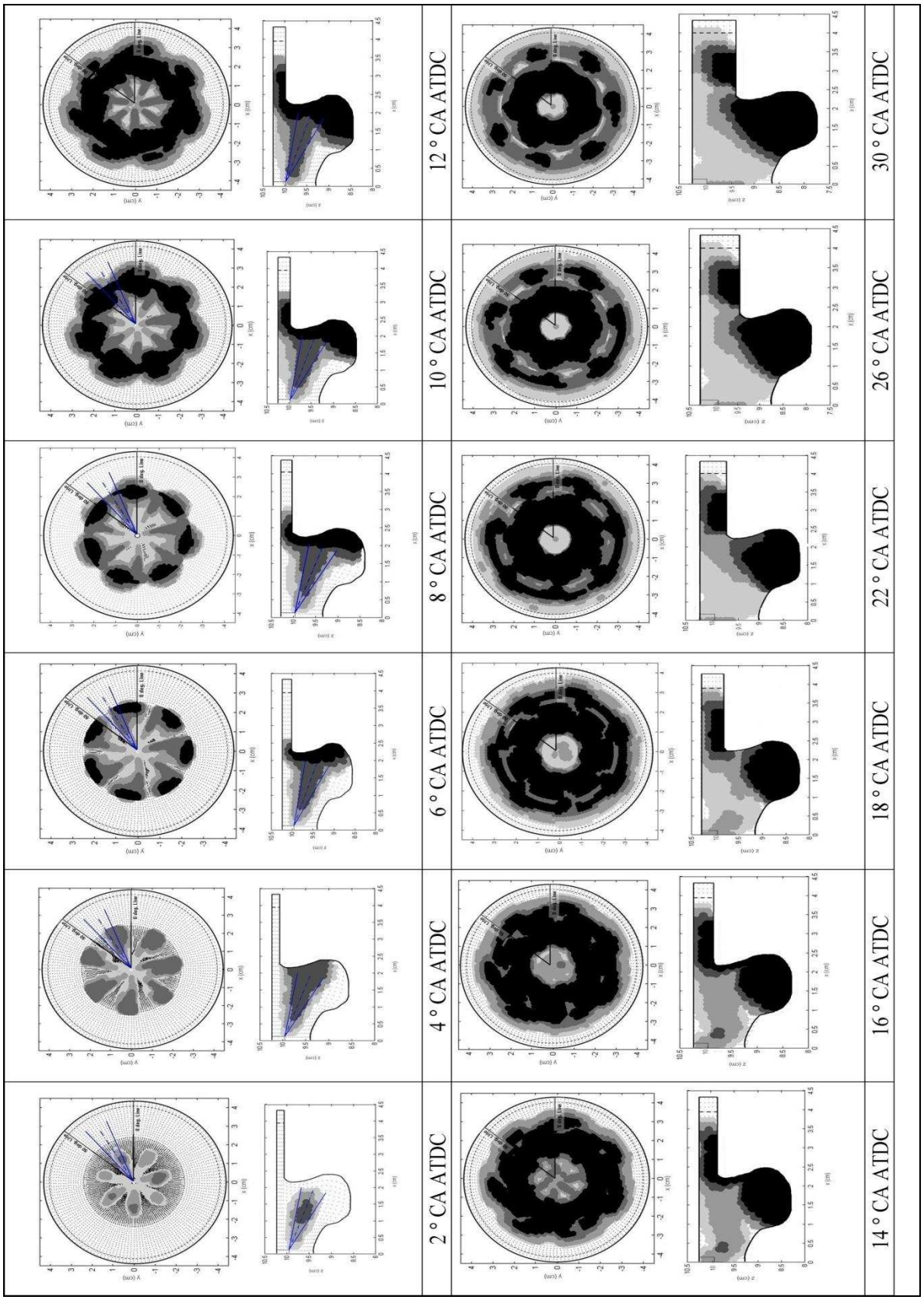

Figure 6.2 Soot distributions from top view and side view of half of the cylinder from 2° CA to 30° CA ATDC

(● > 0 g/cm^3, ● > 1×10^{-7} g/cm^3, ● > 1×10^{-6} g/cm^3, ● > 1×10^{-5} g/cm^3)

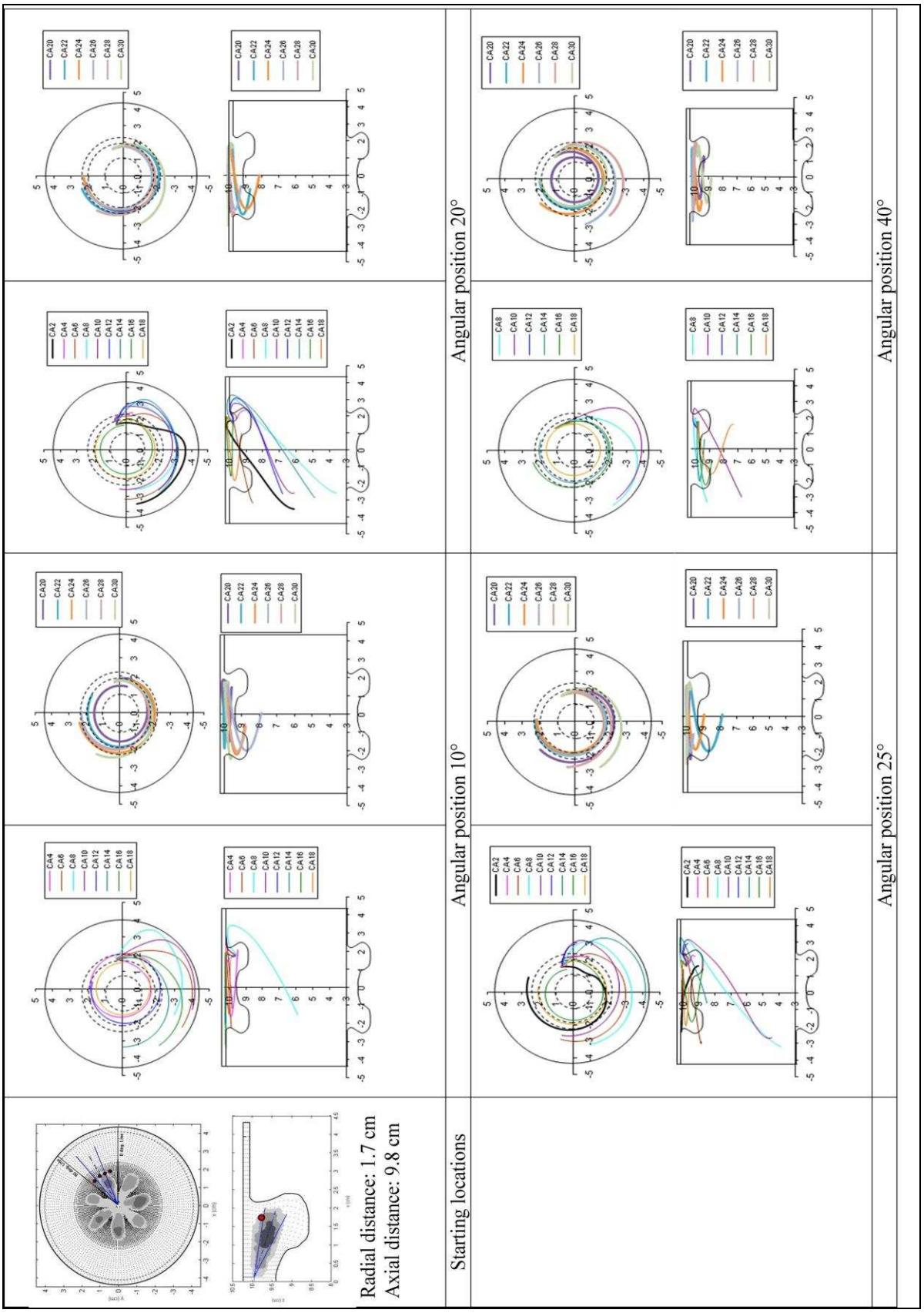

Figure 6.3 Paths of soot particles tracked from above and downstream of the spray at different angular positions with varying crank angle instants of 2° CA to 30° CA ATDC

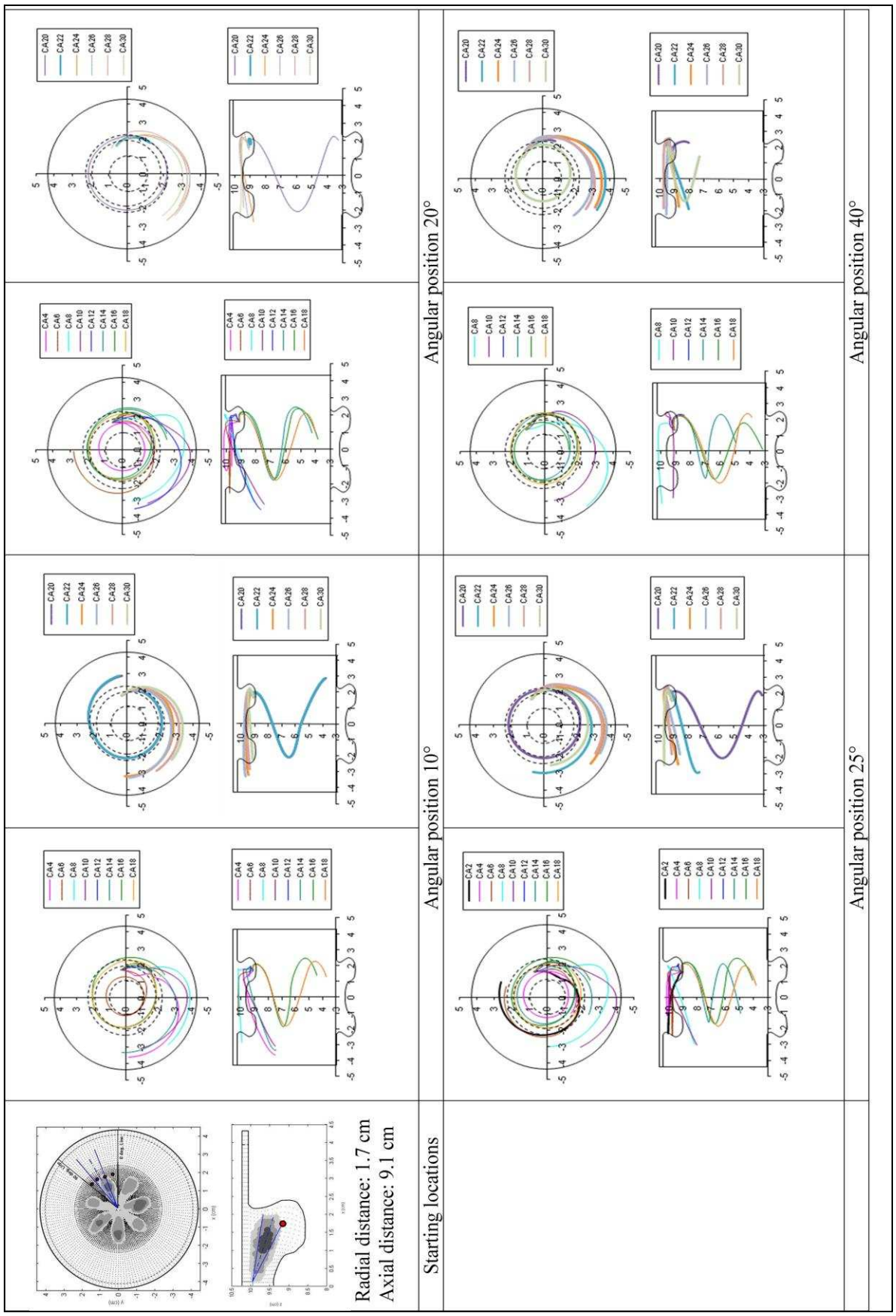

Figure 6.4 Paths of soot particles tracked from below and downstream of the spray at different angular positions with varying crank angle instants of 2° CA to 30° CA ATDC

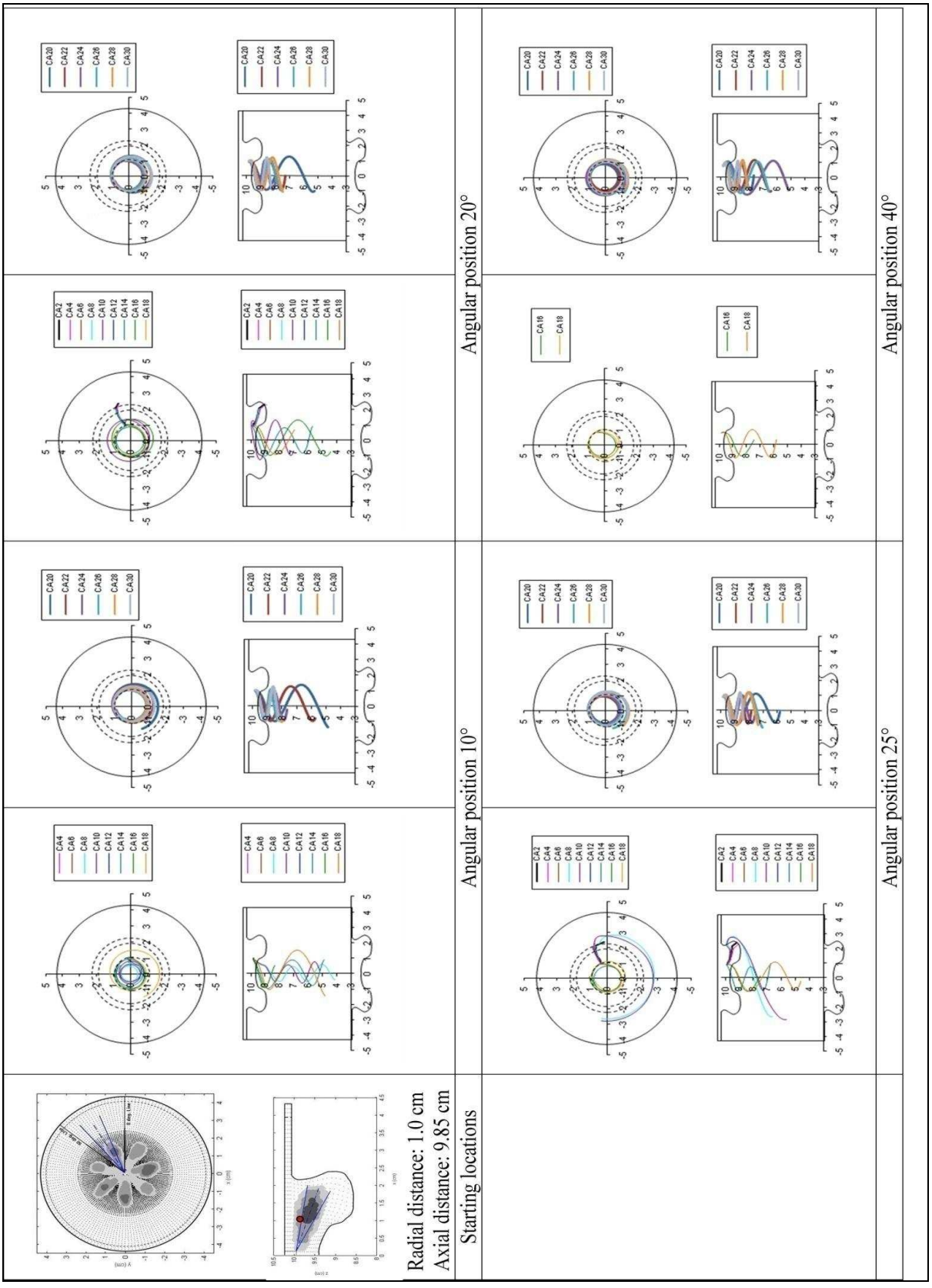

Figure 6.5 Paths of soot particles tracked from above and upstream of the spray at different angular positions with varying crank angle instants of 2° CA to 30° CA ATDC

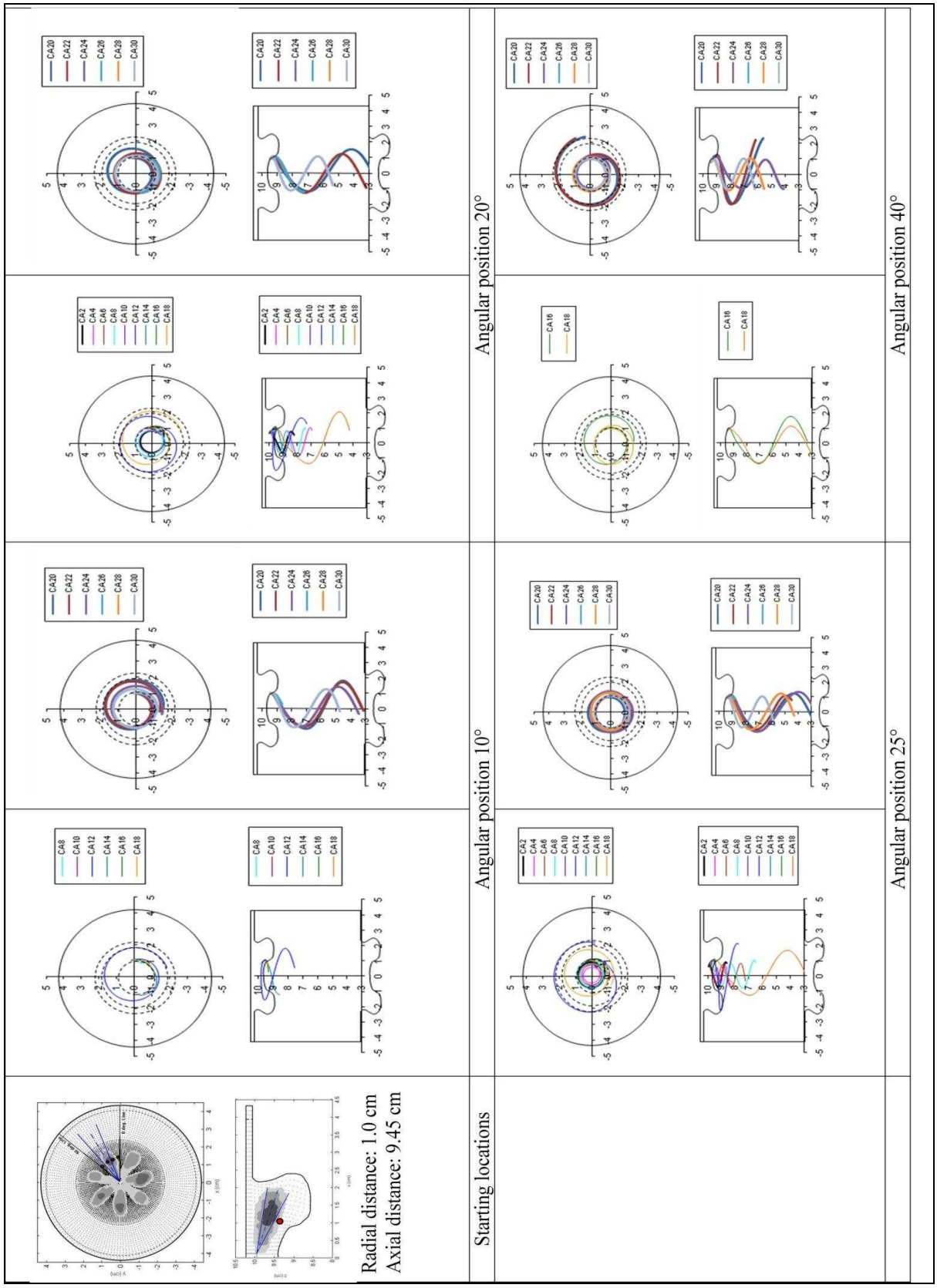

Figure 6.6 Paths of soot particles tracked from below and upstream of the spray at different angular positions with varying crank angle instants of 2° CA to 30° CA ATDC

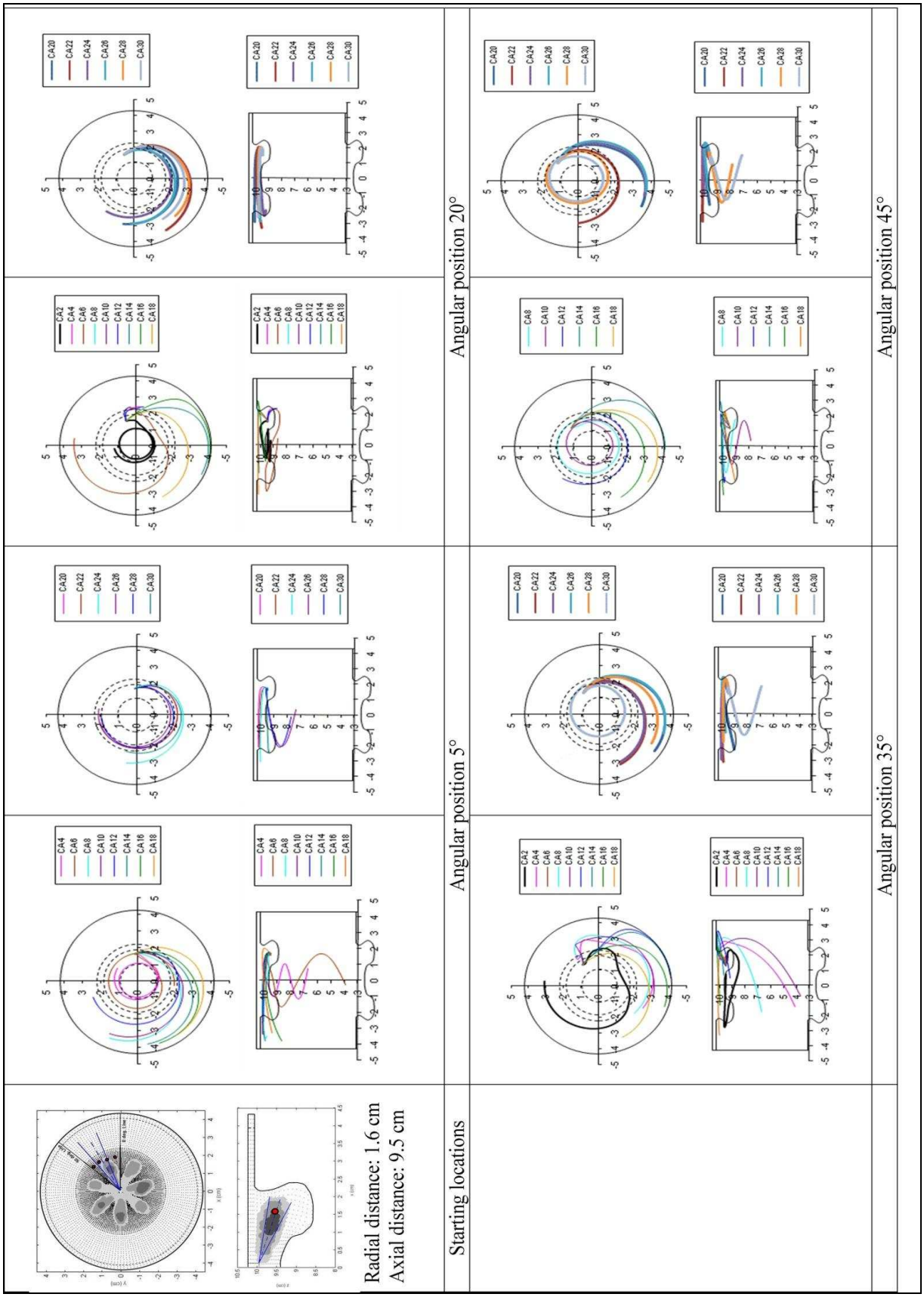

Figure 6.7 Paths of soot particles tracked from the sides of the spray at different angular positions with varying crank angle instants of 2° CA to 30° CA ATDC

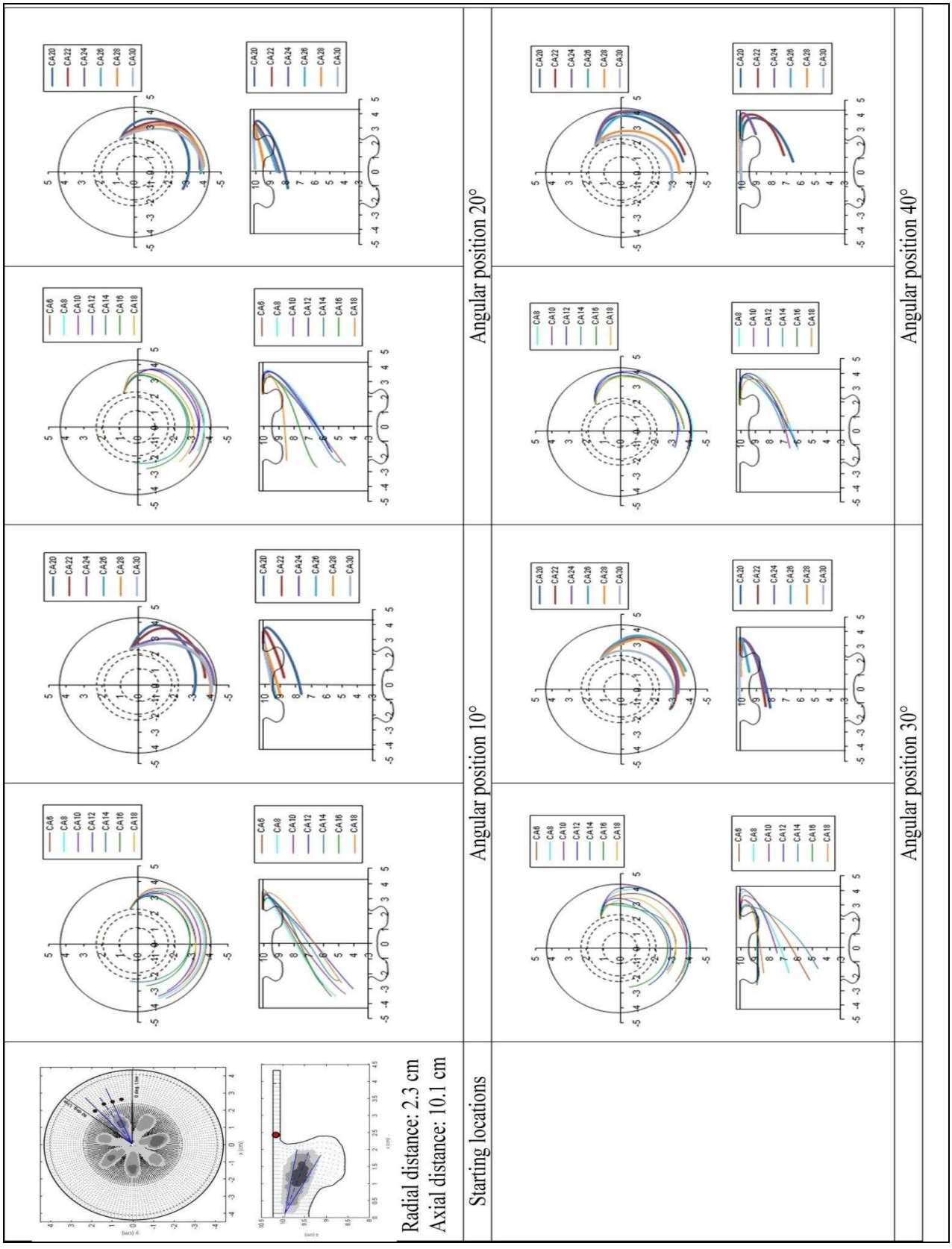

Figure 6.8 Paths of soot particles tracked above the bowl rim at different angular positions with varying crank angle instants of 2° CA to 30° CA ATDC

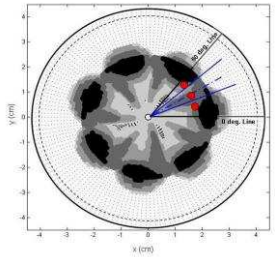

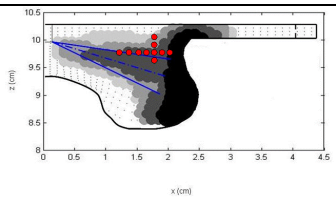

(a) Radial and axial positions of the start of the tracking. Piston position and soot distribution is at crank angle instant of 8° CA ATDC

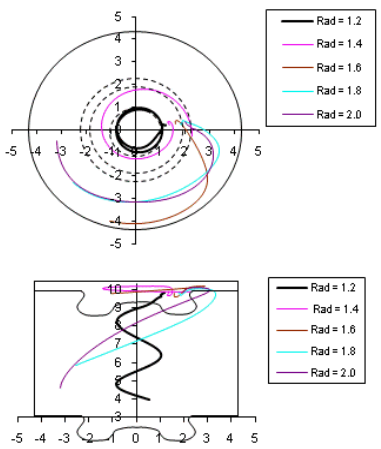

Angular = 10°, Axial = 9.8 cm Radial = varies

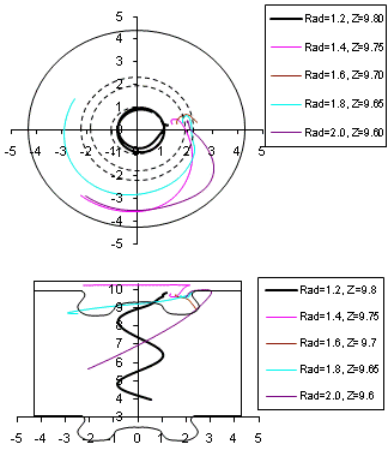

Angular = 10°, Axial = varies Radial = varies

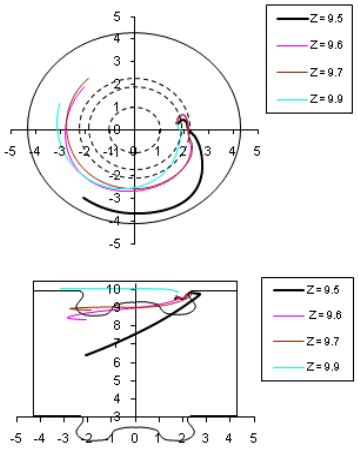

Angular = 10°, Radial = 1.7 cm Axial = varies

(b) Soot particle paths with different radial and axial starting positions at angular position of 10°

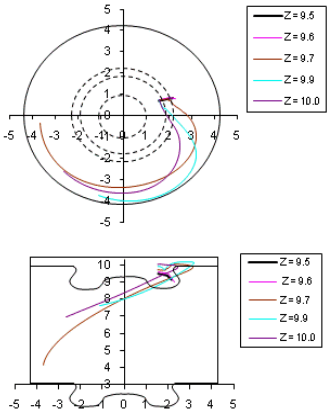

Angular = 25°, Radial = 1.7 cm, Axial = varies

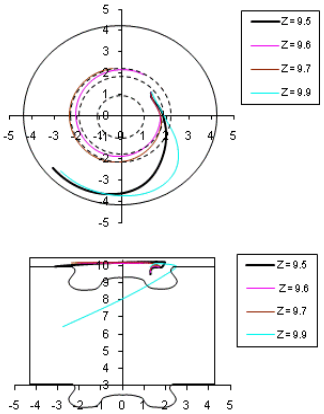

Angular = 40°, Radial = 1.7 cm, Axial = varies

(c) Soot particle paths with different radial and axial starting positions at angular position of 25° and 40°

Figure 6.9 Soot particle paths from the region above the spray axis at 8° CA ATDC

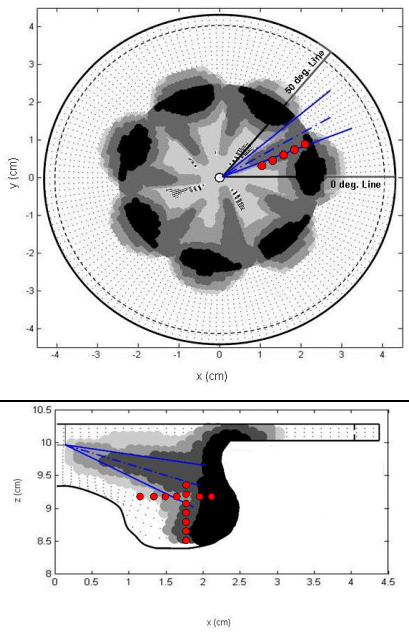

(a) Radial and axial positions of the start of the tracking. Piston position and soot distribution is at crank angle instant of 8° CA ATDC

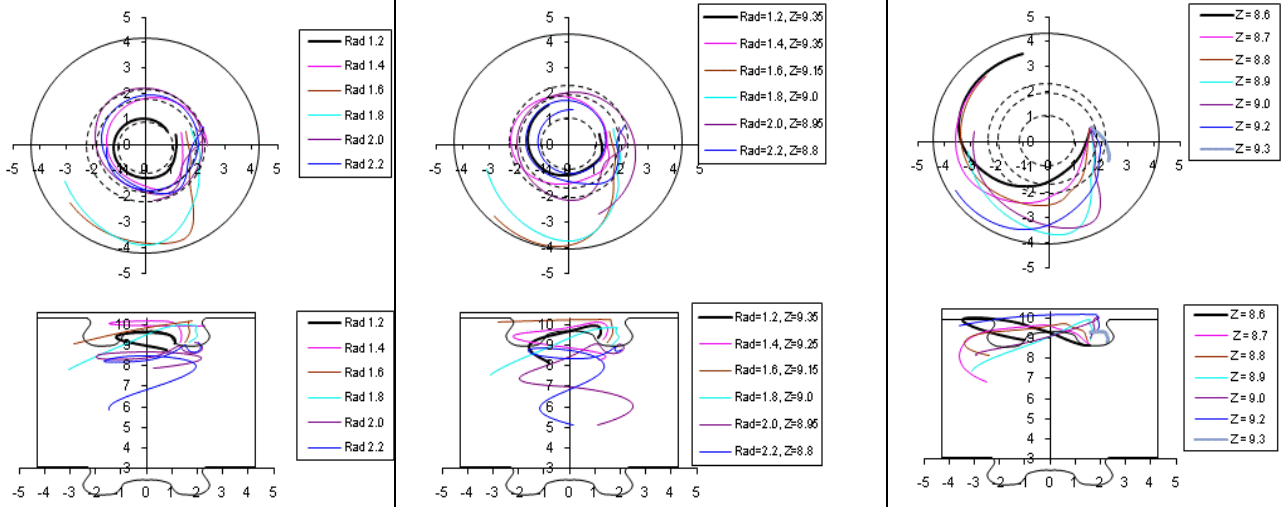

Angular = 20°, Axial = 9.1 cm Radial = varies	Angular = 20°, Axial = varies Radial = varies	Angular = 20°, Radial = 1.7 cm, Axial = varies

(b) Soot particle paths with different radial and axial starting positions at angular position of 20°

Figure 6.10 Soot particle paths from the region below the spray axis at the crank angle instant of 8° CA ATDC

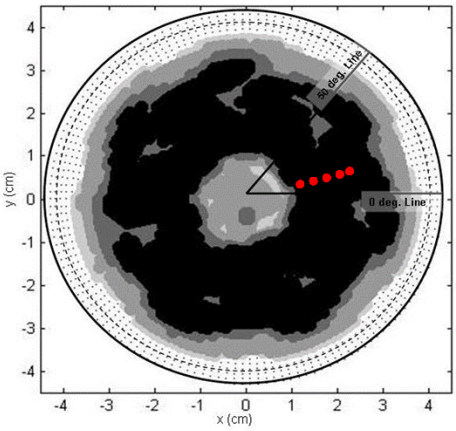

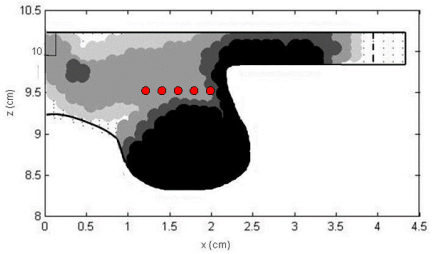

(a) Radial and axial positions of the start of the tracking. Piston position and soot distribution is at crank angle instant of 16° CA ATDC

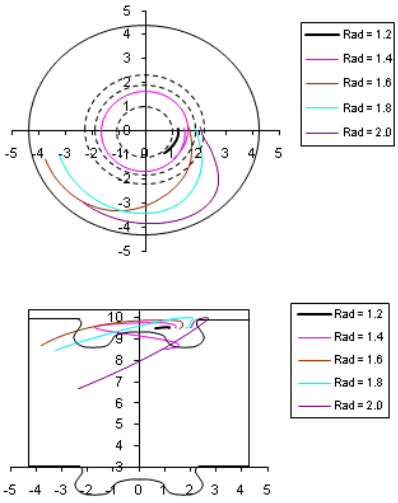

Angular = 5°, Axial = 1.5 cm, Radial = varies

(b) Soot particle paths with different radial and axial starting positions at angular position of 5°

Figure 6.11 Soot particle paths from one side of the spray axis at the crank angle instant of 16° CA ATDC

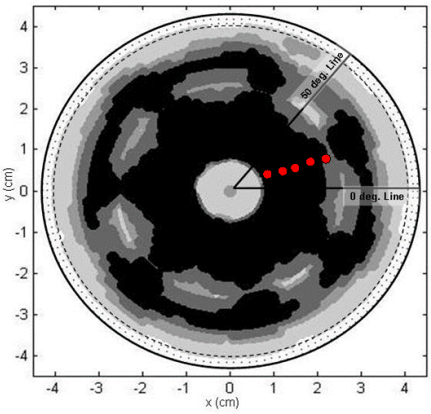

(a) Radial and axial positions of the start of the tracking. Piston position and soot distribution is at crank angle instant of 24° CA ATDC

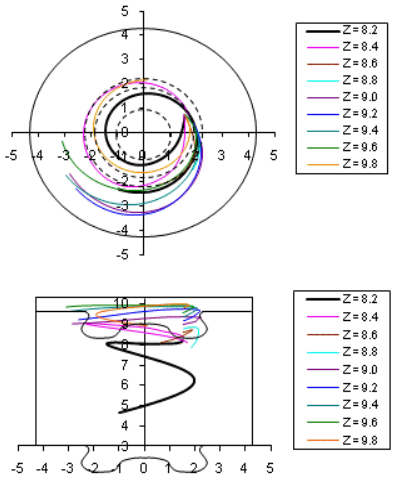

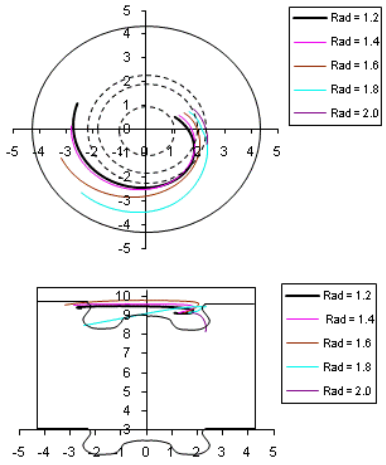

Angular = 25°, Radial = 1.7 cm, Axial = varies

Angular = 25°, Axial = 9.1, Radial = varies

(b) Soot particle paths with different radial and axial starting positions at angular position of 25°

Figure 6.12 Soot particle paths from inside the bowl at the crank angle instant of 24° CA ATDC

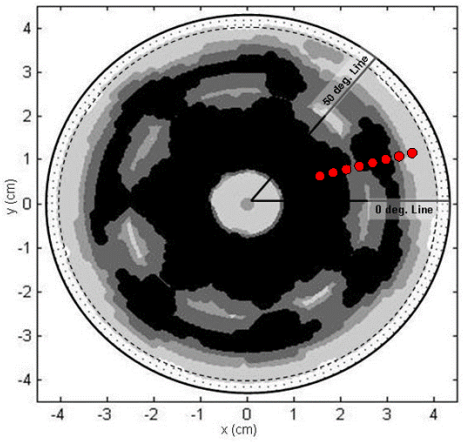

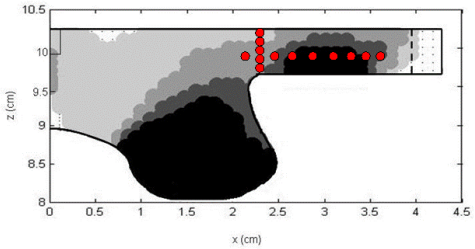

(a) Radial and axial positions of the start of the tracking. Piston position and soot distribution is at crank angle instant of 24° CA ATDC

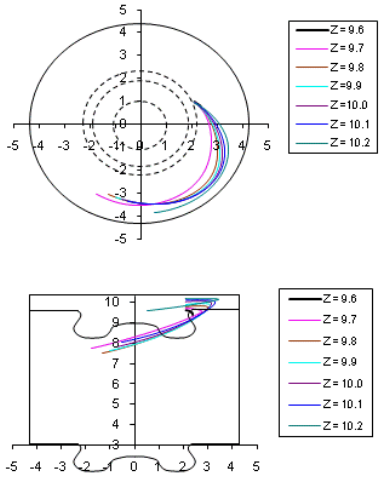

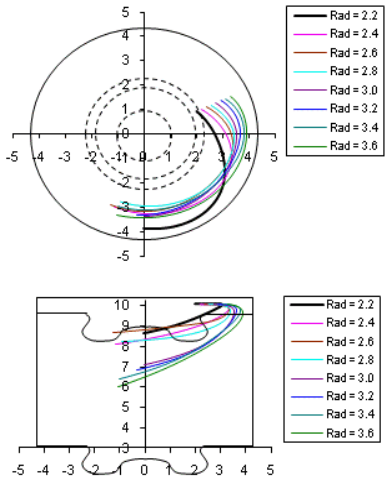

Angular = 25°, Radial = 2.3 cm, Axial = varies

Angular = 25°, Axial = 10.1, Radial = varies

(b) Soot particle paths with different radial and axial starting positions at angular position of 25°

Figure 6.13 Soot particle paths from the region near the bowl rim at the crank angle instant of 24° CA ATDC

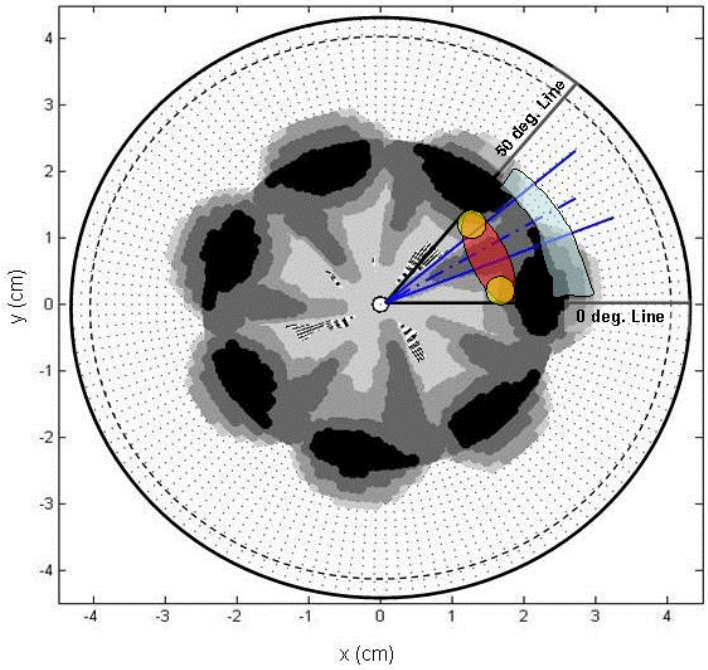

(a) Top view of soot distribution and the markings of regions

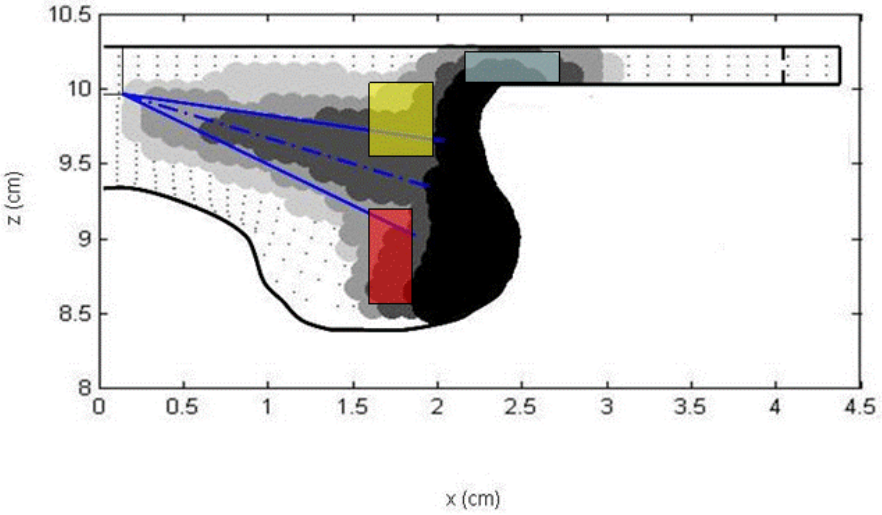

(a) Side view of soot distribution and the markings of regions in half of the cylinder volume

Figure 6.14 Regions of possible sources of soot transfer to the cylinder wall layers at the crank angle instant of 8° CA ATDC

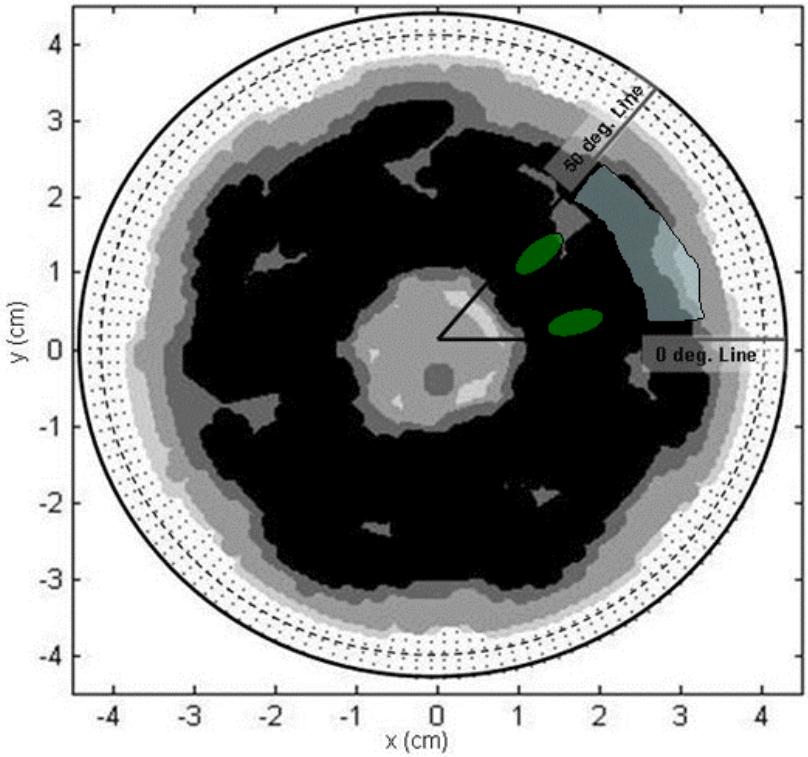

(a) Top view of soot distribution and the markings of regions

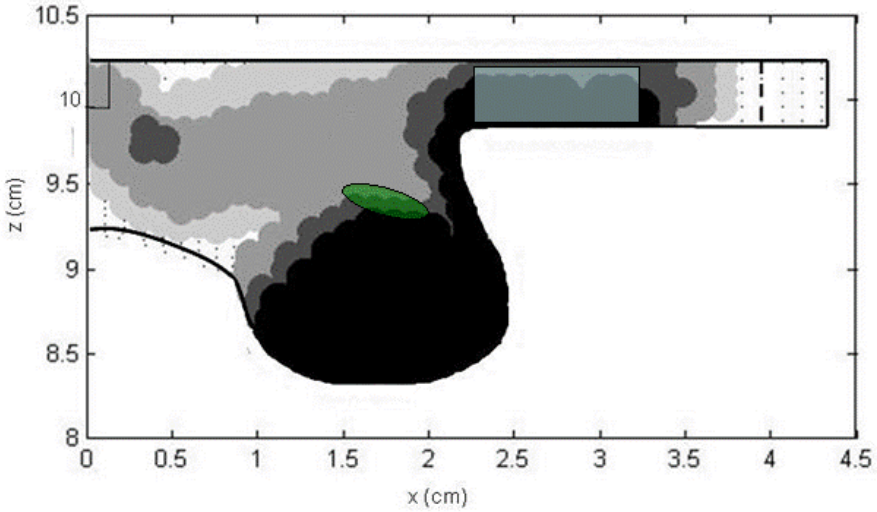

(a) Side view of soot distribution and the markings of regions in half of the cylinder volume

Figure 6.15 Regions of possible sources of soot transfer to the cylinder wall layers at the crank angle instant of 16° CA ATDC

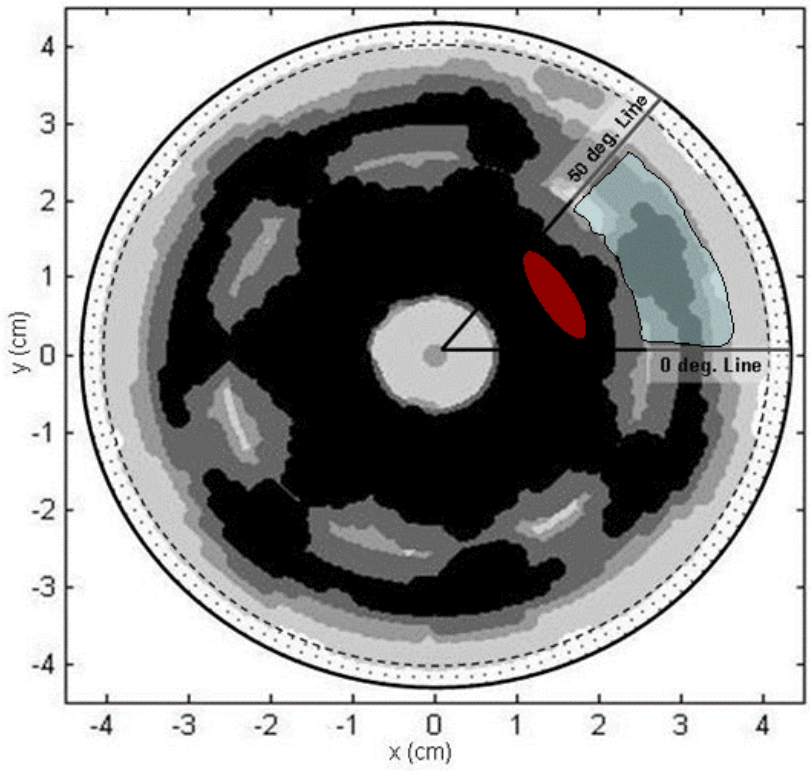

(a) Top view of soot distribution and the markings of regions

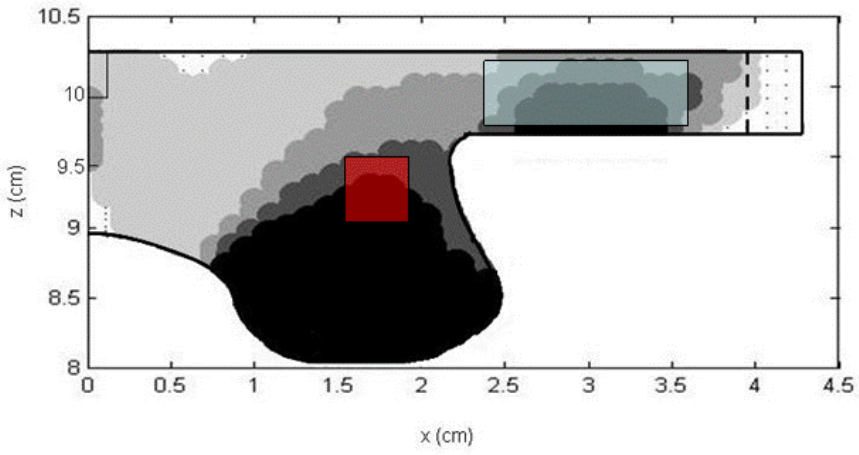

(a) Side view of soot distribution and the markings of regions in half of the cylinder volume

Figure 6.16 Regions of possible sources of soot transfer to the cylinder wall layers at the crank angle instant of 24° CA ATDC

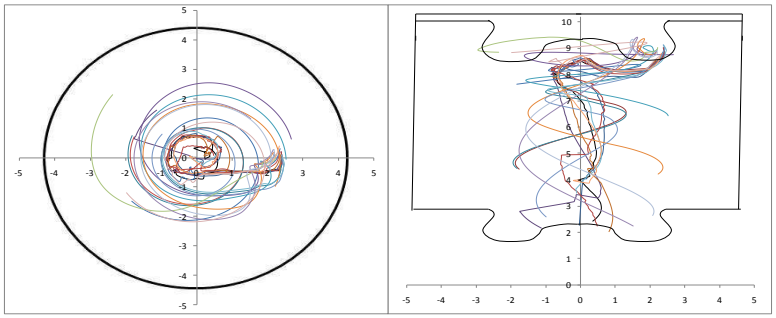

(a) Swirl ratio 1.3

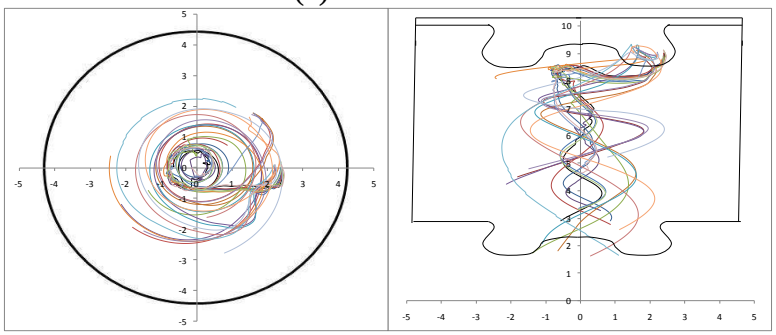

(b) Swirl ratio 1.6

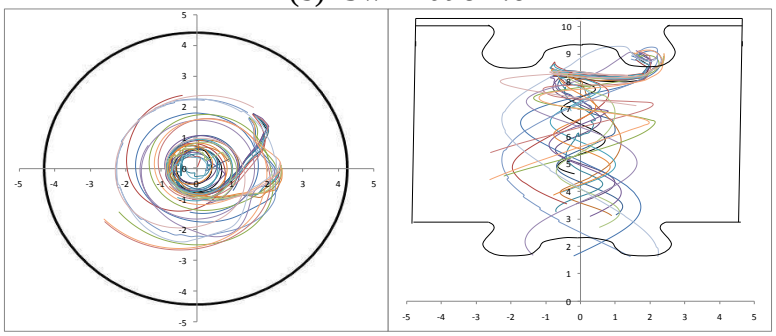

(c) Swirl ratio 1.9

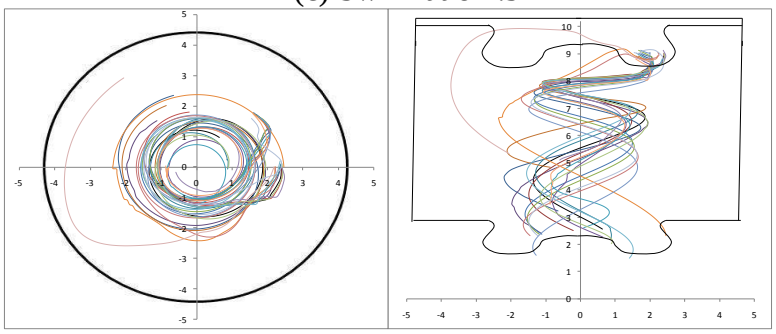

(d) Swirl ratio 2.1

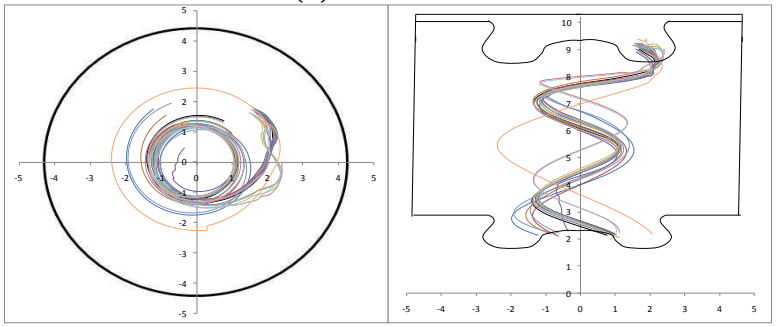

(e) Swirl ratio 2.4

Figure 6.17 Paths from 20 most concentrated points tracked at CA 8° ATDC

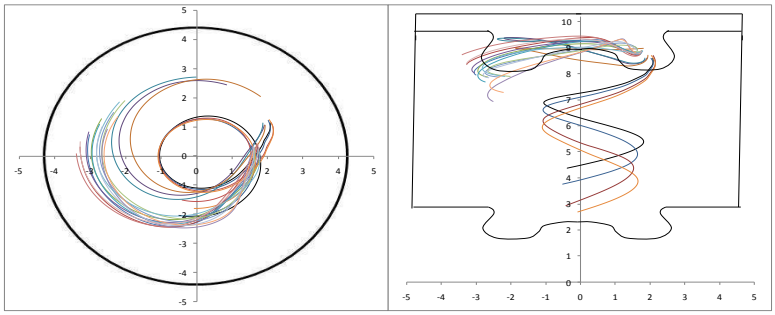

(a) Swirl ratio 1.3

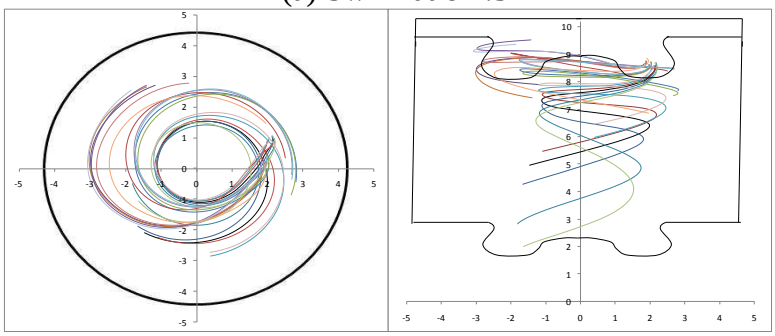

(b) Swirl ratio 1.6

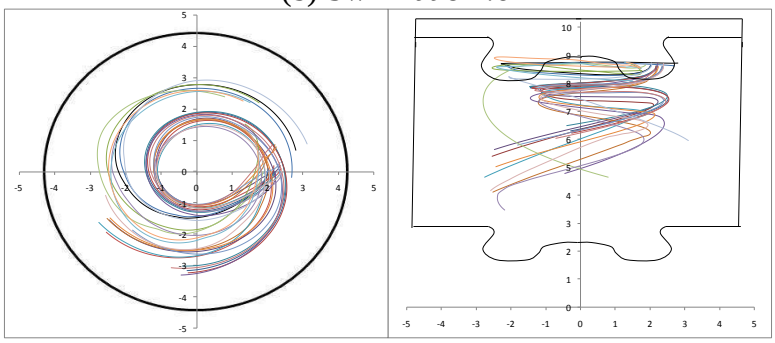

(c) Swirl ratio 1.9

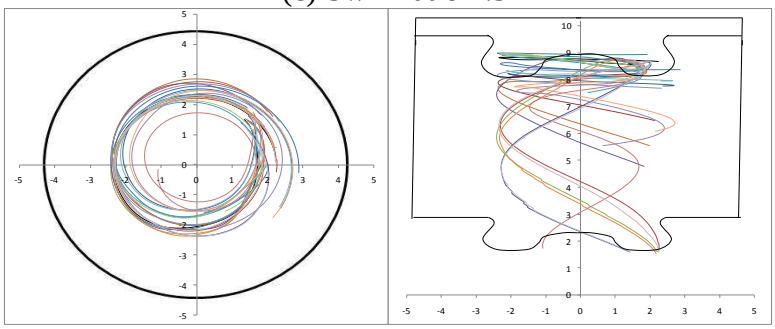

(d) Swirl ratio 2.1

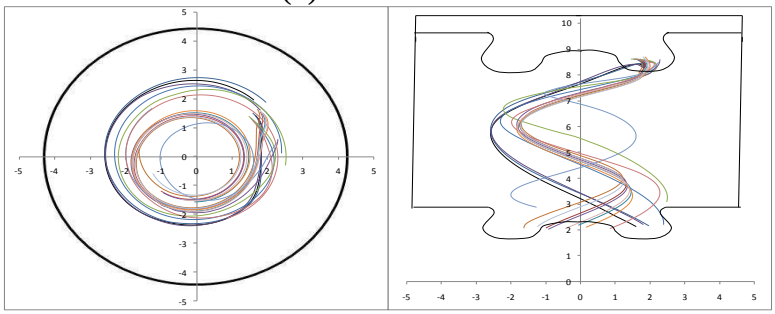

(e) Swirl ratio 2.4

Figure 6.18 Paths from 20 most concentrated points tracked at CA 18° ATDC

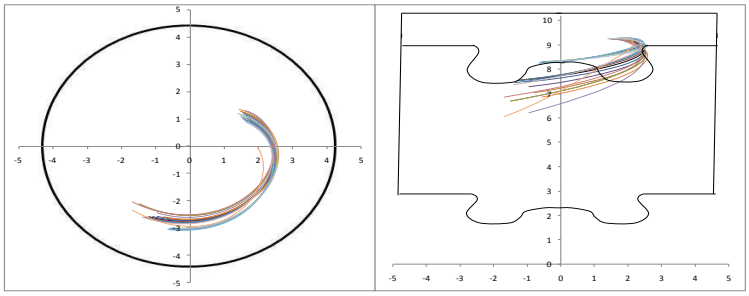

(a) Swirl Ratio 1.3

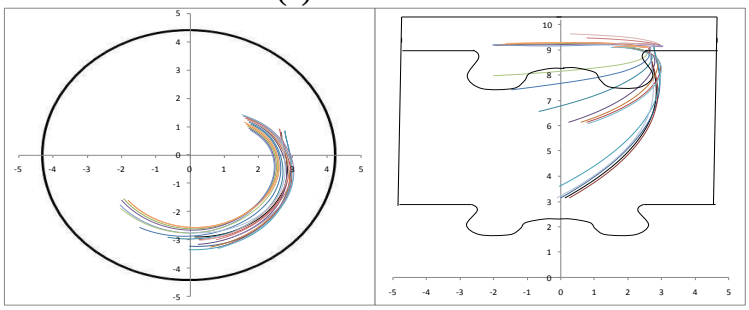

(b) Swirl Ratio 1.6

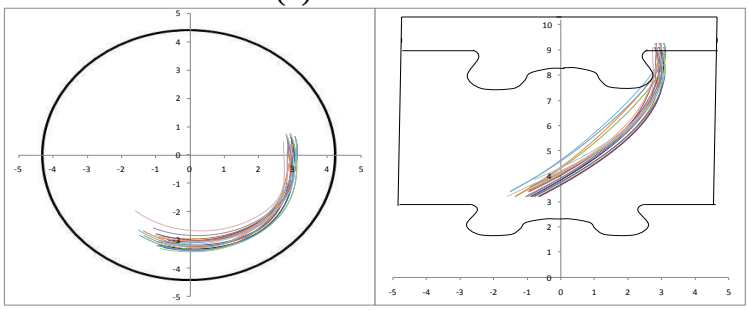

(c) Swirl Ratio 1.9

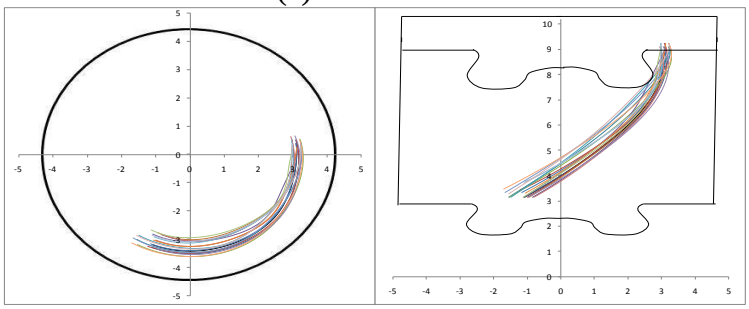

(d) Swirl Ratio 2.1

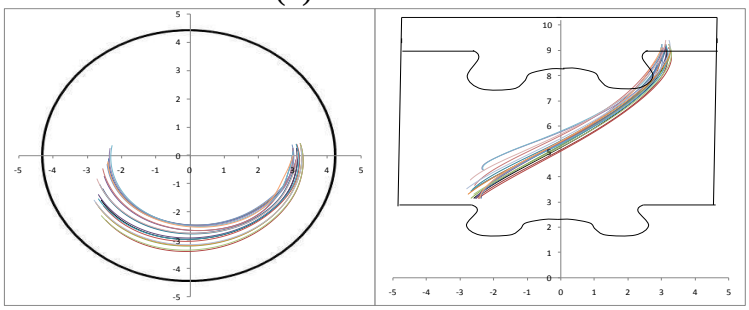

(e) Swirl Ratio 2.4

Figure 6.19 Paths from 20 most concentrated points tracked at CA 35° ATDC

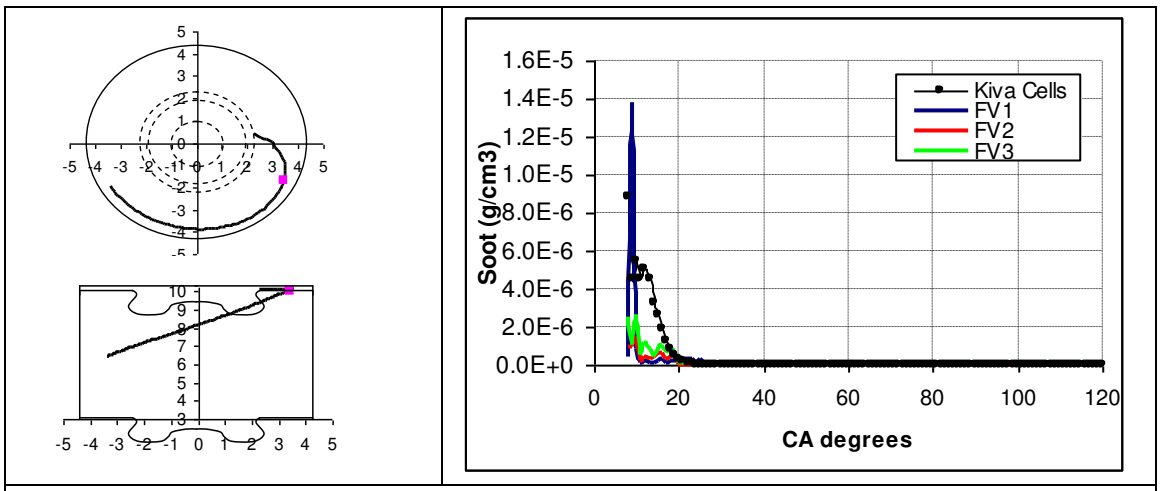

CA 8°ATDC – Zone 1

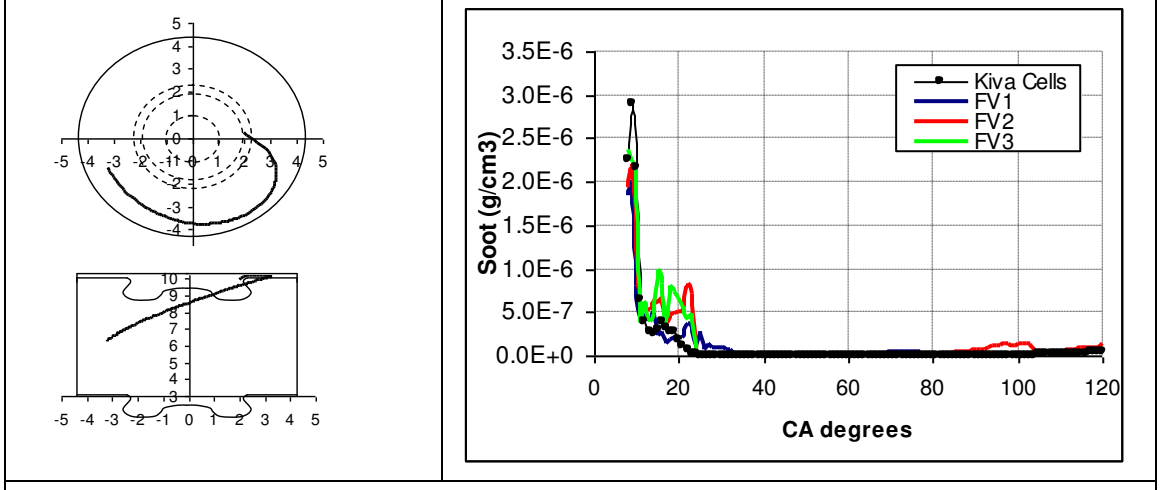

CA 8°ATDC – Zone 2

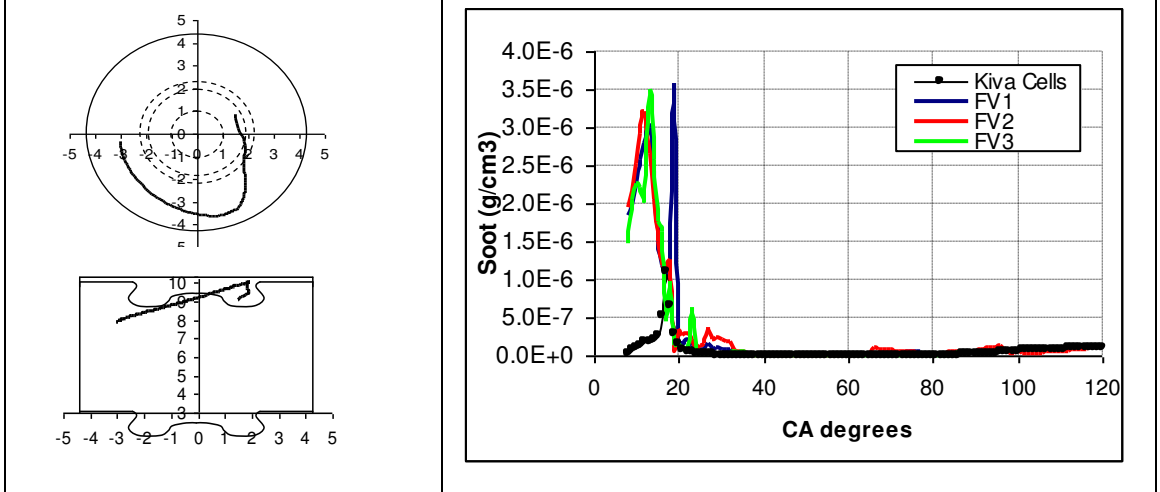

CA 8°ATDC – Zone 3

Figure 6.20(a) Soot distribution along the paths passing through different fractional volumes

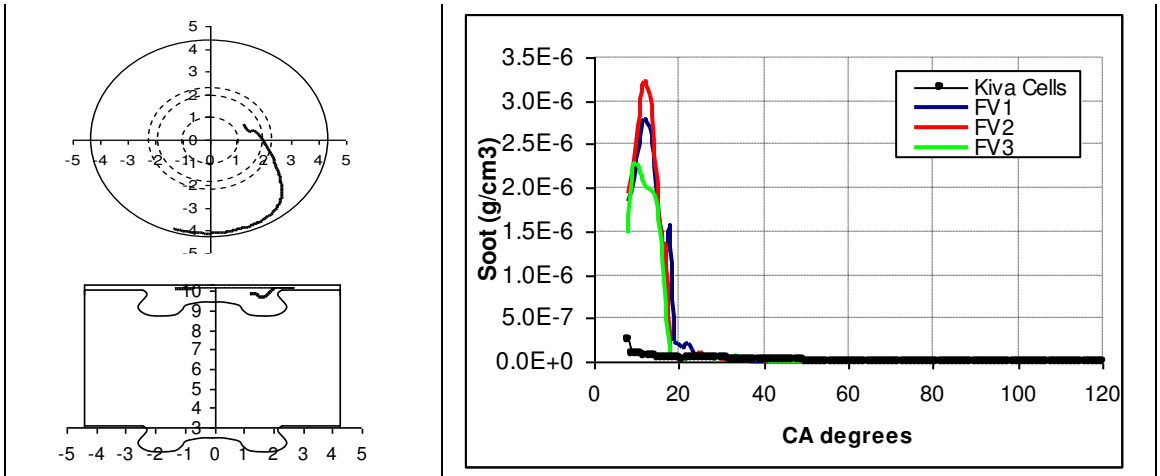

CA 8°ATDC – Zone 4

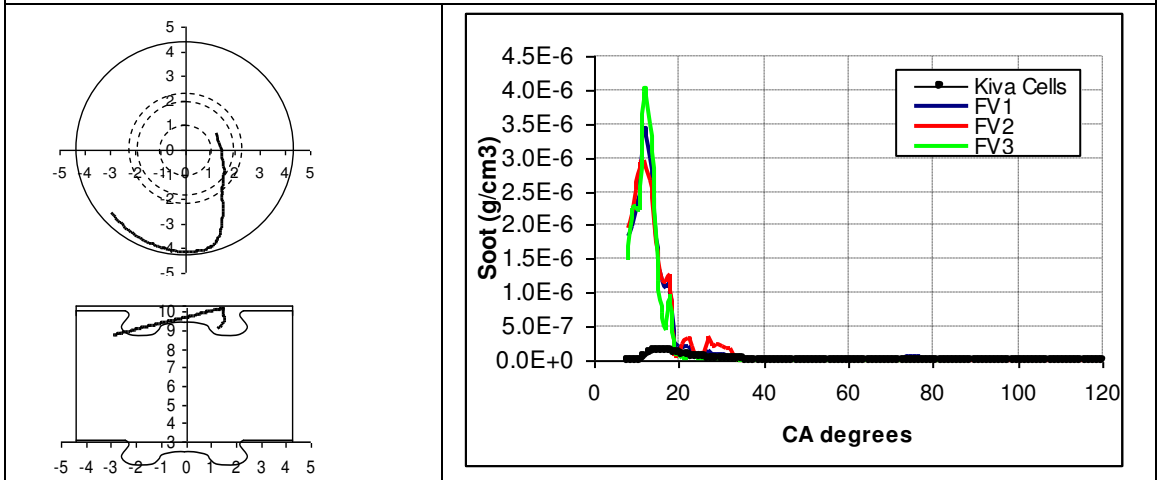

CA 8°ATDC – Zone 5

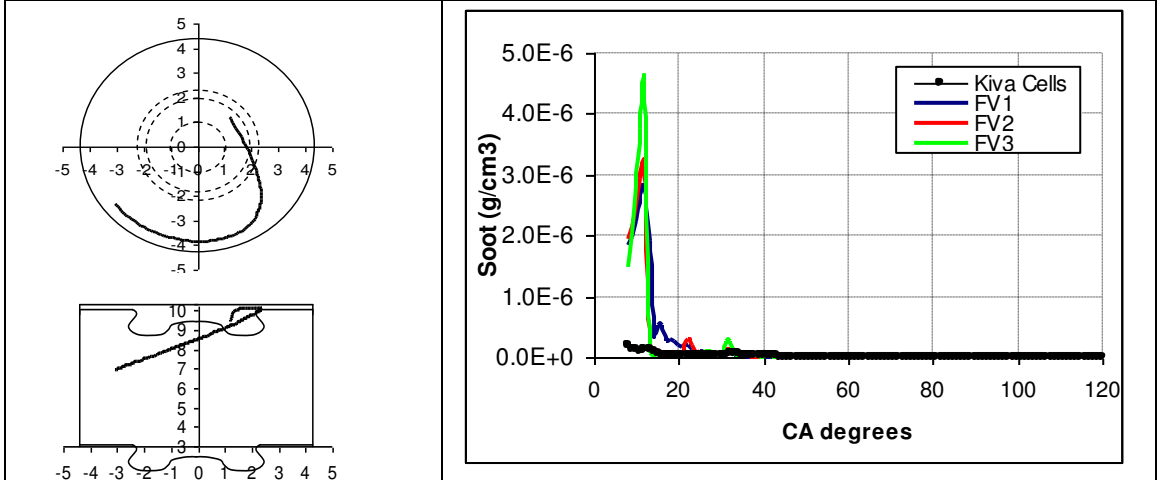

CA 8°ATDC – Zone 6

Figure 6.20(b) Soot distribution along the paths passing through different fractional volumes

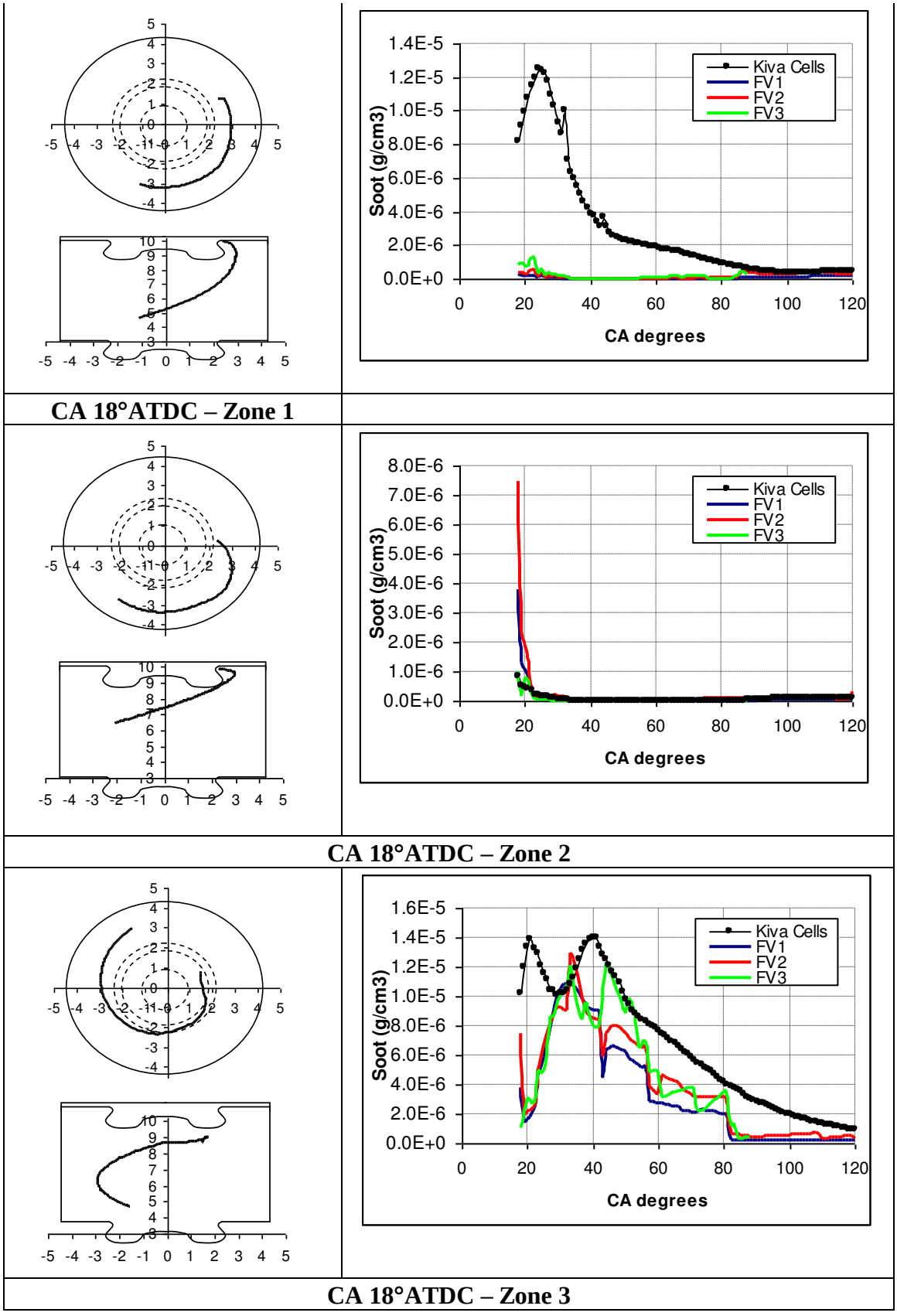

Figure 6.20(c) Soot distribution along the paths passing through different fractional volumes

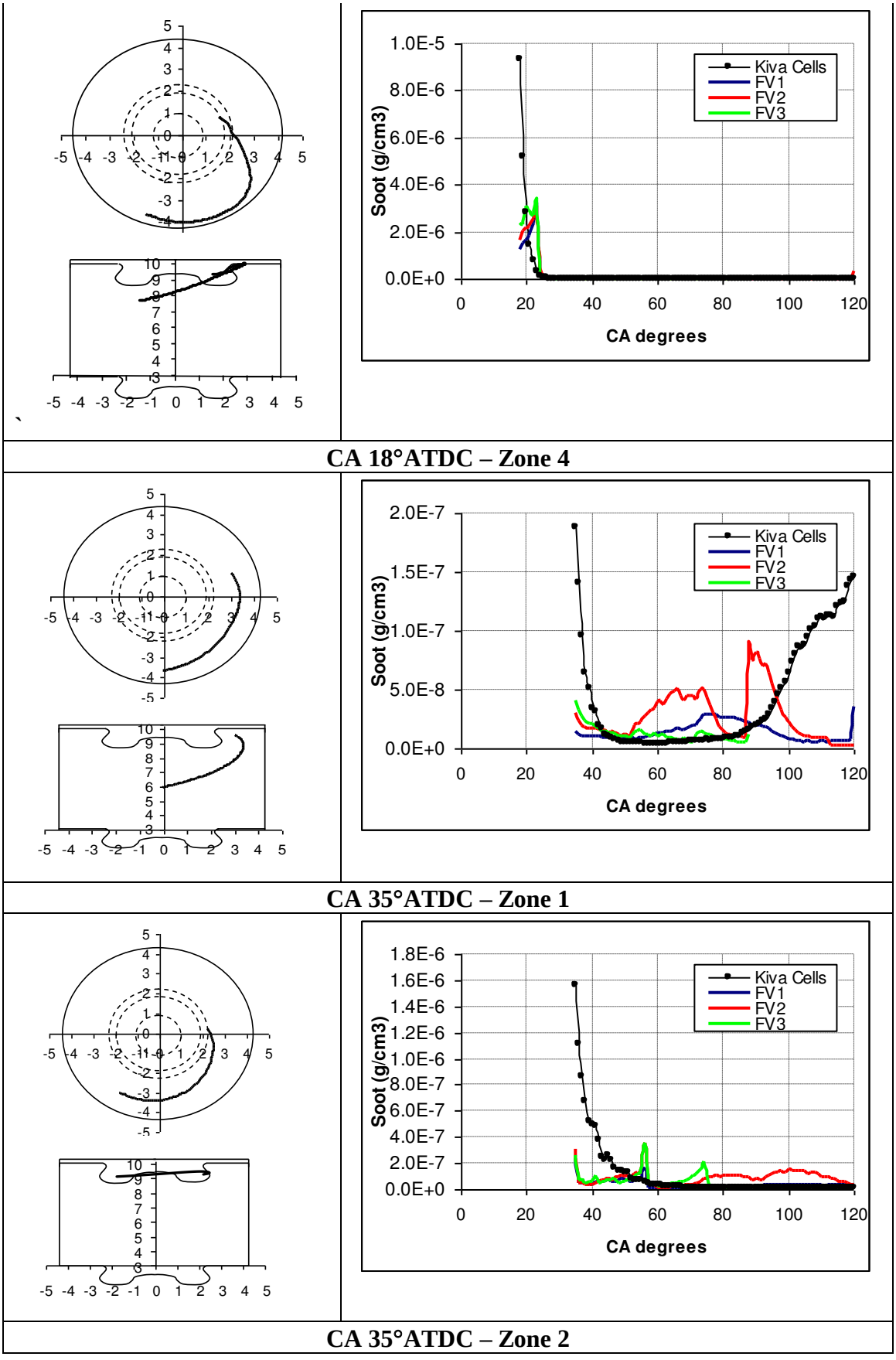

Figure 6.20(d) Soot distribution along the paths passing through different fractional volumes

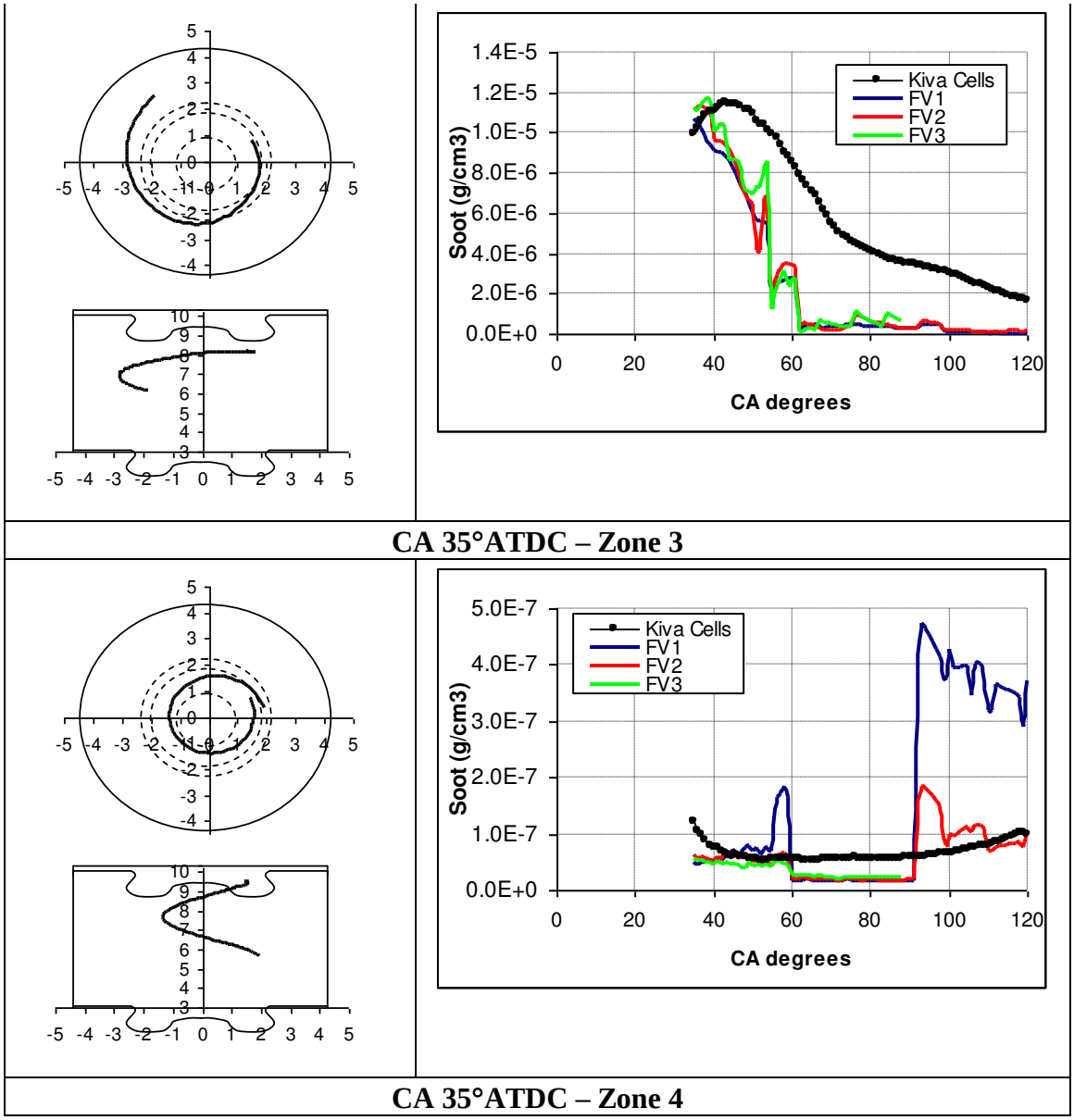

Figure 6.20 (e) Soot distribution along the paths passing through different fractional volumes

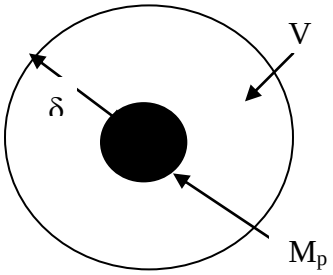

Figure 7.1 Schematic of a soot particle surrounded by a cloud of fuel vapour

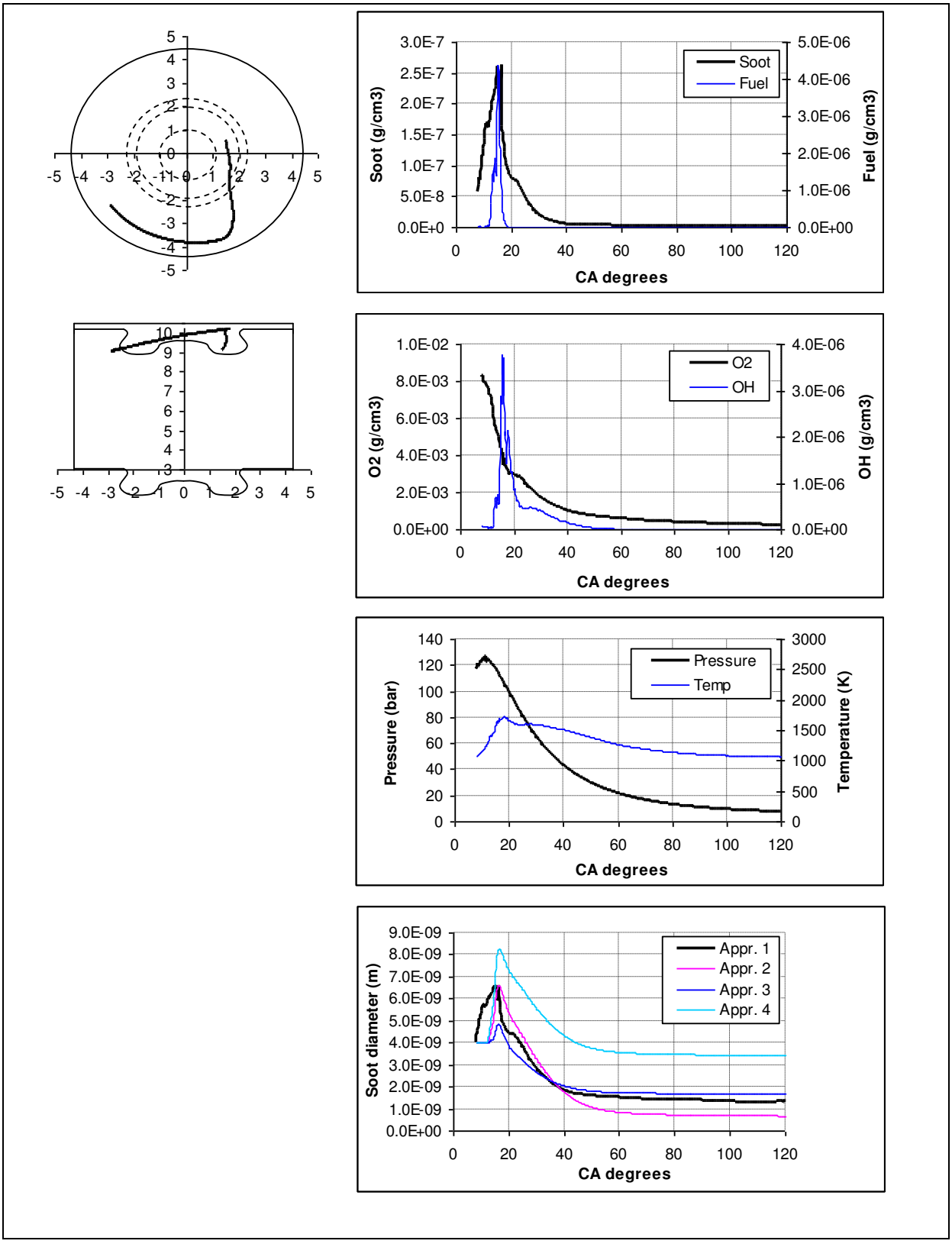

Figure 7.2 Soot particle path, profiles of local species concentrations and conditions along the path, and prediction of soot particle size by different approaches of a starting location below the spray axis at the instant of 8° CA ATDC, radial distance 1.6 cm, axial distance 9.1 cm and angular position 20°

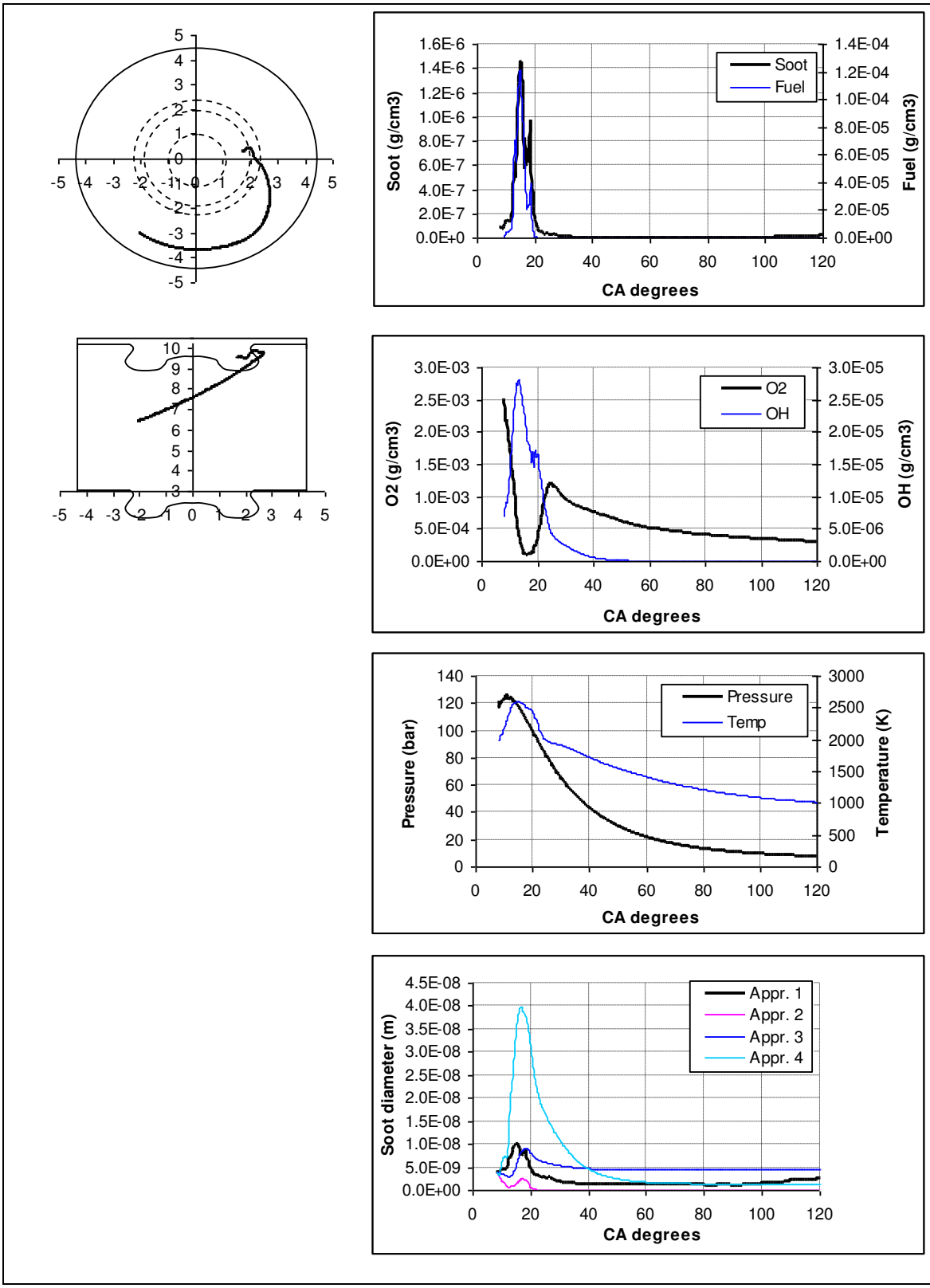

Figure 7.3 Soot particle path, profiles of local species concentrations and conditions along the path, and prediction of soot particle size by different approaches of a starting location above the spray axis at the instant of 8° CA ATDC, radial distance 1.7 cm, axial distance 9.8 cm and angular position 10°

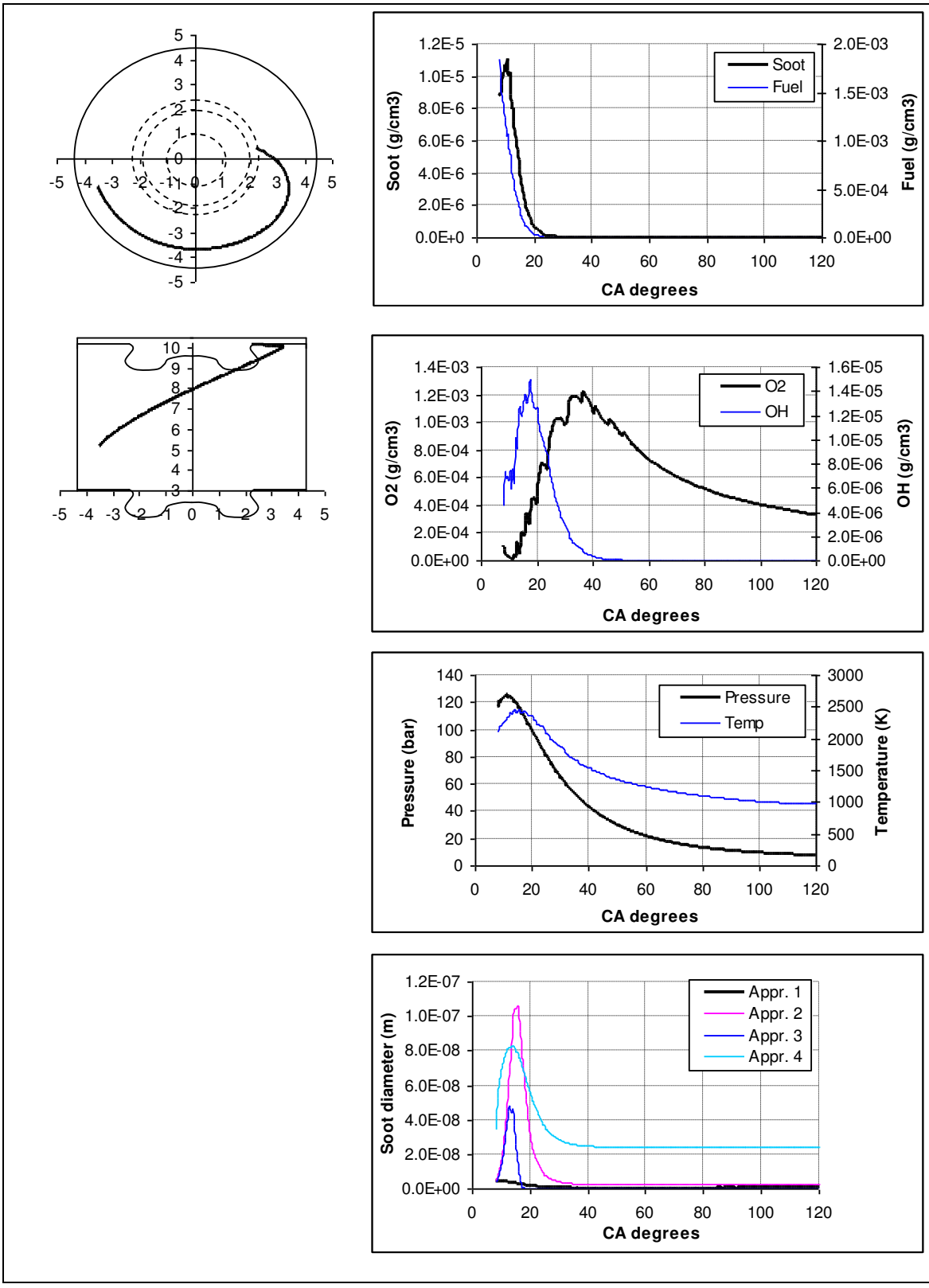

Figure 7.4 Soot particle path, profiles of local species concentrations and conditions along the path, and prediction of soot particle size by different approaches of a starting location above the bowl rim at the instant of 8° CA ATDC, radial distance 2.3 cm, axial distance 10.1 cm and angular position 10°

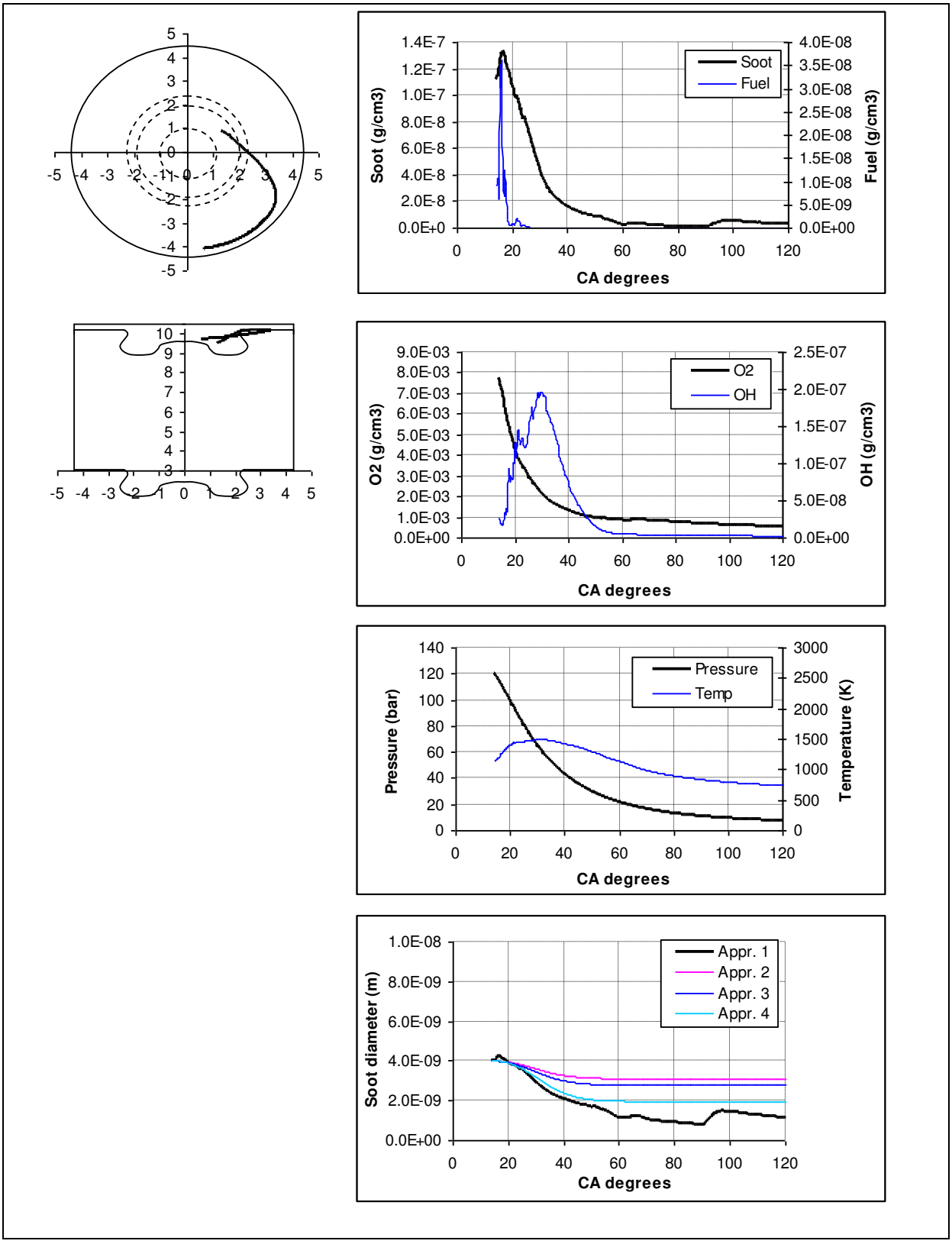

Figure 7.5 Soot particle path, profiles of local species concentrations and conditions along the path, and prediction of soot particle size by different approaches of a starting location at the spray side at the instant of 14° CA ATDC, radial distance 1.5 cm, axial distance 9.5 cm and angular position 45°

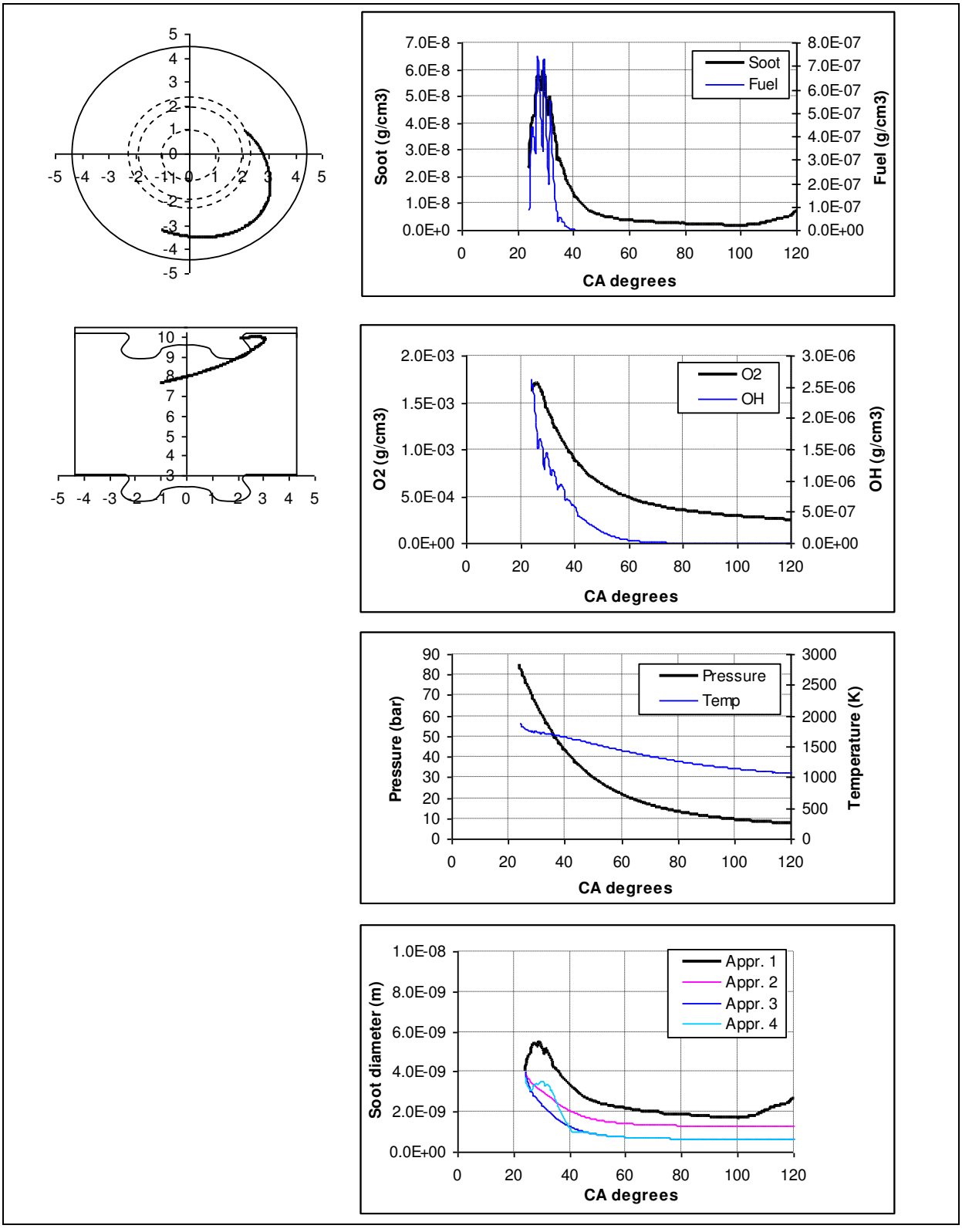

Figure 7.6 Soot particle path, profiles of local species concentrations and conditions along the path, and prediction of soot particle size by different approaches of a starting location at the spray side at the instant of 24° CA ATDC, radial distance 2.3 cm, axial distance 9.9 cm and angular position 25°

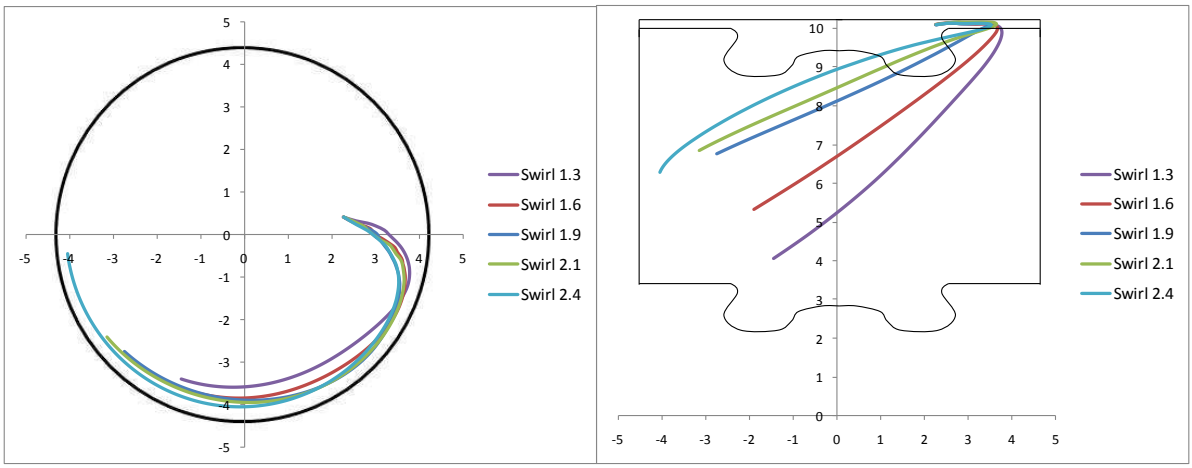

(a) Zone 1

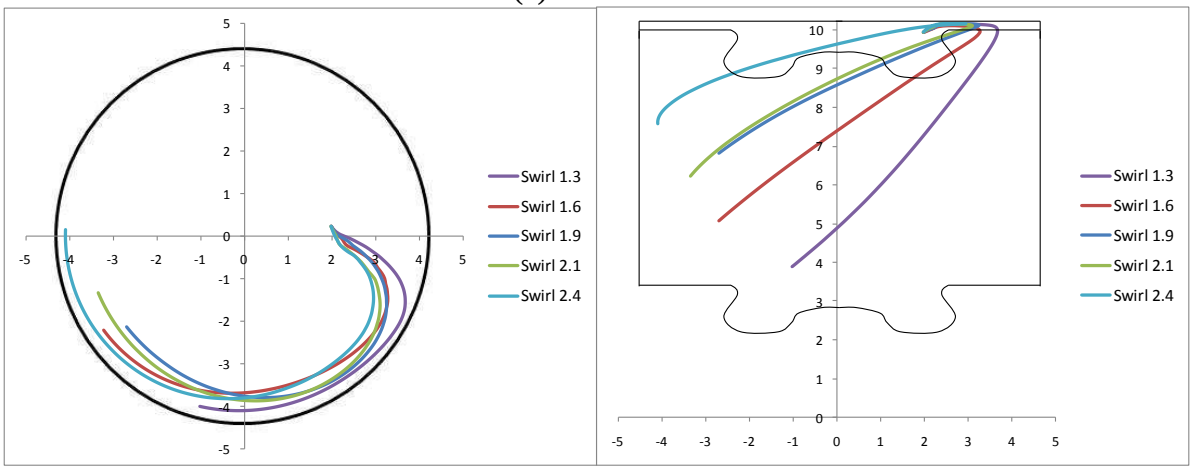

(b) Zone 2

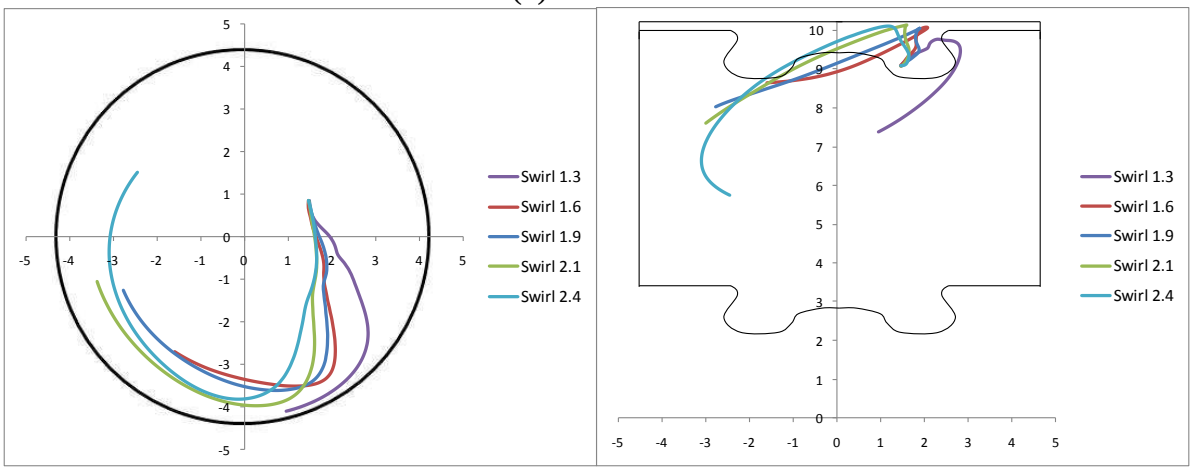

(b) Zone 3

Figure 8.1 Paths of particle formed in Zone 1,2 and 3 tracked from CA 8° ATDC

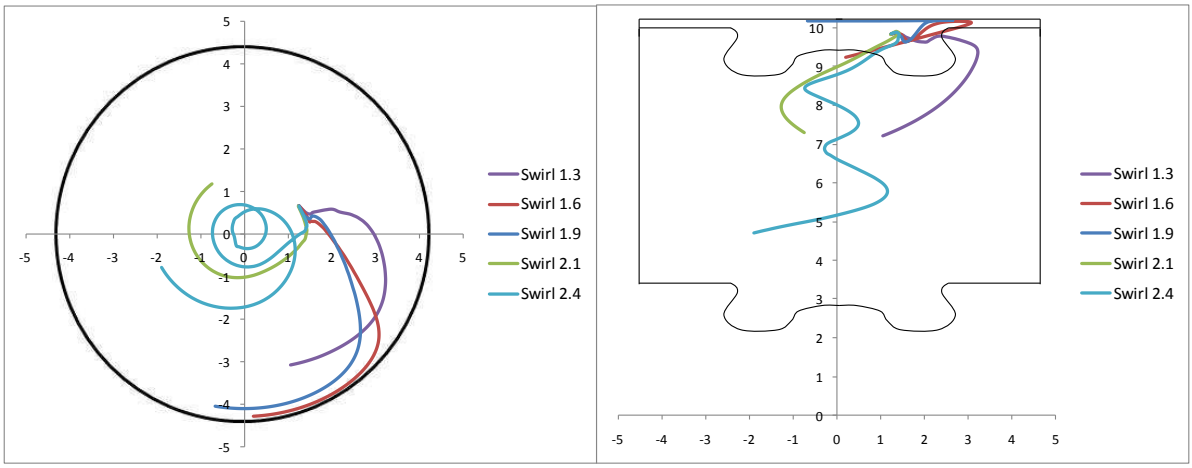

(a) Zone 4

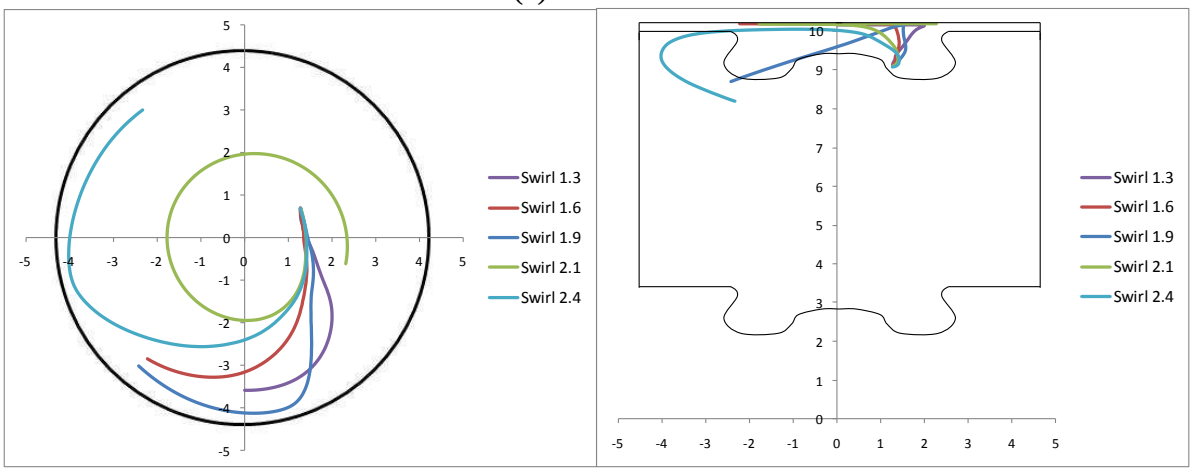

(b) Zone 5

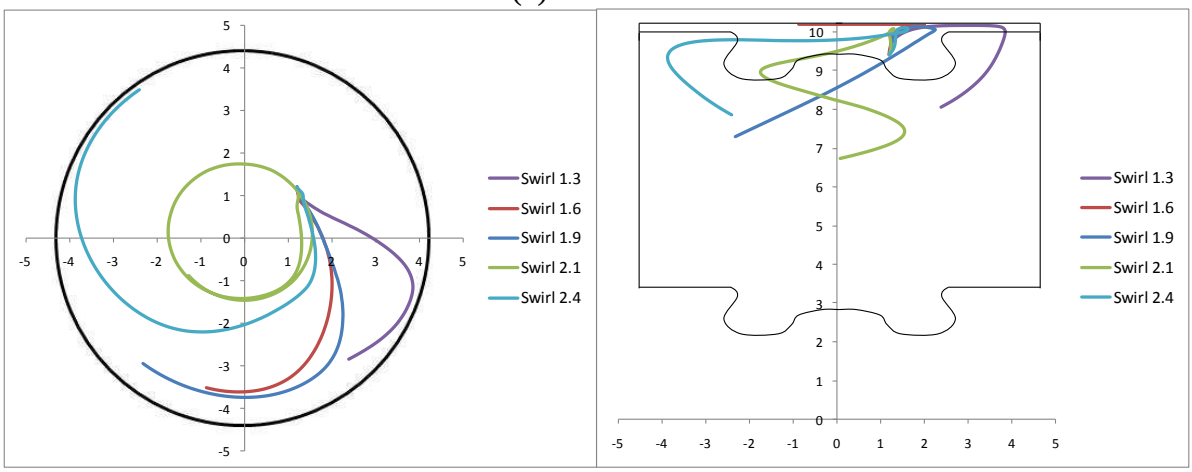

(c) Zone 6

Figure 8.2 Paths of particle formed in Zone 4, 5 and 6 tracked from CA 8° ATDC

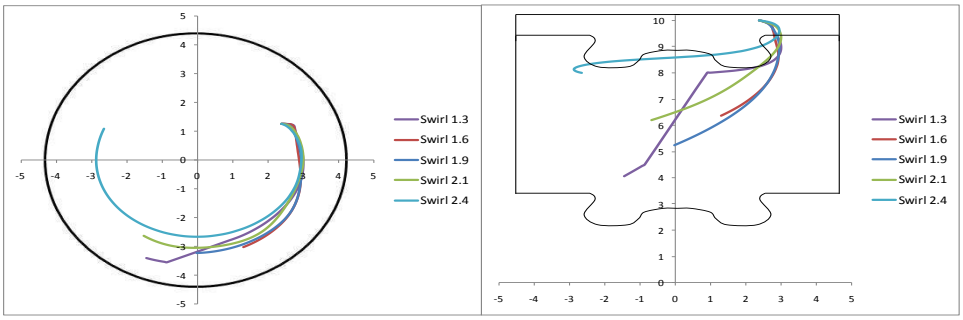

(a) Zone 1

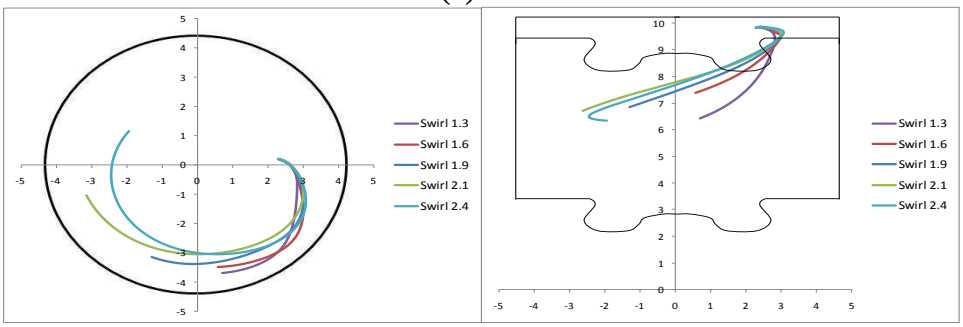

(a) Zone 2

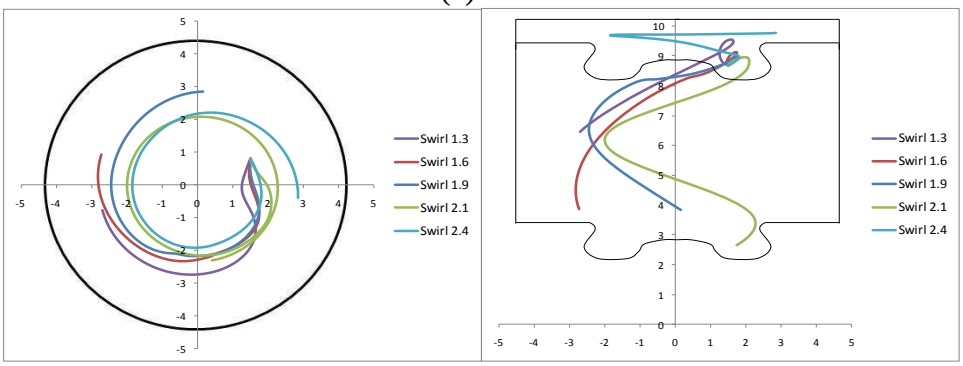

(a) Zone 3

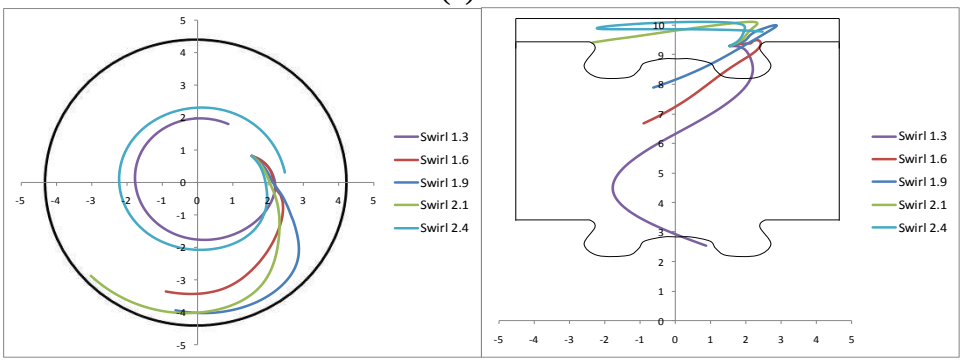

(a) Zone 4

Figure 8.3 Paths of particle formed in Zone 1, 2, 3 and 4 tracked from CA 18° ATDC

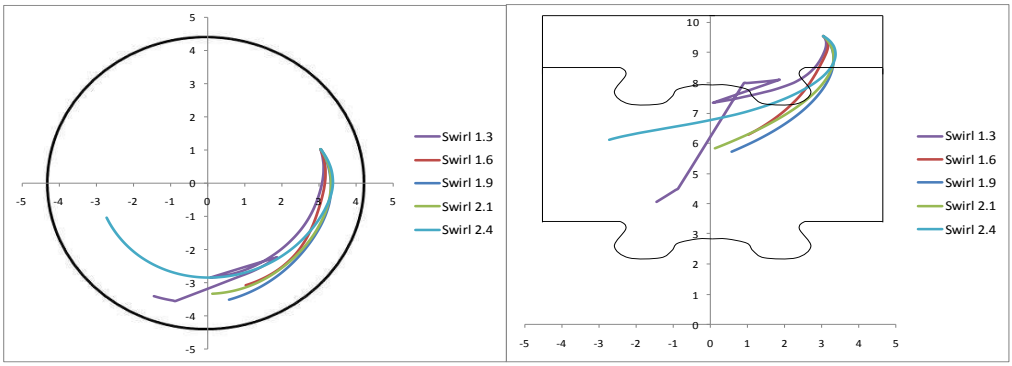

(a) Zone 1

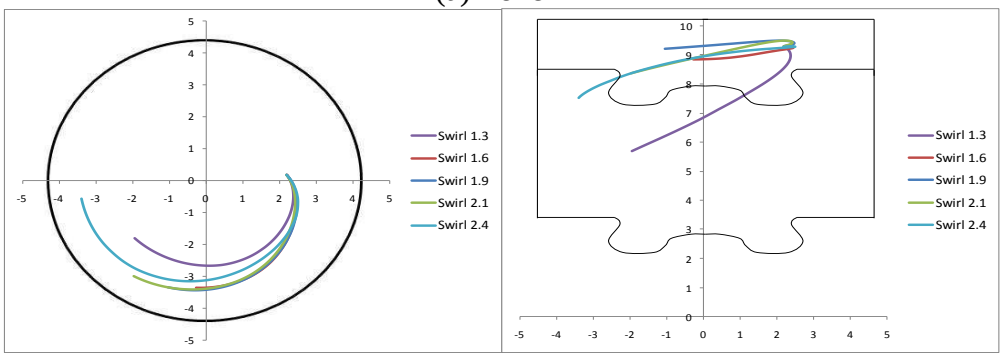

(b) Zone 2

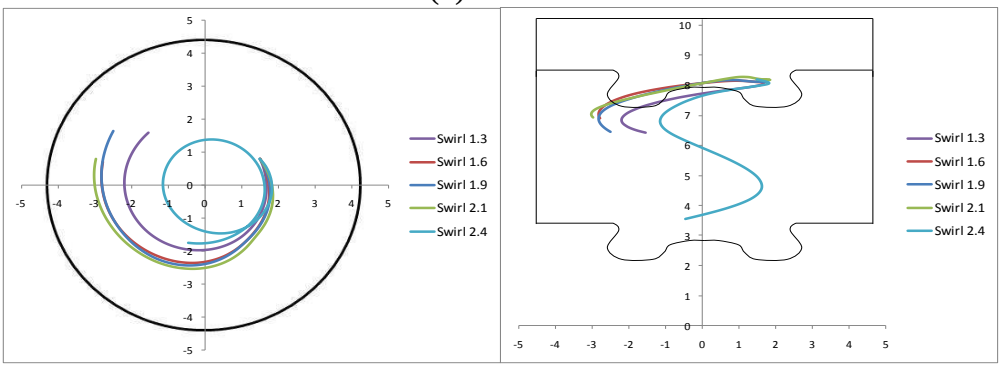

c) Path of particle formed in Zone 3, CA 35

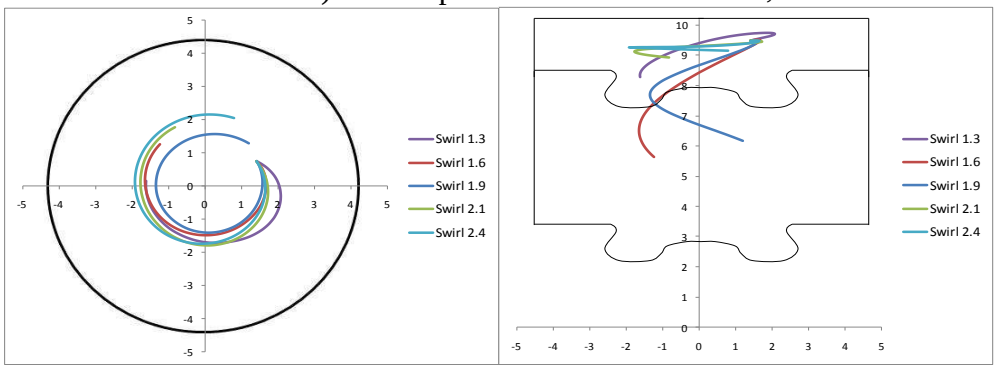

d) Zone 4

Figure 8.4 Paths of particle formed in Zone 1, 2, 3 and 4 tracked from CA 35° ATDC

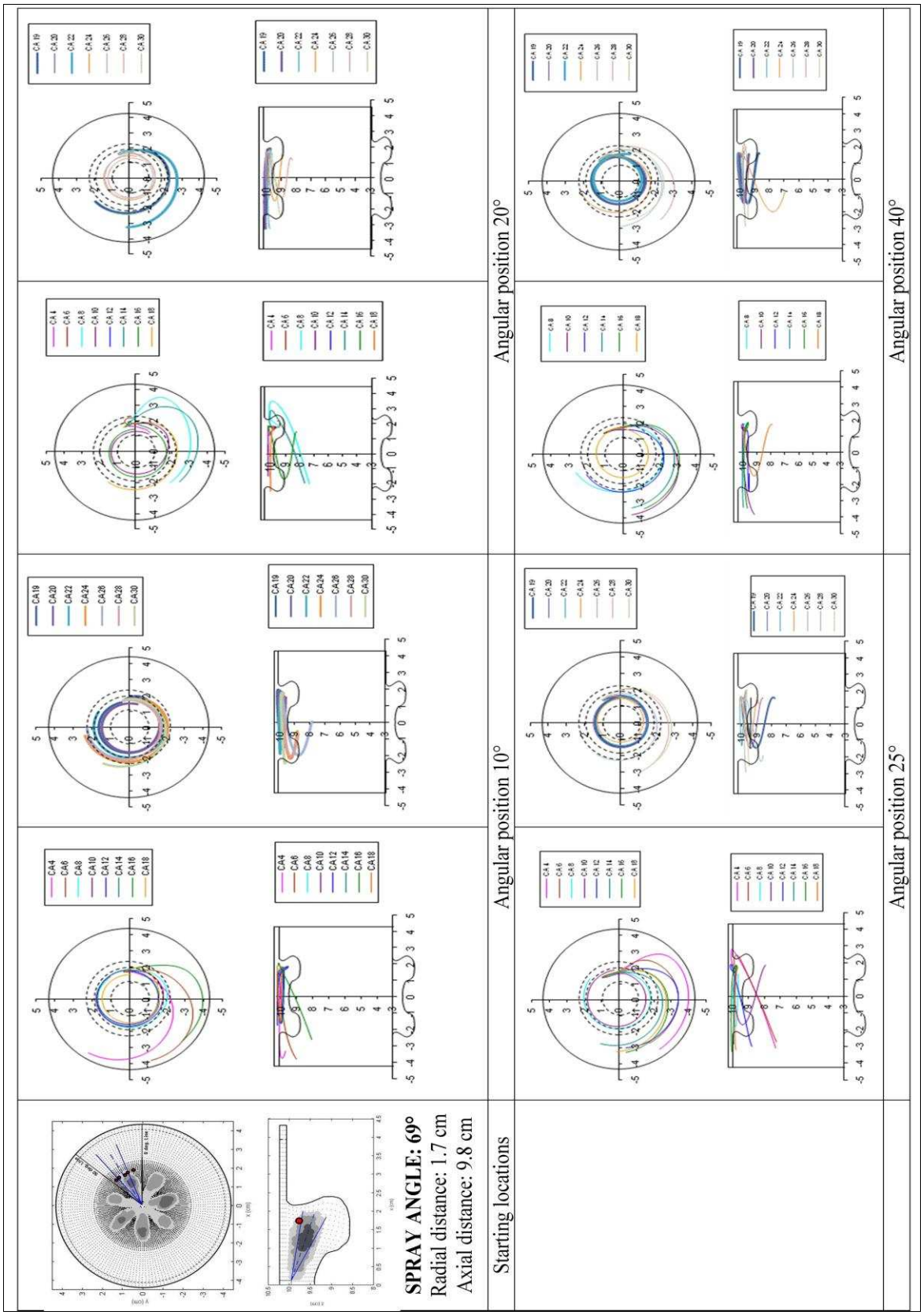

Figure 8.5 Paths of soot particles tracked from above and downstream of the spray with spray angle 69° at different angular positions with varying crank angle instants of 2° CA to 30° CA ATDC

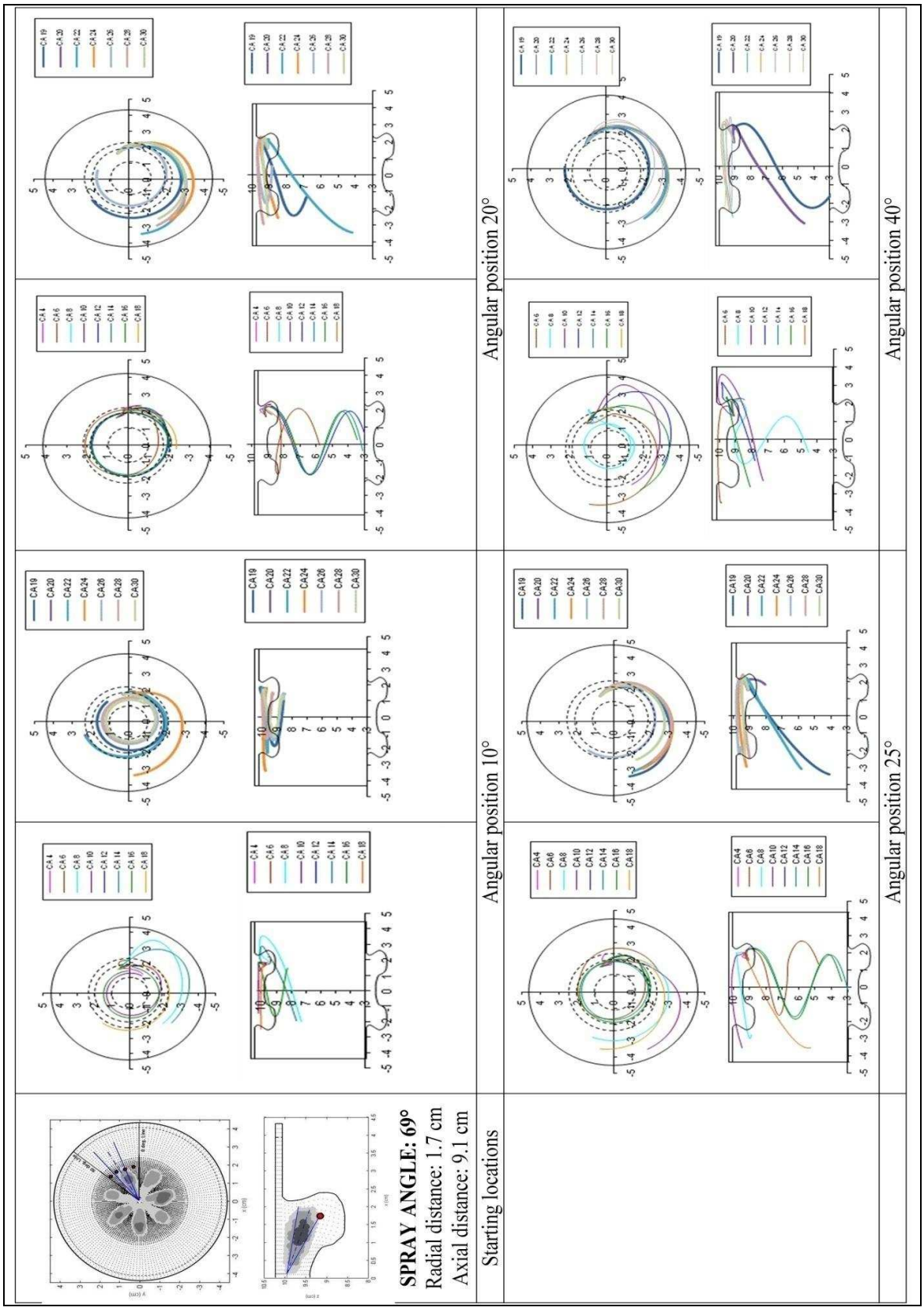

Figure 8.6 Paths of soot particles tracked from below and downstream of the spray with spray angle 69° at different angular positions with varying crank angle instants of 2° CA to 30° CA ATDC

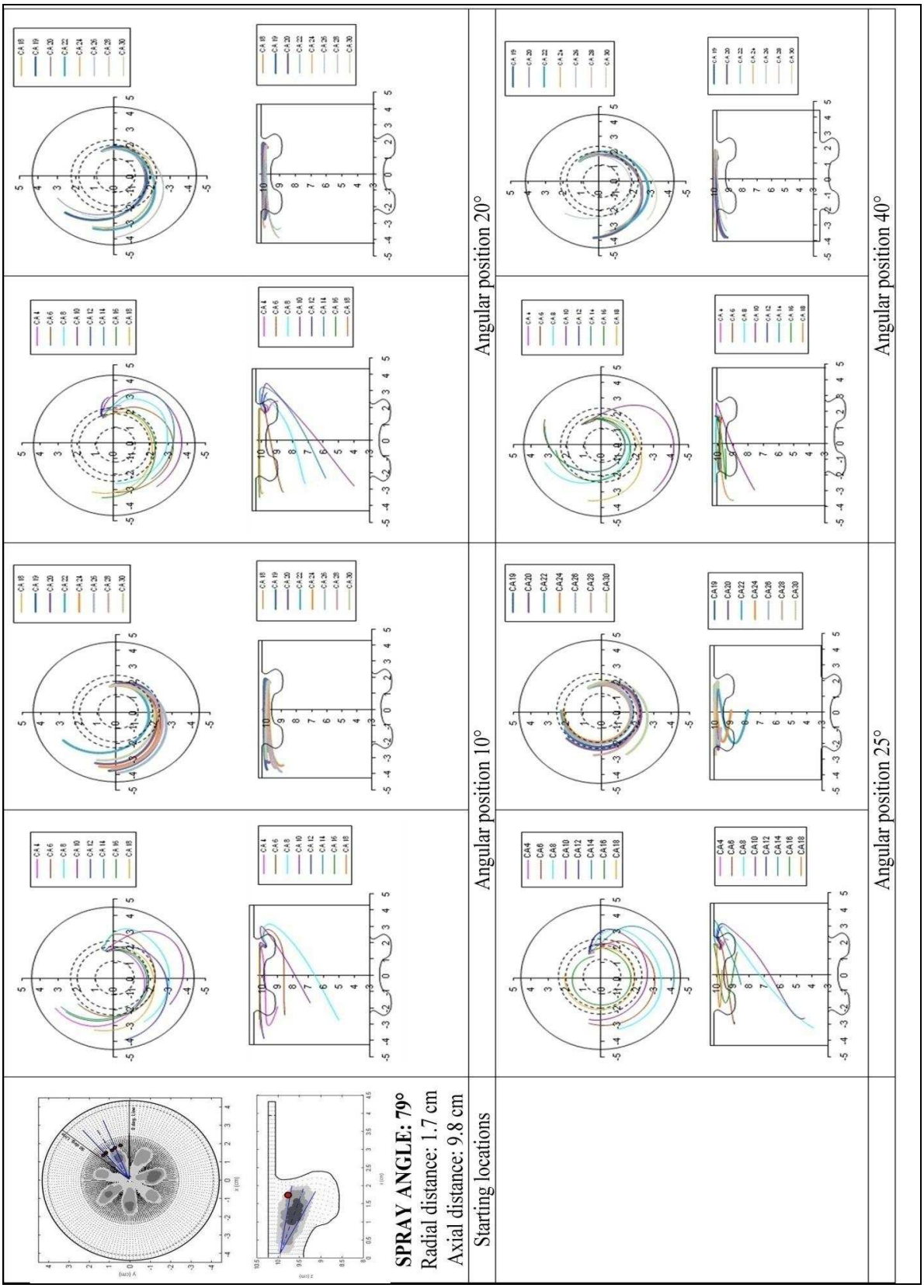

Figure 8.7 Paths of soot particles tracked from above and downstream of the spray with spray angle 79° at different angular positions with varying crank angle instants of 2° CA to 30° CA ATDC

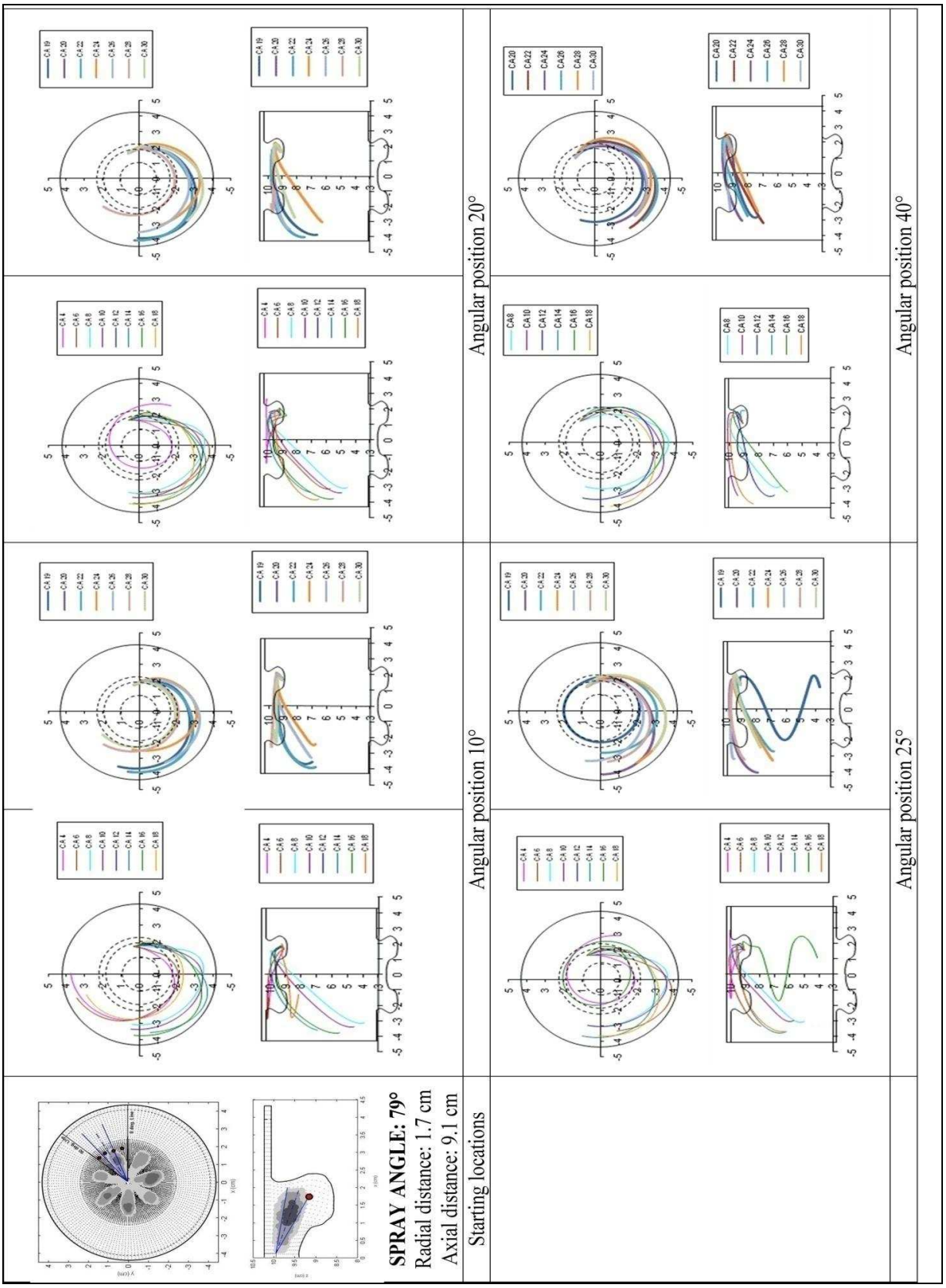

Figure 8.8 Paths of soot particles tracked from below and downstream of the spray with spray angle 79° at different angular positions with varying crank angle instants of 2° CA to 30° CA ATDC

(a) Immediately after soot is formed (i.e ~2º CA ATDC)

(b) Early phase of fuel injection (i.e ~4º CA ATDC)

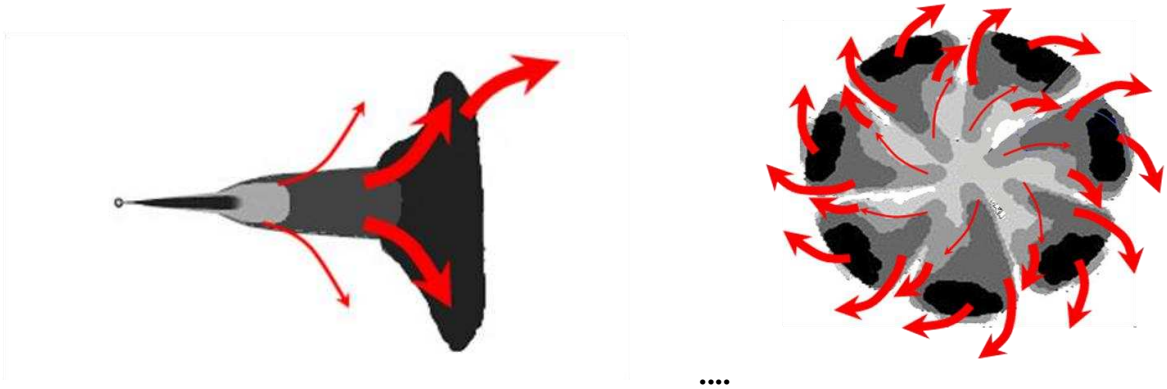

....

(c) Intermediate phase of fuel injection (i.e ~6-8º CA ATDC)

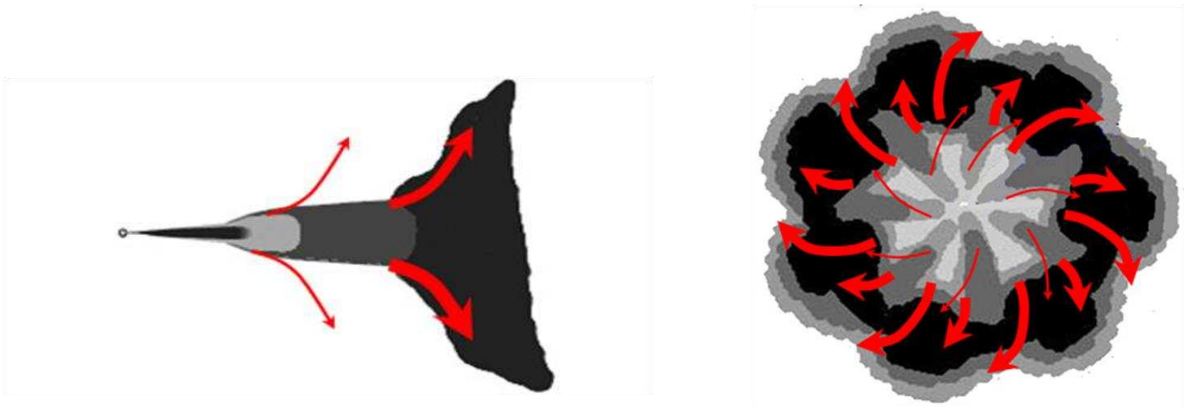

(d) Late phase of fuel injection (i.e ~12º CA ATDC)

Figure 9.1 Subjective illustrations of the likelihood of soot particles transfers to cylinder wall layer with progressively wider line widths of red arrows suggest increasing likelihood of soot transfers, and grey and black colour scales show relative in-cylinder soot concentration

APPENDICES

Appendix A: Influence of Mesh Configurations on Soot Particle Paths

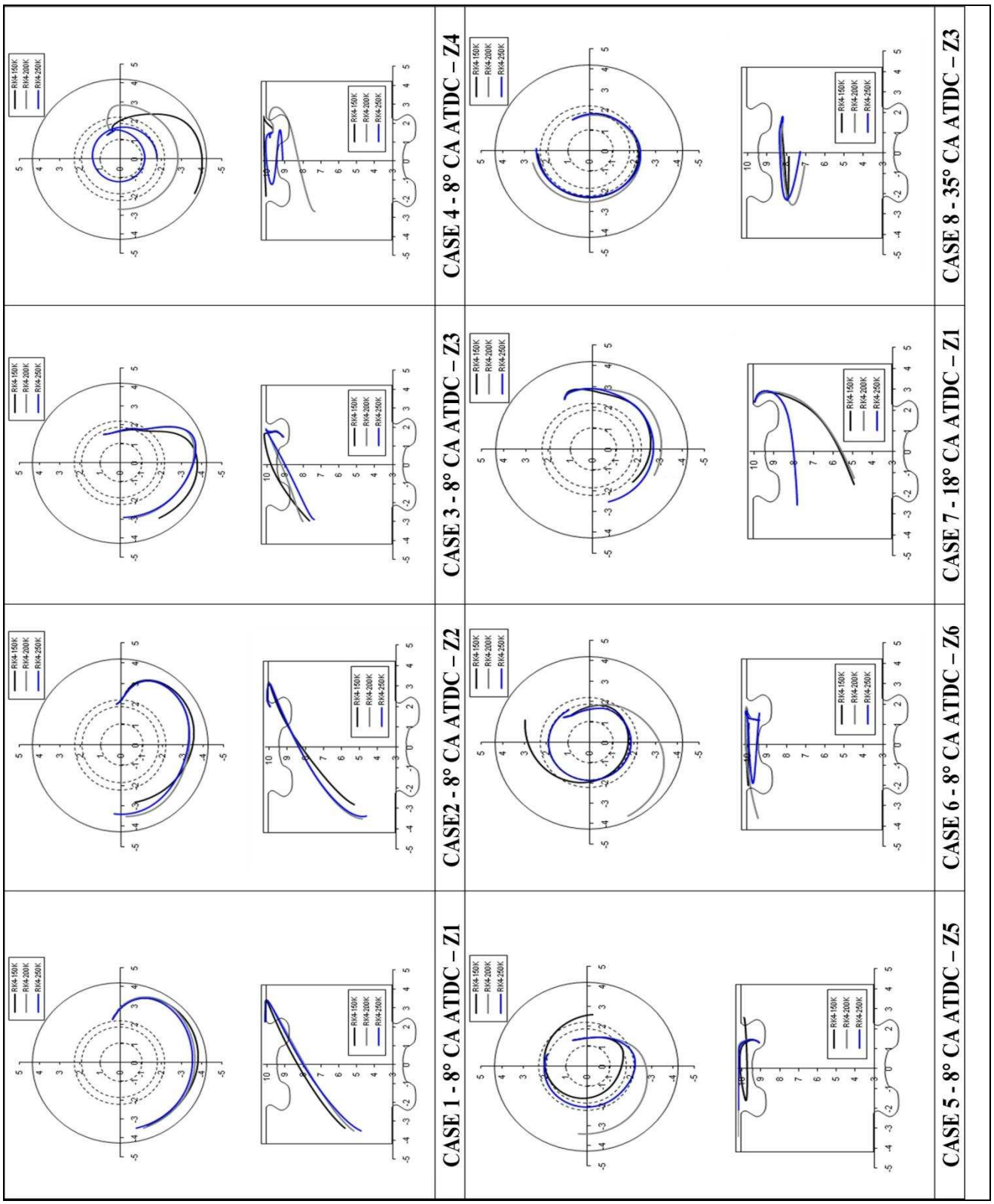

Figure A1.1 Soot particle paths from different starting points with three mesh configurations

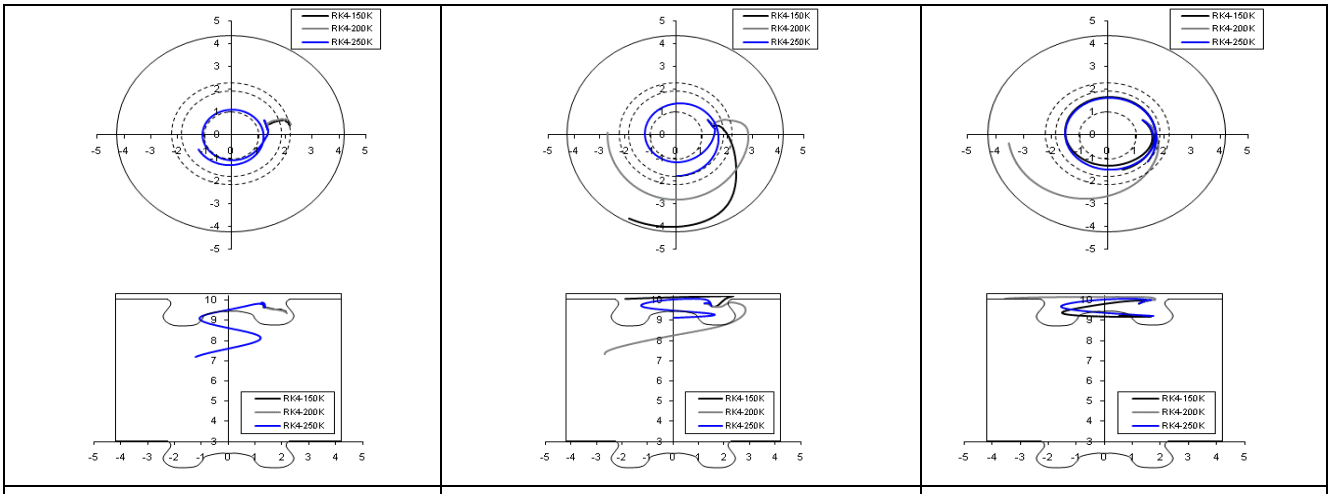

4° CA ATDC	8° CA ATDC	12° CA ATDC
Radial distance =1.4 cm, Angular position=28°, Axial distance = 9.85 cm (Case 4)		

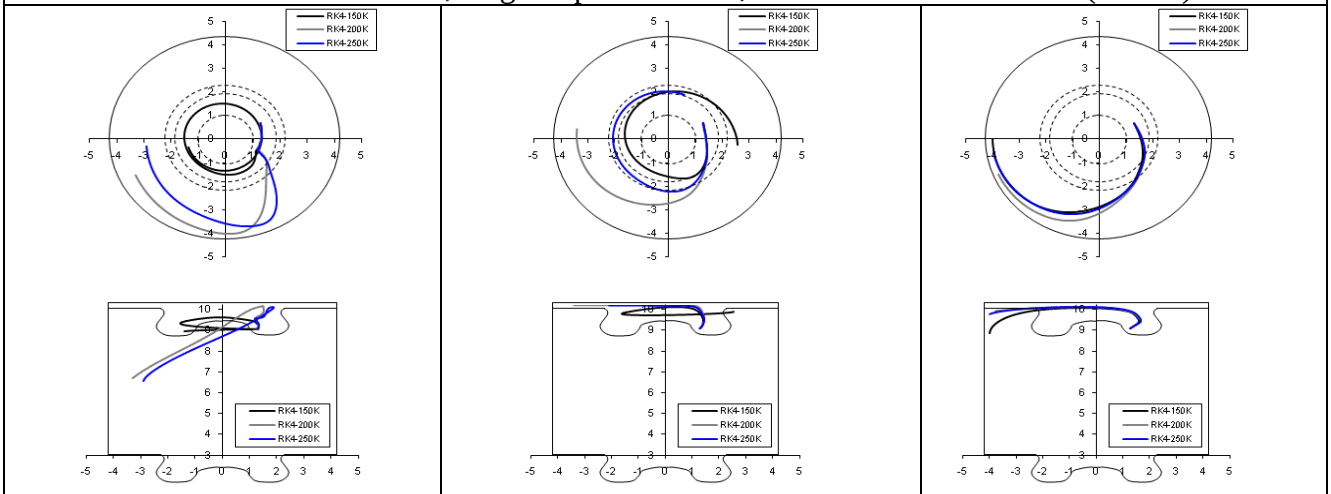

4° CA ATDC	8° CA ATDC	12° CA ATDC
Radial distance =1.45 cm, Angular position = 28°, Axial distance = 9.1 cm (Case 5)		

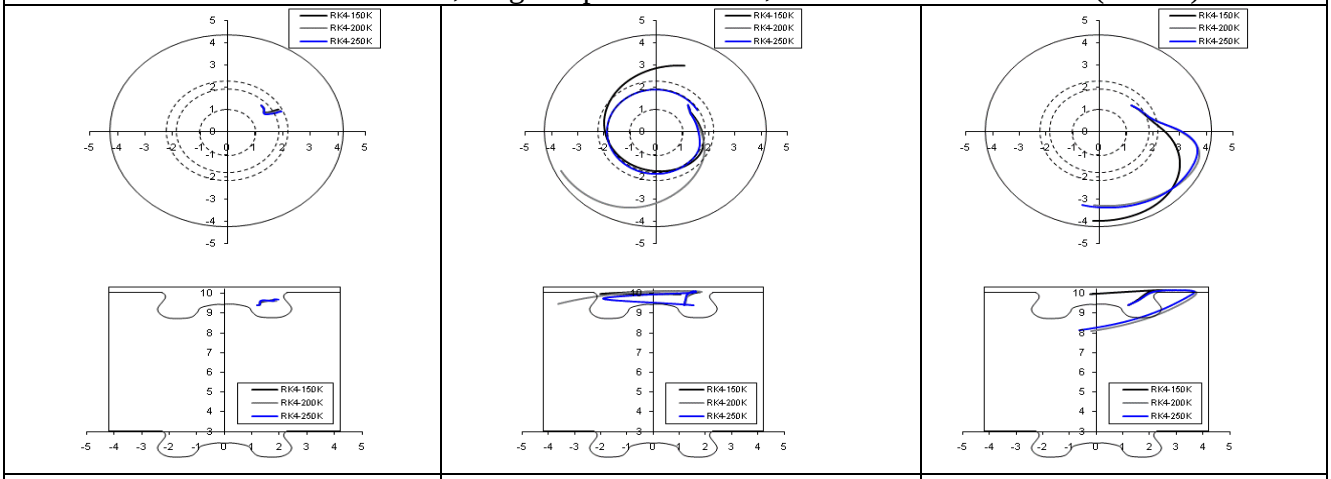

4° CA ATDC	8° CA ATDC	12° CA ATDC
Radial distance =1.7 cm, Angular position = 28°, Axial distance = 9.42 cm (Case 6)		

Figure A1.2 Soot particle paths from different starting instants with three mesh configurations for Case 4, 5 and 6